Characterization and Kinetic Studies of Palladium and Rhodium Catalysts in the Three-Way Catalyst System

---

A

Dissertation

Presented to

the faculty of the School of Engineering and Applied Science

University of Virginia

---

in partial fulfillment

of the requirements for the degree

Doctor of Philosophy

by

Silvia Marino

December 2023

APPROVAL SHEET

This

Dissertation

is submitted in partial fulfillment of the requirements
for the degree of

Doctor of Philosophy

Author: Silvia Marino

This Dissertation has been read and approved by the examing committee:

Advisor: William Epling

Advisor:

Committee Member: Christopher Paolucci

Committee Member: Robert Davis

Committee Member: Jason Bates

Committee Member: Michelle Personick

Committee Member:

Committee Member:

Accepted for the School of Engineering and Applied Science:

Jennifer L. West, School of Engineering and Applied Science

December 2023

Acknowledgement

This whole thesis would not have been possible without a few people I would like to acknowledge.

I would like to begin by thanking my advisor, Professor Epling. First for making my dream of pursuing a PhD come true. Thank you for trusting me, pushing me to prove my ideas, and supporting me even when nothing was working. But most importantly, thank you for giving me, Lai and Yu-Ren a sense of family when we most needed it.

I would like to thank Professor Davis for everything you have taught me during these years and for discussing with me and Bill all those weird chemisorption isotherms, kinetic or spectroscopic data. Also, thank you for sharing with me your love for kinetics, spectroscopy, Italian food and coffee. A special thanks also to Professor Paolucci, for being a great, really great teacher, but also for our numerous discussions about science, but also, really, about literally everything else. Thank you to all the catalysis professors for creating an environment where we all feel like you all are our advisors and consider all the catalysis people in ChemE our labmates.

I'd like to extend an unconventional acknowledgment to three professors, along with their research groups, who have deeply influenced my PhD journey: Professor Iglesia, Professor Flaherty, and Professor Christopher. Their papers inspired me to pursue a PhD program, fired my curiosity about catalysts and specific techniques, and taught me a lot about kinetics and spectroscopy.

Thanks to my labmates and friends at UVA who taught me a lot, scientifically and culturally, and let me annoy them during their time at UVA and after. So, thanks to Kevin, Surya, Carlos, Fatima, Kanika, Zexian, Henry, Colby, Dipesh, Konstantin, Keka, Anu, Anna and Jack for sharing this amazing experience with me and for being my friends. A big thank you to Lai and Yu-Ren, for being the best friends and labmates I could have ever asked for and for all the good moments we

spent together and for having cake for dinner with me, while we all knew it was not the best idea. Thanks to Sugandha, without whom I would have never been able to survive these last two years. My peas in pod. Thank you for the food and coffee dates, for doing infinite puzzles with me, for the many laughs and the tears, for sharing the most difficult moments with me, but also the funniest, for accepting the weirdo in me without judging and for always protecting croissants and guacamole. A loving thanks to Marina, my Spanish sister, the person I started this experience with. Thank you for making me laugh and letting me cry - just on Wednesdays - for eating gigantic burgers with me and also for not killing me after I made you walk a lot. Thank you to Sergio, for giving me the experience instant friendship, for the infinite laughs in the lab and outside and for letting me be your elf. Thanks to Polimi people, Umberto, Eli and Gio, but also to Camilla and Carmelo, for being my little Italian community here in Charlottesville and fighting with me the battle against pineapple on pizza. Thanks to Ashley for being a wonderful friend and having wine nights. For being so similar to me, but also different. You really made grad school way easier. I also would like to thank my favorite roommates: Kylie, Beibei and Jing. For having dinner with me, analyzing people's different social traits, preparing the Christmas tree very early, doing puzzles and making desserts at night. Thank you for making our anonymous apartment(s) a warm home.

I also would like to thank my colleagues at Ford, with a special mention to Bean, who has been a fantastic mentor during my internship and a real role model as a researcher. I would like to thank my colleagues at General Motors. A loving mention goes to Raneen for being my friend and introducing me to the delicious Iraqi food.

I am very grateful to have my Italian friends by my side: Arti, Pilo, Ricky, Kos, Ste, Torna, Giaggia, Paola, Angela, Ally, Mirko, Nando, Beppe, Foppo, Lucione, Gio, Terry, Fra, Marco Sorbona, Zuenni, Carre, Berri, Umbe, Moro, Tia, Ste, Garda, Stefo, Cisco, Taro and Costanzo. Thank you

for working with me on keeping our friendship up, despite the distance and my physical absence in many important moments of your lives.

I also would like to thank Jonathan, for being the kind of man who opens the car door to a woman. Thank you for cheering my successes but also being supportive during challenging times. Thank you for giving me a little bit of your patience and being (very) patient with me while I send so many videos of tortoises.

A huge thanks to my family: my mom, my dad, Dario, my aunt and my grandma. Thank you for supporting me all these years and giving me the education and moral values that have shaped the person I am today. I am deeply grateful for your selflessness as I go far away to chase my dreams.

Abstract

The three-way catalyst (TWC) is a critical component in gasoline fueled vehicles' aftertreatment systems, able to simultaneously convert NO, CO and unburnt hydrocarbons into less harmful products, when the engine works under stoichiometric conditions. The typical TWC consists of Pt-group metals (Rh, Pt, Pd) dispersed onto alumina, along with other additives aimed at improving both catalyst activity and stability. Rh is used because of its ability to reduce NOx, while Pt and Pd are used because of their high activity towards oxidation reactions.

Because of increasingly stringent regulations imposed by the Environmental Protection Agency (EPA) the TWC system continues to evolve to be more efficient and have higher stability. In addition, the price volatility that characterizes the Pt-group metals has challenged automotive companies and catalyst suppliers to seek new solutions to reduce the cost associated with TWC.

To design new catalyst formulations that are efficient, durable and less costly, a detailed understanding of the reaction mechanism during the TWC process is necessary. Here, we focus on the study of two model catalysts: Rh/Al_2O_3 and Pd/CeO_2.

Rh plays a crucial role in the TWC, even though it is present in low amounts due to its activity, but also high price. Rh catalysts are also characterized by high Rh mobility. The presence of reactants, such as CO, O_2, NO and H_2O, induces structural changes that influence the catalyst activity and selectivity. Using a combination of kinetics and spectroscopic studies we investigated Rh single atoms-nanoparticles interconversion during CO oxidation. We observed that Rh catalysts undergo structural changes even at higher temperature under CO/O_2 oxidizing mixtures, affecting the Rh nanoparticle fraction, which are the active sites for CO oxidation. These structural changes exhibit size dependency, with smaller nanoparticles being more prone to disperse into single atoms. In

addition, the presence of water, a major component in the exhaust gas, did not have any effect on nanoparticle disintegration. On the contrary, during the NO reduction by CO reaction, we observed that water led to changes in reaction kinetics and product selectivities when water was present in the feed composition. Preliminary studies suggested that ammonia might induce changes in the fraction of Rh nanoparticle and single atoms present in the catalyst.

The final study of this work focuses on Pd/CeO_2 catalysts. Characterizing these catalysts via conventional techniques presents challenges. For example, when using CO chemisorption, the reaction between CO and ceria lattice oxygen results in carbonate formation, leading to an overestimation of the CO uptake. To address this issue, we proposed a modified CO chemisorption method, which involves CO_2 exposure prior to CO adsorption, with the goal of hindering further carbonate formation during CO chemisorption. This technique was validated through CO oxidation kinetics and DRIFTS studies. This study aims to facilitate the quantification of exposed metal sites on OSC supports, which is crucial for calculating turnover frequency and comparing different catalyst formulations.

List of Figures

Figure 1.1: Tier 3 emission standards. Fleet average of NOx + NMOHC limits for light-duty vehicles (LDT1), and LDT 2 and MDPV (medium duty trucks) up to 10,000 lb. 2

Figure 1.2: TWC system operating window 3

Figure 1.3: price of Rh, Pd and Pt 7

Figure 2.1: Reactor schematic. In this representation, the main manifold is directed towards the microreactor, while the secondary manifold is directed towards the by-pass line. 16

Figure 2.2: Incident beam trajectory for DRIFTS cells 18

Figure 3.1: DRIFTS spectra obtained after He purge after CO adsorption at 35 °C on 0.05%Rh/Al_2O_3, 0.1%Rh/Al_2O_3, 0.1%Rh/Al_2O_3 H_2 -700°C, 0.1%Rh/Al_2O_3 H_2-800°C, 0.1%Rh/Al_2O_3-Cycling-Aged, and 0.1%Rh/Al_2O_3 H_2-900°C – plotted in rank of dispersion as measured by H_2 chemisorption. The CO concentration during exposure was 8400 ppm. Prior to the CO adsorption, the catalysts were reduced at 500 °C in 5% H_2 for 30 min. The Kubelka-Munk intensity of the largest peak in each spectrum was normalized to 1. For the 0.1%Rh/Al_2O_3 H_2-900°C sample, the KM intensity between 1950 and 1840 cm^{-1} was multiplied by 10 and displayed in the inset red-bordered box. 32

Figure 3.2: CO oxidation Arrhenius plots obtained from the 0.05%Rh/Al_2O_3, 0.1%Rh/Al_2O_3 H_2-700°C and 0.1%Rh/Al_2O_3 H_2-900°C samples. CO = 8400-13000 ppm, CO/O_2 = 0.9, total flowrate = 500-750 sccm. The catalysts were pretreated in 5% H_2 at 500 °C for 30 min. The results shown were obtained after reaching steady-state, with the temperature changing from high to low temperature. 33

Figure 3.3: Summary of the temperature at which the change in CO oxidation kinetics occurs for 0.05%Rh/Al_2O_3 (<1 nm), 0.1%Rh/Al_2O_3 (1.1 nm), 0.1%Rh/Al_2O_3 H_2-700°C (1.6 nm), 0.1%Rh/Al_2O_3 H_2-800°C (3.3 nm), and 0.1%Rh/Al_2O_3 H_2-900°C (9.2 nm). CO = 8400-13000 ppm, CO/O_2 = 0.9, flowrate = 500-750 sccm. The catalysts waere pretreated in 5% H_2 at 500 °C for 30 min. 38

Figure 3.4: DRIFTS spectra of 0.1%Rh/Al_2O_3 H_2-700°C during CO oxidation at 220, 240, 260, 280 and 280°C. CO = 8400 ppm; O_2 = 9250 ppm. The catalyst was first exposed to 1% O_2 at 500 °C for 30 min, followed by He purge for 10 min and 5% H_2 at 500 °C for 30 min. The spectra were normalized by the intensity of the peak at 2026 cm^{-1}, after applying the gas phase subtraction. 40

Figure 3.5: Normalized areas of symmetric and asymmetric gem-dicarbonyl features (2090/2026) and linear Rh-CO nanoparticle and asymmetric gem-dicarbonyl species (2070/2026) for each temperature investigate in the range between 220 – 300 °C 41

Figure 3.6: DRIFTS spectra during CO + O_2 exposure at 260 °C on 0.1%Rh/Al_2O_3 H_2-700°C. CO = 8400 ppm; O_2 = 2000, 4200, 6250, or 9250 ppm. The spectra were normalized by the highest intensity peak for comparison. 43

Figure 3.7: Normalized CO oxidation rates obtained on 0.1%Rh/Al_2O_3 H_2-700°C. CO = 8400 ppm O_2 = 9250 ppm; total flowrate = 750 sccm. The catalyst was reduced in 5% H_2 at 500 °C for 30 min. The black squares represent the reaction rates normalized by the number of Rh surface sites obtained from the H_2 chemisorption measurement, the red circles are the reaction rates normalized by the number of Rh surface

sites obtained from the H_2 chemisorption at high temperature and the half that amount at low temperature, based on changes observed in the DRIFTS spectra. 45

Figure 4.1: CO adsorption on 0.05% Rh/Al_2O_3 and 0.01%Rh/Al_2O_3 at 35°C. The catalysts were initially treated in 1% O_2 at 500°C for 30 min, then purged with Ar and finally reduced in 5% H_2 for 30 min. The catalysts were exposed to 8400 ppm CO until saturation. 59

Figure 4.2: 8400 ppm CO/He adsorption at 200°C on 0.05% Rh/Al_2O_3 over time until saturation. The catalyst was initially treated in 1% O_2 at 500°C for 30 min, then purged with Ar and finally reduced in 5% H_2 for 30 min. (a) spectra taken every 5 minutes from time 0 (purple) to 116 min (red); (b) spectra taken at 5 min and 116 showing the isosbestic points. 61

Figure 4.3: 8400 ppm CO/He adsorption at 200°C on 0.05% Rh/Al2O3 over time until saturation. The catalyst was initially treated in 1% O2 at 500°C for 30 min, then purged with Ar and finally reduced with 5% H2 for 30 min. The spectra were taken every 5 minutes from time 0 to 132 min. 62

Figure 4.4: CO_2 profile vs time during CO+O_2 reaction at 327°C on 0.05% Rh/Al_2O_3. CO = 8400 ppm, O_2 = 9200 ppm, diluted in N_2. Prior to the reaction, the catalyst was reduced with 5% H_2 for 30 min. 63

Figure 4.5: 8400 ppm CO + 9200 ppm O_2/He adsorption at 200°C on 0.05% Rh/Al_2O_3. The catalyst was initially treated in 1% O_2 at 500°C for 30 min, then purged with Ar and finally reduced with 5% H_2 for 30 min. The temperature decreased in He to 200°C. The spectra shown were taken during CO + O_2 adsorption at time = 2 min (black) and 125 min (red), when saturation was reached. 64

Figure 4.6: 8400 ppm CO + 9200 ppm O_2/He adsorption at 300°C on 0.05% Rh/Al_2O_3 for 198 minutes. The catalyst was initially treated in 1% O_2 at 500°C for 30 min, then purged with Ar and finally reduced with 5% H_2 for 30 min. The temperature decreased in He to 300°C. The spectra shown were taken during CO + O_2 adsorption from time = 2 min (purple) to time = 198 min (red), when saturation was reached. . 65

Figure 4.7: 8400 ppm CO + H_2O/He adsorption at 200°C on 0.05% Rh/Al_2O_3 for 140 minutes. The catalyst was initially treated in 1% O_2 at 500°C for 30 min, then purged with Ar and finally reduced with 5% H_2 for 30 min. The temperature decreased in He to 200°C and H_2O was introduced. After saturating the catalyst with water, a background was taken and CO was added in the gas stream. The spectra shown were taken during CO + H_2O adsorption from time = 2 min (purple) to time = 140 min (red), when saturation was reached. 66

Figure 4.8: Purge with He + H_2O on 0.05% Rh/Al_2O_3: (a) spectra over time until stabilization; (b) last spectrum 68

Figure 4.9: Dynamics of CO + H_2O adsorption on 0.05% Rh/Al_2O_3 at 300°C.The catalyst was initially treated in 1% O_2 at 500°C for 30 min, then purged with Ar and finally reduced with 5% H_2 for 30 min. The temperature decreased in He to 300°C and H_2O was introduced. After saturating the catalyst with water, a background was taken, and 8400 ppm CO was added in the gas stream. The spectra shown were taken during CO + H_2O adsorption from time = 2 min (purple) to time = 108 min (red), when saturation was reached. 68

Figure 4.10: CO_2 profile vs time during wet CO+O_2 reaction on 0.05% Rh/Al_2O_3. CO = 8400 ppm, O_2 = 9200 ppm, H_2O = 6%, diluted in N_2. Prior to the reaction, the catalyst was reduced with 5% H_2 for 30 min. 70

Figure 4.11: He purge in the presence of water after CO + H_2O adsorption at 300°C. 71

Figure 4.12: CO + O_2 + H_2O adsorption 200°C on 0.05% Rh/Al_2O_3. The catalyst was initially treated in 1% O_2 at 500°C for 30 min, then purged with Ar and finally reduced with 5% H_2 for 30 min. The temperature was decreased in He to 200°C and H_2O was introduced. After saturating the catalyst with water, a background was taken, and 8400 ppm CO and 9200 ppm O_2 were added into the gas stream. (a) Spectra shown were taken during CO + O_2 + H_2O adsorption from time = 2 min (purple) to time = 204 min (red), when saturation was reached; (b) spectra taken during the purge with He and water from time 0 min (purple) to time = 20 min (red) 71

Figure 4.13: CO + O_2 + H_2O adsorption 300°C on 0.05% Rh/Al_2O_3. The catalyst was initially treated in 1% O_2 at 500°C for 30 min, then purged with Ar and finally reduced with 5%H_2 for 30 min. The temperature decreased in He to 300°C and H_2O was introduced. After saturating the catalyst with water, a background was taken, and 8400 ppm CO and 9200 ppm O_2 were added into the gas stream. (a) Spectra shown taken during CO + O_2 + H_2O adsorption from time = 2 min (purple) to time = 144 min (red), when saturation was reached; (b) spectra taken during the purge with He and water from time 0 min (purple) to time = 106 min (red)..... 73

Figure 4.14: CO, CO+O_2 and CO adsorption on 0,1%Rh/Al_2O_3 at 300°C. The catalyst was initially treated in 1% O_2 at 500°C for 30 min, then purged with Ar and finally reduced with 5% H_2 for 30 min. The temperature was decreased in He to 300°C. 74

Figure 5.1: NO reduction by CO kinetics with a 0.05% Rh/Al_2O_3 catalyst. (a) NO (blue) and CO (red) conversion; (b) N_2O (green) and NH_3 (fuscia) selectivity; (c) Arrhenius plot of NO, CO, N_2O and NH_3 rates. The catalyst was reduced in 5% H_2 for 30 min at 500°C. The reaction mixture included 1000 ppm CO, 500 ppm NO and 6% H_2O, diluted in N_2. The conversions shown were taken at steady-state..... 84

Figure 5.2: NO reduction by CO kinetics on 0.1% Rh/Al_2O_3. (a) NO (blue) and CO (red) conversions and (d) N_2O and N_2 selectivity for NO/CO = 2; (b) NO (blue) and CO (red) conversions and (e) N_2O and N_2 selectivity for NO/CO = 1; (c) NO (blue) and CO (red) conversions and (f) N_2O and N_2 selectivity for NO/CO = 0.5. The catalyst was reduced in 5% H_2 for 30 min at 500°C. The reaction mixture included 1000 ppm CO, NO varying to obtain NO/CO = 2, 1 and 0.5, diluted in N_2. The conversions were taken at steady-state. 87

Figure 5.3: NO reduction by CO kinetics on 0.1% Rh/Al_2O_3. Arrhenius plots of NO, CO, N_2O rates. (a) NO/CO = 2; (b) NO/CO = 1; (c) NO/CO = 0.5. The catalyst was reduced in 5% H_2 for 30 min at 500°C. The reaction mixture included 1000 ppm CO, NO varying to obtain NO/CO = 2, 1 and 0.5, diluted in N_2. 89

Figure 5.4: NO reduction by CO in the presence of 6% water over 0.1%Rh/Al_2O_3. NO and CO conversion and N_2, N_2O and NH_3 selectivity. The catalyst was reduced in 5% H_2 for 30 min at 500°C. The reaction mixture included CO = 1000 ppm, NO varying to obtain (a) and (d) NO/CO = 2; (b) and (e) 1 (b); and (e) and (c) and (f) 0.5; and H_2O = 6%, diluted in N_2. 91

Figure 5.5: NO reduction by CO in the presence of water over 0.1%Rh/Al_2O_3. Arrhenius plots of NO, CO, N2O rates. (a) NO/CO = 2; (b) NO/CO = 1; (c) NO/CO = 0.5. The catalyst was reduced in 5% H_2 for 30 min at 500°C. The reaction mixture included 1000 ppm CO, NO varying to obtain NO/CO = 2, 1 and 0.5, H_2O = 6%, diluted in N_2..... 93

Figure 5.6: NO reduction by CO on 0.1% Rh/Al_2O_3 in the absence and in the presence of water. NO/CO = 0.5, 1 and 2. NO conversion, N_2O and NH_3 selectivity. The catalyst was reduced in 5% H_2 for 30 min at

500°C. The reaction mixture included CO = 1000 ppm, NO varying to obtain NO/CO = 2 (a), (d) and (g), 1 (b), (e) and (h) and 0.5 (c), (f) and (i) and H_2O = 1 (green), 3 (red) and 6% (blue), diluted in N_2. 95

Figure 5.7: Comparison of NO conversion profile during dry NO reduction by CO in the presence and absence of 100 ppm NH_3 on 0.1% Rh/Al_2O_3. NO/CO = 1 and 0.5. The catalyst was reduced in 5% H_2 for 30 min at 500°C. The reaction mixture included CO = 1000 ppm, NO varying to obtain (a) NO/CO = 1 and (b) 0.5; NH_3 = 0 ppm (blue) or 100 ppm (red), diluted in N_2. 97

Figure 5.8: Comparison of N_2O selectivity during dry NO reduction by CO in the presence and absence of 100 ppm NH_3 on 0.1% Rh/Al_2O_3. NO/CO = 1 and 0.5. The catalyst was reduced in 5% H_2 for 30 min at 500°C. The reaction mixture included CO = 1000 ppm, NO varying to obtain (a) NO/CO = 1 and (b) 0.5; NH_3 = 0 ppm (blue) or 100 ppm (red), diluted in N_2. 98

Figure 5.9: Comparison of NO conversion profile and product selectivity during wet NO reduction by CO in the presence and absence of 100 ppm NH_3 on 0.1% Rh/Al_2O_3. NO/CO = 0.5. The catalyst was reduced in 5% H_2 for 30 min at 500°C. The reaction mixture included CO = 1000 ppm, NO = 500 ppm; H_2O = 6%; NH_3 = 0 ppm (blue) or 100 ppm (red), diluted in N_2.(a) NO conversion; (b) N_2O and NH_3 selectivity..... 99

Figure 5.10: DRIFTS spectrum of CO adsorption on 0.1% Rh/Al_2O_3. The catalyst was treated in 1% O_2 at 500°C for 30 min, followed by Ar purge and reduced in 5% H_2 at 500°C for 30 min. The temperature was decreased to 265°C in Ar. The catalyst was then exposed to CO = 5000 ppm until no changes in the spectra were observed. (a) CO adsorption; (b) Ar purge. 101

Figure 5.11: NO adsorption on 0.1% Rh/Al_2O_3 using DRIFTS. The catalyst was treated in 1% O_2 at 500°C for 30 min, followed by Ar purge and reduced in 5% H_2 at 500°C for 30 min. The temperature decreased to 265°C in Ar. The catalyst was then exposed to NO = 5000 ppm until saturation. 102

Figure 5.12: NH_3 adsorption on 0.1% Rh/Al_2O_3 using DRIFTS. The catalyst was treated in 1% O_2 at 500°C for 30 min, followed by Ar purge and reduced in 5% H_2 at 500°C for 30 min. The temperature decreased to 265°C in Ar. The catalyst was then exposed to NH_3 = 500 ppm until saturation. 104

Figure 5.13: NO + CO adsorption on 0.1% Rh/Al_2O_3. The catalyst was treated in 1% O_2 at 500°C for 30 min, followed by Ar purge and reduced in 5% H_2 at 500°C for 30 min. The temperature decreased to 265°C in Ar. The catalyst was then exposed to a mixture of CO = 5000 and NO = 5000 ppm until saturation. . 105

Figure 5.14: NO + CO adsorption on 0.1% Rh/Al_2O_3. The catalyst was treated in 1% O_2 at 500°C for 30 min, followed by Ar purge and reduced in 5% H_2 at 500°C for 30 min. The temperature decreased to 265°C in Ar. The catalyst was then exposed to a mixture of CO = 5000 and NO = 5000 ppm until saturation. (a) focus on the 1200-1900 cm^{-1} range; (b) focus on the 2150-2300 cm^{-1} range 106

Figure 5.15: NO + CO adsorption – NO/CO = 2, 1 and 0.5 on 0.1% Rh/Al_2O_3. The catalyst was treated in 1% O_2 at 500°C for 30 min, followed by Ar purge and reduced in 5% H_2 at 500°C for 30 min. The temperature decreased to 265°C in Ar. The catalyst was then exposed to a mixture of CO = 5000 and NO = vary to obtain NO/CO = 0.5 (red), 1 (green) and 2 (blue) until saturation. 108

Figure 5.16: TPD after NO + CO adsorption on 0.1% Rh/Al_2O_3. The catalyst was treated in 1% O_2 at 500°C for 30 min, followed by Ar purge and reduced in 5% H_2 at 500°C for 30 min. The temperature decreased to 265°C in Ar. After the catalyst then exposed to a mixture of CO = 5000 ppm and NO = 5000 ppm and purged with Ar at 265°C, the temperature was increased until 500°C at a ramp rate of 10°C /min. 109

Figure 5.17: after NO + CO + NH_3 adsorption on 0.1% Rh/Al_2O_3. The catalyst was treated in 1% O_2 at 500°C for 30 min, followed by Ar purge and reduced in 5% H_2 at 500°C for 30 min. The temperature decreased to 265°C in Ar. After the catalyst then exposed to a mixture of CO = 5000 ppm; NO = 2500 ppm; NH_3 = 500 ppm. and purged with Ar at 265°C, the temperature was increased until 500°C at a ramp rate of 10°C /min. (a) NO + CO + NH_3 adsorption; (b) Ar purge focused on 1900-2200 cm^{-1} region; (c) TPD focused on 1900-2200 cm^{-1} region..... 111

Figure 5.18: in-situ CO oxidation in the presence and absence of NH_3 on 0.1%Rh/Al2O3 – 700°C 220, 240, 260, 280 and 280°C using DRIFTS. CO = 8400 ppm ; O_2 = 9250 ppm. The catalyst was first exposed to 1% O_2 at 500 °C for 30 min, followed by He purge for 10 min and 5% H_2 at 500 °C for 30 min. The spectra were normalized by the intensity of the peak at 2026 cm^{-1}, after applying the gas phase subtraction.(a) NH_3 = 500 ppm; (b) NH_3 = 0 ppm. 114

Figure 5.19: Comparison of wet NO reduction by CO in the presence and absence of NH_3 on 0.1% Rh/Al_2O_3-1.1 and 9.2 nm. The catalysts were reduced in 5% H_2 for 30 min at 500°C. The reaction mixture included CO = 1000 ppm; NO varying to obtain (a) and (b) NO/CO = 2; (c) and (d) 0.5 (b); and (e) and (f) and (f) 1, NH_3 = 0 (blue) or 100 ppm (fuscia) and H_2O = 6%, diluted in N_2. (a), (c) and (e) 0.1% Rh/Al_2O_3 – 1.1 nm; (b), (d) and (f) 0.1% Rh/Al_2O_3 – 9,2 nm;..... 115

Figure 5.20: Selectivity towards N_2O and NH_3 on 0.1% Rh/Al_2O_3 – 1.1 nm and 9.2 nm. The catalysts were reduced in 5% H_2 for 30 min at 500°C. The reaction mixture included CO = 1000 ppm; NO varying to obtain (a) and (b) NO/CO = 2; (c) and (d) 0.5 (b); and (e) and (f) 1, NH_3 = 0 (dashed line) or 100 ppm (solid line) and H_2O = 6%, diluted in N_2. (a), (c) and (e) 0.1% Rh/Al_2O_3 – 1.1 nm; (b), (d) and (f) 0.1% Rh/Al_2O_3 – 9,2 nm; 118

Figure 5.21: CO + NO adsorption on 0.1% Rh/Al_2O_3 – 9.1nm using DRIFTS. The catalyst was treated in 1% O_2 at 500°C for 30 min, followed by Ar purge and reduced in 5% H_2 at 500°C for 30 min. The temperature decreased to 265°C in Ar. The catalyst was then exposed to NO-CO mixture until no changes in spectra were detected. CO = 5000 ppm; NO varying to obtain NO/CO = 2 (blue), 1 (green) and 0.5 (red). (a) spectral region between 1200 and 2500 cm^{-1}; (b) focus on the region between 1200 and 2500 cm^{-1} . 121

Figure 5.22: NH_3 reaction order on 0.1% Rh/Al_2O_3 1.1 nm.. The catalyst was reduced in 5% H_2 for 30 min at 500°C. The reaction mixture included CO = 1000 ppm; NO varying to obtain (a) NO/CO = 2; (b) NO/CO = 1; (c);NO/CO = 0.5, H_2O = 6%; NH_3 varied between 50 and 150 ppm 122

Figure 5.23: TPD after NO + CO wet – NH_3 reaction order with NO/CO = 0.5. The catalyst was reduced in 5% H_2 for 30 min at 500°C. After the catalyst was exposed to the reaction mixture including CO = 1000 ppm; NO = 500 ppm; H_2O = 6%; NH_3 varied between 50 and 150 ppm, diluted in N_2, the system was purged with N_2 and the temperature was increased to 500°C at 10°C/min..... 123

Figure 5. 24 repeated NO reduction by CO in the presence of water – NO and CO conversion and N_2O and NH_3 selectivity. The catalyst was reduced in 5% H_2 for 30 min at 500°C. The reaction mixture included CO = 1000 ppm; NO = 500 ppm; H_2O = 6%; 124

Figure 5.25: CO adsorption using DRIFTS on 0.05% Rh/Al_2O_3 fresh (purple), NO CO 24 h treated at 300°C (light-blue) and NO CO NH_3 for 24 h treated at 300°C (yellow). The catalyst was exposed to the reaction mixture including CO = 5000 ppm; NO = 2500 ppm for 24 h at 300°C and CO = 5000 ppm; NO = 2500 ppm; NH_3 = 500 ppm for 24 h at 300°C. Prior to CO adsorption, the catalyst was treated in 1% O_2 for 30 min at 500°C, followed by a purge in Ar and reduction in 5% H_2 for 30 min at 500°C. The temperature was then decreased to 35°C in At and the catalysts were exposed to CO = 5000 ppm until saturation..... 125

Figure 5. 26: Ar purge after CO adsorption. using DRIFTS on 0.05% Rh/Al_2O_3 fresh (purple), NO CO 24 h treated at 300°C (light-blue) and NO CO NH_3 for 24 h treated at 300°C (yellow). The catalyst was exposed to the reaction mixture including CO = 5000 ppm; NO = 2500 ppm for 24 h at 300°C and CO = 5000 ppm; NO = 2500 ppm; NH_3 = 500 ppm for 24 h at 300°C. Prior to CO adsorption, the catalyst was treated in 1% O_2 for 30 min at 500°C, followed by a purge in Ar and reduction in 5% H_2 for 30 min at 500°C. The temperature was then decreased to 35°C in Ar and the catalysts were exposed to CO = 5000 ppm until saturation. The system was finally purged with Ar until no changes in spectra were detected. 127

Figure 5.27: NO + CO exposure on 0.1% $Rh-Al_2O_3$ at 300, 350 and 400°C. The catalyst was treated in 1% O_2 for 30 min at 500°C, followed by a purge in Ar and reduction in 5% H_2 for 30 min at 500°C. The catalyst was the exposed to a reaction mixture including CO = 5000 ppm, NO varying to obtain NO/CO = 0.5 (b); NO/CO = 1 (c); NO/CO = 2. The effect of the reaction mixtures on the surface speciation was investigated at 300, 350 and 400°C. Spectra were taken until no changes were detected. 129

Figure 6.1: STEM images of the 1%Pd/CeO_2-10 nm, 1%Pd/CeO_2-25 nm and 1%Pd/CeO_2-100 nm samples 147

Figure 6.2: CO-DRIFTS obtained using the 1% Pd/CeO_2 catalysts characterized by 10 nm (purple), 25 nm (light blue) and 100 nm (blue) ceria nanoparticles. The catalysts were treated in 1% O_2 at 400°C for 30 min, followed by an Ar purge at 300°C and 5% H_2 for 30 minutes at 300°C. The catalysts were exposed to 5000 ppm CO/Ar at 35°C. 149

Figure 6. 3: DRIFTS spectra obtained during the CO_2-CO adsorption experiment using the 1% Pd/CeO_2 25 nm sample. The catalyst was treated in 1% O_2 for 30 min at 400°C, purged in Ar and reduced in 5% H_2 for 30 min at 300°C. The catalyst was exposed to 1% CO_2 at 35°C until saturation. This was followed by purging in Ar until carbonate decomposition/desorption stopped, then a new background was taken, and finally the sample was exposed to 5000 ppm CO. 156

Figure 6.4: Comparison between the dispersion measurements obtained via CO and CO_2-CO chemisorption on 1% Pd/CeO_2-10, 25 and 100 nm, 0.2% Pd/CeO_2-1µm, 0.8% Pd/CeO_2-1µm, 1.2% Pd/CeO_2-1µm and fresh 1.2% Pd/Al_2O_3. 158

Figure 6.5: CO oxidation (a) conversion profiles and (b) Arrhenius plot on 1%Pd/CeO_2 - 10, 25 and 100 nm. The catalysts were reduced at 300°C in 5% H_2 for 30 min. The catalysts were exposed to 5000 ppm CO and 2500 ppm O_2, balanced in N_2. The rates were taken at steady-state. The rates were normalized by Pd perimeter sites. 167

Figure 6.6: CO oxidation Arrhenius plot on 1.2%Pd/Al_2O_3 aged at 650, 750 and 850°C. The catalysts were reduced in 5% H_2 for 30 min at 400°C. The catalysts were exposed to CO = 5000 ppm, O_2 = 2500 ppm, H_2O = 6% balanced in N_2. The rates were taken at steady-state. The rates were normalized by Pd surface sites measured via CO_2-CO chemisorption. 168

Figure A.1: CO oxidation conversion from cordierite. CO = 8400 ppm, CO/O_2 = 0.9, total flowrate = 500. Cordierite = 250 mg. The cordierite was pretreated in 5% H_2 at 500°C for 30 min. All the data were obtained after reaching steady-state. 185

Figure A.2: CO oxidation Arrhenius plots obtained from the 0.05%Rh/Al_2O_3, 0.1%Rh/Al_2O_3, 0.1%Rh/Al_2O_3 H_2-700°C, 0.1%Rh/Al_2O_3 H_2-800°C and 0.1%Rh/Al_2O_3 H_2-900°C samples. CO = 8400-13000 ppm; CO/O_2 = 0.9, total flowrate = 500-750. Catalyst weight = 5-13 mg. The catalysts were

pretreated in 5% H_2 at 500°C for 30 min. The temperature was changed from high to low temperature. All the rate measurements were obtained at steady-state. 186

Figure A.3: CO oxidation Arrhenius plots obtained from the 0.05%Rh/Al_2O_3, 0.1%Rh/Al_2O_3, 0.1%Rh/Al_2O_3 H_2-700°C, 0.1%Rh/Al_2O_3 H_2-800°C, 0.1%Rh/Al_2O_3 Ford aged and 0.1%Rh/Al_2O_3 H_2-900°C. CO = 8400-13000 ppm; CO/O_2 = 0.9, H_2O = 6%, total flowrate = 500-750. Catalyst weight = 5-13 mg. The catalysts were pretreated in 5% H_2 at 500°C for 30 min. The temperature was changed from high to low temperature for all the samples with the exception of the 0.1%Rh/Al_2O_3, for which the temperature was changed from low to high temperature. All the rate measurements were obtained at steady-state. .. 187

Figure A.4: CO oxidation Arrhenius plot obtained from the 0.1%Rh/Al_2O_3. CO = 10000 ppm, H_2O = 6%, total flowrate = 500. Catalyst weight = 5 (w/ H_2O) and 13 (w/ H_2O) mg. The catalysts were pretreated in 5% H_2 at 500°C for 30 min. All the rate measurements were obtained at steady-state. 190

Figure A.5: CO_2 formation during Temperature Programmed Reaction on 0.1%Rh/Al_2O_3 and 0.1%Rh/Al_2O_3 H_2-900°C. CO = 8400 ppm, H_2O = 6%, total flowrate = 500. Catalyst weight = 13 mg. The catalysts were pretreated in 5% H_2 at 500°C for 30 min. The temperature was increased by 10°C/min.. 191

Figure A.6: CO and H_2O consumption during Temperature Programmed Reaction on 0.1%Rh/Al_2O_3 . CO = 8400 ppm, O_2 = 9250 ppm, H_2O = 0.8%, total flowrate = 500. Catalyst weight = 13 mg. The catalyst was pretreated in 5% H_2 at 500°C for 30 min. 192

Figure A.7: DRIFTS spectrum of 0.1%Rh/Al_2O_3 H_2-700°C during CO oxidation at 260°C. CO = 8400 ppm; O_2 = 9250 ppm. The catalyst was exposed to 1% O_2 at 500°C for 30 min, followed by He purge for 10 min and 5% H_2 at 500°C for 30 min. 193

Figure A.8: DRIFTS spectra of 0.1%Rh/Al_2O_3 H_2-700°C during CO adsorption at 220, 240, 260, 280, 300°C. CO = 8400 ppm. The catalyst was exposed to 1% O_2 at 500°C for 30 min, followed by He purge for 10 min and 5% H_2 at 500°C for 30 min 194

Figure A.9: DRIFTS spectrum of 0.1%Rh/Al_2O_3 H2-700°C during CO oxidation at 260°C. CO = 8400 ppm; O_2 = 2000, 4200, 9250 ppm. The catalyst was exposed to 1% O_2 at 500°C for 30 min, followed by He purge for 10 min and 5% H_2 at 500°C for 30 min 195

Figure B.1: STEM images of 1% Pd/CeO_2 10 nm 197

Figure B.2: STEM images of 1% Pd/CeO_2 25 nm 197

Figure B.3: STEM images and EDS of 1% Pd/CeO_2 25 nm 198

Figure B.4: STEM images of 1% Pd/CeO_2 100 nm 198

Figure B.5: EDS of 1% Pd/CeO_2 100 nm 199

Figure B.6: STEM image of 1.2% Pd/CeO_2 1 μm 199

Figure B.7: XRD pattern of the 1% Pd/CeO_2-10, 25 and 100 nm samples 200

Figure B.8: CO adsorption on (a) CeO_2 10 nm; (b) CeO_2 100 nm; the materials were treated in 1% O_2/Ar for 30 min at 400°C, purged in Ar and reduced in 5% H_2/Ar for 30 min at 300°C. Finally, the two materials were exposed to 5000 ppm CO at 35°C until saturation. 201

Figure B.9: CO_2 adsorption on (a) CeO_2 - 10 nm and (b) CeO_2 - 100 nm; the materials were treated in 1% O_2/Ar for 30 min at 400°C, purged in Ar and reduced in 5% H_2/Ar for 30 min at 300°C. The two materials were then exposed to 1% CO_2 at 35°C until saturation. 202

Figure B.10: CO adsorption using DRIFTS over 1.2% Pd/Al_2O_3- fresh, and 650, 750 and 850°C aged samples. The catalyst was treated in 1% O_2/Ar for 30 min at 400°C, purged in Ar and reduced in 5% H_2/Ar for 30 min at 400°C. The catalysts were exposed to 5000 ppm CO until saturation at 35°C. 203

Figure B.11: Time evolution of carbonate species decomposing/desorbing from 1% Pd/CeO_2-25 nm during the Ar purge after CO_2 exposure. 204

Figure B.12: DRIFTS spectra obtained during the CO_2-CO adsorption experiment over (a) 1% Pd/CeO_2-10 nm and (b) 1% Pd/CeO_2-100 nm. The catalysts were treated in 1% O_2/Ar for 30 min at 400°C, purged in Ar and reduced in 5% H_2/Ar for 30 min at 300°C. The catalysts were exposed to 1% CO_2 at 35°C until saturation and purged until no changes in the spectra were detected. A new background was collected before the sample was exposed to 5000 ppm CO until saturation. 205

Figure B.13: DRIFTS spectra obtained during the CO_2-CO adsorption experiment over (a) 1.2% Pd/CeO_2 1um, (b) 0.8% Pd/CeO_2 1um, (c) 0.2% Pd/CeO_2 1um. The catalysts were treated in 1% O_2/Ar for 30 min at 400°C, purged in Ar and reduced in 5% H_2/Ar for 30 min at 400°C. The catalysts were exposed to 1% CO_2 at 35°C until saturation and purged until no changes in the spectra were detected. A new background was collected before exposure to 5000 ppm CO until saturation. 205

Figure B.14: DRIFTS spectra obtained during the CO_2-CO adsorption experiment over 1.2% Pd/Al_2O_3 (a) Fresh, (b) 650°C aged, (c) 750°C aged and (d) 850°C aged. The catalysts were treated in 1% O_2/Ar for 30 min at 400°C, purged in Ar and reduced in 5% H_2/Ar for 30 min at 400°C. The catalysts were exposed to 1% CO_2 at 35°C until saturation and purged until no changes in the spectra were detected. A new background was collected before exposure to 5000 ppm CO until saturation. 206

Figure B.15: H_2 chemisorption isotherms on 1.2% Pd/CeO_2 1um. The catalyst was pretreated at 400°C in H_2 for 1h. The analysis was performed at 35°C 207

Figure B.16: H_2 chemisorption isotherms of 1% Pd/CeO_2 10 nm. The catalyst was pretreated at 400°C in H_2 for 1h. The analysis was performed at 35°C. 208

Figure B.17: XRD pattern of 1.2% Pd/Al_2O_3 that underwent the cyclic ageing treatment at 650°C for 50h 209

Figure B.18: DRIFTS spectra obtained during CO adsorption on 1.2, 0.8 and 0.2% Pd/CeO_2 1µm. 210

Figure B.19: Fraction of surface, perimeter and corner sites based on a geometric model 212

Figure B.20: CO oxidation Arrhenius plot over 1% Pd/CeO_2 10, 25 and 100 nm. The turnover frequency was obtained by normalizing the reaction rates by the number of total Pd surface sites. 213

Figure B.21: CO oxidation Arrhenius plot over 1% Pd/CeO_2 10, 25 and 100 nm. The turnover frequency was obtained by normalizing the reaction rates by the number of Pd corner sites. 214

Figure C.1: C_3H_6 oxidation + H_2O on 0.2% Pt-7.5% SrO/Al_2O_3. 50 mg of catalyst was diluted with 150 mg silica. Pellet size was 250-420µm. The catalyst was reduced in 5% H_2/N_2 for 45 minutes at 600°C. The catalyst was then exposed to the reaction mixture including C_3H_6 = 1000 ppm; O_2 = 4500 ppm; H_2O = 6%, diluted in N_2. Total flowrate = 500 sccm. The conversions were obtained at steady-state. (a) C_3H_6 conversion; (b) Arrhenius plot obtained from C_3H_6 consumption rate and CO_2 and CO formation rates.216

Figure C.2: C_3H_6 oxidation + NO + H_2O on 0.2% Pt-7.5% SrO/Al_2O_3. 50 mg of catalyst was diluted with 150 mg silica. The catalyst was reduced in 5% H_2/N_2 for 45 minutes at 600°C. The catalyst was then exposed to the reaction mixture including C_3H_6 = 1000 ppm; O_2 = 4000 ppm; NO = 1000 ppm; H_2O = 6%, diluted in N_2. Total flowrate = 500 sccm. The conversions were obtained at steady-state. (a) C_3H_6 and NO conversions; (b) N_2O, NH_3 and N_2O Selectivity. 217

Figure C.3: C_3H_6 oxidation + NO + H_2O on 0.2% Pt-7.5% SrO/Al_2O_3. 50 mg of catalyst was diluted with 150 mg silica.The catalyst was reduced in 5% H_2/N_2 for 45 minutes at 600°C. The catalyst was then exposed to the reaction mixture including C_3H_6 = 1000 ppm; O_2 = 4000 ppm; NO = 1000 ppm; H_2O = 6%, diluted in N_2. Total flowrate = 500 sccm. The conversions were obtained at steady-state. (a) Arrhenius plot obtained from C_3H_6 consumption rate and CO_2 and CO formation rates; (b) Arrhenius plot obtained from NO consumption rate and N_2O, NH_3 and N_2 formation rates. N_2 rates were obtained from N-material balance. 217

Figure C.4: NO reaction order at 300C – C_3H_6 oxidation + NO + H_2O on 0.2% Pt-7.5% SrO/Al_2O_3. 50 mg of catalyst was diluted with 150 mg silica. The catalyst was reduced in 5% H_2/N_2 for 45 minutes at 600°C. The catalyst was then exposed to the reaction mixture including C_3H_6 = 1000 ppm; O_2 = 4000 ppm; NO = 720-1500 ppm; H_2O = 6%, diluted in N_2. Total flowrate = 500sccm. The conversions were obtained at steady-state. (a) C_3H_6 order with respect of C_3H_6 consumption rate and CO_2 and CO formation rates; (b) Arrhenius plot obtained from NO consumption rate and N_2O, NH_3 and N_2 formation rates. N_2 rates were obtained from N-material balance..... 218

Figure C.5: C_3H_6 reaction order at 300C – C_3H_6 oxidation + NO + H_2O on 0.2% Pt-7.5% SrO/Al_2O_3. 50 mg of catalyst was diluted with 150 mg silica. The catalyst was reduced in 5% H_2/N_2 for 45 minutes at 600°C. The catalyst was then exposed to the reaction mixture including C_3H_6 = 720-1500 ppm; O_2 = 4000 ppm; NO = 1000 ppm; H_2O = 6%, diluted in N_2. Total flowrate = 500sccm. The conversions were obtained at steady-state. (a) C_3H_6 order with respect of C_3H_6 consumption rate and CO_2 and CO formation rates; (b) Arrhenius plot obtained from NO consumption rate and N_2O, NH_3 and N_2 formation rates. N_2 rates were obtained from N-material balance..... 218

Figure C.6: O_2 reaction order at 300C – C_3H_6 oxidation + NO + H_2O on 0.2% Pt-7.5% SrO/Al_2O_3. 50 mg of catalyst was diluted with 150 mg silica. The catalyst was reduced in 5% H_2/N_2 for 45 minutes at 600°C. The catalyst was then exposed to the reaction mixture including C_3H_6 = 1000 ppm; O_2 = 3500-5000 ppm; NO = 1000 ppm; H_2O = 6%, diluted in N_2. Total flowrate = 500sccm. The conversions were obtained at steady-state. (a) C_3H_6 order with respect of C_3H_6 consumption rate and CO_2 and CO formation rates; (b) Arrhenius plot obtained from NO consumption rate and N_2O, NH_3 and N_2 formation rates. N_2 rates were obtained from N-material balance..... 219

Figure C.7: C_3H_6 oxidation + H_2O on 0.2% Rh-7.5% SrO/Al_2O_3. 50 mg of catalyst was diluted with 150 mg silica. Pellet size was 250-420µm. The catalyst was reduced in 5% H_2/N_2 for 45 minutes at 600°C. The catalyst was then exposed to the reaction mixture including C_3H_6 = 1000 ppm; O2 = 4500 ppm; H_2O = 6%, diluted in N_2. Total flowrate = 500 sccm. The conversions were obtained at steady-state. (a) C_3H_6 conversion; (b) Arrhenius plot obtained from C_3H_6 consumption rate and CO_2 and CO formation rates.220

Figure C.8: C_3H_6 oxidation + NO + H_2O on 0.2% Rh-7.5% SrO/Al_2O_3. 50 mg of catalyst was diluted with 150 mg silica. The catalyst was reduced in 5% H_2/N_2 for 45 minutes at 600°C. The catalyst was then exposed to the reaction mixture including C_3H_6 = 1000 ppm; O_2 = 4000 ppm; NO = 1000 ppm; H_2O = 6%, diluted in N_2. Total flowrate = 500 sccm. The conversions were obtained at steady-state. (a) C_3H_6 and NO conversions; (b) N_2O, NH_3 and N_2O Selectivity. 221

Figure C.9: C_3H_6 oxidation + NO + H_2O on 0.2% Rh-7.5% SrO/Al_2O_3. 50 mg of catalyst was diluted with 150 mg silica. The catalyst was reduced in 5% H_2/N_2 for 45 minutes at 600°C. The catalyst was then exposed to the reaction mixture including C_3H_6 = 1000 ppm; O_2 = 4000 ppm; NO = 1000 ppm; H_2O = 6%, diluted in N_2. Total flowrate = 500 sccm. The conversions were obtained at steady-state. (a) Arrhenius plot obtained from C_3H_6 consumption rate and CO_2 and CO formation rates; (b) Arrhenius plot obtained from NO consumption rate and N_2O, NH_3 and N_2 formation rates. N_2 rates were obtained from N-material balance. 221

Figure C.10: C_3H_6 reaction order at 320°C – C_3H_6 oxidation + NO + H_2O on 0.2% Rh-7.5% SrO/Al_2O_3. 50 mg of catalyst was diluted with 150 mg silica. The catalyst was reduced in 5% H_2/N_2 for 45 minutes at 600°C. The catalyst was then exposed to the reaction mixture including C_3H_6 = 720-1500 ppm; O_2 = 4000 ppm; NO = 1000 ppm; H_2O = 6%, diluted in N_2. Total flowrate = 500sccm. The conversions were obtained at steady-state. (a) C_3H_6 order with respect of C_3H_6 consumption rate and CO_2 and CO formation rates; (b) Arrhenius plot obtained from NO consumption rate and N_2O, NH_3 and N_2 formation rates. N_2 rates were obtained from N-material balance..... 222

Figure C.11: NO reaction order at 320°C – C_3H_6 oxidation + NO + H_2O on 0.2% Rh-7.5% SrO/Al_2O_3. 50 mg of catalyst was diluted with 150 mg silica. The catalyst was reduced in 5% H_2/N_2 for 45 minutes at 600°C. The catalyst was then exposed to the reaction mixture including C_3H_6 = 1000 ppm; O_2 = 4000 ppm; NO = 720-1500 ppm; H_2O = 6%, diluted in N_2. Total flowrate = 500sccm. The conversions were obtained at steady-state. (a) C_3H_6 order with respect of C_3H_6 consumption rate and CO_2 and CO formation rates; (b) Arrhenius plot obtained from NO consumption rate and N_2O, NH_3 and N_2 formation rates. N_2 rates were obtained from N-material balance..... 223

Figure C.12: O_2 reaction order at 320°C – C_3H_6 oxidation + NO + H_2O on 0.2% Pt-0.2% Rh-7.5% SrO/Al_2O_3. 50 mg of catalyst was diluted with 150 mg silica. The catalyst was reduced in 5% H_2/N_2 for 45 minutes at 600°C. The catalyst was then exposed to the reaction mixture including C_3H_6 = 1000 ppm; O_2 = 3500-5000 ppm; NO = 1000 ppm; H_2O = 6%, diluted in N_2. Total flowrate = 500sccm. The conversions were obtained at steady-state. (a) C_3H_6 order with respect of C_3H_6 consumption rate and CO_2 and CO formation rates; (b) Arrhenius plot obtained from NO consumption rate and N_2O, NH_3 and N_2 formation rates. N_2 rates were obtained from N-material balance..... 223

Figure C.13: C_3H_6 oxidation + H_2O on 0.2% Pt-0.2% Rh-7.5% SrO/Al_2O_3. 50 mg of catalyst was diluted with 150 mg silica. Pellet size was 250-420µm. The catalyst was reduced in 5% H_2/N_2 for 45 minutes at 600°C. The catalyst was then exposed to the reaction mixture including C_3H_6 = 1000 ppm; O2 = 4500 ppm; H_2O = 6%, diluted in N_2. Total flowrate = 500 sccm. The conversions were obtained at steady-state. (a) C_3H_6 conversion; (b) Arrhenius plot obtained from C_3H_6 consumption rate and CO_2 and CO formation rates. 224

Figure C.14: C_3H_6 oxidation + NO + H_2O on 0.2% Pt-0.2% Rh-7.5% SrO/Al_2O_3. 50 mg of catalyst was diluted with 150 mg silica. The catalyst was reduced in 5% H_2/N_2 for 45 minutes at 600°C. The catalyst was then exposed to the reaction mixture including C_3H_6 = 1000 ppm; O_2 = 4000 ppm; NO = 1000 ppm; H_2O = 6%, diluted in N2. Total flowrate = 500 sccm. The conversions were obtained at steady-state. (a) C_3H_6 and NO conversions; (b) N_2O, NH_3 and N_2O Selectivity. 225

Figure C.15: C_3H_6 oxidation + NO + H_2O on 0.2% Pt-0.2% Rh-7.5% SrO/Al_2O_3. 50 mg of catalyst was diluted with 150 mg silica. The catalyst was reduced in 5% H_2/N_2 for 45 minutes at 600°C. The catalyst was then exposed to the reaction mixture including C_3H_6 = 1000 ppm; O_2 = 4000 ppm; NO = 1000 ppm; H_2O = 6%, diluted in N_2. Total flowrate = 500 sccm. The conversions were obtained at steady-state. (a) Arrhenius plot obtained from C_3H_6 consumption rate and CO_2 and CO formation rates; (b) Arrhenius plot obtained from NO consumption rate and N_2O, NH_3 and N_2 formation rates. N_2 rates were obtained from N-material balance. 225

Figure C.16: C_3H_6 reaction order at 250°C – C_3H_6 oxidation + NO + H_2O on 0.2% Pt-0.2% Rh-7.5% SrO/Al_2O_3. 50 mg of catalyst was diluted with 150 mg silica. The catalyst was reduced in 5% H_2/N_2 for 45 minutes at 600°C. The catalyst was then exposed to the reaction mixture including C_3H_6 = 720-1500 ppm; O_2 = 4000 ppm; NO = 1000 ppm; H_2O = 6%, diluted in N_2. Total flowrate = 500sccm. The conversions were obtained at steady-state. (a) C_3H_6 order with respect of C_3H_6 consumption rate and CO_2 and CO formation rates; (b) Arrhenius plot obtained from NO consumption rate and N_2O, NH_3 and N_2 formation rates. N_2 rates were obtained from N-material balance..... 226

Figure C.17: NO reaction order at 250°C – C_3H_6 oxidation + NO + H_2O on 0.2% Pt-0.2% Rh-7.5% SrO/Al_2O_3. 50 mg of catalyst was diluted with 150 mg silica. The catalyst was reduced in 5% H_2/N_2 for 45 minutes at 600°C. The catalyst was then exposed to the reaction mixture including C_3H_6 = 1000 ppm; O_2 = 4000 ppm; NO = 720-1500 ppm; H_2O = 6%, diluted in N_2. Total flowrate = 500sccm. The conversions were obtained at steady-state. (a) C_3H_6 order with respect of C_3H_6 consumption rate and CO_2 and CO formation rates; (b) Arrhenius plot obtained from NO consumption rate and N_2O, NH_3 and N_2 formation rates. N_2 rates were obtained from N-material balance. 227

Figure C.18: O_2 reaction order at 250°C – C_3H_6 oxidation + NO + H_2O on 0.2% Pt-0.2% Rh-7.5% SrO/Al_2O_3. 50 mg of catalyst was diluted with 150 mg silica. The catalyst was reduced in 5% H_2/N_2 for 45 minutes at 600°C. The catalyst was then exposed to the reaction mixture including C_3H_6 = 1000 ppm; O_2 = 3500-5000 ppm; NO = 1000 ppm; H_2O = 6%, diluted in N_2. Total flowrate = 500sccm. The conversions were obtained at steady-state. (a) C_3H_6 order with respect of C_3H_6 consumption rate and CO_2 and CO formation rates; (b) Arrhenius plot obtained from NO consumption rate and N_2O, NH_3 and N_2 formation rates. N_2 rates were obtained from N-material balance..... 227

Figure C.19: C_3H_6 oxidation + H_2O on 0.2% Pt-0.2% Rh/Al_2O_3. 50 mg of catalyst was diluted with 150 mg silica. Pellet size was 250-420µm. The catalyst was reduced in 5% H_2/N_2 for 45 minutes at 600°C. The catalyst was then exposed to the reaction mixture including C_3H_6 = 1000 ppm; O_2 = 4500 ppm; H_2O = 6%, diluted in N_2. Total flowrate = 500 sccm. The conversions were obtained at steady-state. (a) C_3H_6 conversion; (b) Arrhenius plot obtained from C_3H_6 consumption rate and CO_2 and CO formation rates.228

Figure C.20: C_3H_6 oxidation + NO + H_2O on 0.2% Pt-0.2% Rh/Al_2O_3. 50 mg of catalyst was diluted with 150 mg silica. The catalyst was reduced in 5% H_2/N_2 for 45 minutes at 600°C. The catalyst was then exposed to the reaction mixture including C_3H_6 = 1000 ppm; O_2 = 4000 ppm; NO = 1000 ppm; H_2O = 6%, diluted in N_2. Total flowrate = 500 sccm. The conversions were obtained at steady-state. (a) C_3H_6 and NO conversions; (b) N_2O, NH_3 and N_2O Selectivity. 229

Figure C.21: C_3H_6 oxidation + NO + H_2O on 0.2% Pt-0.2% Rh/Al_2O_3. 50 mg of catalyst was diluted with 150 mg silica.The catalyst was reduced in 5% H_2/N_2 for 45 minutes at 600°C. The catalyst was then exposed to the reaction mixture including C_3H_6 = 1000 ppm; O_2 = 4000 ppm; NO = 1000 ppm; H_2O = 6%, diluted in N_2. Total flowrate = 500 sccm. The conversions were obtained at steady-state. (a) Arrhenius plot obtained from C_3H_6 consumption rate and CO_2 and CO formation rates; (b) Arrhenius plot obtained from NO consumption rate and N_2O, NH_3 and N_2 formation rates. N_2 rates were obtained from N-material balance. 229

Figure C.22: C_3H_6 reaction order at 260°C – C_3H_6 oxidation + NO + H_2O on 0.2% Pt-0.2% Rh/Al_2O_3. 50 mg of catalyst was diluted with 150 mg silica. The catalyst was reduced in 5% H_2/N_2 for 45 minutes at 600°C. The catalyst was then exposed to the reaction mixture including C_3H_6 = 720-1500 ppm; O_2 = 4000 ppm; NO = 1000 ppm; H_2O = 6%, diluted in N_2. Total flowrate = 500sccm. The conversions were obtained at steady-state. (a) C_3H_6 order with respect of C_3H_6 consumption rate and CO_2 and CO formation rates; (b) Arrhenius plot obtained from NO consumption rate and N_2O, NH_3 and N_2 formation rates. N_2 rates were obtained from N-material balance..... 230

Figure C.23: NO reaction order at 260°C – C_3H_6 oxidation + NO + H_2O on 0.2% Pt-0.2% Rh/Al_2O_3. 50 mg of catalyst was diluted with 150 mg silica. The catalyst was reduced in 5% H_2/N_2 for 45 minutes at 600°C. The catalyst was then exposed to the reaction mixture including C_3H_6 = 1000 ppm; O_2 = 4000 ppm; NO = 720-1500 ppm; H_2O = 6%, diluted in N_2. Total flowrate = 500sccm. The conversions were obtained at steady-state. (a) C_3H_6 order with respect of C_3H_6 consumption rate and CO_2 and CO formation rates; (b) Arrhenius plot obtained from NO consumption rate and N_2O, NH_3 and N_2 formation rates. N_2 rates were obtained from N-material balance..... 231

Figure C.24: O_2 reaction order at 260°C – C_3H_6 oxidation + NO + H_2O on 0.2% Pt-0.2% Rh/Al_2O_3. 50 mg of catalyst was diluted with 150 mg silica. The catalyst was reduced in 5% H_2/N_2 for 45 minutes at 600°C. The catalyst was then exposed to the reaction mixture including C_3H_6 = 1000 ppm; O_2 = 3500-5000 ppm; NO = 1000 ppm; H_2O = 6%, diluted in N_2. Total flowrate = 500sccm. The conversions were obtained at steady-state. (a) C_3H_6 order with respect of C_3H_6 consumption rate and CO_2 and CO formation rates; (b) Arrhenius plot obtained from NO consumption rate and N_2O, NH_3 and N_2 formation rates. N_2 rates were obtained from N-material balance..... 232

List of Tables

Table 3.1: Particle size measurements via H_2 chemisorption 31

Table 4.1: Dispersion and particle size measurements performed on 0.05% Rh/Al_2O_3 and 0.1%Rh/Al_2O_3 via H_2 chemisorption..... 57

Table 5.1: List of apparent activation energies measured from NO, CO, N_2O and NH_3 rates during NO reduction by CO in the absence and presence of 1, 3 and 6% over 0.1% Rh/Al_2O_3. NO/CO = 2, 1 and 0.5 The catalyst was reduced in 5% H_2 for 30 min at 500°C. The reaction mixture included CO = 1000 ppm, NO varying to obtain NO/CO = 2, 1 and 0.5 96

Table 5.2: Apparent activation energy during dry and wet NO reduction by CO in the presence and absence of NH_3 The catalyst was reduced in 5% H_2 for 30 min at 500°C. The reaction mixture included CO = 1000 ppm, NO varying to obtain NO/CO = 2, 1 and 0.5, NH_3 = 0/100 ppm; 0/6% H_2O. 99

Table 5 3: Apparent activation energy measured on 0.1% Rh/Al_2O_3 – 1.1 nm and 9.2 nm during NO reduction by CO in the presence of water. The catalysts were reduced in 5% H_2 for 30 min at 500°C. The reaction mixture included CO = 1000 ppm; NO varying to obtain NO/CO = 0.5, 1 and 2, NH3 = 0 or 100 ppm and H_2O = 6%, diluted in N_2..... 118

Table 5. 4: H_2 chemisorption dispersion measurements, assuming the stoichiometry of H:Rh = 1:1 128

Table 6.1: Ceria particle sizes obtained using the Scherrer equation. The particle sizes were obtained by averaging the results from the features at 28, 32, 47 and 56° 148

Table 6.2: CO_2-CO and CO chemisorption results: dispersion and particle size. The dispersion was obtained using the total chemisorption isotherm, and the particle size was calculated as 100/D[%]. The ceria-containing catalysts were reduced in H_2 at 300°C, while the Pd/Al_2O_3 catalyst was reduced in H_2 at 400°C. 156

Table A.1: Dispersion and particle size measurements on Rh/Al_2O_3 catalysts 184

Table B.1: BET surface areas measured on bare 10, 15 and 100 nm ceria and 1% Pd/CeO_2 10, 25 and 100 nm 200
Table B.2: Dispersion measurements via H_2 chemisorption at 35°C on 1% Pd/CeO_2-10 25, 100 nm and 1.2% CeO_2-1µm..... 210
Table B.3: Dispersions obtained via CO_2-CO and CO chemisorption. The catalysts were reduced in H_2 at 400°C for 1h. The analysis was performed at 35°C..... 211

Table of Contents

Acknowledgement i

Abstract i

List of Figures iii

List of Tables xv

Table of Contents xvi

Chapter 1: Introduction 1

1.1 Emission regulations 1

1.2 Three-way catalyst 3

1.3 The commercial catalysts 5

1.4 PGM price 5

1.5 TWC formulation adapted to new configurations or to technological innovations 7

1.6 References 11

Chapter 2: Experimental methods 16

2.1 Bench scale reactor 16

2.2 Diffuse Reflectance Infrared Fourier Transform Spectroscopy (DRIFTS) 17

2.3 X-ray diffraction (XRD) 19

2.4 STEM and EDS 20

2.5 Physisorption and Chemisorption 20

2.6 References 23

Chapter 3: Rhodium catalyst structural changes during, and their impacts on the kinetics of, CO oxidation 24

3.1 Introduction 24

3.2 Material and methods 27

3.2.1 Catalysts 27

3.2.2 Chemisorption 27

3.2.3 CO oxidation kinetic experiments 28

3.2.4 DRIFTS experiments 29

3.3 Results and Discussion 30

3.3.1 Catalyst characterization: H_2 chemisorption and CO DRIFTS 30

3.3.2 CO oxidation kinetics 33

3.3.3 In-situ CO + O_2 DRIFTS 38

3.3.4 The effect of O_2 on Rh speciation 42

3.3.5 Bridging the spectroscopic and kinetic data 43

3.4 Conclusions 45

3.5 References 47

Chapter 4: Spectroscopic investigation of Rh mobility in the presence of CO, O_2 and H_2O 54

4.1 Introduction 54

4.2 Material and Methods 56

4.3 Results and Discussion 57

4.4 Conclusions 75

4.5 References 77

Chapter 5: NO reduction by CO: H_2O and NH_3 effects on the kinetics 81

5.1 Introduction 81

5.2 Material and Methods 82

5.3 Results and Discussion 84

5.4 Conclusions 130

5.5 References 132

Chapter 6 : Adapted CO chemisorption technique to measure metal particle dispersion on ceria-containing catalysts 139

6.3.1 Physical characterization 147

6.3.2 CO DRIFTS 149

6.3.3 CO_2-CO DRIFTS 153

6.3.4 CO and CO_2-CO chemisorption 156

6.3.5 CO oxidation kinetics 164

Chapter 7: Conclusions and future work 178

7.1 Conclusions 178

7.2 Future work 180

Appendix A - Supporting Information of Chapter 3: Rhodium catalyst structural changes during CO oxidation 183

Section A1. Dispersion measurements 184

Section A2. Cordierite activity 185

Section A3. CO oxidation Arrhenius plots 186

A 3.1 CO oxidation 186

A 3.2 CO oxidation in the presence of water 187

A 3.3 Internal mass transfer check 187

A 3.4 External mass transfer check 188

A 3.5 Internal heat transfer check 188

A 3.6 External heat transfer check 188

Section A.4. Water effect on CO oxidation 190

Section A5. DRIFTS Spectra 193

A 5.1 CO + O_2 at 260°C on 0.1% Rh/Al_2O_3 – H_2 700°C 193

Appendix B - Supporting information of Chapter 6: Adapted CO chemisorption technique to measure metal particle dispersion on ceria-containing catalysts 196

Section B1: Physical characterization 197

Section B2: CO and CO_2 adsorption on bare CeO_2 201

Section B3: CO and H_2 chemisorption 210

Section B4: CO oxidation kinetics 212

Section B5: Reference 215

Appendix C – Kinetic studies of C_3H_6 oxidation in the presence and absence of NO on newly formulated TWC catalysts 216

Section C1 0.2% Pt – 7.5% SrO/Al_2O_3 216

C 1.1 C_3H_6 oxidation + H_2O kinetics 216

C 1.2 C_3H_6 oxidation + NO + H_2O kinetics 217

Section C2 0.2% Rh – 7.5% SrO/Al_2O_3 220

C 2.1 C_3H_6 oxidation + H_2O 220

C 2.2 C_3H_6 oxidation + NO + H_2O 221

Section C3: 0.2% Pt-0.2% Rh-7.5% SrO/Al_2O_3 224

C 3.1 CO oxidation + H_2O 224

C 3.2 CO oxidation + NO + H_2O 225

Section 4: 0.2% Pt-0.2% Rh/Al_2O_3 228

C 4.1 C_3H_6 oxidation + H_2O 228

C 4.2 C_3H_6 oxidation + NO + H_2O 229

Chapter 1: Introduction

In the combustion of gasoline, the ideal products should be limited to CO_2 and H_2O. However, due to incomplete combustion, we end up with undesired byproducts such as CO and unburnt hydrocarbons. In addition, in the high temperature environment of the combustion chamber, nitrogen oxides (NO_x) are formed due to the N_2 fixation.[1] CO, unburnt hydrocarbons (HC) and NOx are detrimental for human health and the environment.[2,3]

The three-way catalyst (TWC) is the key component of the aftertreatment system used in gasoline engine vehicles. It is able to simultaneously convert these three pollutants into less environmentally harmful products, such as CO_2 and N_2, when the engine works under stoichiometric conditions.[4–8] The TWC has been critical in addressing emission regulations since 1975, as a part of the Clean Air Act, enforced by the Environmental Protection Agency (EPA), which aimed to make substantial improvements in air quality. Over the years, emissions regulations have continued to evolve and become more stringent. This led automotive companies and catalyst suppliers to improve the aftertreatment system and make TWC formulations more active and durable.

1.1 Emission regulations

The most recent emission regulations for light duty vehicles in the United States are described as the Tier 3 standards. These standards impose a reduction in the fleet average of non-methane organic gas hydrocarbons (NMOG) plus NOx to 30 mg/mi for all vehicles by 2025, as shown in Figure 1.1.[9,10] In addition, these regulations extend the catalyst durability requirements to 150,000 miles or 15 years, whichever comes first. The US standards also require a reduction of CO_2 emissions, targeting a 25% decrease. This translates to values dropping from 202 to 143 g/mi. Meeting

these stringent requirements impose advancements not only in engine design and fuel efficiency, but also in catalyst design.

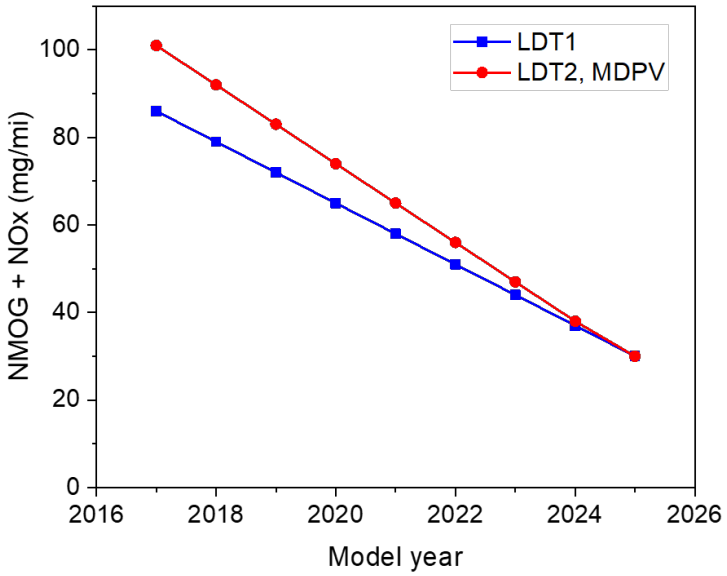

Figure 1.1: Tier 3 emission standards. Fleet average of NOx + NMOHC limits for light-duty vehicles (LDT1), and LDT 2 and MDPV (medium duty trucks) up to 10,000 lb.

The commitment to reduce emissions extends worldwide. In Europe, emission regulations have been made more stringent with the implementation of Euro 6 standards.[11] China implemented China 6a emission standards, aligned with Euro 6, and plans to introduce China 6b, which not only tightens the NOx and HC emission regulations, but introduces limitations on N_2O emissions.[6] Similarly, India adopted Bharat Stage 6 standards, which are based on Euro 6, and they aim to enforce more stringent regulations for NOx, HC and CO emissions.[6,12]

To meet these strict regulations and mitigate the environmental impact of tailpipe emissions, it is necessary to continuously develop new catalytic technologies able to comply with increasingly demanding emission standards and to demonstrate extended durability.

1.2 Three-way catalyst

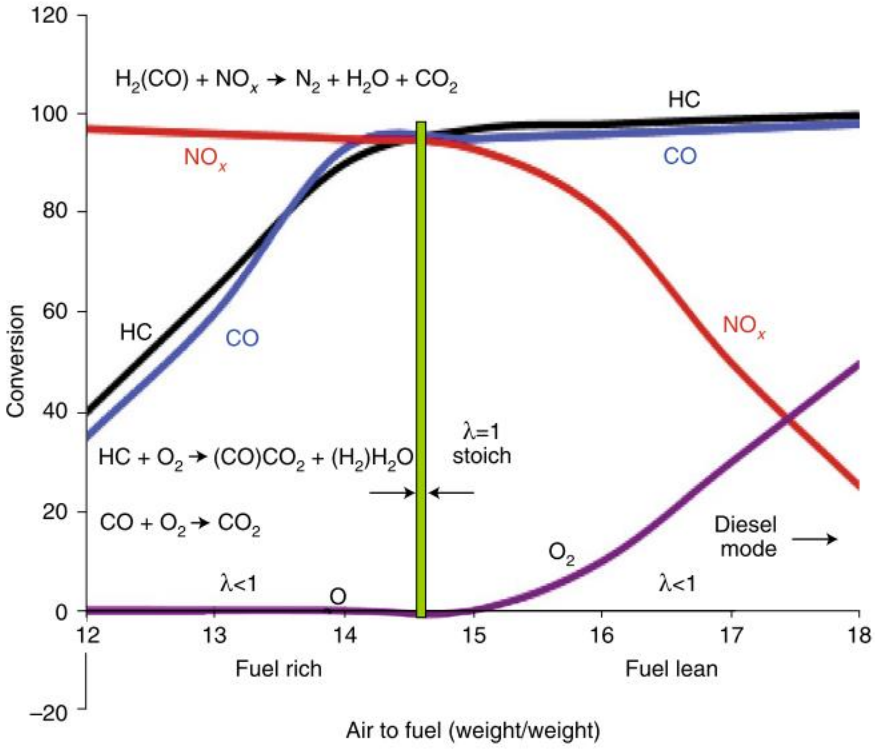

Figure 1.2: TWC system operating window. [6]

The system that has successfully met the regulations imposed by the EPA is the TWC. Figure 1.2 displays the typical operation of a three-way catalyst and shows the conversion of the three main pollutants based to the air-to-fuel ratio. The main three reactions occurring simultaneously on the TWC are the following:

$$CO + ½\ O_2 \rightarrow CO_2 \qquad (R1)$$

$$C_3H_6 + 4.5\ O_2 \rightarrow 3CO_2 + 3H_2O \qquad (R2)$$

$$CO + NO \rightarrow CO_2 + 1/2\ N_2 \qquad (R3)$$

In addition to these reactions, steam reforming and water gas shift also take place, leading to the formation of H_2, which contributes to conversion of NOx to N_2.

The TWC typically operates within a range close to stoichiometric combustion conditions. Under stoichiometric conditions, which correspond to the O_2 concentration required to combust the HC fuel and is equal to an air-to-fuel ratio by weight of 14.7 for gasoline engines, simultaneous conversion of all pollutant can be high. When the engine works under lean conditions, with an air-to-fuel ratio higher than 14.7, corresponding to an oxidizing environment, CO and HC conversions are high, because of excess of O_2. However, NO conversion is low, since there would be insufficient reducing agents, such as CO and HC, to reduce NO. When the exhaust gas is fuel-rich and lacks O_2, NO conversion is high, due to the abundance of reducing agents. However, CO and HC conversions are low, because of the deficiency of oxygen, necessary for their oxidation.

The air-to-fuel ratio is controlled by an O_2 sensor, which is able to detect the O_2 concentration in the exhaust gas. It then sends an electric signal to control the fuel injection, adjusting the air-to-fuel ratio to maintain the desired combustion conditions.[13,14]

The non-ideal response of the O_2 sensor often leads to strong fluctuations in feed composition and air-to-fuel ratio, resulting in reduced catalytic efficiency. To address this issue, oxygen storage materials have been incorporated into the TWC formulation.[15,16] Typically, a mixture of CeO_2-ZrO_2 is used as storage materials.[17–20] Ceria is used as a buffer to reduce the fluctuations in conversion during the transition between lean and rich conditions.[18,21–23] Under reducing conditions, with an air-to-fuel ratio lower than 14.7, ceria can supply oxygen to oxidize CO and HC, through reaction R5. Under oxidizing conditions, with an air-to-fuel ratio higher than 14.7, the excess O_2 can oxidize ceria back to its original state, as described in reaction R6.

$$CO + Ce\text{-}O\text{-}Ce \rightarrow CO_2 + Ce\text{-}\square\text{-}Ce \quad (R4)$$

$$Ce\text{-}\square\text{-}Ce + \tfrac{1}{2}\, O_2 \rightarrow Ce\text{-}O\text{-}Ce \quad (R5)$$

Where □ is the oxygen vacancy.

ZrO_2 is usually included in the mixture to stabilize the ceria, preventing sintering, and to enhance ceria redox properties.[18–20,24] The increased durability of these components allows the TWC to resist too severe of changes under the high temperature conditions experienced during its operation.

1.3 The commercial catalysts

Current commercial TWC catalysts use Pt-group metals (PGM) as active components. Pd, Pt and Rh are the key metal sites in use. Pd and Pt are historically used because of their ability to oxidize CO and HC, while Rh is used for its ability to dissociate NO and its high selectivity towards N_2, which is the desired product. These metals are usually deposited onto an alumina support. Due to its high surface area, alumina ensures high metal dispersion, while its high thermal stability, mechanical strength and low cost make it an optimal support for TWC application, helping achieve high catalyst performance and long durability. The support usually contains promoters, such as La, Y, Pr, which help to stabilize and enhance the catalytic activity, and ceria to take advantage of its redox properties.

Over the years, the catalyst design of commercial TWCs has been influenced by a combination of factors, including the PGM price and the evolving emission regulations, which require not only highly efficient, but also durable catalysts. In addition, catalyst formulations must adapt to new technological innovations needed to meet environmental regulations.

1.4 PGM price

Automotive companies and catalyst suppliers carefully consider PGM prices when designing new catalytic technologies. Given the global limited production, the price of Rh, Pt and Pd are subject to significant volatility, which impacts the TWC cost.

For example, a previous TWC generation relied on Pd-only TWC. In fact, back in 1989, the use of Pd was a desirable alternative to Pt and Rh, primarily because of the high cost of the latter two metals.[25,26] However, the implementation of stricter regulations required the reintroduction of Rh, necessary for its high activity in NO reduction reactions.[7,8] Nowadays, the prevalent configuration of catalytic converters includes a combination of both Pd and Rh. However, as shown in Figure 1.3, over the past few years, the sharp increase in Rh price has challenged catalyst manufacturers to explore innovative solutions aimed to minimize Rh use while preserving the catalytic performance. Some cost-effective approaches have included the use of single atom catalysts (SACs), which ensure 100% dispersion of active metal atoms, leading to high mass activity. The use of SACs has been proposed to allow and consequently maximize precious metal utilization, to reduce their content.[27–33]

The utilization of Pt-Rh catalysts represents another alternative proposed to minimize the Rh content in TWC formulations.[34–45] This strategy relies on properties of Pt-Rh alloys to optimize the performance, while reducing the catalyst cost.

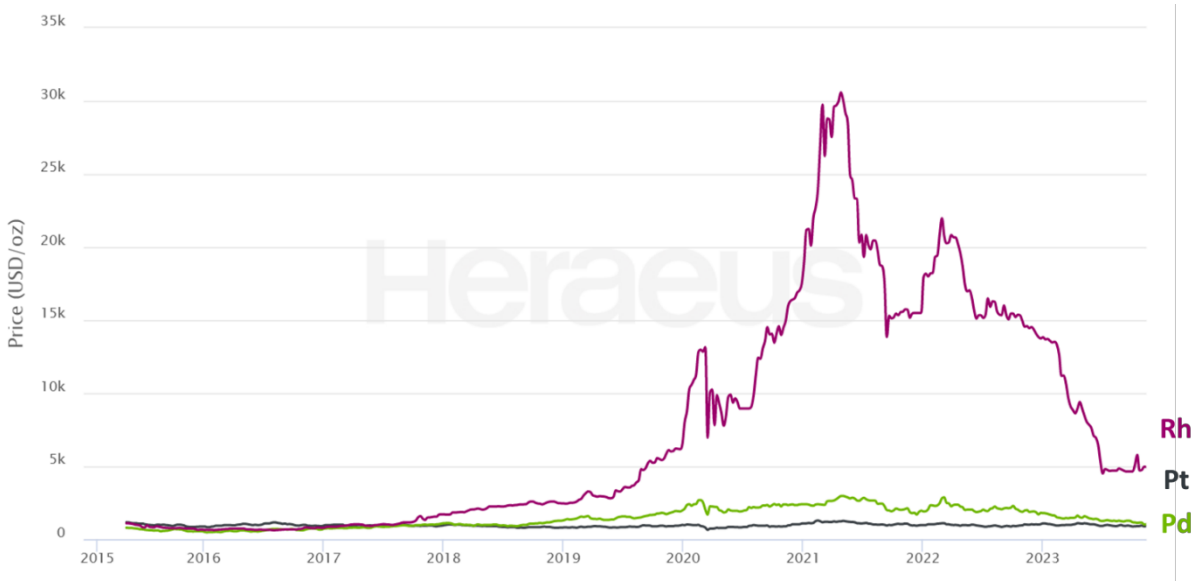

Figure 1.3: price in $/once of Rh (purple), Pd (green) and Pt (blue)- https://www.heraeus.com accessed on 11/18/2023

1.5 TWC formulation adapted to new configurations or to technological innovations

The new, stricter emission regulations have emphasized the need to reduce emissions during cold start. Cold start refers to the initial phase of an internal combustion engine's operation when the engine is cold and the catalyst is not yet active, resulting in higher emissions of CO, HC and NO.

One proposed solution included the use of close-coupled catalysts, which involves positioning the catalyst in closer proximity to the engine. This approach allows the catalyst to reach a temperature where reaction conversion occurs more rapidly, leading to more effective emissions control. However, the proximity to the engine can expose the catalyst to higher temperature, potentially leading to deactivation through sintering and overall reduced durability. Therefore, catalyst design must ensure that close-coupled TWC systems mitigate emissions without compromising catalyst performance and durability.[46]

In addition, with the increasingly stringent regulations imposing limits on CO_2 emissions, the new generation of engines is required to be more efficient and optimize fuel economy. This results in

lower temperature exhaust gas, which presents challenges in meeting emission standards.[47] As a result, there is growing demand for catalytic converters with enhanced low-temperature activity and high thermal stability.[48]

Another method for reducing CO_2 emissions involves a fuel cut, which results in lower fuel consumption. During the acceleration period, the engine operates under slightly fuel-rich conditions to increase the power. However, during deceleration, fuel cut is employed, subjecting the TWC to highly oxidizing conditions. While oxidizing conditions restore the oxygen storage materials to their initial state, they have negative effects on Rh in the catalysts. At high temperature and under oxidizing conditions, Rh/Al_2O_3 experiences deactivation. It has been suggested that under oxidizing conditions (lean) and at temperature higher than 600°C, Rh^{3+} ions diffuse into the alumina to form rhodium aluminate species ($RhAlO_x$), along with rhodium oxides, Rh_2O_3:[49,50]

$$Rh/Al_2O_3 \xrightarrow{O2,>600C} RhAl_2O_x$$

Rhodium aluminate species have been found inactive for reactions such as CO oxidation and NO reduction. The characterization for these species has been challenging, because they have not been observed using traditional techniques, such as XRD. However, the presence of these species was supported by H_2 temperature programmed reduction (TPR) experiments, which revealed reduction features at temperatures higher than 700°C.[51] More recently, a direct observation was provided using STEM. It was shown that Rh ions diffuse into the alumina interstitial sites and are preferentially located in the octahedral sites of the cubic spinel Al_2O_3 structure.[52]

While Rh aluminate may form under oxidizing conditions and high temperature, it has also been reported that Rh can be partially restored when the catalyst is exposed to a reducing environment at temperatures higher than 800°C, leading to the following regeneration process:[50,51,53]

$RhAl_2O_x + H_2 \rightarrow Rh + Al_2O_3$

However, at these elevated temperatures, Rh tends to sinter, leading to a decrease in active surface area, which represents a second Rh deactivation mode.

Efforts have been made to minimize the deactivation process occurring during severe ageing. Strategies involved the stabilization of the support by adding additives such as La, promoters, such as Pr or Y, and oxygen storage materials.[54–56] Another strategy included the use of alloy catalysts. It was shown that the addition of Pt to Rh catalysts increased the catalyst dispersion, while simultaneously preventing Rh from diffusing into the alumina support and maintaining activity even after severe ageing.[34]

Catalytic converters have made significant progress and are now capable of reducing 99% of emissions during FTP test cycles. However, they continue to face challenges due to new stricter emissions regulations, new technology advancements and fluctuating PGM prices. The next generation of TWC must meet several demands, including being active at low temperatures, more durable and less costly. Achieving these goals, while minimizing the PGM usage, needs a detailed understanding of the reaction mechanism. This approach to catalyst design is crucial for meeting emission standards while optimizing precious metal utilization.

This work focuses on Rh/Al_2O_3 and Pd/CeO_2 catalysts, considered model catalysts for TWC applications.

Rh catalysts are usually characterized by low loadings due to their high price and optimization in use over the years. This results in a distribution of Rh nanoparticles and single atoms. The presence of reactants induces changes in the distribution of nanoparticles and single atoms, which results in changes in reaction rates. Through a combination of kinetic and spectroscopy studies we

investigated Rh restructuring and the consequences on CO oxidation activity, in Chapter 3. Further, spectroscopy studies were carried out to understand the role of O_2 and H_2O on the CO-induced Rh mobility and these results are presented in Chapter 4. With newfound insights on Rh restructuring, we proceeded in Chapter 5 to explore the effects of H_2O in NO reduction by CO reaction and how the reaction products influence both the kinetics as well as the catalyst structure. Finally, Appendix C shows a preliminary kinetic exploration of C_3H_6 oxidation in the presence and absence of NO on a new catalyst formulation: Pt-Rh-Sr/Al_2O_3. This is a collaborative study involving the University of Central Florida, General Motors and Pacific Northwest National Lab.

The final segment of this work presented on Chapter 6 was conducted on Pd/CeO_2 catalysts. Given the difficulty of quantifying surface metal sites on ceria-supported catalysts, we proposed a modified approach for measuring metal dispersion. This method was validated via kinetic and spectroscopic studies. The ability to count surface metal sites is essential for the evaluation and comparison of different catalysts.

1.6 References

(1) Spindt, R. S.; Wolfe, C. L.; Stevens, D. R. Nitrogen Oxides, Combustion, and Engine Deposits. *J Air Pollut Control Assoc* **1956**, *6* (3), 127–133. https://doi.org/10.1080/00966665.1956.10467741.

(2) Haagen-smit, A. J. Chemistry and Physiology of Los Angeles Smog. *Eng. Sci. (Calif. Inst. Tech.)* **1942**, *9* (3), 299–312.

(3) Hill, J.; Polasky, S.; Nelson, E.; Tilman, D.; Huo, H.; Ludwig, L.; Neumann, J.; Zheng, H.; Bonta, D. *Climate Change and Health Costs of Air Emissions from Biofuels and Gasoline*; 2009. www.pnas.orgcgidoi10.1073pnas.0812835106.

(4) Twigg, M. V. Progress and Future Challenges in Controlling Automotive Exhaust Gas Emissions. *Appl Catal B* **2007**, *70* (1–4), 2–15. https://doi.org/10.1016/j.apcatb.2006.02.029.

(5) Shelef, M.; Mccabe, R. W. *Twenty-Five Years after Introduction of Automotive Catalysts: What Next?*; 2000; Vol. 62.

(6) Farrauto, R. J.; Deeba, M.; Alerasool, S. Gasoline Automobile Catalysis and Its Historical Journey to Cleaner Air. *Nature Catalysis*. Nature Publishing Group July 1, 2019, pp 603–613. https://doi.org/10.1038/s41929-019-0312-9.

(7) Heck, R. M.; Farrauto, R. J. Automobile Exhaust Catalysts. *Appl Catal A Gen* **2001**, *221*, 443–457.

(8) Farrauto, R. J.; Heck, R. M. Catalytic Converters : State of the Art and Perspectives. **1999**, *51*, 351–360.

(9) *Vehicles and engines. US Environmental Protection Agency*.

(10) *United States: Cars and Light-Duty Trucks: Tier 3*.

(11) *Europe: Light-Duty Emissions*.

(12) Dey, S.; Mehta, N. S. Automobile Pollution Control Using Catalysis. *Resources, Environment and Sustainability*. Elsevier B.V. December 1, 2020. https://doi.org/10.1016/j.resenv.2020.100006.

(13) Auckenthaler·, T. S.; Onder·, C. H.; Geering·, H. P. *ASPECTS OF DYNAMIC THREE-WAY CATALYST BEHAVIOUR INCLUDING OXYGEN STORAGE*. www.elsevier.comllocatelifac.

(14) Moos, R.; Spörl, M.; Hagen, G.; Gollwitzer, A.; Wedemann, M.; Fischerauer, G. *TWC: Lambda Control and OBD without Lambda Probe - an Unitial Approach*; 2008.

(15) Di Monte, R.; KasˇparKasˇpar, J. *On the Role of Oxygen Storage in Three-Way Catalysis*.

(16) Rood, S.; Eslava, S.; Manigrasso, A.; Bannister, C. Recent Advances in Gasoline Three-Way Catalyst Formulation: A Review. *Proceedings of the Institution of Mechanical Engineers, Part D: Journal of Automobile Engineering*. SAGE Publications Ltd March 1, 2020, pp 936–949. https://doi.org/10.1177/0954407019859822.

(17) Matsumoto, S. Recent Advances in Automobile Exhaust Catalysts. In *Catalysis Today*; 2004; Vol. 90, pp 183–190. https://doi.org/10.1016/j.cattod.2004.04.048.

(18) Di Monte, R.; Fornasiero, P.; Desinan, S.; Kašpar, J.; Gatica, J. M.; Calvino, J. J.; Fonda, E. Thermal Stabilization of CexZr1-XO2 Oxygen Storage Promoters by Addition of Al2O3: Effect of Thermal Aging on Textural, Structural, and Morphological Properties. *Chemistry of Materials* **2004**, *16* (22), 4273–4285. https://doi.org/10.1021/cm048829q.

(19) Sugiura, M.; Ozawa, M.; Suda, A.; Suzuki, T.; Kanazawa, T. Development of Innovative Three-Way Catalysts Containing Ceria-Zirconia Solid Solutions with High Oxygen Storage/Release Capacity. *Bull Chem Soc Jpn* **2005**, *78* (5), 752–767. https://doi.org/10.1246/bcsj.78.752.

(20) Si, R.; Zhang, Y. W.; Wang, L. M.; Li, S. J.; Lin, B. X.; Chu, W. S.; Wu, Z. Y.; Yan, C. H. Enhanced Thermal Stability and Oxygen Storage Capacity for Ce XZr1-XO2 (x = 0.4-0.6) Solid Solutions by Hydrothermally Homogenous Doping of Trivalent Rare Earths. *Journal of Physical Chemistry C* **2007**, *111* (2), 787–794. https://doi.org/10.1021/jp0630875.

(21) Duprez, D.; Descorme, C.; Birchem, T.; Rohart, E. *Topics in Catalysis Vols*; 2001; Vol. 16.

(22) Trovarelli, A. Catalytic Properties of Ceria and CeO2-Containing Materials. *Catal Rev Sci Eng* **1996**, *38* (4), 439–520. https://doi.org/10.1080/01614949608006464.

(23) Trovarelli, A.; De Leitenburg, C.; Boaro, M.; Dolcetti, G. The Utilization of Ceria in Industrial Catalysis. *Catal Today* **1999**, *50*, 353–367. https://doi.org/https://doi.org/10.1016/S0920-5861(98)00515-X.

(24) Devaiah, D.; Reddy, L. H.; Park, S. E.; Reddy, B. M. Ceria–Zirconia Mixed Oxides: Synthetic Methods and Applications. *Catal Rev Sci Eng* **2018**, *60* (2), 177–277. https://doi.org/10.1080/01614940.2017.1415058.

(25) Matsuura, S.; Hirai, A.; Arimura, K.; Shinjoh, H. *Development of Three-Way Catalyst with Using Only Pd as Activator*; 1995; Vol. 104. https://about.jstor.org/terms.

(26) Wang, J.; Chen, H.; Hu, Z.; Yao, M.; Li, Y. A Review on the Pd-Based Three-Way Catalyst. *Catalysis Reviews - Science and Engineering*. Taylor and Francis Inc. January 2, 2015, pp 79–144. https://doi.org/10.1080/01614940.2014.977059.

(27) Jeong, H.; Kwon, O.; Kim, B. S.; Bae, J.; Shin, S.; Kim, H. E.; Kim, J.; Lee, H. Highly Durable Metal Ensemble Catalysts with Full Dispersion for Automotive Applications beyond Single-Atom Catalysts. *Nat Catal* **2020**, *3* (4), 368–375. https://doi.org/10.1038/s41929-020-0427-z.

(28) Pham, H. N.; DeLaRiva, A.; Peterson, E. J.; Alcala, R.; Khivantsev, K.; Szanyi, J.; Li, X. S.; Jiang, D.; Huang, W.; Sun, Y.; Tran, P.; Do, Q.; DiMaggio, C. L.; Wang, Y.; Datye, A. K. Designing Ceria/Alumina for Efficient Trapping of Platinum Single Atoms. *ACS Sustain Chem Eng* **2022**. https://doi.org/10.1021/ACSSUSCHEMENG.2C01380.

(29) Porter, S.; Datye, A. Identifying Individual Atoms in Single Atom Pt/CeO 2 Catalysts . *Microscopy and Microanalysis* **2021**, *27* (S1), 2608–2610. https://doi.org/10.1017/s1431927621009260.

(30) Liu, L.; Corma, A. Metal Catalysts for Heterogeneous Catalysis: From Single Atoms to Nanoclusters and Nanoparticles. *Chem. Rev.* **2018**, *118* (10), 4981–5079. https://doi.org/10.1021/acs.chemrev.7b00776.

(31) Lou, Y.; Xu, J.; Zhang, Y.; Pan, C.; Dong, Y.; Zhu, Y. Metal-Support Interaction for Heterogeneous Catalysis: From Nanoparticles to Single Atoms. *Mater Today Nano* **2020**, *12*. https://doi.org/10.1016/j.mtnano.2020.100093.

(32) Kunwar, D.; Zhou, S.; Delariva, A.; Peterson, E. J.; Xiong, H.; Pereira-Hernández, X. I.; Purdy, S. C.; Ter Veen, R.; Brongersma, H. H.; Miller, J. T.; Hashiguchi, H.; Kovarik, L.; Lin, S.; Guo, H.; Wang, Y.; Datye, A. K. Stabilizing High Metal Loadings of Thermally Stable Platinum Single Atoms on an Industrial Catalyst Support. *ACS Catal* **2019**, *9* (5), 3978–3990. https://doi.org/10.1021/acscatal.8b04885.

(33) Alexander J. Hoffman, Chithra Asokan, Nicholas Gadinas, Pavlo Kravchenko, Andrew "Bean" Getsoian, Phillip Christopher, and D. H. Experimental and Theoretical Characterization of Rh Single Atoms Supported on Γ-Al2O3 with Varying Hydroxyl Contents during NO Reduction by CO. **2022**, *12*, 11697–11715. https://doi.org/10.1021/acscatal.2c02813.

(34) Li, Y.; Low, K.-B.; Sundermann, A.; Zhu, H.; Betancourt, L. E.; Kang, C.; Johnson, S.; Xie, S.; Liu, F. Understanding the Nature of Pt-Rh Synergy for Three-Way Conversion Catalysis. *Appl Catal B* **2023**, *334*, 122821. https://doi.org/10.1016/j.apcatb.2023.122821.

(35) Cai, Y.; Stenger, H. G.; Lyman, C. E. Catalytic CO Oxidation over Pt-Rh/γ-Al2O3 Catalysts. *J Catal* **1996**, *161* (1), 123–131. https://doi.org/10.1006/jcat.1996.0169.

(36) L.Pirault a, D. El Azami El Idrissi a, p. Mar6cot a, J.M. Dominguez b, G. M. c; A., M. P. c and J. B.; A. Preparation of Pt-Rh/Al2O3-CeO2 Catalysts by Surface Redox Reactions. **1995**, *96*, 193–202.

(37) Anderson, J. A.; Rochester, C. H. Infrared Study of CO Adsorption on Pt-Rh/Al2O3 Catalysts. *Journal of the Chemical Society, Faraday Transactions* **1991**, *87* (9), 1479–1483. https://doi.org/10.1039/FT9918701479.

(38) Lecomte, J. J.; Haydar, S.; Granger, P.; Leclercq, L.; Leclercq, G.; Joly, J. P. Investigation of Oxygen Interaction with a Pt-Rh/Al2O 3 Catalyst by a Differential Temperature-Programmed Desorption Method. *Langmuir* **2003**, *19* (22), 9266–9270. https://doi.org/10.1021/la0344635.

(39) Dimick, P. S.; Kross, J. L.; Roberts, E. G.; Herman, R. G.; Stenger, H. G.; Lyman, C. E. Examining the Surface of a Synergistic Pt-Rh/γ-Al2O3 Catalyst Using NO as a Probe Molecule. *Appl Catal B* **2009**, *89* (1–2), 1–11. https://doi.org/10.1016/j.apcatb.2008.11.025.

(40) Pirault, L.; Guérin, M.; Maire, F.; Marécot, P.; Barbier, J. Catalytic Activity and EXAFS Characterisation of Three Way Automative Pt-Rh/Al2O3-CeO2 Catalysts from Different Preparations. *Appl Catal A Gen* **1998**, *172* (2), 249–258. https://doi.org/10.1016/S0926-860X(98)00131-8.

(41) Savargaonkar, N.; Khanra, B. C.; Pruski, M.; King, T. S. Influence of Hydrogen Chemisorption on the Surface Composition of Pt-Rh/Al2O3 Catalysts. *J Catal* **1996**, *162* (2), 277–283. https://doi.org/10.1006/jcat.1996.0285.

(42) Nikolaidis, G.; Baier, T.; Zapf, R.; Kolb, G.; Hessel, V.; Maier, W. F. Kinetic Study of CO Preferential Oxidation over Pt-Rh/γ-Al2O3 Catalyst in a Micro-Structured Recycle Reactor. *Catal Today* **2009**, *145* (1–2), 90–100. https://doi.org/10.1016/j.cattod.2008.06.008.

(43) Ohtsuka, H. Pt-Rh/CeO2-Al2O3 for Controlling Emissions from Natural Gas Engines: Three-Way Catalytic Activity at Low Temperatures and Effects of SO2 Aging. *Emission Control Science and Technology* **2015**, *1* (1), 108–116. https://doi.org/10.1007/s40825-014-0009-0.

(44) Hérault, N.; Olivet, L.; Pirault-Roy, L.; Especel, C.; Vicerich, M. A.; Pieck, C. L.; Epron, F. Controlled Preparation and Characterization of Pt-Rh/Al2O3 Bimetallic Catalysts for Reactions in Reducing Conditions. *Appl Catal A Gen* **2016**, *517*, 81–90. https://doi.org/10.1016/j.apcata.2016.02.024.

(45) Hangas, J.; Chen, A. E. Comparative Analytical Study of Two Pt-Rh Three-Way Catalysts. *Catal Letters* **2006**, *108* (1–2), 103–111. https://doi.org/10.1007/s10562-006-0016-z.

(46) Hu, Z.; Heck, R. M. *High Temperature Ultra Stable Close-Coupled Catalysts*; 1995; Vol. 104. https://www.jstor.org/stable/44615082.

(47) Zammit, M.; Dimaggio, C.; Kim, C.; Lambert, C.; Muntean, G.; Peden, C.; Parks, J.; Howden, K. Future Automotive Aftertreatment Solutions : The 150 °C Challenge Workshop Report. *US DRIVE Work shop* **2012**.

(48) Getsoian, A. (Bean); Theis, J. R.; Paxton, W. A.; Lance, M. J.; Lambert, C. K. Remarkable Improvement in Low Temperature Performance of Model Three-Way Catalysts through Solution Atomic Layer Deposition. *Nat Catal* **2019**, *2* (7), 614–622. https://doi.org/10.1038/s41929-019-0283-x.

(49) Yao, H. C.; Shelef, A. M. *Surface Interactions in the System Rh/AI,O*; 1977; Vol. 50.

(50) Wong, C.; McCabe, R. W. Effects of High-Temperature Oxidation and Reduction on the Structure and Activity of Rh Al2O3and Rh SiO2 Catalysts. *J Catal* **1989**, *119* (1), 47–64. https://doi.org/10.1016/0021-9517(89)90133-4.

(51) Hwang, C. P.; Yeh, C. T.; Zhu, Q. Rhodium-Oxide Species Formed on Progressive Oxidation of Rhodium Clusters Dispersed on Alumina. *Catal Today* **1999**, *51* (1), 93–101. https://doi.org/10.1016/S0920-5861(99)00011-5.

(52) Li, C.; Wu, J.; Getsoian, A. B.; Cavataio, G.; Jinschek, J. R. Direct Observation of Rhodium Aluminate (RhAlO x) and Its Role in Deactivation and Regeneration of Rh / Al 2 O 3 under Three-Way Catalyst Conditions. **2022**. https://doi.org/10.1021/acs.chemmater.1c03513.

(53) Burch, R.; Loader, P. K.; Cruise, N. A. An Investigation of the Deactivation of Rh/Alumina Catalysts under Strong Oxidising Conditions. *Appl Catal A Gen* **1996**, *147* (2), 375–394. https://doi.org/10.1016/S0926-860X(96)00212-8.

(54) Zheng, Q.; Farrauto, R.; Deeba, M.; Valsamakis, I. Part I: A Comparative Thermal Aging Study on the Regenerability of Rh/Al2O3 and Rh/CexOy-ZrO2 as Model Catalysts for Automotive Three Way Catalysts. *Catalysts* **2015**, *5* (4), 1770–1796. https://doi.org/10.3390/catal5041770.

(55) Machida, M.; Uchida, Y.; Iwashita, S.; Yoshida, H.; Tsushida, M.; Ohyama, J.; Nagao, Y.; Endo, Y.; Wakabayashi, T. Catalyst Deactivation via Rhodium-Support Interactions under High-Temperature Oxidizing Conditions: A Comparative Study on Hexaaluminates versus Al2O3. *ACS Catal* **2021**, *11* (15), 9462–9470. https://doi.org/10.1021/acscatal.1c01695.

(56) Ayumi Fujiwara, Yutaro Tsurunari, Shundai Iwashita, Hiroshi Yoshida, Junya Ohyama, and M. M. Dynamic Change of Rh Oxidation State During Lean-Rich Perturbation and Light-Off of Three-Way Catalysis Analysed Using In Situ Diffuse Reflectance UV–Vis Spectroscopy. *ChemCatChem* **2023**, No. Ii, 0–3. https://doi.org/10.1002/cnma.202300020.

Chapter 2: Experimental methods

2.1 Bench scale reactor

CO oxidation and NO reduction by CO steady-state experiments and temperature programmed desorption (TPD) experiments were performed using a lab bench scale reactor. The design, depicted in Figure 2.1, involved two independent manifolds: the "main" manifold which contains the gases needed for the reaction, including N_2, CO, O_2, NO and C_3H_6; and a "secondary" manifold which is used to pretreat the catalyst and includes gases such as, N_2, O_2 and H_2. The gas concentrations are controlled by varying the flowrates using MKS mass flow controllers. Experiments in the presence of water were performed using a controlled evaporator mixer (CEM), purchased from Bronkhost, able to introduce water into the main manifold gas stream. Each line is heated and held at 120°C to avoid water condensation.

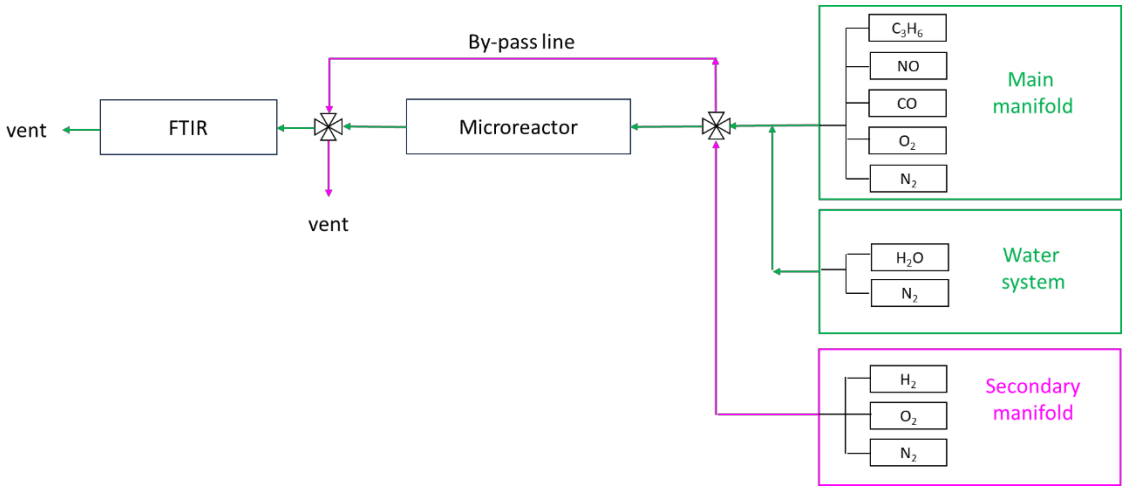

Figure 2.1: Reactor schematic. In this representation, the main manifold is directed towards the microreactor, while the secondary manifold is directed towards the by-pass line.

The main and secondary manifolds, each with independent lines, are connected to two four-way valves, purchased from Swagelok. The first four-way valve directs the flow from the main

manifold to either the reactor or the by-pass line, while the flow from the secondary manifold is directed to the other available line. The second four-way valve, located downstream of the micro-reactor, directs the flow to the analyzer or to the vent. The two four-way valves are controlled by a Labview program which switches the two valves simultaneously such that the main manifold flow is sent to the analyzer.

Certain gas concentrations were measured using a MG2030 FTIR analyzer. Before each experiment, a background spectrum was taken with flowing N_2 and averaging 16 scans. The data are recorded every second with a resolution of 0.5 cm^{-1}.

The reactor consisted of a quartz tube loaded with a powder catalyst. The quartz tube has an internal diameter of 4 mm and a length of 45 mm. The powder catalyst was diluted with cordierite or silica to avoid heat transfer limitations.[1] The catalyst was pelletized and sieved to obtain a pellet size of 250-400 μm or 53-177 μm, depending on the experiment.

The micro-reactor was horizontally placed in a Lindberg Blue furnace. The temperature was measured using K-type thermocouples placed at the inlet and the outlet of the catalytic bed.

2.2 Diffuse Reflectance Infrared Fourier Transform Spectroscopy (DRIFTS)

DRIFTS is an infra-red spectroscopic technique used here to characterize catalyst component speciation and study the species adsorbed on the catalyst surface under reaction conditions.[2] As shown in Figure 2.2, the IR beam trajectory involves the incident beam striking the sample. The diffuse reflected light is then collected by curved and flat mirrors and reaches the detector. The optics are designed to minimize the contribution from the reflected light, while maximizing the contribution from the diffuse reflected light. The diffuse reflected light contains the information about the catalyst.[3]

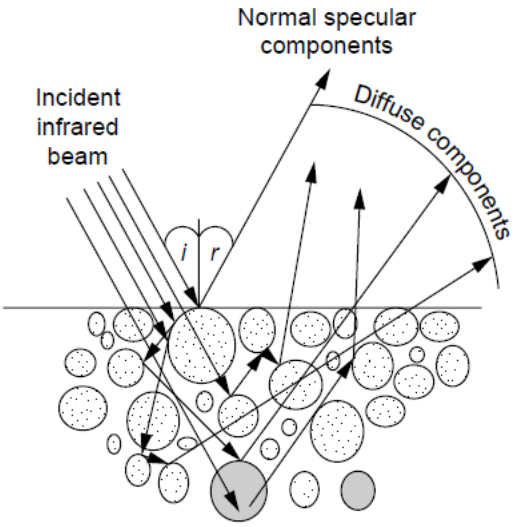

Figure 2.2: Incident beam trajectory for DRIFTS cells

DRIFTS experiments were performed with a Thermo Scientific Nicolet iS50 FTIR with an MCT liquid nitrogen cooled detector. The catalyst was loaded in a custom-made Harrick Scientific reaction chamber.

The custom-made reaction chamber is characterized by a low dead volume which minimizes the gas phase species contribution. In addition, the sample holder is divided into two parts: one can be loaded with the catalyst, while the other one with an inert/reference material. The reaction chamber is installed on a movable stage, allowing the user to switch the position from the catalyst to the inert material. This feature allowed us to acquire spectra from both the catalyst and the reference material, perform a gas phase subtraction and study the surface species on the catalyst, without the need of purging the gas phase. The reaction chamber is equipped with one ZnSe flat window.

While the reaction chamber can reach temperatures up to 910°C under an Ar flow, during our experiments, the temperature did not exceed 500°C. The temperature is controlled using a K type

thermocouple which communicates with a Harrick Scientific temperature controller. To preserve the reaction chamber and the ZnSe window from overheating, the reaction chamber is equipped with a water-cooling jacket.

The DRIFTS setup includes a series of MKS mass flow controllers to control the inlet gas composition. The reaction mixture passes through a dry-acetone or liquid nitrogen cold trap to remove any water residue from the gas stream. The gases are introduced into the reaction chamber though the inlet and pass through the sample from the top to underneath the sample. All the lines were heated to 120°C to prevent water condensation. Wet experiments were performed by introducing water into the system through a bubbler maintained at 60°C.

Before collecting the spectra, a background was taken. Each spectrum was obtained by averaging 32 scans, in a range between 4000 to 600 cm^{-1}, with a resolution of 4 cm^{-1}. The spectra are presented in Kubelka-Munk units. Semi-quantitative analysis was performed after deconvoluting spectra using a Gaussian function.

2.3 X-ray diffraction (XRD)

XRD is a technique which provides information on the structure of crystalline materials. It is based on the interactions between the X-ray and crystalline materials. When the x-ray beam is directed at a crystalline sample, the x-rays are scattered by the crystal lattice leading to the formation of a diffraction pattern on a detector. The angles and the intensities of the diffraction contain information about the crystal structure. XRD patterns were obtained on an Empyrean Multipurpose X-ray diffractometer with a Cu anode ($\lambda = 0.1542$ nm).

From the XRD pattern, the crystal size could be calculated using the Scherrer equation:

$$d = \frac{K\,\lambda}{\beta\,cos\theta}$$

where d is the average crystallite size, λ is the wavelength of the x-ray source, K is the shape constant, β is the reflection width and θ the Bragg angle.

Generally, the detection limit for XRD is up to 100 nm particle size. [4–6]

2.4 STEM and EDS

Scanning Transmission Electron Microscopy (STEM), integrated with Energy-Dispersive Spectroscopy (EDS) is a microscopy technique that allows high resolution imaging and elemental mapping of samples at the nanoscale, and it allows particle size measurement.

For some samples, STEM and EDS were employed to confirm particle size measurements and were performed using a Themis 60-300 kV transmission electron microscope in high angle annular dark field (HAADF) mode. HAADF provides contrast based on the atomic number. In the case of catalysts, such as Pd/CeO_2, this technique was unsuccessful given the poor Z contrast between Pd and ceria.[7]

2.5 Physisorption and Chemisorption

A Micromeritics ASAP2020 Plus was used to perform physisorption and chemisorption.

N_2 physisorption is widely employed to characterize mesoporous catalysts surface area and porosity. The working principle involves the physisorption of nitrogen on the catalyst surface through van der Waals forces at different pressures. By measuring the quantity of N_2 adsorbed, we can determine specific surface area using the Brunauer-Emmett-Teller (BET) equation.[8] Along with surface area, from the adsorption isotherms it is possible to obtain pore size distribution, by using mathematical modeling, such as Barrett-Joyner-Halenda (BJH) method, and the total pore volume, calculated from the volume of nitrogen adsorbed.[9]

Before starting the analysis, the catalyst underwent degassing, which involves a pretreatment where heat and vacuum are applied to remove adsorbed contaminants, such as water and carbon dioxide, which could potentially interfere with the analysis. The catalyst is then cooled under vacuum to -196°C and N_2 is dosed with incremental increases in pressure. After each dose the system is allowed to equilibrate, and the quantity adsorbed is calculated. From the resulting adsorption isotherm, the quantity of gas necessary to form a monolayer is measured, enabling the determination of the catalyst surface area.

Static volumetric chemisorption is a technique used to measure the metal dispersion of a catalyst. It involves the adsorption of a probe molecule, such as CO and H_2, which forms bonds with the metal surface.[10] The strength of adsorption can vary, with weak adsorption usually indicated as reversible chemisorption, and strong adsorption categorized as irreversible chemisorption. After reducing the catalyst in H_2, the catalyst is exposed to precise doses of the probe molecule at varying pressures, from 10 to 450 mmHg. The analysis is usually conducted at 35°C; however, exceptions may apply, and higher temperatures can be used.[11] After dosing the gas, the system is allowed to equilibrate and the amount adsorbed is measured. Each point obtained at different pressures contributes to the adsorption isotherm. The volume adsorbed increases with increasing the pressure, until it reaches a linear regime, which corresponds to monolayer coverage. The first isotherm, also called total isotherm, includes molecules that are physiosorbed, and strongly and weakly adsorbed. After the first isotherm the system is evacuated, causing the desorption of weakly adsorbed probe molecules, and a new isotherm is obtained, under the same conditions. This last isotherm is associated with only reversible chemisorption, as the catalyst surface is already covered with strongly adsorbed molecules. The quantity of gas required to form a monolayer coverage is obtained by

extrapolating the linear portion of the total isotherm back to the y-axis. With the quantity of gas adsorbed it is possible to measure the active surface atoms participating in the chemisorption:

$$N_{surf\ atoms} = S \cdot N_{gas\ ads}$$

Where $N_{surf\ atoms}$ corresponds to the number of metal atoms active on the catalyst surface active for the chemisorption, S is the stoichiometric factor and $N_{gas\ ads}$ is the number of molecules adsorbed. The metal dispersion is then obtained from the ratio of the number of the exposed atoms to the total number of metal atoms in the catalyst.

The stoichiometric factor depends on the number of metal atoms involved during the adsorption process. For example, in the case of H_2, which dissociatively adsorbs on metals, as:

$H_2 + 2M \rightarrow 2M - H$

the stoichiometric factor S is 2.[12]

In the case of CO, there are several bonding configurations, therefore the stoichiometry can vary. CO can adsorb on metals in the following forms:[10,13]

- Dicarbonyls, $M - (CO)_2$, S = 0.5
- Linear, M – CO, S = 1
- Bridged, M_2 – CO, S = 2.

The choice of the adsorbate to use mainly depends on the metal and the catalyst support under investigation and how the probe molecule and the metal interact with each other. For example, in this work, Rh dispersion was measured via H_2 chemisorption, since Rh undergoes structural changes in the presence of CO,[14,15] while in the case of Pd/CeO_2 catalysts, CO was used as probe molecule to avoid the formation of Pd hydride and hydrogen spillover to the support.[11,16]

2.6 References

(1) Perego, C.; Peratello, S. Experimental Methods in Catalytic Kinetics. *Catal Today* **1999**, *52* (2–3), 133–145. https://doi.org/10.1016/S0920-5861(99)00071-1.

(2) Lamberti, C.; Zecchina, A.; Groppo, E.; Bordiga, S. Probing the Surfaces of Heterogeneous Catalysts by in Situ IR Spectroscopy. *Chem Soc Rev* **2010**, *39* (12), 4951–5001. https://doi.org/10.1039/C0CS00117A.

(3) Armaroli, T.; Bécue, T.; Gautier, S. *Diffuse Reflection Infrared Spectroscopy (DRIFTS): Application to the in Situ Analysis of Catalysts*; 2004; Vol. 59.

(4) Gakehan, P.; Kuo, H. K.; Saavedha, A.; J, A. R. *Particle Size Distribution Function of Supported Metal Catalysts by X-Ray Diffraction*; 1978; Vol. 52.

(5) Hargreaves, J. S. J. Some Considerations Related to the Use of the Scherrer Equation in Powder X-Ray Diffraction as Applied to Heterogeneous Catalysts. *Catalysis, Structure and Reactivity* **2016**, *2* (1–4), 33–37. https://doi.org/10.1080/2055074X.2016.1252548.

(6) Langford, J. I.; Wilson, A. J. C. Scherrer after Sixty Years: A Survey and Some New Results in the Determination of Crystallite Size. *J Appl Crystallogr* **1978**, *11* (2), 102–113. https://doi.org/10.1107/s0021889878012844.

(7) Hill, A. J.; Seo, C. Y.; Chen, X.; Bhat, A.; Fisher, G. B.; Lenert, A.; Schwank, J. W. Thermally Induced Restructuring of Pd@ceo2 and Pd@sio2 Nanoparticles as a Strategy for Enhancing Low-Temperature Catalytic Activity. *ACS Catal* **2020**, *10* (3), 1731–1741. https://doi.org/10.1021/acscatal.9b05224.

(8) Dollimore, D.; Spooner, P.; Turner, A. The Bet Method of Analysis of Gas Adsorption Data and Its Relevance to the Calculation of Surface Areas. *Surface Technology* **1976**, *4* (2), 121–160. https://doi.org/10.1016/0376-4583(76)90024-8.

(9) Leofanti, G.; Padovan, M.; Tozzola, G.; Venturelli, B. Surface Area and Pore Texture of Catalysts. *Catal Today* **1998**, *41* (1–3), 207–219. https://doi.org/10.1016/S0920-5861(98)00050-9.

(10) Scholten, J. J. F. Metal Surface Area and Metal Dispersion in Catalysts. *Stud Surf Sci Catal* **1979**, *3* (C), 685–714. https://doi.org/10.1016/S0167-2991(09)60244-5.

(11) Boudart, M.; Hwang, H. S. Solubility of Hydrogen in Small Particles of Palladium. *J Catal* **1975**, *39*, 44–52. https://doi.org/https://doi.org/10.1016/0021-9517(75)90280-8.

(12) Christmann, K. *Some General Aspects of Hydrogen Chemisorption on Metal Surfaces*; 1995; Vol. 48.

(13) Gundry, P. M.; Tompkins, F. C. *CHEMISORPTION OF GASES ON METALS*.

(14) Yates, J. T.; Kolasinski, K. Infrared Spectroscopic Investigation of the Rhodium Gem-Dicarbonyl Surface Species. *J Chem Phys* **1983**, *79* (2), 1026–1030. https://doi.org/10.1063/1.445844.

(15) Cavanagh, R. R.; Yates, J. T. Site Distribution Studies of Rh Supported on Al2O3 - An Infrared Study of Chemisorbed CO. *J Chem Phys* **1981**, *74* (7), 4150–4155. https://doi.org/10.1063/1.441544.

(16) Lee, J.; Tieu, P.; Finzel, J.; Zang, W.; Yan, X.; Graham, G.; Pan, X.; Christopher, P. How Pt Influences H 2 Reactions on High Surface-Area Pt /CeO2 Powder Catalyst Surfaces. **2023**, 1–27. https://doi.org/10.1021/jacsau.3c00330.

Chapter 3: Rhodium catalyst structural changes during, and their impacts on the kinetics of, CO oxidation

This chapter has been adapted from the article published in JACS Au: "Silvia Marino, Lai Wei, Marina Cortes-Reyes, Yisun Cheng, Paul Laing, Giovanni Cavataio, Christopher Paolucci and William Epling, JACS Au, 2023, 3, 2, 459–467"

3.1 Introduction

It is becoming more recognized that catalyst structure can be dynamic, changing with time on stream and reactor and reaction conditions.[1–6] These catalyst structural changes can alter the catalyst activity and the selectivity towards desired products.[7,8] And they can of course also complicate kinetic analysis due to site type and density changes. Therefore, studying catalyst dynamics under reaction conditions is critical in understanding reactions, mechanisms and designing catalysts.

There are several literature studies that demonstrate reductant or oxidant induced mobility of catalytically active sites. Structural evolution of single atoms to nanoparticles with exposure to high temperature reducing treatments has been widely reported for Pt and Pd supported on oxide supports and zeolites. [9,10,11,12] These structural changes can also be reversible with fragmentation of nanoparticles into isolated single atoms occurring when the catalyst is exposed to oxidizing conditions and high temperature.[13,14]

In some cases, adsorbate-induced structural changes have been observed under reaction conditions. Pt restructuring was observed via IR spectroscopy during CO oxidation, where the fraction of well-coordinated and under-coordinated sites changed.[15] Operando electron microscopy was used to track unsupported Pd nanoparticle structural changes as a function of temperature during CO oxidation. At low temperature, Pd nanoparticles would present low index planes that showed low activity towards CO oxidation, while at high temperature, the nanoparticles assumed a rounder

surface leading to a higher CO conversion.[16] Theoretical studies combined with X-ray absorption experiments showed that in the presence of NH_3, Cu ions become solvated by the NH_3 and mobile, enabling them to combine and form ion pairs that participate in the selective catalytic reduction (SCR) redox cycle.[17,18] Pd nanoparticles disintegration into single atoms on Pd/Al_2O_3 was observed during methane oxidation in an excess of O_2. Pd nanoparticle redispersion caused by the oxidative environment led to the loss of active sites and therefore to lower activity.[19] In all these cases the number of active sites changed when the catalysts were exposed to the reaction mixture.

Here, we focus on Rh structural changes occurring during CO oxidation. Changes in Rh particle distribution have been widely reported.[11,20–31] These changes have been characterized using diffuse reflectance infrared Fourier transform spectroscopy (DRIFTS),[20,31–35] temperature programmed reduction (TPR),[36] extended X-ray absorption spectroscopy (EXAFS),[35–38] scanning tunnel microscopy (STM),[39] scanning transmission electron microscopy (STEM),[40] nuclear magnetic resonance (NMR)[41] and x-ray photoelectron spectroscopy (XPS)[42] and predicted in theoretical studies.[43–45] At low temperature, CO breaks apart Rh nanoparticles, dispersing them into single atoms. One proposed mechanism suggests that the bond energy between CO and Rh overcomes the Rh-Rh and Rh-support bond energies, favoring nanoparticle disintegration.[35,38,46] Other studies have proposed that Rh particle disintegration involves an oxidative process where the Rh oxidation state changes from 0 to +1 with the assistance of OH groups on the support.[20,24,47] CO-induced Rh particle disintegration can be reversible, for example STM imaging and infra-red spectroscopy experiments show that Rh single atoms re-aggregate into nanoparticles during CO exposure at high temperature.[39] With structural changes occurring during the reaction, when CO is present, the number of active sites may change, affecting the activity of the reaction. As a consequence, counting active sites via ex-situ measurements may not provide an accurate representation of the system

under study and can lead to an incorrect calculation of the turnover frequency. Indeed, some previous studies have used the rates of CO oxidation as a probe reaction to estimate the active metal surface area, since its reaction kinetics on Pt-group metals (PGM) is well known.[48,49]

CO oxidation is likely the most studied reaction in heterogeneous catalysis and has been often used to answer mechanistic and catalyst structural questions due to its relative simplicity.[50,51] However, in the case of CO oxidation on Rh catalysts, due to CO-induced Rh structural changes, quantifying the number of active sites and therefore turnover frequency when CO is a reactant or intermediate is challenging. Furthermore, a better understanding of the active site's dynamics during Rh restructuring under reaction conditions and its consequences on catalyst activity would allow catalyst design optimization, which is critical in light of the recent volatility in Rh price.

Here, we monitored kinetic parameters, specifically the activation energy and pre-exponential factor, to identify when structural changes occurred during the reaction. We found that under conditions with a stoichiometric excess of oxygen, Rh nanoparticles are readily dispersed into single atoms and that the temperature at which dispersion occurs depends on the initial Rh particle size. CO-induced nanoparticle disintegration in the presence of an excess of O_2 was also observed using DRIFTS. The concentration of oxygen in the gas mixture affects the extent of particle dispersion caused by CO. Combining kinetic and spectroscopic studies we were able to quantify the extent of particle disintegration and calculate the turnover frequency.

3.2 Material and methods

3.2.1 Catalysts

A series of Rh/Al_2O_3 catalysts were synthesized using the incipient wetness method. $Rh(NO_3)_3$ was used as the precursor, with the rhodium (III) nitrate solution (10% w/w Rh in >5wt% HNO_3 solution) purchased from Sigma Aldrich, and was deposited onto γ-Al_2O_3, also purchased from Sigma Aldrich, to achieve 0.05% and 0.1% Rh weight loadings. The Rh-containing catalysts were dried in a Thermo Scientific Lindberg muffle furnace at 120°C for 4 h in static air, and then the temperature was ramped to 600 °C at 1 °C/min and held there for 4 h. To obtain different particle sizes, different samples were placed in a quartz tube, which was put inside a Lindberg Blue M tube furnace purchased from Thermo Scientific and exposed to 5% H_2 in N_2 at 700°C for 4 h, 800 °C for 4 h or 900 °C for 72 h. Another 0.1wt% Rh/Al_2O_3 catalyst provided by Ford Motor Company was also evaluated as part of this study. This sample was synthesized by wetness impregnation using a $Rh(NO_3)_3$ (10%w/w in 20-25% HNO_3 solution) precursor, purchased from Acros Organics, deposited onto γ-Al_2O_3 (Puralox Sasol). The catalyst was calcined at 500 °C for 8 h. The catalyst was then aged following Ford's 4-mode ageing protocol,[52] to simulate the performance of a high-mileage catalyst. This sample is referred to as "Cycling Aged" below.

3.2.2 Chemisorption

H_2 chemisorption was performed using a Micromeritics ASAP2020 Plus. Prior to the measurements, the catalysts were reduced in H_2 at 500 °C for 1 h, then evacuated for 2 h at 500 °C, cooled to 35 °C and maintained under vacuum for 1 h. H_2 adsorption isotherms were collected at 35 °C. The dispersion was calculated assuming a H:metal ratio = 1:1. We used the inverse of dispersion to calculate the particle size, assuming hemispherical clusters.

3.2.3 CO oxidation kinetic experiments

The catalyst was placed in a quartz tube having an internal diameter of 4 mm. The tube was placed in a Thermo Scientific Lindberg Blue M tube furnace. The inlet and outlet temperatures were measured using K-type thermocouples purchased from Omega. Inlet and outlet stainless steel tubing were maintained at 150 °C to avoid water condensation. The amount of catalyst used was 5 to 13 mg. In order to avoid heat transfer limitations, the catalyst was diluted with crushed cordierite, originating from a Corning cordierite monolith, with a catalyst:cordierite weight ratio varying between 1:18-50. Cordierite is a common support material for monolith-supported catalysts, and typical in automotive catalysis[53]. The cordierite inactivity during reaction was confirmed with results shown in Figure S1. To avoid internal diffusion limitations, the catalysts were pelletized and sieved to obtain 80-170 mesh (0.177 – 0.088 mm) pellets. The flowrates used were between 500 and 750 sccm, which according to our calculations, is enough to avoid external mass transfer limitations. The absence of these transport limitations at conversions typically below 20% was confirmed using the Weisz-Prater number[54] and the Anderson and Mear's criteria[55,56]. N_2, CO, O_2 and H_2 flowrates were controlled with MKS mass flow controllers. Experiments that included H_2O were also performed, with 6% H_2O, using a Bronkhorst controlled evaporator mixer (CEM). The catalysts were pretreated in 5% H_2 in N_2 at 500 °C for 30 min. CO oxidation experiments were performed using CO concentrations between 8400 – 13000 ppm. The O_2 concentration was adjusted to maintain a target CO/O_2 ratio. CO, CO_2 and H_2O concentrations were measured using a MKS MG2030 FT-IR analyzer. The conversions shown in the figures below were obtained under steady-state conditions, with decreasing reaction temperature between data points.

3.2.4 DRIFTS experiments

DRIFTS experiments were performed using a Nicolet iS50 FT-IR, with adsorption of CO to characterize Rh speciation. The flowrate used for the pretreatments and experiments was 50 sccm. The pretreatment consisted of exposure to 1% O_2 in He at 500 °C for 30 minutes, followed by a 10 minute He purge, with a final exposure to 5% H_2 in N_2 at 500 °C for 30 minutes. The temperature was then decreased in He to 35 °C. The catalysts were exposed to 8400 ppm of CO in 16% N_2 and 83% He until saturation, which was verified by the unchanging spectra.

DRIFTS experiments with the goal of simulating reactor experiments were performed using the 0.1wt% Rh/Al_2O_3 sample that had been treated in H_2 at 700 °C as described above, using a custom-made split cell design purchased from Harrick Scientific. The cell includes two sample holders, one for the catalyst and one for a reference material. The chamber is mounted on a movable stage that allows to switch from the catalyst position to the reference. Half of the cell was loaded with the catalyst and the other half with inert SiC. This split cell design allowed us to subtract the gas phase spectrum, obtained when collecting the IR signal from the inert material side, from the spectrum obtained when collecting from the catalyst side, at each temperature. The catalyst underwent the pretreatment protocol described above and was then cooled to 300 °C in He. Prior to the experiments, the background spectra for the catalyst and SiC were taken at each temperature in He. The catalysts were exposed to a gas mixture containing 8400 ppm CO and 9250 ppm O_2 diluted in 16% N_2 and 82% He and the species present on the catalyst surface were analyzed every 20 °C between 300 and 220 °C. The gas phase subtraction was performed using absorbance as intensity units. In the plots shown, the spectra have been converted into Kubelka-Munk units.

3.3 Results and Discussion

3.3.1 Catalyst characterization: H_2 chemisorption and CO DRIFTS

Samples with a range of Rh particle sizes were synthesized by varying the Rh loading and the H_2 reduction temperature, with Table 3.1 listing the particle size measurements obtained using H_2 chemisorption. The values obtained from the H_2 chemisorption corresponds to an average value. A separate sample was synthesized and aged at high temperature with exposure to oxidizing and reducing conditions[68], which is labelled "Cycling Aged", and is included to demonstrate that the trends observed extrapolate beyond those samples exposed to simpler conditions and synthesized with a different alumina or precursor. CO DRIFTS has been used to characterize Rh speciation, enabling the identification of Rh oxidation states as well as distinguishing between single atoms, via the presence of Rh gem-dicarbonyls, and Rh nanoparticles[20,24,27,32,57,58]. To characterize our samples, CO adsorption spectra were obtained after reducing the catalysts in H_2 at 500 °C. The spectra contain three main features, at 2030, 2060 and 2100 cm^{-1}. The features at 2100 and 2030 cm^{-1} correspond to the IR symmetric and asymmetric stretches of single atom Rh as a gem-dicarbonyl ($Rh^+(CO)_2$), respectively. The feature between 2040 – 2070 cm^{-1} corresponds to CO linearly bound to Rh nanoparticles[25,32,57], displayed as Rh^0-CO. The Rh^0-CO peak position depends on particle size, CO coverage and local coordination environment[25,59–62]. For the catalysts with particle sizes 3.3 nm or larger, as was calculated from the H_2 chemisorption results, there was also a small feature in the 1800-1900 cm^{-1} range, indicating the presence of bridge-bound CO on Rh nanoparticles (Rh_x-CO). An example is shown in the inset for the 0.1% Rh sample aged at 900°C for 72h. Overall, with increasing dispersion there are more $Rh(CO)_2$ single atoms relative to nanoparticles. This increased $Rh(CO)_2$ amount relative to nanoparticles might simply be due to the lower reduction temperature used in synthesis or the lower Rh loading, both of which would

normally lead to less metal agglomeration. However, it is widely reported that at low temperature, CO is able to break apart Rh particles, dispersing them into single atoms, and that the relative fraction of Rh single atoms and nanoparticles formed during CO exposure at low temperature changes as a function of particle size[20,21,24,25,32,57,58]. We hypothesize that CO exposure at 35°C during the DRIFTS experiment led to an increase in $Rh(CO)_2$ amount relative to nanoparticles.

Table 3.1: Particle size measurements via H_2 chemisorption

Catalyst	**Average particle size [nm]**
0.05%Rh/Al_2O_3	<1
0.1%Rh/Al_2O_3	1.1
0.1%Rh/Al_2O_3 H_2-700°C	1.6
0.1%Rh/Al_2O_3 H_2-800°C	3.3
0.1%Rh/Al_2O_3 - Cycling Aged	5
0.1%Rh/Al_2O_3 H_2-900°C - 72h	9.2

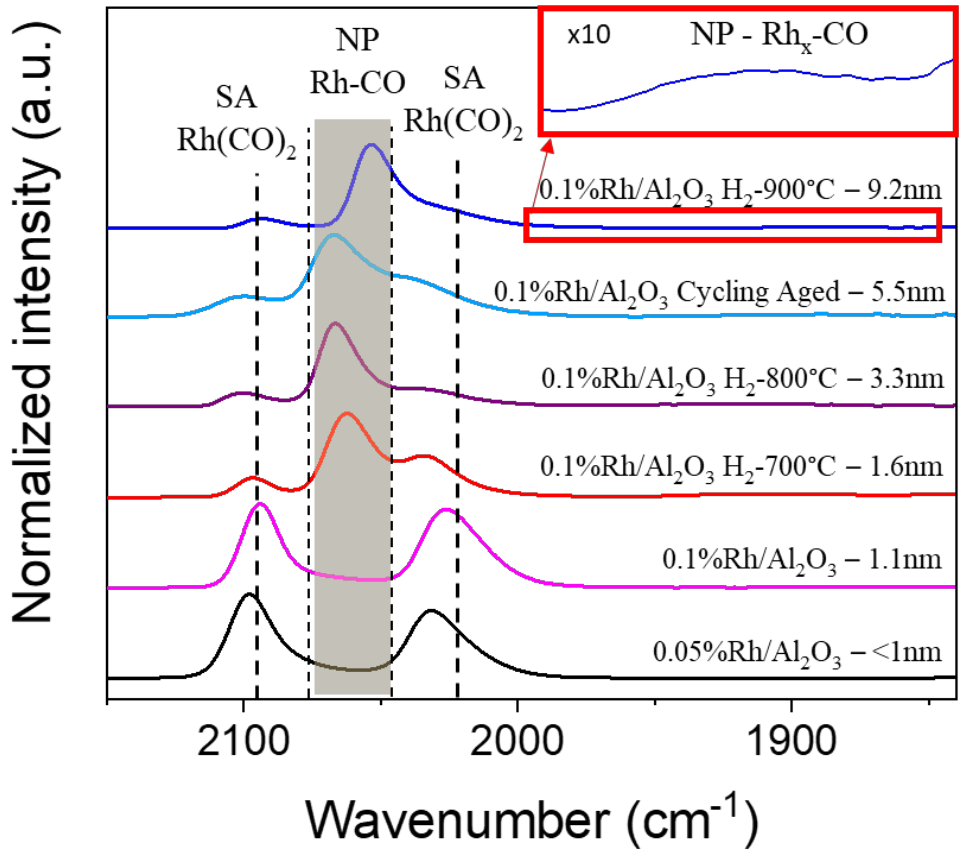

Figure 3.1: DRIFTS spectra obtained after He purge after CO adsorption at 35 °C on 0.05%Rh/Al_2O_3, 0.1%Rh/Al_2O_3, 0.1%Rh/Al_2O_3 H_2 -700°C, 0.1%Rh/Al_2O_3 H_2-800°C, 0.1%Rh/Al_2O_3-Cycling-Aged, and 0.1%Rh/Al_2O_3 H_2-900°C – plotted in rank of dispersion as measured by H_2 chemisorption. The CO concentration during exposure was 8400 ppm. Prior to the CO adsorption, the catalysts were reduced at 500 °C in 5% H_2 for 30 min. The Kubelka-Munk intensity of the largest peak in each spectrum was normalized to 1. For the 0.1%Rh/Al_2O_3 H_2-900°C sample, the KM intensity between 1950 and 1840 cm^{-1} was multiplied by 10 and displayed in the inset red-bordered box.

3.3.2 CO oxidation kinetics

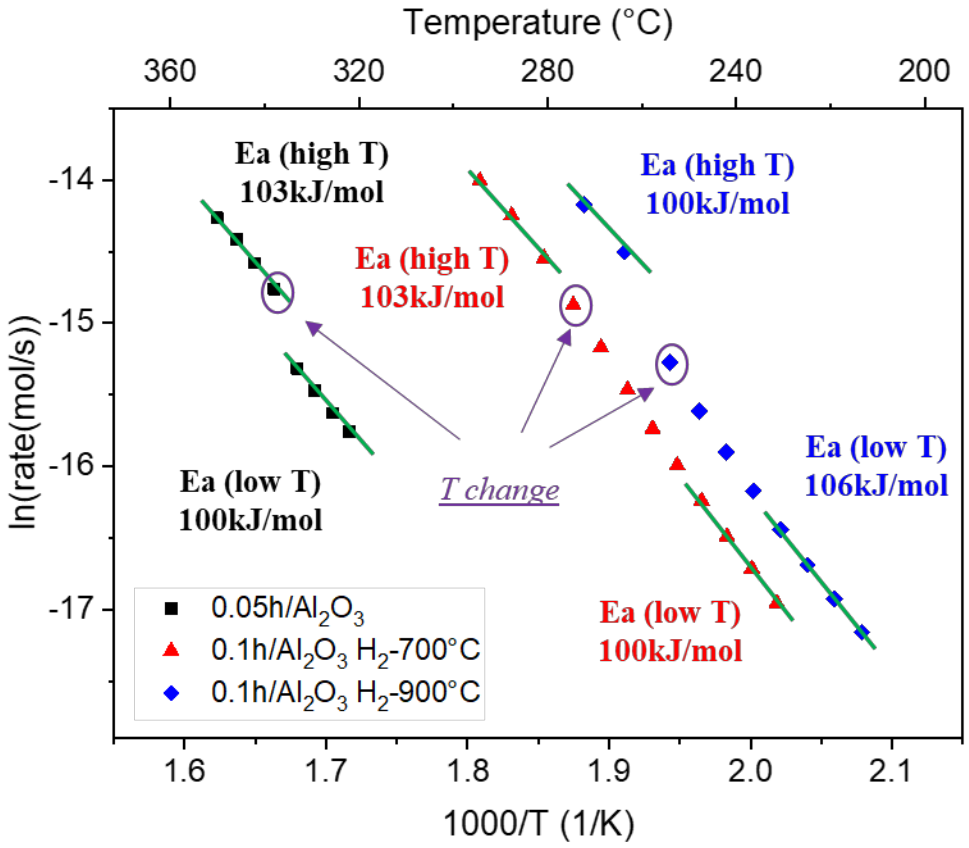

Figure 3.2: CO oxidation Arrhenius plots obtained from the 0.05%Rh/Al_2O_3, 0.1%Rh/Al_2O_3 H_2-700°C and 0.1%Rh/Al_2O_3 H_2-900°C samples. CO = 8400-13000 ppm, CO/O_2 = 0.9, total flowrate = 500-750 sccm. The catalysts were pretreated in 5% H_2 at 500 °C for 30 min. The results shown were obtained after reaching steady-state, with the temperature changing from high to low temperature.

CO oxidation is one of the most studied reactions in heterogeneous catalysis, and the generally accepted active site for Pt-group metals on irreducible oxide supports is the metallic phase, when the reaction is performed under stoichiometric or slightly oxidizing conditions.[58,63–69]. Since it is so well studied, and often used as a probe reaction, calculating true rates is needed, and to do so for Rh-supported catalysts, we need to understand how the number of active sites changes under reaction conditions. Here, we use CO oxidation rates to understand when the number of active

sites changes under reaction conditions and, ultimately, in combination with spectroscopy to calculate the true rates.

Figure 3.2 shows the Arrhenius plots originating from the experiments using the 0.05%Rh/Al_2O_3, 0.1%Rh/Al_2O_3 H_2-700°C and 0.1%Rh/Al_2O_3 H_2-900°C catalysts. Results from the rest of the samples are shown in Figure S2. These catalysts have initial Rh particle sizes that span from <1 to 9.2 nm. Results are shown from an experiment with decreasing temperature; however, similar results were obtained with increasing temperature. In the Arrhenius plots in Figure 3.2, we expressed the rate in mol/s of CO_2 formed. We refrained from normalizing them by the moles of surface Rh measured via H_2 chemisorption, due to the redistribution of Rh speciation and/or structure that occurs in the presence of CO, as hinted at from the CO DRIFTS spectra in Figure 3.1 and the literature discussed in the Introduction section. CO-induced particle restructuring makes the number of active sites unknown under reaction conditions as the number of active sites will be different from that obtained from H_2 chemisorption or other ex-situ measurements.

All three Arrhenius plots in Figure 3.2 show the presence multiple regimes. At low temperature, for all three catalysts described in Figure 3.2, and for all the catalysts tested (Figure S2), the apparent activation energies are 100-110 kJ/mol. This is consistent with Langmuir Hinshelwood type kinetics previously reported, that involves the adsorption of CO and O_2, the dissociation of O_2 and a surface reaction forming CO_2.[70–74] At low temperature, the metal surface is covered by CO, resulting in reaction inhibition. CO has to desorb in order to allow O_2 to adsorb and dissociate.[75,74,76] As a consequence, the step limiting the reaction is the desorption of CO from the metal. The CO oxidation activation energy is similar to the CO desorption energy, consistent with our results.[68]

In the middle temperature range, the Arrhenius plot slopes increase, as the measured reaction rates deviate from the linear fitting resulting in an activation energy of 100-110 kJ/mol. At high

temperature, the calculated apparent activation energies are once again 100-110 kJ/mol, similar to the values calculated in the low temperature regime. These results suggest that the rate-limiting step at high and low temperature is the same and that the apparent activation energies in both temperature ranges correspond to the CO desorption energy from a Rh metal particle.[68] It is worth emphasizing that heat and mass transfer phenomena were negligible under these conditions - as mentioned in the Materials and Methods section, the absence of heat and mass transfer limitations was confirmed by calculating the Mear's and Anderson criteria and the Weisz-Prater number, all of which are further described in the SI, Appendix A, section A4. The increase in the slope in the mid-temperature range, or consistency between the low- and high-temperature ranges further excludes the presence of mass transfer limitations.

Although the apparent activation energies obtained for all the catalysts in the low and high temperature regimes are similar, the derived linear fitting for each pair of temperature regimes do not show the same y-intercept. Therefore, the pre-exponential factor differs between the high and low temperature regimes and is higher in the high temperature regime. With the pre-exponential factor being a function of the number of active sites, these data suggest that the number of active sites changed between the low and high temperature regimes. As previously mentioned, at low temperature CO is able to disperse Rh nanoparticles into single atoms, which leads to a decrease in the number of active sites for CO oxidation.[77] This is consistent with our results, as the catalysts show lower pre-exponential factors at low temperature. However, with increasing temperature, the isolated single atoms reaggregate into nanoparticles in the presence of CO[39,78], increasing the number of active sites for CO oxidation, and thus the pre-exponential factor.

For the 1.6 and 9.2 nm samples, there are data points in the transition, or mid-temperature regime, between the low and high temperature regimes. In this transition temperature region, the Arrhenius

plot slopes cannot be used to calculate an activation energy because the number of active sites is different for each data point. Therefore, a calculated higher "activation energy" in this transition does not represent a different rate-liming step, but simply reflects changes in rate due to changes in the number of active sites as we move to higher temperature. The presence of a transition regime suggests that there might be a particle size distribution, with the smaller particles dispersing to single atoms before the larger as we decrease temperature, resulting in a decreased rate, until all the particles that will break apart do. However, the 0.05%Rh/Al_2O_3 catalyst does not show this intermediate/transition regime. Based on our interpretation of particle disruption or agglomeration being a function of particle size, this lack of a transition regime is due to particle sizes being relatively uniform such that they all disperse into single atoms between two experimental temperature points.

The temperatures at which the Arrhenius plot slopes change in Figure 3.2 show a particle size dependence. Figure 3.3 summarizes the temperatures at which we start to see a deviation from the linear fitting in the high temperature region of the Arrhenius plots, which we here refer to as *T change*, for all the catalysts we studied. This *T change* value initially decreases with increasing particle size, reaching a plateau for samples with initial Rh particle sizes larger than 5 nm. Going from high to low temperature, smaller particles break apart into single atoms before larger particles. A particle size dependence is consistent with previously reported computationally predicted behavior of CO-induced disruption of Rh particles, where small particles in the presence of CO have a lower free energy of disintegration, leading to fragmentation to single atoms, while larger particles are more difficult to disintegrate.[43,44] The inclusion of water, which is commonly present in many reactions, either as a reactant or a product, was investigated during CO oxidation. As shown and discussed in the SI (Appendix A, Section A3.3), water does not affect CO oxidation

mechanism, because the measured apparent activation energies correspond to the CO desorption energy, similar to the case without water. In addition, the presence of water did not alter the observed changes in the slope and the *T change* resulted unchanged, suggesting that the interconversion between single atoms and nanoparticles is not affected.

Once the *T change* temperature is reached, CO-induced Rh particle disintegration occurs and the pre-exponential factor decreases due to formation of inactive single atoms. When the starting average particle size is small, disintegration occurs at higher temperatures because the particles are not stable, due to their high surface energy and the formation of $Rh(CO)_2$ single atom complexes is more favorable – the adsorbate/Rh single atom, $Rh(CO)_2$, free energy is lower than that of the CO bound to Rh nanoparticle structure[79]. At larger particle sizes, the temperature has to be lower for CO-induced disintegration to occur because the larger particles are more stable, thus the particle cohesive energy is more competitive with the free energy of CO-induced nanoparticle disintegration.

In characterizing the more traditional sintering process, the cohesive energy of a small particle is weaker than a large particle, which means a lower temperature would lead to sintering for small nanoparticles compared to that required for larger particles. The trend with particle size via the adsorbate-induced disintegration observed here is opposite of the traditional sintering trend.

Since this process is reversible, one can also consider the nanoparticles-single atoms dynamics from low to high temperature. As temperature increases, for these CO-induced changes, bigger particles with their greater cohesive energy remain intact. Smaller particles will not form until higher temperature since CO-induced nanoparticle disintegration free energy of the smaller particles more easily overcomes the lesser cohesive energy needed to maintain their agglomerated state. This is consistent with theoretical studies[43] where with first-principle calculations on Rh/TiO_2, it

was shown that the driving force that leads to particle disintegration increases with a decrease in particle size as the free energy of disintegration shows substantially lower values.

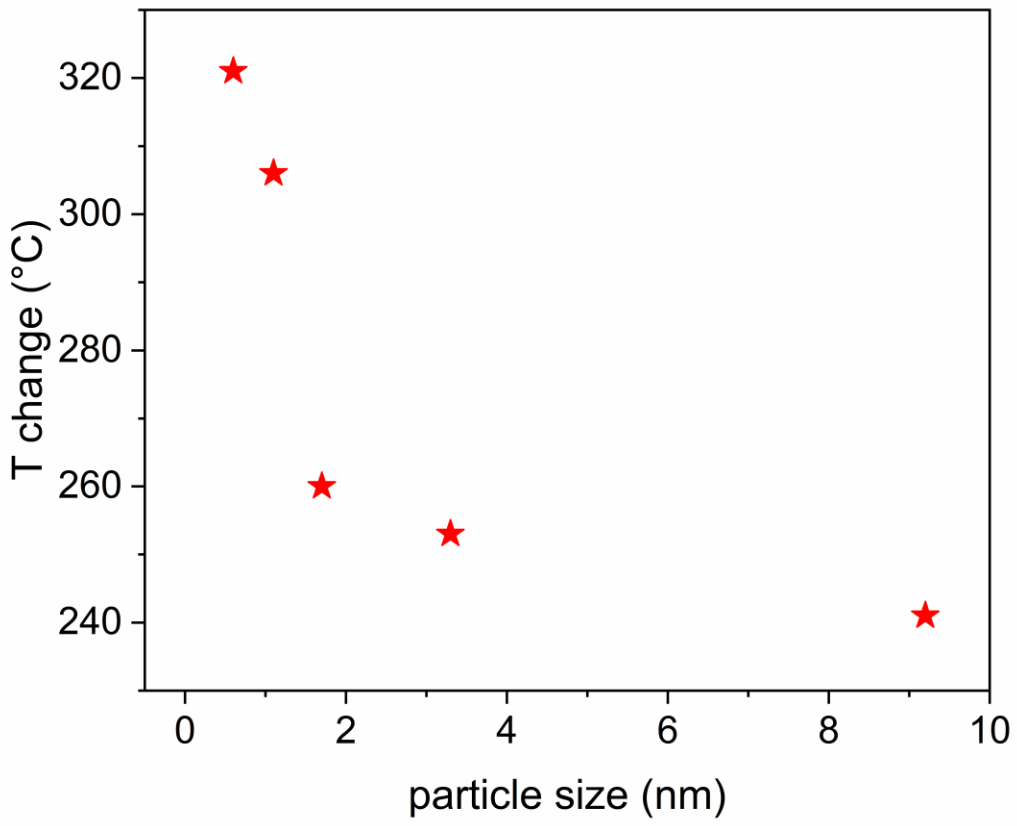

Figure 3.3: Summary of the temperature at which the change in CO oxidation kinetics occurs for 0.05%Rh/Al_2O_3 (<1 nm), 0.1%Rh/Al_2O_3 (1.1 nm), 0.1%Rh/Al_2O_3 H_2-700°C (1.6 nm), 0.1%Rh/Al_2O_3 H_2-800°C (3.3 nm), and 0.1%Rh/Al_2O_3 H_2-900°C (9.2 nm). CO = 8400-13000 ppm, CO/O_2 = 0.9, flowrate = 500-750 sccm. The catalysts waere pretreated in 5% H_2 at 500 °C for 30 min.

3.3.3 In-situ CO + O_2 DRIFTS

In order to further investigate the structural dynamics occurring during the reaction, DRIFTS spectra were collected while exposing the 0.1%Rh/Al_2O_3 H_2-700°C sample, characterized by a 1.6 nm particle size, to a CO and O_2 mixture with CO/O_2 = 0.9, a similar ratio used in the kinetic experiments described above. The spectra collected in the temperature range between 220 and 300 °C

are shown in Figure 3.4. All the spectra were normalized by the intensity of the asymmetric Rh gem-dicarbonyl peak, centered at ~2020 cm^{-1}. The spectra contain 4 peaks: 2070 cm^{-1}, assigned to the linear bound CO on Rh^0, 2090 and 2026 cm^{-1}, corresponding to the symmetric and asymmetric gem-dicarbonyl species respectively, and 2120 cm^{-1}, corresponding to Rh(CO)(O)[80], previously identified as a precursor to CO_2 on a Rh particle[61,81]. Overall, it is evident that with a decrease in temperature, the peak assigned to CO bound to the Rh nanoparticle decreased in intensity, while the relative intensities of the single atom features increased, providing additional evidence that CO induces particle disintegration with decreasing temperature.

To evaluate relative changes in sites, the features in this region of each spectrum were deconvoluted and the areas under each peak were integrated. See Figure A8 and section A6 of the SI for an example of the deconvolution. Figure 3.5 shows the peak area ratios for the symmetric gem-dicarbonyls, indicated as 2090/2026, and the linear CO-Rh, indicated as 2070/2026. The ratio of the area of the two gem-dicarbonyl species is equal to 1, consistent with findings in the literature[32], and this ratio remains 1 throughout the experiment, within the temperature range studied here. The ratios between the nanoparticle and the asymmetric gem-dicarbonyl are similar at 220 and 240 °C, but increase with a further increase in temperature. In comparing the transition temperatures shown here and that in Figure 3.3, they are similar – the 0.1%Rh/Al_2O_3 H_2-700°C sample is characterized by an average initial particle size of 1.6 nm and its *T change* during the CO oxidation kinetic study was 260 °C. The normalized Rh-CO area at 300 °C is 2-fold the initial area at 220-240 °C. These results are consistent with our kinetic data and provide additional evidence that the fractions of Rh particles and single atoms are changing during CO oxidation, and therefore the fraction of active sites increases with an increase in temperature.

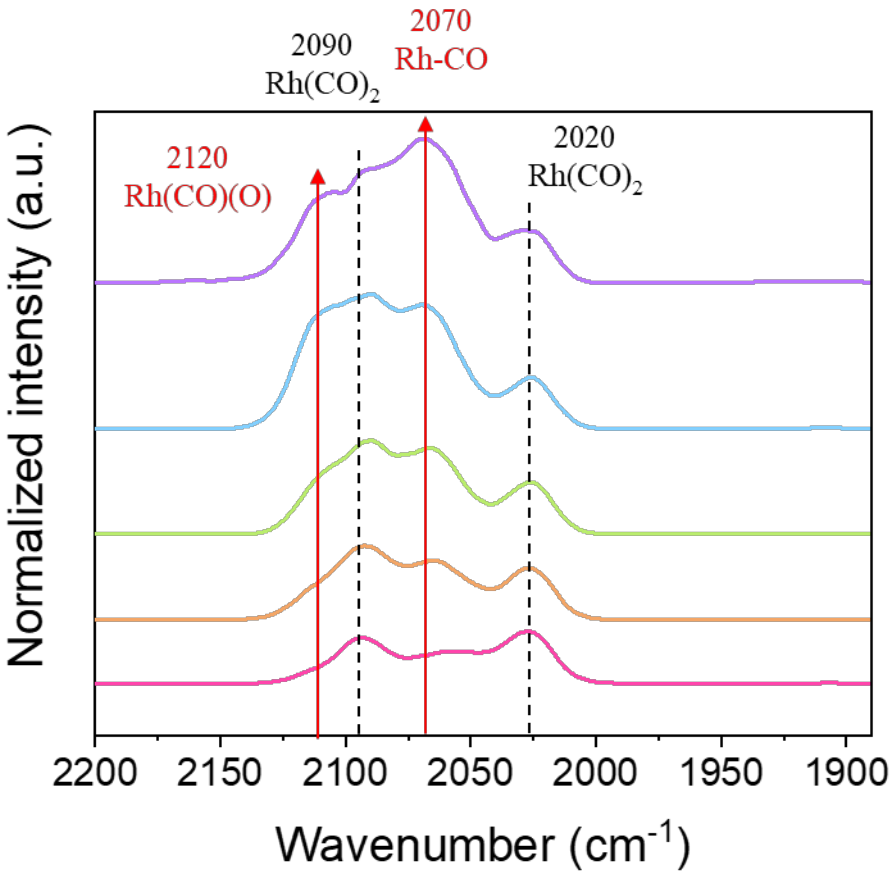

Figure 3.4: DRIFTS spectra of 0.1%Rh/Al_2O_3 H_2-700°C during CO oxidation at 220, 240, 260, 280 and 300°C. CO = 8400 ppm; O_2 = 9250 ppm. The catalyst was first exposed to 1% O_2 at 500 °C for 30 min, followed by He purge for 10 min and 5% H_2 at 500 °C for 30 min. The spectra were normalized by the intensity of the peak at 2026 cm^{-1}, after applying the gas phase subtraction.

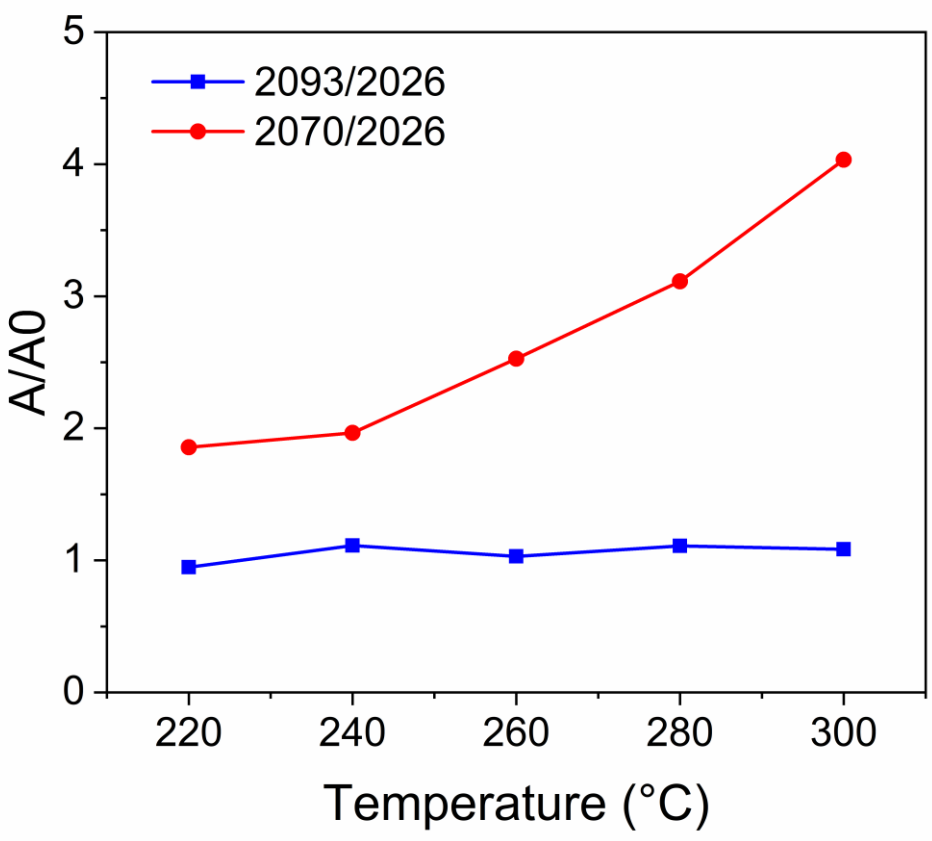

Figure 3.5: Normalized areas of symmetric and asymmetric gem-dicarbonyl features (2090/2026) and linear Rh-CO nanoparticle and asymmetric gem-dicarbonyl species (2070/2026) for each temperature investigate in the range between 220 – 300 °C

3.3.4 The effect of O_2 on Rh speciation

The single atoms-nanoparticle interconversion during CO oxidation was observed only under conditions with an excess of oxygen, relative to stoichiometric CO oxidation. In fact, CO oxidation performed under oxygen deficient and stochiometric conditions showed a continuously linear Arrhenius plot, resulting in an activation energy of 110 kJ/mol. This suggests that oxygen enhances the oxidative process of CO-induced nanoparticle disruption. The effect of O_2 amount during CO adsorption/oxidation on 0.1% Rh/Al_2O_3 H_2-700°C was investigated spectroscopically at 260 °C, which based on the results shown in Figure 3.3, is the single atom-nanoparticle transition region for this sample. The following concentrations were investigated: 2000, 4200, 6500 and 9250 ppm. The spectra in Figure 3.6 show that under stoichiometric conditions and conditions where there is excess CO, Rh speciation is not altered, as the only features present were the linear and bridge bound CO on Rh particles. However, when the O_2 concentration increased past the stoichiometric point, there was an increase in single atom fraction. Simultaneously, as shown in Figure A10, as the O_2 concentration increased, the negative feature in the 3600-3800 cm^{-1} OH region became more pronounced, suggesting that OH groups on the Al_2O_3 surface were consumed. The increase in single atom formation and depletion of the OH groups with an increase in O_2 concentration is consistent with previous reports which postulated that the OH groups are involved in the Rh nanoparticle dispersion[82–84]. These spectra indicate that oxygen favors the CO-induced oxidative disruption of Rh nanoparticles (Rh^0) into $Rh^I(CO)_2$. This is consistent with our kinetic experiments performed under similar conditions where a deviation from the typical linear regime of an Arrhenius plot was not detected unless there was an excess of oxygen.

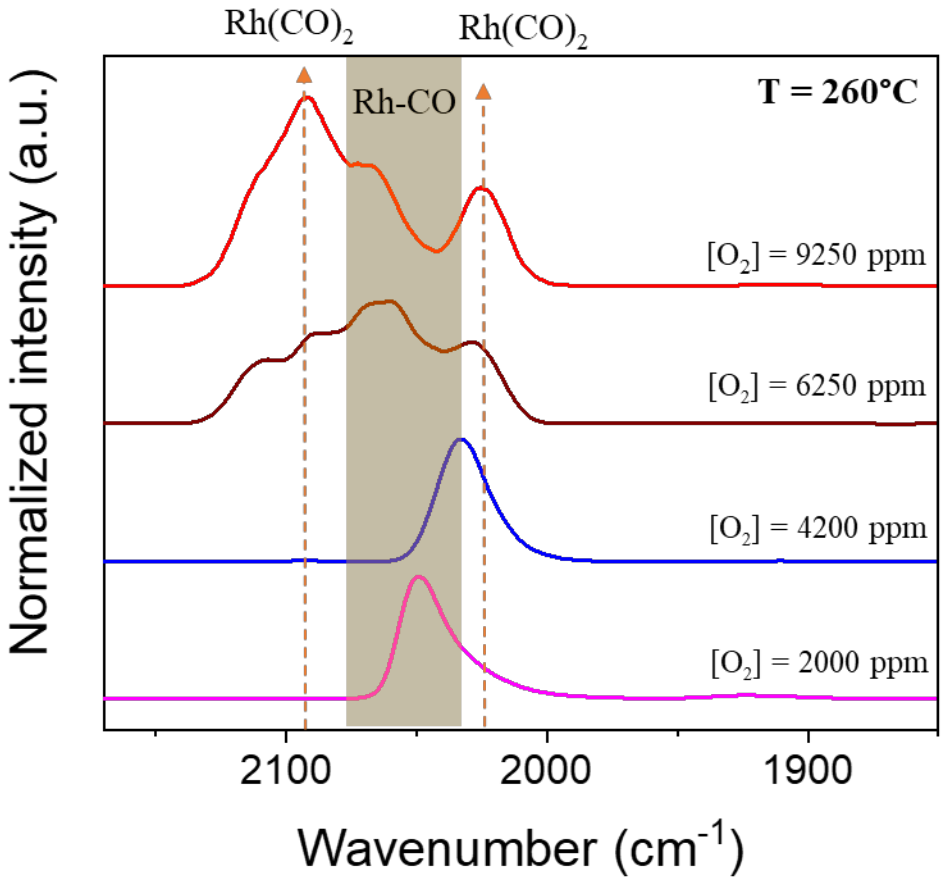

Figure 3.6: DRIFTS spectra during CO + O_2 exposure at 260 °C on 0.1%Rh/Al_2O_3 H_2-700°C. CO = 8400 ppm; O_2 = 2000, 4200, 6250, or 9250 ppm. The spectra were normalized by the highest intensity peak for comparison.

3.3.5 Bridging the spectroscopic and kinetic data

As mentioned above, the Arrhenius plots in Figure 3.2 show the CO_2 formation rates expressed in mol/s, due to the challenge in counting Rh active sites with their dynamics during reaction. However, a quantitative interpretation of the spectroscopic data showed that at high temperature, the fraction of nanoparticles, thus the active sites, is two times higher than the fraction at low temperature. This information can be, and here was, used to normalize the reaction rates and obtain the CO oxidation turnover frequency.

The black squares in Figure 3.7 display the CO oxidation rate measured at high and low temperature on 0.1%Rh/Al_2O_3 H_2-700°C, normalized by the amount of surface Rh sites calculated via H_2 chemisorption. As previously shown, from the linear fitting derived from the low and high temperature, the activation energies are similar and equal to 100-110 kJ/mol, but the pre-exponential factors are different depending on the temperature region used. However, based on the DRIFTS results, the low temperature regime has more single atoms and less particles, with a factor of 2 calculated when comparing relative peak intensities at 220 to 300 °C. We can therefore renormalize the pre-exponential factor by dividing the amount of Rh surface atoms obtained from H_2 chemisorption by 2, and use this quantity to normalize the rate measurements in the low temperature regime. The red circles display the rate measurements normalized by two different active Rh amounts at low and high temperature. The resulting line fitting the red squares still gives an activation energy of 100 kJ/mol, consistent with our previous measurements.

This combined in-situ spectroscopy and kinetic measurement method allows the quantification of the extent of particle disintegration and active sites loss. The estimation of the active sites at all temperatures during the reaction allows the calculation a true turn over frequency that otherwise was not possible with just the reactor-based approach and ex-situ active sites measurements, which do not track the dynamics of nanoparticle-single atoms interconversion.

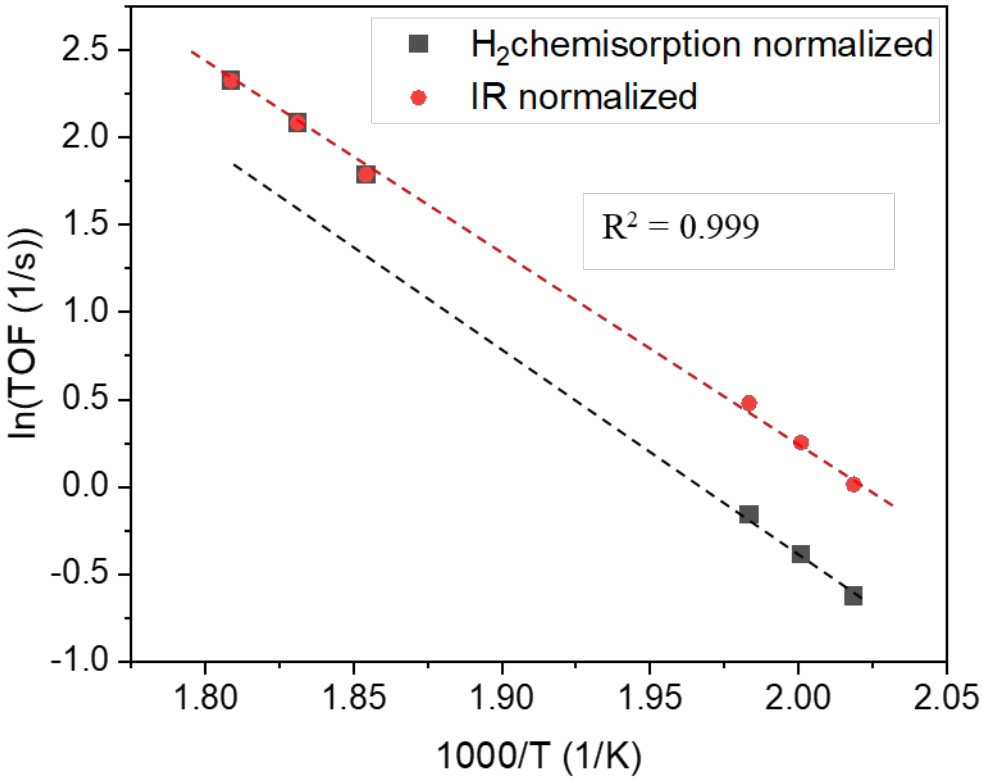

Figure 3.7: Normalized CO oxidation rates obtained on 0.1%Rh/Al_2O_3 H_2-700°C. CO = 8400 ppm O_2 = 9250 ppm; total flowrate = 750 sccm. The catalyst was reduced in 5% H_2 at 500 °C for 30 min. The black squares represent the reaction rates normalized by the number of Rh surface sites obtained from the H_2 chemisorption measurement, the red circles are the reaction rates normalized by the number of Rh surface sites obtained from the H_2 chemisorption at high temperature and the half that amount at low temperature, based on changes observed in the DRIFTS spectra.

3.4 Conclusions

CO oxidation structure insensitivity is an important tool that can be, and has been, used to identify and estimate the number of catalytically active sites. In this study, a combination of IR spectroscopy and CO oxidation kinetics was used to track the structural changes occurring on Rh/Al_2O_3 catalysts. We showed that the ability of CO to break Rh nanoparticles reduces the number of active sites during CO oxidation and the conditions where this occurs depends on Rh particle size. With

decreasing temperature, smaller particles broke apart to single atoms first, and the temperature required to break the particles decreased with increasing particle size up to 5 nm, after which the catalysts showed similar behavior. While H_2O does not affect the temperature at which the structural dynamics occur during the reaction, O_2 present in excess of the stoichiometric amount enhances CO-induced particle dispersion into single atoms. Spectroscopic studies were consistent with this behavior in the presence of excess of O_2. Rh nanoparticle features were more intense at higher temperature compared to the IR features associated with single atoms, while at low temperature the opposite was observed, implying that Rh nanoparticles were broken into single atoms at low temperature. In addition, semi-quantitative analysis of the DRIFTS spectra was consistent with the kinetic experiments, demonstrating that at low temperature only half of the original number of Rh active sites are present on the catalyst surface, compared to that at high temperature. Combining the relative changes in the DRIFTS spectra with the reactor-based kinetic experiments allowed the turn over frequency to be calculated on an exposed surface Rh basis.

3.5 References

(1) Vogt, C.; Meirer, F.; Monai, M.; Groeneveld, E.; Ferri, D.; van Santen, R. A.; Nachtegaal, M.; Unocic, R. R.; Frenkel, A. I.; Weckhuysen, B. M. Dynamic Restructuring of Supported Metal Nanoparticles and Its Implications for Structure Insensitive Catalysis. *Nat. Commun.* **2021**, *12,*7096. https://doi.org/10.1038/s41467-021-27474-3.

(2) Batteas, J. D.; Dunphy, J. C.; Somorjai, G. A.; Salmeron, M. Coadsorbate Induced Reconstruction of a Stepped Pt(111) Surface by Sulfur and CO: A Novel Surface Restructuring Mechanism Observed by Scanning Tunneling Microscopy. *Phys. Rev. Lett.* **1996**, *77* (3), 534–537. https://doi.org/10.1103/PhysRevLett.77.534.

(3) Somorjai, G. A. The Experimental Evidence of the Role of Surface Restructuring during Catalytic Reactions. *Catal. Lett. 1992 121* **1992**, *12* (1), 17–34. https://doi.org/10.1007/BF00767185.

(4) Yan, G.; Tang, Y.; Li, Y.; Li, Y.; Nguyen, L.; Sakata, T.; Higashi, K.; Tao, F. F.; Sautet, P. Reaction Product-Driven Restructuring and Assisted Stabilization of a Highly Dispersed Rh-on-Ceria Catalyst. *Nat. Catal.* **2022**, *5* (2), 119–127. https://doi.org/10.1038/s41929-022-00741-2.

(5) Eren, B.; Zherebetskyy, D.; Patera, L. L.; Wu, C. H.; Bluhm, H.; Africh, C.; Wang, L. W.; Somorjai, G. A.; Salmeron, M. Activation of Cu(111) Surface by Decomposition into Nanoclusters Driven by CO Adsorption. *Science (80-.).* **2016**, *351* (6272), 475–478. https://doi.org/10.1126/science.aad8868.

(6) Felvey, N.; Guo, J.; Rana, R.; Xu, L.; Bare, S. R.; Gates, B. C.; Katz, A.; Kulkarni, A. R.; Runnebaum, R. C.; Kronawitter, C. X. Interconversion of Atomically Dispersed Platinum Cations and Platinum Clusters in Zeolite ZSM-5 and Formation of Platinum Gem-Dicarbonyls. *J. Am. Chem. Soc.* **2022**, *2022* (20), 34. https://doi.org/10.1021/jacs.2c05386.

(7) Matsubu, J. C.; Yang, V. N.; Christopher, P. Isolated Metal Active Site Concentration and Stability Control Catalytic CO_2 Reduction Selectivity. *J. Am. Chem. Soc.* **2015**, *137* (8), 3076–3084. https://doi.org/10.1021/ja5128133.

(8) Asokan, C.; Yang, Y.; Dang, A.; Getsoian, A. "Bean"; Christopher, P. Low-Temperature Ammonia Production during NO Reduction by CO Is Due to Atomically Dispersed Rhodium Active Sites. *ACS Catal.* **2020**, 10 (9), 5217–5222. https://doi.org/10.1021/acscatal.0c01249.

(9) Theis, J. R.; Ura, J. A. Assessment of Zeolite-Based Low Temperature NOx Adsorbers: Effect of Reductants during Multiple Sequential Cold Starts. *Catal. Today* **2021**, *360*, 340–349. https://doi.org/10.1016/j.cattod.2020.01.040.

(10) Gu, Y.; Zelinsky, R. P.; Chen, Y.; Epling, W. S. Investigation of an Irreversible NOx Storage Degradation Mode on a Pd / BEA Passive NOx Adsorber. *Appl. Catal. B Environ.* **2019**,

258, 118032. https://doi.org/10.1016/j.apcatb.2019.118032.

(11) Solymosi, F.; Novák; Molnár, A. Infrared Spectroscopic Study on CO-Induced Structural Changes of Iridium on an Alumina Support. *J. Phys. Chem* **1990**, *94*, 7250–7255.

(12) Newton, M. A.; Belver-Coldeira, C.; Martínez-Arias, A.; Fernández-García, M. Dynamic in Situ Observation of Rapid Size and Shape Change of Supported Pd Nanoparticles during CO/NO Cycling. *Nat. Mater.* **2007**, *6* (7), 528–532. https://doi.org/10.1038/nmat1924.

(13) Moliner, M.; Gabay, J. E.; Kliewer, C. E.; Carr, R. T.; Guzman, J.; Casty, G. L.; Serna, P.; Corma, A. Reversible Transformation of Pt Nanoparticles into Single Atoms inside High-Silica Chabazite Zeolite. *J. Am. Chem. Soc.* **2016**, *138* (48), 15743–15750. https://doi.org/10.1021/jacs.6b10169.

(14) Lardinois, T. M.; Mandal, K.; Yadav, V.; Wijerathne, A.; Bolton, B. K.; Lippie, H.; Li, C. W.; Paolucci, C.; Gounder, R. Kinetic and Thermodynamic Factors Influencing Palladium Nanoparticle Redispersion into Mononuclear Pd(II) Cations in Zeolite Supports. *J. Phys. Chem. C* **2022**, 126, (19), 8337-8353. https://doi.org/10.1021/acs.jpcc.2c01613.

(15) Kale, M. J.; Christopher, P. Utilizing Quantitative in Situ FTIR Spectroscopy to Identify Well-Coordinated Pt Atoms as the Active Site for CO Oxidation on Al_2O_3-Supported Pt Catalysts. *ACS Catal.* **2016**, *6* (8), 5599–5609. https://doi.org/10.1021/acscatal.6b01128.

(16) Chee, S. W.; Arce-Ramos, J. M.; Li, W.; Genest, A.; Mirsaidov, U. Structural Changes in Noble Metal Nanoparticles during CO Oxidation and Their Impact on Catalyst Activity. *Nat. Commun. 2020 111* **2020**, *11* (1), 1–9. https://doi.org/10.1038/s41467-020-16027-9.

(17) Gao, F.; Walter, E. D.; Kollar, M.; Wang, Y.; Szanyi, J.; Peden, C. H. F. Understanding Ammonia Selective Catalytic Reduction Kinetics over Cu/SSZ-13 from Motion of the Cu Ions. *J. Catal.* **2014**, *319*, 1–14. https://doi.org/10.1016/j.jcat.2014.08.010.

(18) Paolucci, C.; Khurana, I.; Parekh, A. A.; Li, S.; Shih, A. J.; Li, H.; Di Iorio, J. R.; Albarracin-Caballero, J. D.; Yezerets, A.; Miller, J. T.; Delgass, W. N.; Ribeiro, F. H.; Schneider, W. F.; Gounder, R. Dynamic Multinuclear Sites Formed by Mobilized Copper Ions in NOx Selective Catalytic Reduction. *Science (80-.).* **2017**, *357* (6354), 898–903. https://doi.org/10.1126/science.aan5630

(19) Goodman, E. D.; Johnston-Peck, A. C.; Dietze, E. M.; Wrasman, C. J.; Hoffman, A. S.; Abild-Pedersen, F.; Bare, S. R.; Plessow, P. N.; Cargnello, M. Catalyst Deactivation via Decomposition into Single Atoms and the Role of Metal Loading. *Nat. Catal.* **2019**, *2* (9), 748–755. https://doi.org/10.1038/s41929-019-0328-1.

(20) Panayotov, P. B.; Yates, J. T. Rhodium-Carbon Monoxide Surface Chemistry: The Involvement of Surface Hydroxyl Groups on A12O3 and SiO2Supports. *J. Am. Chem. Soc.* **1988**, *110* (7), 2074–2081. https://doi.org/10.1021/ja00215a010.

(21) Yates, J. T.; Duncan, T. M.; Vaughan, R. W. Infrared Spectroscopic Study of Activated Surface Processes: CO Chemisorption on Supported Rh. *J. Chem. Phys.* **1979**, *71* (10), 3908–3915. https://doi.org/10.1063/1.438159.

(22) Bergeret, G.; Gallezot, P.; Gelin, P.; Ben Taarit, Y.; Lefebvre, F.; Naccache, C.; Shannon, R. D. CO-Induced Disintegration of Rhodium Aggregates Supported in Zeolites: In Situ

Synthesis of Rhodium Carbonyl Clusters. *J. Catal.* **1987**, *104* (2), 279–287. https://doi.org/10.1016/0021-9517(87)90359-9.

(23) Zaki, M. I.; Kunzmann, G.; Gates, B. C.; Knözinger, H. Highly Dispersed Rhodium on Alumina Catalysts: Influence of the Atmosphere on the State and Dispersion of Rhodium. *J. Phys. Chem.* **1987**, *91* (6), 1486–1493. https://doi.org/10.1021/j100290a041.

(24) Basu, P.; Panayotov, D.; Yates, J. T. Spectroscopic Evidence for the Involvement of OH Groups in the Formation of $Rh^{I}(CO)_2$ on Metal Oxide Supports. *J. Am. Chem. Soc.* **1987**, No. 22, 3133–3136. https://doi.org/10.1021/j100296a007.

(25) Cavanagh, R. R.; Yates, J. T. Site Distribution Studies of Rh Supported on Al2O3 - An Infrared Study of Chemisorbed CO. *J. Chem. Phys.* **1981**, *74* (7), 4150–4155. https://doi.org/10.1063/1.441544.

(26) Chen, J. G.; Colaianni, M. L.; Chen, P. J.; Yates, J. T.; Fisher, G. B. Thermal Behavior of a Rh/Al_2O_3 Model Catalyst: Disappearance of Surface Rh upon Heating. *J. Phys. Chem.* **1990**, *94* (12), 5059–5062. https://doi.org/10.1021/j100375a055.

(27) Duncan, T. M.; Yates, J. T.; Vaughan, R. W. A ^{13}C NMR Study of the Adsorbed States of CO on Rh Dispersed on Al203. *J. Chem. Phys.* **1980**, *73* (2), 975–985. https://doi.org/10.1063/1.440746.

(28) Kiss, J. T.; Gonzalez, R. D. Catalytic Oxidation of Carbon Monoxide over Rh/SiO_2. An in Situ Infrared and Kinetic Study. *J. Phys. Chem.* **1984**, *88* (5), 898–904. https://doi.org/10.1021/j150649a015.

(29) Wang, H. P.; Yates, J. T. Spectroscopic Study of the Interconversion of Chemisorbed Surface Species: The Reaction $Rh^{I}(CO)_2 + CO \rightarrow Rh^{I}(CO)_3$. *J. Catal.* **1984**, *89* (1), 79–92. https://doi.org/10.1016/0021-9517(84)90282-3.

(30) Yates, J. T.; Duncan, T. M.; Worley, S. D.; Vaughan, R. W. Infrared Spectra of Chemisorbed CO on Rh. *J. Chem. Phys.* **1979**, *70* (3), 1219–1224. https://doi.org/10.1063/1.437603.

(31) Thiel, P. A.; Williams, E. D.; Yates, J. T.; Weinberg, W. H. The Chemisorption of CO on Rh(111). *Surf. Sci.* **1979**, *84* (1), 54–64. https://doi.org/10.1016/0039-6028(79)90279-6.

(32) Yates, J. T.; Duncan, T. M.; Worley, S. D.; Vaughan, R. W. Infrared Spectra of Chemisorbed CO on Rh. *J. Chem. Phys.* **1979**, *70* (3), 1219–1224. https://doi.org/10.1063/1.437603.

(33) Wang, H. P.; Yates, J. T. Infrared Spectroscopic Study of N_2 Chemisorption on Rhodium Surfaces. *J. Phys. Chem.* **1984**, *88* (5), 852–856. https://doi.org/10.1021/j150649a006.

(34) Yates, J. T.; Kolasinski, K. Infrared Spectroscopic Investigation of the Rhodium Gem-Dicarbonyl Surface Species. *J. Chem. Phys.* **1983**, *79* (2), 1026–1030. https://doi.org/10.1063/1.445844.

(35) Goellner, J. F.; Gates, B. C.; Vayssilov, G. N.; Rösch, N. Structure and Bonding of a Site-Isolated Transition Metal Complex: Rhodium Dicarbonyl in Highly Dealuminated Zeolite Y. *J. Am. Chem. Soc.* **2000**, *122* (33), 8056–8066. https://doi.org/10.1021/ja001209f.

(36) H. F. J. van't Blik, J. B. A. D. van Zon, T. Huizinga, J. C. Vis, D. C. Koningsberger, and R.

P. Structure of Rhodium in an Ultradispersed Rh/Al_2O_3 Catalyst as Studied by EXAFS and Other Techniques. *J. Am. Chem. Soc.* **1985**, *107* (1), 3139–3147.

(37) Van't Blik, H. F. J.; Van Zon, J. B. A. D.; Koningsberger, D. C.; Prins, R. EXAFS Determination of the Change in the Structure of Rhodium in Highly Dispersed $Rh/\gamma\text{-}Al_2O_3$ Catalysts after CO and/or H_2 Adsorption at Different Temperatures. *J. Mol. Catal.* **1984**, *25* (1–3), 379–396. https://doi.org/10.1016/0304-5102(84)80060-7.

(38) Dohmae, K.; Nagai, Y.; Tanabe, T.; Suzuki, A.; Inada, Y.; Nomura, M. Real-Time XAFS Analysis of Rh/Alumina Catalyst. *Surf. Interface Anal.* **2008**, 40 (13), 1751–1754. https://doi.org/10.1002/sia.3003.

(39) Berkó, A.; Solymosi, F. Adsorption-Induced Structural Changes of Rh Supported by TiO_2(110)-(1×2): An STM Study. *J. Catal.* **1999**, *183* (1), 91–101. https://doi.org/10.1006/jcat.1998.2368.

(40) Matsubu, J. C.; Zhang, S.; DeRita, L.; Marinkovic, N. S.; Chen, J. G.; Graham, G. W.; Pan, X.; Christopher, P. Adsorbate-Mediated Strong Metal-Support Interactions in Oxide-Supported Rh Catalysts. *Nat. Chem.* **2017**, *9* (2), 120–127. https://doi.org/10.1038/nchem.2607.

(41) Robbins, J. L. Rhodium Dicarbonyl Sites on Alumina Surface. Preparation and Characterization of a Model System. *J. Phys. Chem. C* **1986**, *90*, 3381–3386..

(42) Al, R. /; Rh, C. /; Al, /K-; Iordan, A.; Zaki, M. I.; Kappenstein, C.; Géron, C.; Al, B.; Al, K.-. XPS and in Situ IR Spectroscopic Studies of $CO/Rh/Al_2O_3$ and $CO/Rh/K–Al_2O_3$ at High Temperatures: Probing the Impact of the Potassium Functionalization of the Support. *Phys. Chem. Chem. Phys.* **2003**, *5* (8), 1708–1715. https://doi.org/10.1039/B300962A.

(43) Ouyang, R.; Liu, J. X.; Li, W. X. Atomistic Theory of Ostwald Ripening and Disintegration of Supported Metal Particles under Reaction Conditions. *J. Am. Chem. Soc.* **2013**, *135* (5), 1760–1771. https://doi.org/10.1021/ja3087054.

(44) Goldsmith, B. R.; Sanderson, E. D.; Ouyang, R.; Li, W. X. CO- and NO-Induced Disintegration and Redispersion of Three-Way Catalysts Rhodium, Palladium, and Platinum: An Ab Initio Thermodynamics Study. *J. Phys. Chem. C* **2014**, *118* (18), 9588–9597. https://doi.org/10.1021/jp502201f.

(45) Yan, G.; Tang, Y.; Li, Y.; Li, Y.; Nguyen, L.; Sakata, T.; Higashi, K.; Tao, F. F.; Sautet, P. Reaction Product-Driven Restructuring and Assisted Stabilization of a Highly Dispersed Rh-on-Ceria Catalyst. *Nat. Catal. 2022 52* **2022**, *5* (2), 119–127. https://doi.org/10.1038/s41929-022-00741-2.

(46) Van 't Blik, H. F. J.; Zon, J. B. A. D. Van; Hulzlnga, T.; Vis, J. C.; Koningsberger, D. C.; Prlns, R. An Extended X-Ray Absorptlon Flne Structure Spectroscopy Study of a Highly Dispersed Rh/Al_2O_3 Catalyst: The Influence of CO Chemisorption on the Topology of Rhodium. *J. Phys. Chem* **1983**, *87* (7), 2264–2267. https://doi.org/10.1021/j100236a002.

(47) van't Blik, H. F. J.; Huizinga, T.; van Zon, J. B. A. D.; Vis, J. C.; Koningsberger, D. C.; Prins, R. Structure of Rhodium in an Ultradispersed Rh/Al_2O_3 Catalyst as Studied by EXAFS and Other Techniques. *J. Am. Chem. Soc.* **1985**, *107* (11), 3139–3147.

https://doi.org/10.1021/ja00297a020.

(48) Rainer, D. R.; Koranne, M.; Vesecky, S. M.; Goodman, D. W. CO + O_2 and CO + NO Reactions over Pd/Al_2O_3 Catalysts. *J. Phys. Chem. B* **1997**, *101* (50), 10769–10774. https://doi.org/10.1021/jp971262z.

(49) Cargnello, M.; Doan-Nguyen, V. V. T.; Gordon, T. R.; Diaz, R. E.; Stach, E. A.; Gorte, R. J.; Fornasiero, P.; Murray, C. B. Control of Metal Nanocrystal Size Reveals Metal-Support Interface Role for Ceria Catalysts. *Science.* **2013**, *341* (6147), 771–773. https://doi.org/10.1126/science.1240148.

(50) Freund, H. J.; Meijer, G.; Scheffler, M.; Schlögl, R.; Wolf, M. CO Oxidation as a Prototypical Reaction for Heterogeneous Processes. *Angew. Chemie - Int. Ed.* **2011**, *50* (43), 10064–10094. https://doi.org/10.1002/anie.201101378.

(51) Chee, S. W.; Arce-Ramos, J. M.; Li, W.; Genest, A.; Mirsaidov, U. Structural Changes in Noble Metal Nanoparticles during CO Oxidation and Their Impact on Catalyst Activity. *Nat. Commun.* **2020**, *11* (1), 2133. https://doi.org/10.1038/s41467-020-16027-9.

(52) Hepburn, J. S.; Dobson, D. A.; Hubbard, C. P.; Otto, K. The Pulse Flame Combustor Revisited. *SAE Tech. Pap.* **1996**, *105* (4), 2296-2331. https://doi.org/10.4271/962118.

(53) Farrauto, R. J.; Deeba, M.; Alerasool, S. Gasoline Automobile Catalysis and Its Historical Journey to Cleaner Air. *Nat. Catal.* **2019**, *2* (7), 603–613. https://doi.org/10.1038/s41929-019-0312-9.

(54) Weisz, P. B.; Prater, C. D. Interpretation of Measurements in Experimental Catalysis. *Adv. Catal.* **1954**, *6*, 143–196. https://doi.org/10.1016/S0360-0564(08)60390-9.

(55) Mears, D. E. Diagnostic Criteria for Heat Transport Limitations in Fixed Bed Reactors. *J. Catal.* **1971**, *20* (2), 127–131. https://doi.org/10.1016/0021-9517(71)90073-X.

(56) Mears, D. E. Tests for Transport Limitations in Experimental Catalytic Reactors. *Ind. Eng. Chem. Process Des. Dev.* **1971**, *10* (4), 541–547. https://doi.org/10.1021/i260040a020.

(57) Yates, D. J. C.; Murrell, L. L.; Prestridge, E. B. Ultradispersed Rhodium Rafts: Their Existence and Topology. *J. Catal.* **1979**, *57* (1), 41–63. https://doi.org/10.1016/0021-9517(79)90042-3.

(58) Yates, D. J. C.; Sinfelt, J. H. The Catalytic Activity of Rhodium in Relation to Its State of Dispersion. *J. Catal.* **1967**, *8* (4), 348–358. https://doi.org/10.1016/0021-9517(67)90331-4.

(59) Asokan, C.; DeRita, L.; Christopher, P. Using Probe Molecule FTIR Spectroscopy to Identify and Characterize Pt-Group Metal Based Single Atom Catalysts. *Cuihua Xuebao/Chinese J. Catal.* **2017**, *38* (9), 1473–1480. https://doi.org/10.1016/S1872-2067(17)62882-1.

(60) Asokan, C.; Thang, H. V.; Pacchioni, G.; Christopher, P. Reductant Composition Influences the Coordination of Atomically Dispersed Rh on Anatase TiO_2. *Catal. Sci. Technol.* **2020**, *10* (6), 1597–1601. https://doi.org/10.1039/d0cy00146e.

(61) Rice, C. A.; Worley, S. D.; Curtis, C. W.; Guin, J. A.; Tarrer, A. R. The Oxidation State of

Dispersed Rh on Al_2O_3. *J. Chem. Phys.* **1981**, *74* (11), 6487–6497. https://doi.org/10.1063/1.440987.

(62) Tang, Y.; Asokan, C.; Xu, M.; Graham, G. W.; Pan, X.; Christopher, P.; Li, J.; Sautet, P. Rh Single Atoms on TiO_2 Dynamically Respond to Reaction Conditions by Adapting Their Site. *Nat. Commun.* No. 2019, 1–10. https://doi.org/10.1038/s41467-019-12461-6.

(63) Szanyi, J.; Goodman, D. W. CO Oxidation on Palladium. 1. A Combined Kinetic-Infrared Reflection Absorption Spectroscopic Study of Pd(100). *J. Phys. Chem.* **1994**, *98* (11), 2972–2977. https://doi.org/10.1021/j100062a038.

(64) Song, J.; Yang, Y.; Liu, S.; Li, L.; Yu, N.; Fan, Y.; Chen, Z.; Kuai, L.; Geng, B. Dispersion and Support Dictated Properties and Activities of Pt/Metal Oxide Catalysts in Heterogeneous CO Oxidation. *Nano Res.* **2021**, *14* (12), 4841–4847. https://doi.org/10.1007/s12274-021-3443-7.

(65) Farber, R. G.; Turano, M. E.; Killelea, D. R. Identification of Surface Sites for Low-Temperature Heterogeneously Catalyzed CO Oxidation on Rh(111). *ACS Catal.* **2018**, *8* (12), 11483–11490. https://doi.org/10.1021/acscatal.8b03887.

(66) Gustafson, J.; Balmes, O.; Zhang, C.; Shipilin, M.; Schaefer, A.; Hagman, B.; Merte, L. R.; Martin, N. M.; Carlsson, P.-A.; Jankowski, M.; Crumlin, E. J.; Lundgren, E. The Role of Oxides in Catalytic CO Oxidation over Rhodium and Palladium. *ACS Catal.* **2018**, *8*, 4438–4445. https://doi.org/10.1021/acscatal.8b00498.

(67) Allian, A. D.; Takanabe, K.; Fujdala, K. L.; Hao, X.; Truex, T. J.; Cai, J.; Buda, C.; Neurock, M.; Iglesia, E. Chemisorption of CO and Mechanism of CO Oxidation on Supported Platinum Nanoclusters. *J. Am. Chem. Soc.* **2011**, *133* (12), 4498–4517. https://doi.org/10.1021/ja110073u.

(68) Gao, F.; Cai, Y.; Gath, K. K.; Wang, Y.; Chen, M. S.; Guo, Q. L.; Goodman, D. W. CO Oxidation on Pt-Group Metals from Ultrahigh Vacuum to Near Atmospheric Pressures. 1. Rhodium. *J. Phys. Chem. C* **2009**, *113* (1), 182–192. https://doi.org/10.1021/jp8077979.

(69) Gao, F.; Wang, Y.; Cai, Y.; Goodman, D. W. CO Oxidation on Pt-Group Metals from Ultrahigh Vacuum to Near Atmospheric Pressures . 2. Palladium and Platinum. **2009**, 113 (1), 174–181. https://doi.org/10.1021/jp8077985

(70) Engel, T.; Ertl, G. Elementary Steps in the Catalytic Oxidation of Carbon Monoxide on Platinum Metals. *Adv. Catal.* **1979**, *28*, 1–78. https://doi.org/10.1016/S0360-0564(08)60133-9.

(71) McClure, S. M.; Goodman, D. W. New Insights into Catalytic CO Oxidation on Pt-Group Metals at Elevated Pressures. *Chem. Phys. Lett.* **2009**, *469* (1–3), 1–13. https://doi.org/10.1016/j.cplett.2008.12.066.

(72) Oh, S. H.; Eickel, C. C. Influence of Metal Particle Size and Support on the Catalytic Properties of Supported Rhodium: CO-O_2 and CO-NO Reactions. *J. Catal.* **1991**, *128* (2), 526–536. https://doi.org/10.1016/0021-9517(91)90310-Z.

(73) Peden, C. H. F.; Goodman, D. W.; Blair, D. S.; Berlowitz, P. J.; Fisher, G. B.; Oh, S. H. Kinetics of CO Oxidation by O_2 or NO on Rh(111) and Rh(100) Single Crystal. *J. Phys.*

Chem. **1988**, *92* (6), 1563–1567. https://doi.org/10.1021/j100317a038.

(74) Oh, S. H.; Fisher, G. B.; Carpenter, J. E.; Goodman, D. W. Comparative Kinetic Studies of CO-O_2 and CO-NO Reactions over Single Crystal and Supported Rhodium Catalysts. *J. Catal.* **1986**, *100* (2), 360–376. https://doi.org/10.1016/0021-9517(86)90103-X.

(75) Leung, L.-W. H.; Wayne, D. The Oxidation of Carbon Monoxide on Rh(100) Under Steady State Conditions: An FT-IR Study. *Catal. Letters* **1990**, *5*, 353–360. https://doi.org/10.1007/bf00765177

(76) Rainer, D. R.; Koranne, M.; Vesecky, S. M.; Goodman, D. W. CO + O_2 and CO + NO Reactions over Pd/Al_2O_3 Catalysts . *J. Phys. Chem. B* **2002**, *101* (50), 10769–10774. https://doi.org/10.1021/jp971262z.

(77) Cavers, M.; Davidson, J. M.; Harkness, I. R.; Rees, L. V. C.; McDougall, G. S. Spectroscopic Identification of the Active Site for CO Oxidation on Rh/Al_2O_3 by Concentration Modulation in Situ DRIFTS. *J. Catal.* **1999**, *188* (2), 426–430. https://doi.org/10.1006/jcat.1999.2672.

(78) van't Blik, H. F. J.; Van Zon, J. B. . A. D.; Koningsberger, D. C.; Prins, R. EXAFS Determination of the Change in the Structure of Rhodium in Highly Dispersed Rh/γ-Al_2O_3 Catalysts After CO and/or H_2, Adsorption At Different Temperatures. *J. Mol. Cat.,* **1984**, *25*, 379–396. https://doi.org/10.1016/0304-5102(84)80060-7

(79) Ouyang, R.; Liu, J.; Li, W. Atomistic Theory of Ostwald Ripening and Disintegration of Supported Metal Particles under Reaction Conditions. *J. Am. Chem. Soc.,* **2013**, 135 (5), 1760-1771. https://doi.org/10.1021/ja3087054.

(80) Wovchko, E. A.; Yates, J. T. Activation of O_2 on a Photochemically Generated Rh^I Site on an Al_2O_3 Surface: Low-Temperature O_2 Dissociation and CO Oxidation. *J. Am. Chem. Soc.* **1998**, *120* (40), 10523–10527. https://doi.org/10.1021/ja981241Y.

(81) Cavers, M.; Davidson, J. M.; Harkness, I. R.; Rees, L. V. C.; McDougall, G. S. Spectroscopic Identification of the Active Site for CO Oxidation on Rh/Al_2O_3 by Concentration Modulation in Situ DRIFTS. *J. Catal.* **1999**, *188* (2), 426–430. https://doi.org/10.1006/jcat.1999.2672.

(82) Basu, P.; Panayotov, D.; Yates, J. T. Spectroscopic Evidence for the Involvement of Hydroxyl Groups in the Formation of $Rh^I(CO)_2$ on Metal Oxide Supports. *J. Phys. Chem.* **1987**, *91* (12), 3133–3136. https://doi.org/10.1021/j100296a007.

(83) Solymosi, F.; Pásztor, M. An Infrared Study of the Influence of CO Chemisorption on the Topology of Supported Rhodium. *J. Phys. Chem.* **1985**, *89* (22), 4789–4793. https://doi.org/10.1021/j100268a026.

(84) Solymosi, F.; Pásztor, M. Infrared Study of the Effect of H_2 on CO-Induced Structural Changes in Supported Rh. *J. Phys. Chem.* **1986**, *90* (21), 5312–5317. https://doi.org/10.1021/j100412a081.

Chapter 4: Spectroscopic investigation of Rh mobility in the presence of CO, O_2 and H_2O

Spectroscopic investigation of Rh mobility in the presence of CO, O_2 and H_2O

4.1 Introduction

Recently, research groups have been focused on studying catalyst dynamics and their impact on reactivity and selectivity.[1,2] When exposed to a reactive gas, metal nanoparticles can alter their structure in various ways.[3,4] This can involve a change in shape or exposed facets. For example, when Pt is exposed to CO, (100) facets are reconstructed into high index facets.[5] Metal nanoparticles can also change their size and sinter forming larger nanoparticles, resulting in a loss of active sites, which constitutes the main deactivation mode of Pt and Pd three-way catalysts. Lastly, metal nanoparticles can undergo structural changes leading to their redispersion into single atoms. This particular change can influence both the activity and the selectivity of the catalyst. For example, in the reaction between CO_2 and H_2, Rh nanoparticles are selective towards CH_4, while Rh single atoms are more selective towards CO.[6] In the previous chapter we showed how the reactivity towards CO oxidation at higher temperature is affected by the relative fraction nanoparticles and single atoms, with Rh nanoparticles being more active than single atoms.[7]

Structural changes depend on several physical parameters, including cohesive energy, surface energy of the nanoparticle, the adhesion of the nanoparticle on the support, the heat of adsorption of the reactant with the metal particles and their surface coverage.[8–10] Metal nanoparticle surface and cohesive energy are size dependent parameters. As previously described, the cohesive energy decreases as the particle size decreases.[9,10] This leads to higher instability and therefore smaller metal nanoparticles are easier to break apart into single atoms. However, as nanoparticles become larger,

their surface energy tends to decrease. This typically leads to the exposure of low-index surface planes and to a higher stability, therefore reducing the possibility of particle disintegration.[11]

The particle size dependence of single atoms-nanoparticle interconversion is well shown by the CO adsorption on Rh/Al_2O_3 catalysts performed at room temperature, where smaller nanoparticles are more prone to redisperse into single atoms and form gem-dicarbonyl species, $Rh^+(CO)_2$, while larger nanoparticles are more stable, and CO simply adsorbs as mostly linear and bridge bound CO on metal Rh.[12–16]

To detect structural changes, several techniques are commonly employed. In situ transmission electron microscopy (TEM) and scanning tunneling microscopy (STM) can monitor the changes in nanoparticle shape or size in the presence of reactants.[1] However, nanoparticle damage from the beam can occur and care must be taken.[17,18] X-ray spectroscopy (XAS) and in particular EXAFS can be used to obtain more detail of the local metal structure.[19,20] However, it can become less precise as the nanoparticle increases in size.[19] In addition, a high-flux density X-ray beam can affect the catalyst structure and induce catalyst reduction and agglomeration, as shown for Rh/Al_2O_3 and Ni/zeolite catalysts.[21]

In this chapter, we used in-situ IR spectroscopy to study CO-induced Rh structural changes in the presence of different feed compositions. IR-spectroscopy has been often used to study structural changes of Rh,[12,14,22] Cu,[23,24] Pd[25,26] and Pt,[5,27,28] because it is a more accessible technique.[29,30] Here we investigated the effect of water and O_2 on the Rh single atom and nanoparticle interconversion induced by CO. In addition, considering the fluctuating feed composition during TWC operation,[31] varying from oxidizing to reducing conditions, the reversibility of CO-induced structural changes in the presence of O_2 is also investigated.

O_2 and water are significant components of gasoline exhaust gas and details on their effect on the catalyst structure are needed to optimize the catalyst design effectively.

4.2 Material and Methods

4.2.1 Catalysts

0.05% and 0.1% Rh/Al_2O_3 were synthesized via incipient wetness impregnation. $Rh(NO_3)_3$ was added drop by drop on a γ-Al_2O_3 support. The catalysts were first dehydrated at 120°C for 4 h and then calcined in static air at 600°C for 4 h, with the temperature increased at 1°C/min.

4.2.2 Characterization

H_2 chemisorption was performed using a Micromeritics ASAP2020 Plus. Prior to the measurements, the catalysts were reduced in H_2 at 500 °C for 1 h, then evacuated for 2 h at 500 °C, cooled to 35 °C and maintained under vacuum for 1 h. H_2 adsorption isotherms were collected at 35 °C. The dispersion was calculated assuming a H:metal ratio = 1:1.

4.2.3 DRIFTS experiments

DRIFTS experiments were carried on an iS50 Nicolet FTIR. The catalyst was loaded in a custom-made Harrick Scientific reaction chamber. The sample holder is divided into two parts: one part was loaded with the catalyst and the other part was loaded with SiC, an inert material. The temperature was controlled using a K-type thermocouple positioned underneath the sample holder.

Prior to each experiment, the catalysts were initially treated in 1% O_2/He at 500°C for 30 min, then purged with He and finally reduced in 5% H_2/He for 30 min.

The catalyst surface was studied while exposing the catalyst to 8400 ppm CO and a mixture of CO + O_2, with CO/O_2 = 0.9. The effect of water was studied by introducing water into these 2 feed compositions. During dry experiments the gas mixtures passed through a liquid nitrogen cold trap.

Wet experiments were carried out by introducing water using a bubbler. The surface speciation was analyzed by exposing the reaction mixture at 200 and 300°C. Afterwards, the system was purged with He and the desorption of the species initially adsorbed was tracked under isothermal conditions.

Before taking spectra, a background was obtained. For wet experiments, the catalyst was first saturated with water, the background spectrum was obtained and then the full feed composition was added. Each spectrum was taken by averaging 32 scans.

4.3 Results and Discussion

4.3.1 Characterization

Table 4.1: Dispersion and particle size measurements performed on 0.05% Rh/Al_2O_3 and 0.1%Rh/Al_2O_3 via H_2 chemisorption.

Catalyst	H:Rh	Particle size (nm)
0.05% Rh/Al_2O_3	1.5	<1
0.1% Rh/Al_2O_3	0.9	1.1

0.05% Rh/Al_2O_3 and 0.1%Rh/Al_2O_3 were characterized via H_2 chemisorption and CO DRIFTS at 35°C. Table 4.1 lists the dispersion measurements for 0.05% Rh/Al_2O_3 and 0.1%Rh/Al_2O_3 determined via H_2 chemisorption. Both catalysts exhibit high metal dispersion, with an average Rh particle size of 1 nm or less. In the case of the 0.05% Rh/Al_2O_3 catalyst, the H:Rh ratio exceeds unity, consistent with previous literature reporting a hydrogen-to-metal ratios larger than one for highly dispersed Pt, Rh and Ir catalysts. These metals can indeed adsorb multiple hydrogen atoms per metal atom.[32]

Consistent with H_2 chemisorption measurements, CO DRIFTS displayed in Figure 4.1 shows the presence on features at 2094 and 2026 cm^{-1}, corresponding to the symmetric and asymmetric stretches of $Rh(CO)_2$ single atoms, respectively.

In fact, Rh catalysts undergo structural changes when exposed to CO.[12,13,33–38] These structural changes involve nanoparticle disintegration into single atoms through an oxidative process involving the OH group from the support. During the disintegration process, Rh is oxidized from Rh^0 to Rh^+. The proposed mechanism is as follow:

$$Rh^0 + OH\text{-}Al + 2CO \rightarrow Rh^+(CO)_2 + 1/2\ H_2$$

Experimental and theoretical studies have demonstrated that Rh structural changes are size dependent and smaller nanoparticles are more prone to be dispersed into single atoms, compared to larger nanoparticles.[9,33,39,40] Our spectra, which show only the presence of CO adsorbed on Rh single atoms, are consistent with previous literature as this suggests that either we began with only single atoms or we induced the total disintegration of 1 nm Rh particles.

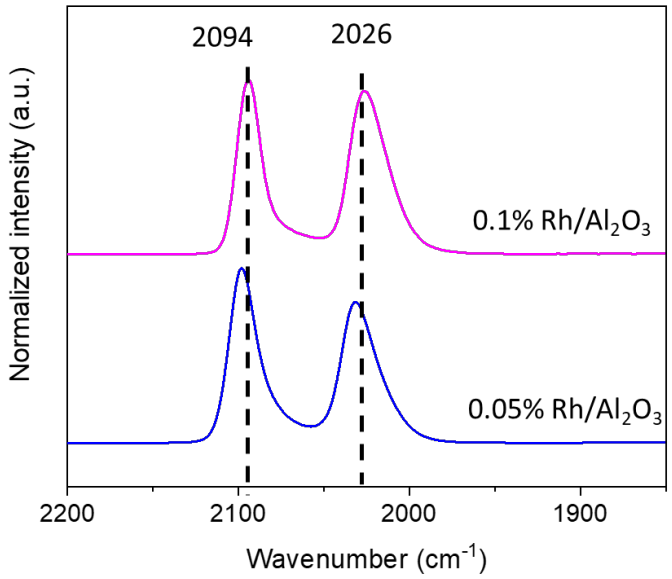

Figure 4.1: CO adsorption on 0.05% Rh/Al_2O_3 and 0.1%Rh/Al_2O_3 at 35°C. The catalysts were initially treated in 1% O_2 at 500°C for 30 min, then purged with Ar and finally reduced in 5% H_2 for 30 min. The catalysts were exposed to 8400 ppm CO until saturation.

4.3.2 CO adsorption at 200 and 300°C

To obtain a deeper understanding of the structural dynamics occurring during CO oxidation kinetics, particularly before the system reached steady-state, we investigated via IR spectroscopy the temporal evolution of Rh structural changes. This was achieved by exposing the 0.05% Rh/Al_2O_3 catalyst to CO at 200 and 300°C.

Figure 4.2 (a) and (b) show the spectra taken during CO adsorption at 200°C over a period of time of almost 2 h. This extended time frame was needed to stabilize the species and observe no further changes in the spectra. In Figure 4.2 (a), we observe that Rh speciation changes over time. In the first few minutes of CO adsorption, three features are present: two peaks centered at 2090 and 2019 cm^{-1}, assigned to symmetric and asymmetric gem-dicarbonyl species, respectively,[12,13] and a

peak at 2055 cm^{-1},[14] corresponding to CO linearly bound to Rh. The absence of the feature assigned to bridge CO-Rh in consistent with the high dispersion measured via H_2 chemisorption. In fact, typically, the bridge bound CO-Rh feature is observed in spectra obtained on catalysts characterized by nanoparticles larger than 2 nm.[41]

As exposure time increases, we observe a decrease in the intensity of the feature associated with CO linearly bound to Rh_{NP}, while the gem-dicarbonyl species increase in intensity. This is consistent with the oxidative process of Rh nanoparticle fragmentation into single atoms. Furthermore, we observe that the gem-dicarbonyl species stretching frequencies do not change. This behavior is a characteristic of CO adsorbed on isolated metal single atom features, as they do not exhibit a change in peak position with varying coverage due to CO dipole-dipole coupling, unlike CO adsorbed on nanoparticles.[42]

Figure 4.2(b) provides a clearer difference in Rh speciation by displaying the spectra taken after 5 and 116 minutes. Here, we observe the presence of two isosbestic points at 2065 and 2038 cm^{-1}, which suggest that Rh_{NP} converts directly into Rh_{SA} with no intermediates. A similar trend was identified through energy-dispersive X-ray absorption fine structure in previous literature.[43] Two isosbestic points were also detected and were assigned to two structural changes occurring in sequence: the first change included the transformation from $Rh_{10}(CO)$, nanoparticle Rh, to $Rh(CO)_{10}$, where each Rh single atom was bound to ten CO molecules, and the second and final change was associated the formation of Rh gem-dicarbonyl species, $Rh(CO)_2$. [43]

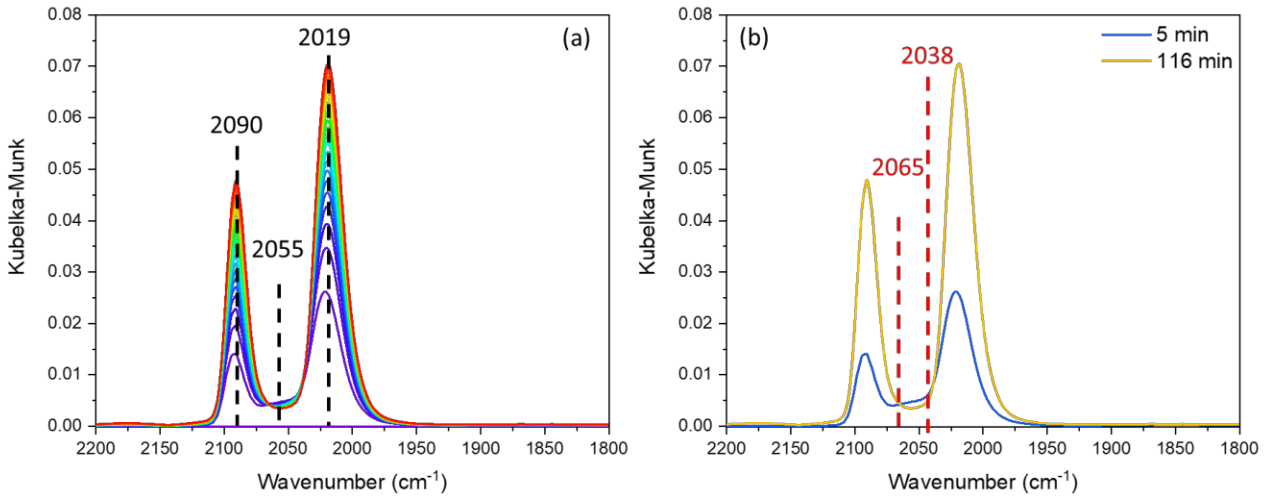

Figure 4.2: 8400 ppm CO/He adsorption at 200°C on 0.05% Rh/Al_2O_3 over time until saturation. The catalyst was initially treated in 1% O_2 at 500°C for 30 min, then purged with Ar and finally reduced in 5% H_2 for 30 min. (a) spectra taken every 5 minutes from time 0 (purple) to 116 min (red); (b) spectra taken at 5 min and 116 showing the isosbestic points.

A similar experiment was conducted at 300°C to study the extent of Rh particle disintegration at higher temperature (Figure 4.3).

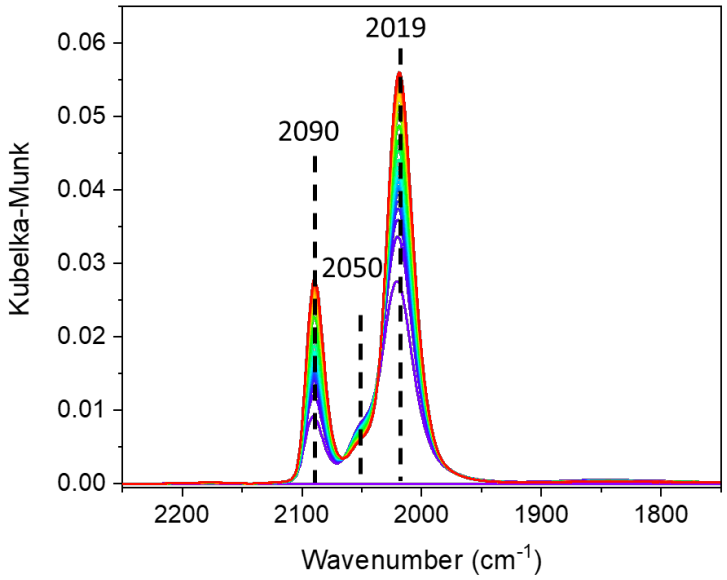

Figure 4.3: 8400 ppm CO/He adsorption at 200°C on 0.05% Rh/Al2O3 over time until saturation. The catalyst was initially treated in 1% O2 at 500°C for 30 min, then purged with Ar and finally reduced with 5% H2 for 30 min. The spectra were taken every 5 minutes from time 0 to 132 min.

Similar to the spectra obtained at 200°C, also at 300°C we observe the presence of the two features at 2090 and 2019 cm^{-1} associated with the Rh gem-dicarbonyl species ($Rh_{SA}(CO)_2$), along with the feature of CO linearly bound to a Rh nanoparticle (CO-Rh_{NP}) at 2050 cm^{-1}. The trend in changes in intensity is similar to the one observed at 200°C, with the intensity of Rh_{NP} decreasing and that of Rh_{SA} increasing. However, unlike at 200°C, at 300°C we still observe the feature of CO-Rh_{NP}, suggesting that the Rh nanoparticle disintegration process is not complete. In fact, at higher temperature, it was proposed that CO promotes single atom agglomeration, by reducing Rh from +1 to 0. This catalyst, as suggested by the H:Rh ratio higher than 1, primarily consists of sub nanometer clusters, which have high surface energy and remain unstable in the presence of CO even at

high temperature and tend to redisperse into single atoms.[9,39] However, as expected, the extent of particle disintegration is lower, since this process is more favored at lower temperature.[12,13]

4.3.3 CO + O_2 adsorption at 200 and 300°C

Following the investigation of the CO-only feed, we introduced O_2 into the reaction mixture with the goal of comparing the trend between the change in speciation and the activity data. In fact, during kinetic steady-state experiments we observed a decline in conversion at fixed temperature, as shown in Figure 4.4, where the profile of CO_2 concentration is plotted over time, during CO + O_2 exposure at 327°C. Based on the spectra shown in Figure 4.2 and Figure 4.3, we hypothesize that the decline in CO_2 formed is associated with the reduction in the relative fraction of Rh nano-particles, which are reported to be the active sites for CO oxidation.[44]

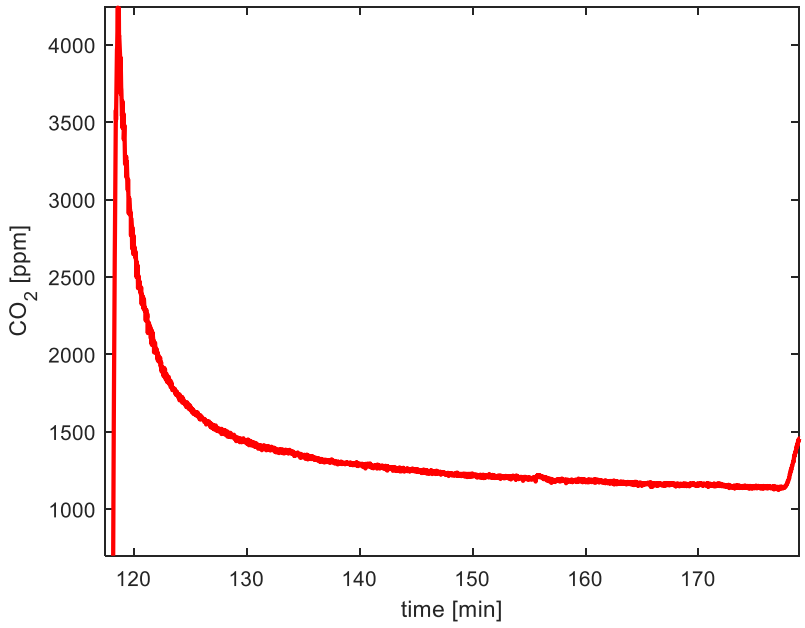

Figure 4.4: CO_2 profile vs time during CO+O_2 reaction at 327°C on 0.05% Rh/Al_2O_3. CO = 8400 ppm, O_2 = 9200 ppm, diluted in N_2. Prior to the reaction, the catalyst was reduced with 5% H_2 for 30 min.

Similar to CO only experiments, we proceeded with studying the evolution of Rh speciation at 200°C and 300°C.

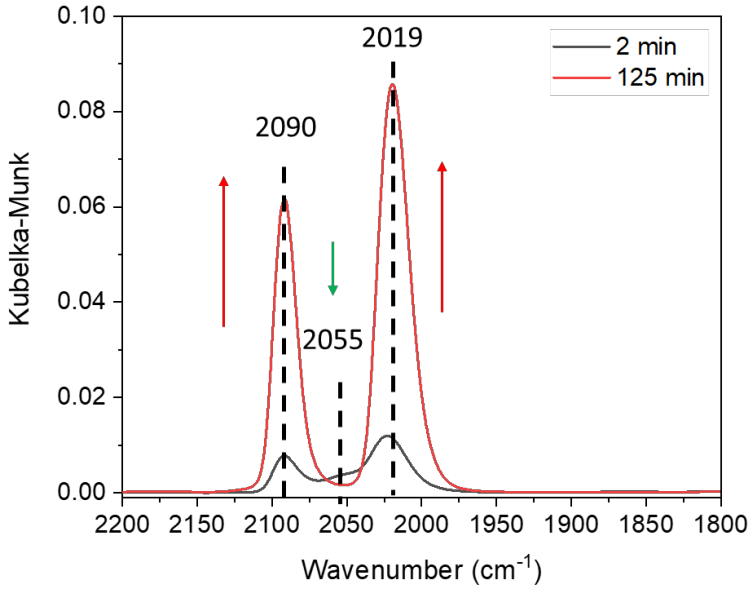

Figure 4.5: 8400 ppm CO + 9200 ppm O_2/He adsorption at 200°C on 0.05% Rh/Al_2O_3. The catalyst was initially treated in 1% O_2 at 500°C for 30 min, then purged with Ar and finally reduced with 5% H_2 for 30 min. The temperature decreased in He to 200°C. The spectra shown were taken during CO + O_2 adsorption at time = 2 min (black) and 125 min (red), when saturation was reached.

CO + O_2 exposure at 200°C spectra are shown in Figure 4.5 and we continue to observe the transformation of Rh_{NP}, at 2055 cm^{-1} as CO-Rh, into Rh_{SA}, at 2090 and 2019 cm^{-1} as $Rh(CO)_2$. The relative fraction of these species changes over time, with single atoms progressively increasing. In addition, when CO and O_2 are both present in the gas mixture, the extent of particle disintegration is enhanced because O_2 favors this oxidative process.[45,46]

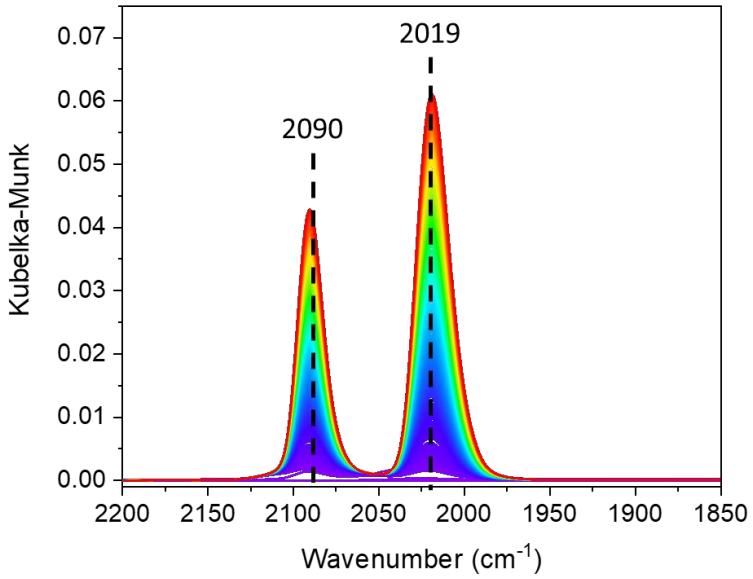

Figure 4.6: 8400 ppm CO + 9200 ppm O_2/He adsorption at 300°C on 0.05% Rh/Al_2O_3 for 198 minutes. The catalyst was initially treated in 1% O_2 at 500°C for 30 min, then purged with Ar and finally reduced with 5% H_2 for 30 min. The temperature decreased in He to 300°C. The spectra shown were taken during CO + O_2 adsorption from time = 2 min (purple) to time = 198 min (red), when saturation was reached.

The trend of nanoparticle disintegration persists during CO + O_2 adsorption at 300°C, shown in Figure 4.6. When the catalyst is exposed to CO + O_2, with $CO/O_2 = 0.9$, once again, Rh nanoparticles undergo redispersion into single atoms. The relative fraction of Rh_{NP} detected on DRIFTS, located at 2050 cm^{-1}, decreases in intensity as the exposure time increases. This behavior is consistent with the activity data shown in Figure 4.4. Given that Rh_{NP} is the active site for CO oxidation, CO_2 formation decreases with time because of the redispersion of the active sites into single atoms, which have been found inactive for CO oxidation at high temperature.[44] We note that the presence of Rh particles is not readily discernable, suggesting that they are either absent or exist in minimal quantities, making them challenging to observe due to their low extinction coefficient.[6,12,14,47] This is consistent with the low activity observed during CO oxidation kinetics at this

temperature, whereas higher activity is achieved at temperature higher than 320°C, because of the single atom aggregation.

4.3.4 CO + H_2O adsorption

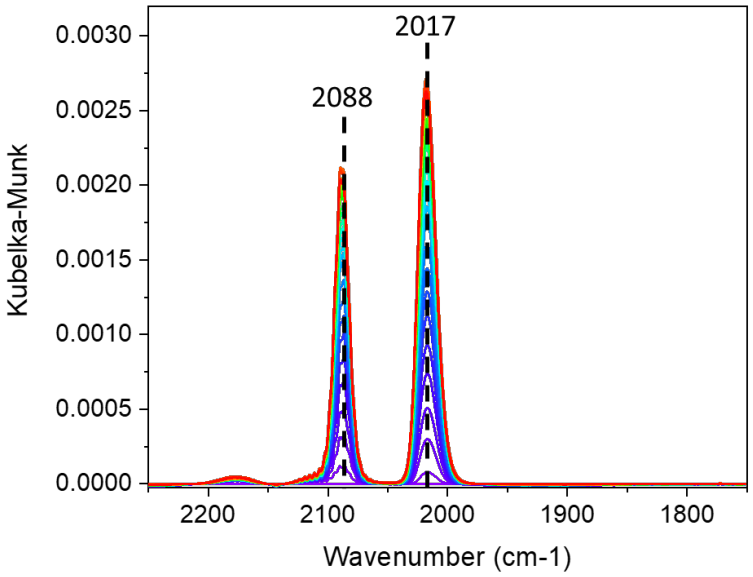

Figure 4.7: 8400 ppm CO + H_2O/He adsorption at 200°C on 0.05% Rh/Al_2O_3 for 140 minutes. The catalyst was initially treated in 1% O_2 at 500°C for 30 min, then purged with Ar and finally reduced with 5% H_2 for 30 min. The temperature decreased in He to 200°C and H_2O was introduced. After saturating the catalyst with water, a background was taken and CO was added in the gas stream. The spectra shown were taken during CO + H_2O adsorption from time = 2 min (purple) to time = 140 min (red), when saturation was reached.

The effect of water on Rh mobility and interconversion between single atoms and nanoparticles was investigated by initially saturating the catalyst with H_2O and subsequently introducing CO into the feed. During CO and H_2O adsorption, shown in Figure 4.7, we only notice the presence of CO adsorbed on Rh single atoms in the form of gem-dicarbonyl species. There is no Rh_{NP}–CO, in the frequency range between 2030 and 2070 cm^{-1}, where it is usually located. In this region, the

baseline is zero, which contrasts with previous experiments, where the baseline never reaches zero, suggesting the minimal presence of CO on Rh_{NP}.

The position of the two gem-dicarbonyls exhibited a slight red-shift compared to the position of the experiment without water. Experimental and theoretical studies showed that the gem-dicarbonyl species position is related to the coordination environment. A less hydroxylated region causes a blue shift, while the more hydroxylated region causes a red shift.[22] We can therefore speculate that the larger presence of OH groups may cause the shift compared to the dry experiments. In addition, the narrower width of $Rh(CO)_2$ features suggests that in the presence of water, the Rh coordination environment is more uniform[48] as contrasted with the dry case.

After purging the CO from the gas phase, while flowing He and water, the gem-dicarbonyl species desorbed or decomposed (Figure 4.8 a), and a new species becomes noticeable at 2170 cm^{-1} (Figure 4.8b), where it was previously obscured by the presence of CO gas phase (2200-2050 cm^{-1}). This species could be assigned to CO bound on Rh oxide or CO on alumina.[49–51] However, the latter option appears less likely, since CO on Al_2O_3 is usually only physisorbed, with weak binding energy, and usually desorbs during a He purge.

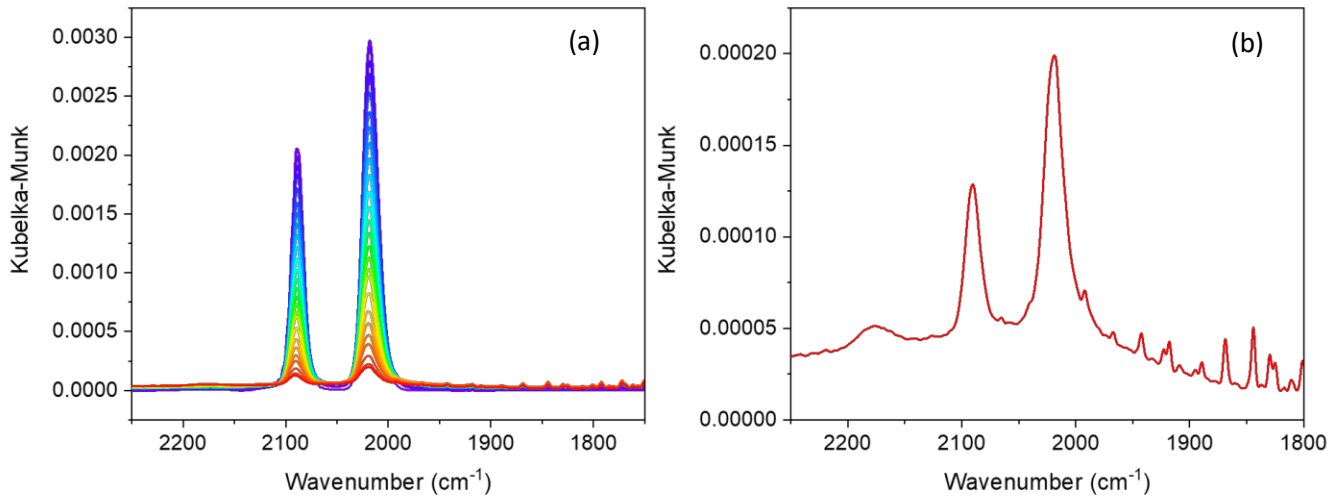

Figure 4.8: Purge with He + H_2O on 0.05% Rh/Al_2O_3: (a) spectra over time until stabilization; (b) last spectrum

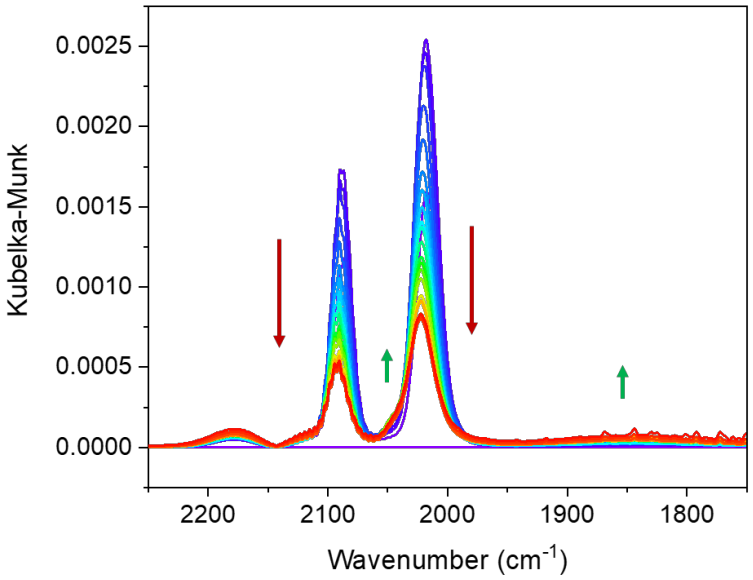

Figure 4.9: Dynamics of CO + H_2O adsorption on 0.05% Rh/Al_2O_3 at 300°C.The catalyst was initially treated in 1% O_2 at 500°C for 30 min, then purged with Ar and finally reduced with 5% H_2 for 30 min. The temperature decreased in He to 300°C and H_2O was introduced. After saturating the catalyst with water, a background was taken, and 8400 ppm CO was added in the gas stream. The spectra shown were taken during CO + H_2O adsorption from time = 2 min (purple) to time = 108 min (red), when saturation was reached.

Figure 4.9 shows the spectra obtained with exposure to CO + H_2O on 0.05% Rh/Al_2O_3 at 300°C. In this case, the dynamics of the species present on the catalyst surface are quite different from the previous, dry experiments. As time progresses, we observe that the intensity of the features assigned to $Rh(CO)_2$ centered at 2087 and 2018 cm^{-1} initially intensify and then decline, while shifting to higher wavenumber. Simultaneously, we observe an increase in intensity of the feature corresponding to CO linearly bound to Rh nanoparticles at 2050 cm^{-1}, along with the emergence of the bridge bound CO on Rh nanoparticle feature, spanning from 1800 to 1950 cm^{-1}. The dynamics shown in Figure 4.9 can provide insights into the mobility of gem-dicarbonyl species as well as the mechanism of single atom aggregation. The dynamics of aggregation of Rh single atoms into nanoparticles is consistent with the CO_2 formation profile during CO oxidation in the presence of water (Figure 4.10). Unlike the dry experiment, the CO_2 profile slowly increases before reaching the steady-state, which is consistent with the single atom aggregation dynamics in Figure 4.9. We can hypothesize that H_2O enhances the mobility of single atoms and favors aggregation. In addition, the blueshift observed in single atom peak positions suggests that the local coordination environment influences their mobility and it further indicates that the doublets at lower wavenumber (more hydroxylated) exhibit greater mobility in the presence of water.

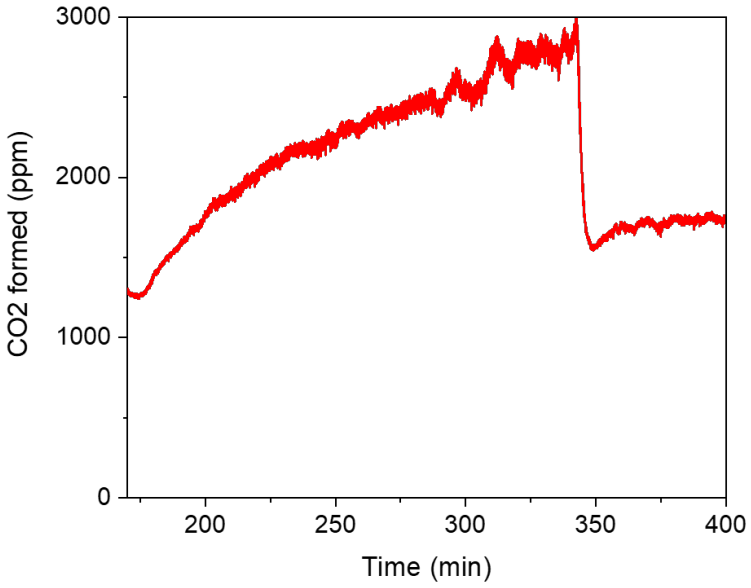

Figure 4.10: CO_2 profile vs time during wet $CO+O_2$ reaction on 0.05% Rh/Al_2O_3. CO = 8400 ppm, O_2 = 9200 ppm, H_2O = 6%, diluted in N_2. Prior to the reaction, the catalyst was reduced with 5% H_2 for 30 min.

The stability of the species adsorbed on the catalyst surface was verified during the He purge, in the presence of water, at 300°C (Figure 4.11). All the species, including CO on Rh nanoparticles, both linear and bridged, as well as CO on Rh single atoms, completely desorb from the catalyst surface, with CO on Rh nanoparticles desorbing faster, consistent with previous reports.[52] During the desorption process, we observe a blue shift in gem-dicarbonyl species features, suggesting again that the gem-dicarbonyl species at lower stretching frequencies are less stable in the presence of water. During the purge, at 300°C the feature centered at 2178 cm^{-1} is not present, suggesting that at 300°C this species might not be stable.

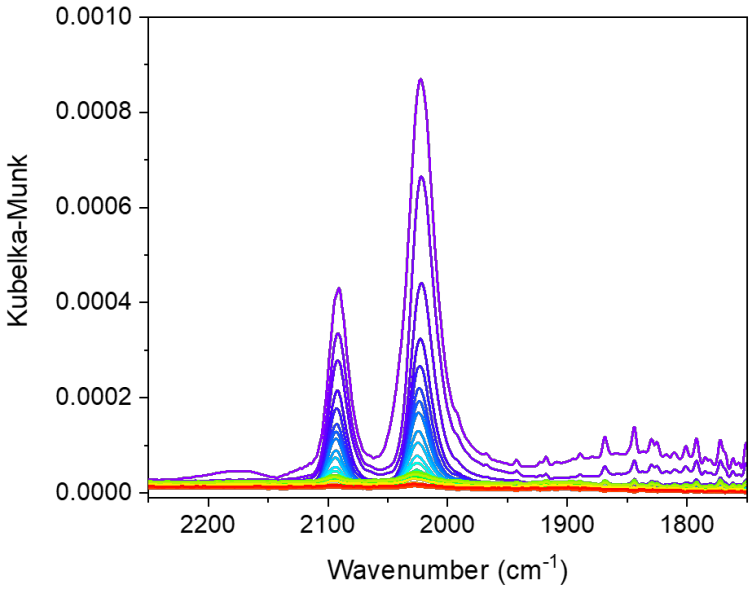

Figure 4.11: He purge in the presence of water after CO + H_2O adsorption at 300°C.

4.3.5 CO + O_2 + H_2O adsorption

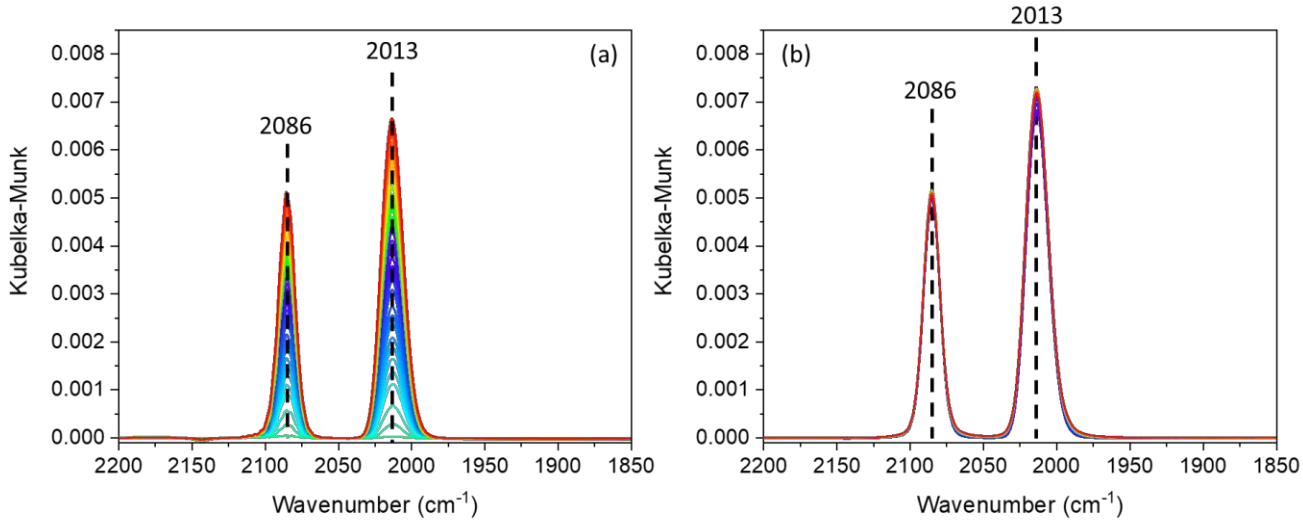

Figure 4.12: CO + O_2 + H_2O adsorption 200°C on 0.05% Rh/Al_2O_3. The catalyst was initially treated in 1% O_2 at 500°C for 30 min, then purged with Ar and finally reduced with 5% H_2 for 30 min. The temperature was decreased in He to 200°C and H_2O was introduced. After saturating the

catalyst with water, a background was taken, and 8400 ppm CO and 9200 ppm O_2 were added into the gas stream. (a) Spectra shown were taken during CO + O_2 + H_2O adsorption from time = 2 min (purple) to time = 204 min (red), when saturation was reached; (b) spectra taken during the purge with He and water from time 0 min (purple) to time = 20 min (red)

The spectra in Figure 4.12 (a) show the adsorption of CO, O_2 and H_2O, conditions similar to those employed during wet CO oxidation kinetics. The only two features present are the gem-dicarbonyl species and no CO absorbed on nanoparticles is detected. In the presence of O_2, the two gem-dicarbonyl peaks exhibit positions located at lower stretching frequencies, suggesting the presence of a coordination environment populated by OH groups. No shifts in position are observed, suggesting that the coordination environment remains consistent and uniform, as also hinted by the narrow full half max width (FHMW).

These gem-dicarbonyl species are more stable when CO is co-adsorbed with O_2 and H_2O, as shown in Figure 4.12 (b), where $Rh(CO)_2$ features do not decompose. This behavior is in sharp contrast to the case where only CO and H_2O are present, as shown in Figure 4.7, where the species all decomposed. In addition, in Figure 4.12 (b), no change in frequency is observed. This suggests that O_2 helps stabilize $Rh(CO)_2$, located at lower wavenumbers.

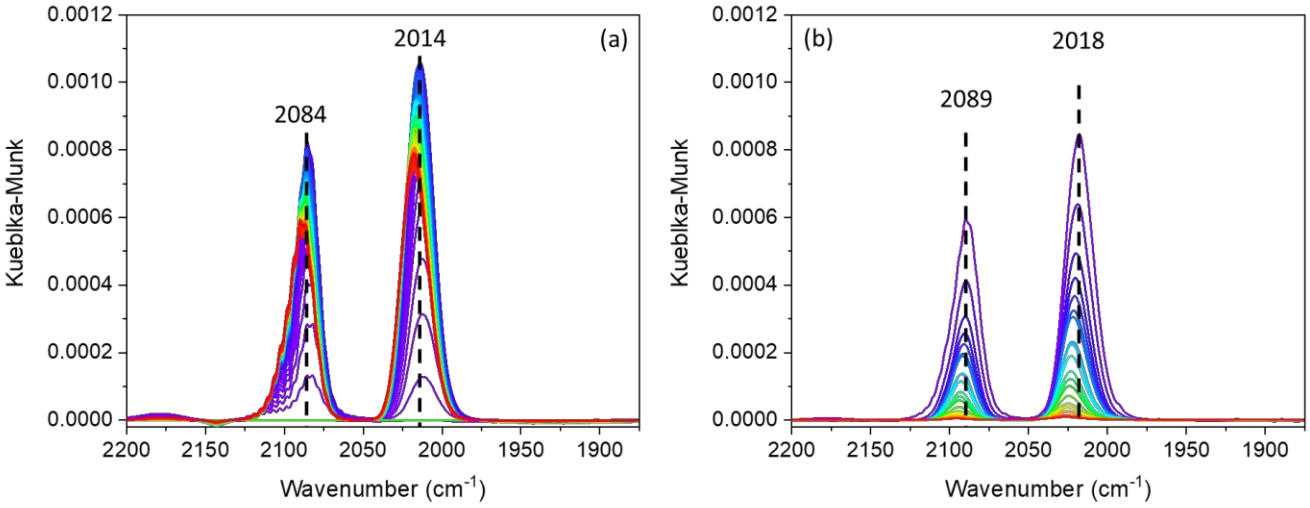

Figure 4.13: CO + O_2 + H_2O adsorption 300°C on 0.05% Rh/Al_2O_3. The catalyst was initially treated in 1% O_2 at 500°C for 30 min, then purged with Ar and finally reduced with 5%H_2 for 30 min. The temperature decreased in He to 300°C and H_2O was introduced. After saturating the catalyst with water, a background was taken, and 8400 ppm CO and 9200 ppm O_2 were added into the gas stream. (a) Spectra shown taken during CO + O_2 + H_2O adsorption from time = 2 min (purple) to time = 144 min (red), when saturation was reached; (b) spectra taken during the purge with He and water from time 0 min (purple) to time = 106 min (red)

The spectra obtained at 300°C in Figure 4.13 (a) show, once again, the presence of exclusively gem-dicarbonyl species, resembling the experiments without water. The absence of discernible nanoparticle features is consistent with the process of nanoparticles disintegration accelerated by the presence of oxygen. In the presence of O_2, water does not have a significant influence in mobilizing Rh single atoms and promoting their aggregation, consistent with the kinetics observation in Chapter 3. In fact, we observed that during CO oxidation and in the presence of excess oxygen, H_2O does not modify the oxidative process induced by CO. The temperature at which the rates change, associated with the Rh nanoparticle and single atom interconversion, has similar values under dry and wet conditions.

However, in Figure 4.13 (a) we observe that, as time progresses, during CO + O_2 + H_2O adsorption the features at 2084 and 2014 cm^{-1} initially increase in intensity, but then decrease, while shifting their position to higher frequencies. This dynamic suggests that at 300℃ there is a competitive interaction between the stabilizing effect of Rh gem-dicarbonyls induced by O_2 and the mobilizing effect of H_2O.

4.3.6 Reversibility of Rh nanoparticle disintegration

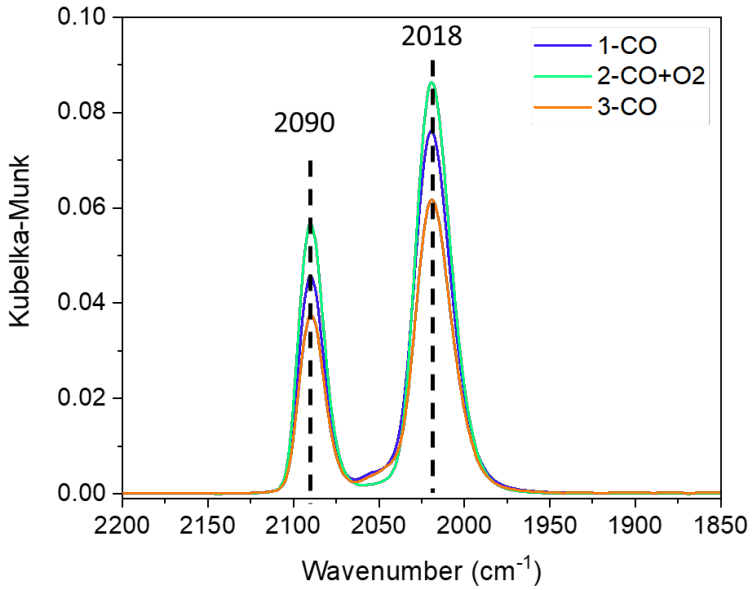

Figure 4.14: CO, CO+O_2 and CO adsorption on 0,1%Rh/Al_2O_3 at 300°C. The catalyst was initially treated in 1% O_2 at 500°C for 30 min, then purged with Ar and finally reduced with 5% H_2 for 30 min. The temperature was decreased in He to 300°C.

To assess the reversibility of the enhancement of O_2 on CO-assisted nanoparticle disintegration, we exposed the catalyst to (i) CO only, (ii) CO + O_2, and (iii) CO only, sequentially. We chose to perform the analysis at 300°C, because, as shown in Figure 4.3, at this temperature we could observe the nanoparticle feature. This experiment was performed with the 0.1% Rh/Al_2O_3 sample.

Even though it was a different catalyst, H_2 chemisorption still showed a high dispersion value and CO DRIFTS at 35°C exhibited only gem-dicarbonyl species, suggesting that 0.1 and 0.05% Rh/Al_2O_3 catalysts are both characterized by high dispersion and small particle size, and therefore present similarities.

Similarly to CO adsorption at 300°C on 0.05% Rh/Al_2O_3, after exposing 0.1% Rh/Al_2O_3 to CO (Figure 4.14), we observe the presence of the symmetric and asymmetric gem-dicarbonyl species at 2090 and 2018 cm^{-1}, respectively, as well as a feature with small intensity at 2050 cm^{-1}, assigned to Rh_{NP}-CO. In the second step, with the addition of 9200 ppm O_2, the gem-dicarbonyl intensity increased, while the RhNP-CO peak disappeared, consistent with the enhanced CO-assisted disintegration process. When O_2 was removed from the feed composition, the two features assigned to CO on single atoms decreased in intensity, while the CO linearly adsorbed on Rh nanoparticle peak increases. All the features do not shift their peak position, suggesting that the coordination environment remained unchanged. This suggests that the O_2 enhanced CO-assisted nanoparticle disintegration is a reversible process, consistent with our kinetic data where we showed that the data could be collected from high to low temperature or from low to high temperature, without changing the Rh nanoparticle-single atoms disintegration process.

4.4 Conclusions

Structural changes induced by adsorbates can vary the activity and the selectivity of a catalyst. In the context of a three-way catalyst, O_2 and water are critical components of a reaction mixture, it is important to understand their effect on the catalyst structure and gain insights on how the active site(s) evolves with time and feed composition.

Here we investigated the impact of H_2O and O_2 at different temperatures. We observed that at low temperature, 200°C, regardless of the feed composition, Rh nanoparticles break apart into single

atoms during CO exposure. However, the stability of the resulting gem-dicarbonyl species is influenced by the presence of H_2O and/or O_2. When CO and H_2O are both present in the feed, the gem-dicarbonyl species almost completely decompose/desorb. However, when O_2 is added, during the adsorption process, these two features remain stable at 200°C. This indicates that the gem-dicarbonyl species mobility varies according to their coordination environment and the presence of OH groups may enhance their mobility.

At higher temperature, at 300°C, the mobility is enhanced in the presence of water, leading to single atoms aggregating into nanoparticles. For any feed composition however, under wet or dry conditions, O_2 always causes the formation of gem-dicarbonyl species, suggesting an enhancement of CO-induced particle disintegration for both dry and wet environments.

The reversibility of CO-induced particle dispersion was confirmed by introducing and then removing O_2 in the feed composition, which included CO. The presence of O_2 enhanced the particle disintegration process. However, when O_2 was removed from the feed composition, and the catalyst was exposed to CO alone, the catalyst returns to its initial state.

The investigation of the effects of H_2O and O_2 on the interconversion of Rh nanoparticle and single atoms can provide insights into the single atoms mobility. This knowledge can help in the engineering of the local coordination environment around the metal, leading to improved catalyst design and performance.

4.5 References

(1) Bergmann, A.; Roldan Cuenya, B. Operando Insights into Nanoparticle Transformations during Catalysis. *ACS Catal* **2019**, *9* (11), 10020–10043. https://doi.org/10.1021/acscatal.9b01831.

(2) Vogt, C.; Meirer, F.; Monai, M.; Groeneveld, E.; Ferri, D.; van Santen, R. A.; Nachtegaal, M.; Unocic, R. R.; Frenkel, A. I.; Weckhuysen, B. M. Dynamic Restructuring of Supported Metal Nanoparticles and Its Implications for Structure Insensitive Catalysis. *Nat Commun* **2021**, *12* (1). https://doi.org/10.1038/S41467-021-27474-3.

(3) Vendelbo, S. B.; Elkjær, C. F.; Falsig, H.; Puspitasari, I.; Dona, P.; Mele, L.; Morana, B.; Nelissen, B. J.; Van Rijn, R.; Creemer, J. F.; Kooyman, P. J.; Helveg, S. Visualization of Oscillatory Behaviour of Pt Nanoparticles Catalysing CO Oxidation. *Nat Mater* **2014**, *13* (9), 884–890. https://doi.org/10.1038/nmat4033.

(4) Newton, M. A. Dynamic Adsorbate/Reaction Induced Structural Change of Supported Metal Nanoparticles: Heterogeneous Catalysis and Beyond. *Chem Soc Rev* **2008**, *37* (12), 2644–2657. https://doi.org/10.1039/b707746g.

(5) Avanesian, T.; Dai, S.; Kale, M. J.; Graham, G. W.; Pan, X.; Christopher, P. Quantitative and Atomic-Scale View of CO-Induced Pt Nanoparticle Surface Reconstruction at Saturation Coverage via DFT Calculations Coupled with in Situ TEM and IR. *J Am Chem Soc* **2017**, *139* (12), 4551–4558. https://doi.org/10.1021/jacs.7b01081.

(6) Matsubu, J. C.; Yang, V. N.; Christopher, P. Isolated Metal Active Site Concentration and Stability Control Catalytic CO2 Reduction Selectivity. *J Am Chem Soc* **2015**, *137* (8), 3076–3084. https://doi.org/10.1021/ja5128133.

(7) Marino, S.; Wei, L.; Cortes-reyes, M.; Cheng, Y.; Laing, P.; Cavataio, G. Rhodium Catalyst Structural Changes during , and Their Impacts on the Kinetics of , CO Oxidation. 1–17.

(8) Bazin, D. *Solid State Concepts to Understand Catalysis Using Nanoscale Metallic Particles*; 2002; Vol. 18.

(9) Ouyang, R.; Liu, J. X.; Li, W. X. Atomistic Theory of Ostwald Ripening and Disintegration of Supported Metal Particles under Reaction Conditions. *J Am Chem Soc* **2013**, *135* (5), 1760–1771. https://doi.org/10.1021/ja3087054.

(10) Goldsmith, B. R.; Sanderson, E. D.; Ouyang, R.; Li, W. X. CO- and NO-Induced Disintegration and Redispersion of Three-Way Catalysts Rhodium, Palladium, and Platinum: An Ab Initio Thermodynamics Study. *Journal of Physical Chemistry C* **2014**, *118* (18), 9588–9597. https://doi.org/10.1021/jp502201f.

(11) Siem, E. J.; Carter, W. C.; Chatain, D. The Equilibrium Shape of Anisotropic Interfacial Particles. *Philosophical Magazine* **2004**, *84* (10), 991–1010. https://doi.org/10.1080/14786430310001639897.

(12) Yates, J. T.; Kolasinski, K. Infrared Spectroscopic Investigation of the Rhodium Gem-Dicarbonyl Surface Species. *J Chem Phys* **1983**, *79* (2), 1026–1030. https://doi.org/10.1063/1.445844.

(13) Panayotov, P. B.; Yates, J. T. Rhodium-Carbon Monoxide Surface Chemistry: The Involvement of Surface Hydroxyl Groups on A12O3 and SiO2Supports. *J Am Chem Soc* **1988**, *110* (7), 2074–2081. https://doi.org/10.1021/ja00215a010.

(14) Cavanagh, R. R.; Yates, J. T. Site Distribution Studies of Rh Supported on Al2O3 - An Infrared Study of Chemisorbed CO. *J Chem Phys* **1981**, *74* (7), 4150–4155. https://doi.org/10.1063/1.441544.

(15) Yates, J. T.; Duncan, T. M.; Vaughan, R. W. Infrared Spectroscopic Study of Activated Surface Processes: CO Chemisorption on Supported Rh. *Journal of Chemical Physics* **1979**, *71* (10), 3908–3915. https://doi.org/10.1063/1.438159.

(16) Yates, J. T.; Duncan, T. M.; Worley, S. D.; Vaughan, R. W. Infrared Spectra of Chemisorbed CO on Rh. *J Chem Phys* **1979**, *70* (3), 1219–1224. https://doi.org/10.1063/1.437603.

(17) Jiang, N. Electron Beam Damage in Oxides: A Review. *Reports on Progress in Physics*. Institute of Physics Publishing December 18, 2015. https://doi.org/10.1088/0034-4885/79/1/016501.

(18) Su, D. Advanced Electron Microscopy Characterization of Nanomaterials for Catalysis. *Green Energy and Environment*. KeAi Publishing Communications Ltd. April 1, 2017, pp 70–83. https://doi.org/10.1016/j.gee.2017.02.001.

(19) Finzel, J.; Gutierrez, K. M. S.; Hoffman, A. S.; Resasco, J.; Christopher, P.; Bare, S. R. Limits of Detection for EXAFS Characterization of Heterogeneous Single-Atom Catalysts. **2023**. https://doi.org/10.1021/acscatal.3c01116.

(20) Rehr, J. J.; Albers, R. C. *Theoretical Approaches to X-Ray Absorption Fine Structure*.

(21) Albrahim, M.; Thompson, C.; Leshchev, D.; Shrotri, A.; Unocic, R. R.; Hong, J.; Hoffman, A. S.; Meloni, M. J.; Runnebaum, R. C.; Bare, S. R.; Stavitski, E.; Karim, A. M. Reduction and Agglomeration of Supported Metal Clusters Induced by High-Flux X-Ray Absorption Spectroscopy Measurements. *Journal of Physical Chemistry C* **2021**, *125* (20), 11048–11057. https://doi.org/10.1021/acs.jpcc.1c01823.

(22) Alexander J. Hoffman, Chithra Asokan, Nicholas Gadinas, Pavlo Kravchenko, Andrew “Bean” Getsoian, Phillip Christopher, and D. H. Experimental and Theoretical Characterization of Rh Single Atoms Supported on Γ-Al2O3 with Varying Hydroxyl Contents during NO Reduction by CO. **2022**, *12*, 11697–11715. https://doi.org/10.1021/acscatal.2c02813.

(23) Paolucci, C.; Khurana, I.; Parekh, A. A.; Li, S.; Shih, A. J.; Li, H.; Di Iorio, J. R.; Albarracin-Caballero, J. D.; Yezerets, A.; Miller, J. T.; Delgass, W. N.; Ribeiro, F. H.; Schneider, W. F.; Gounder, R. Dynamic Multinuclear Sites Formed by Mobilized Copper Ions in NOx Selective Catalytic Reduction. *Science (1979)* **2017**, *357* (6354), 898–903. https://doi.org/10.1126/SCIENCE.AAN5630/SUPPL_FILE/AAN5630_PAOLUCCI_SM.PDF.

(24) Deplano, G.; Signorile, M.; Crocellà, V.; Porcaro, N. G.; Atzori, C.; Solemsli, B. G.; Svelle, S.; Bordiga, S. Titration of Cu(I) Sites in Cu-ZSM-5 by Volumetric CO Adsorption. *ACS Appl Mater Interfaces* **2022**. https://doi.org/10.1021/acsami.2c03370.

(25) Mandal, K.; Gu, Y.; Westendorff, K. S.; Li, S.; Pihl, J. A.; Grabow, L. C.; Epling, W. S.; Paolucci, C. Condition-Dependent Pd Speciation and NO Adsorption in Pd/Zeolites. *ACS Catal* **2020**. https://doi.org/10.1021/acscatal.0c03585.

(26) Felvey, N.; Guo, J.; Rana, R.; Xu, L.; Bare, S. R.; Gates, B. C.; Katz, A.; Kulkarni, A. R.; Runnebaum, R. C.; Kronawitter, C. X. Interconversion of Atomically Dispersed Platinum Cations and Platinum Clusters in Zeolite ZSM-5 and Formation of Platinum Gem-Dicarbonyls. *J Am Chem Soc* **2022**, *2022* (20), 34. https://doi.org/10.1021/JACS.2C05386.

(27) Dessal, C.; Len, T.; Morfin, F.; Rousset, J. L.; Aouine, M.; Afanasiev, P.; Piccolo, L. Dynamics of Single Pt Atoms on Alumina during CO Oxidation Monitored by Operando X-Ray and Infrared Spectroscopies. *ACS Catal* **2019**, *9* (6), 5752–5759. https://doi.org/10.1021/acscatal.9b00903.

(28) Kale, M. J.; Christopher, P. Utilizing Quantitative in Situ FTIR Spectroscopy to Identify Well-Coordinated Pt Atoms as the Active Site for CO Oxidation on Al2O3-Supported Pt Catalysts. *ACS Catal* **2016**, *6* (8), 5599–5609. https://doi.org/10.1021/acscatal.6b01128.

(29) Groppo, E.; Rojas-Buzo, S.; Bordiga, S. The Role of In Situ Operando IR Spectroscopy in Unraveling Adsorbate-Induced Structural Changes in Heterogeneous Catalysis. *Chem Rev* **2023**. https://doi.org/10.1021/acs.chemrev.3c00372.

(30) Asokan, C.; DeRita, L.; Christopher, P. Using Probe Molecule FTIR Spectroscopy to Identify and Characterize Pt-Group Metal Based Single Atom Catalysts. *Cuihua Xuebao/Chinese Journal of Catalysis* **2017**, *38* (9), 1473–1480. https://doi.org/10.1016/S1872-2067(17)62882-1.

(31) Farrauto, R. J.; Deeba, M.; Alerasool, S. Gasoline Automobile Catalysis and Its Historical Journey to Cleaner Air. *Nature Catalysis*. Nature Publishing Group July 1, 2019, pp 603–613. https://doi.org/10.1038/s41929-019-0312-9.

(32) Kip, B. J.; Duivenvoorden, F. B. M.; Koningsberger, D. C.; Prins, R. Determination of Metal Particle Size of Highly Dispersed Rh, Ir, and Pt Catalysts by Hydrogen Chemisorption and EXAFS. *J Catal* **1987**, *105* (1), 26–38. https://doi.org/10.1016/0021-9517(87)90005-4.

(33) Berkó, A.; Solymosi, F. Adsorption-Induced Structural Changes of Rh Supported by TiO2(110)-(1×2): An STM Study. *J Catal* **1999**, *183* (1), 91–101. https://doi.org/10.1006/JCAT.1998.2368.

(34) Solymosit, F.; Knozinger, H. Infrared Study on the Interaction of CO with Alumina-Supported Rhodium. **1990**, *86* (2), 389–395.

(35) Solymosi, F.; Pásztor, M. Infrared Study of the Effect of H2 on CO-Induced Structural Changes in Supported Rh. *Journal of Physical Chemistry* **1986**, *90* (21), 5312–5317. https://doi.org/10.1021/j100412a081.

(36) Solymosi, F.; Pásztor, M. An Infrared Study of the Influence of CO Chemisorption on the Topology of Supported Rhodium. *Journal of Physical Chemistry* **1985**, *89* (22), 4789–4793. https://doi.org/10.1021/j100268a026.

(37) Solymosi, F.; Knözinger, H. Infrared Study on the Interaction of CO with Alumina-Supported Rhodium. *Journal of the Chemical Society, Faraday Transactions* **1990**, *86* (2), 389–395. https://doi.org/10.1039/FT9908600389.

(38) Solymosi, F.; Erdöhelyi, A.; Kocsis, M. Surface Interaction between H2 and CO2 on Rh/Al2O3, Studied by Adsorption and Infrared Spectroscopic Measurements. *J Catal* **1980**, *65*, 428–436. https://doi.org/10.1016/0021-9517(80)90319-X.

(39) Marino, S.; Wei, L.; Cortes-Reyes, M.; Cheng, Y.; Laing, P.; Cavataio, G.; Paolucci, C.; Epling, W. Rhodium Catalyst Structural Changes during, and Their Impacts on the Kinetics of, CO Oxidation. *JACS Au* **2023**, *3* (2), 459–467. https://doi.org/10.1021/jacsau.2c00595.

(40) Frank, M.; Baumer, M. From Atoms to Crystallites: Adsorption on Oxide-Supported Metal Particles. *Physical Chemistry Chemical Physics* **2000**, *2* (17), 3723–3737. https://doi.org/10.1039/b004091f.

(41) Cervantes Uribe, A.; Del Angel Montes, G. A.; Torres-Torres, G.; Vázquez-Zavala, A.; González-García, F.; Cordero-García, A.; Ojeda-López, R. Correlation of Rh Particle Size with CO Chemisorption: Effect on the Catalytic Oxidation of MTBE. *Journal of Composites Science* **2019**, *3* (3), 81. https://doi.org/10.3390/jcs3030081.

(42) Asokan, C.; Derita, L.; Christopher, P. *Using Probe Molecule FTIR Spectroscopy to Identify and Characterize Pt-Group Metal Based Single Atom Catalysts*; 2017; Vol. 38. www.cjcatal.org.

(43) Suzuki, A.; Inada, Y.; Yamaguchi, A.; Chihara, T.; Yuasa, M.; Nomura, M.; Iwasawa, Y.; Iwasawa, Y.; Suzuki, A.; Inada, Y.; Yamaguchi, A.; Yuasa, M. Time Scale and Elementary Steps of CO-Induced Disintegration of Surface Rhodium Clusters. *Angewandte Chemie* **2003**, *115* (39), 4943–4947. https://doi.org/10.1002/ANGE.200352318.

(44) Cavers, M.; Davidson, J. M.; Harkness, I. R.; Rees, L. V. C.; McDougall, G. S. Spectroscopic Identification of the Active Site for CO Oxidation on Rh/Al2O3 by Concentration Modulation in Situ DRIFTS. *J Catal* **1999**, *188* (2), 426–430. https://doi.org/10.1006/jcat.1999.2672.

(45) Worley, S. D.; Rice, C. A.; Mattson, G. A.; Curtis, C. W.; Guin, J. A.; Tarrer, A. R. The Effect of Rhodium Precursor on Rh/Al2O3 Catalysts. *J Chem Phys* **1982**, *76* (1), 20–25. https://doi.org/10.1063/1.442760.

(46) Solymosi, F.; Sárkány, J. An Infrared Study of the Surface Interaction between NO and CO on Rh/Al2O3 Catalyst. *Applications of Surface Science* **1979**, *3* (1), 68–82. https://doi.org/10.1016/0378-5963(79)90061-8.

(47) Duncan, T. M.; Yates, J. T.; Vaughan, R. W. A 13C NMR Study of the Adsorbed States of CO on Rh Dispersed on Al203. *J Chem Phys* **1980**, *73* (2), 975–985. https://doi.org/10.1063/1.440746.

(48) Hoffman, A. S.; Fang, C. Y.; Gates, B. C. Homogeneity of Surface Sites in Supported Single-Site Metal Catalysts: Assessment with Band Widths of Metal Carbonyl Infrared Spectra. *Journal of Physical Chemistry Letters* **2016**, *7* (19), 3854–3860. https://doi.org/10.1021/acs.jpclett.6b01825.

(49) Busca, G.; Lorenzelli, V. INFRARED SPECTROSCOPIC IDENTIFICATION OF SPECIES ARISING FROM REACTIVE ADSORPTION OF CARBON OXIDES ON METAL OXIDE SURFACES G BUSCA, V LORENZELLI. *Materials Chemistry* **1982**, *7*, 89–126. https://doi.org/10.1016/0390-6035(82)90059-1.

(50) *Infrared Spectroscopy at High Pressure: Interaction of CO with Oxidized Rh/Al203*; 1992.

(51) Han, J.; Yang, J.; Zhang, Z.; Jiang, X.; Liu, W.; Qiao, B.; Mu, J.; Wang, F. Strong Metal–Support Interaction Facilitated Multicomponent Alloy Formation on Metal Oxide Support. *J Am Chem Soc* **2023**, *145* (41), 22671–22684. https://doi.org/10.1021/jacs.3c07915.

(52) Asokan, C.; Thang, H. V.; Pacchioni, G.; Christopher, P. Supporting Information Reductant Composition Influences the Coordination of Atomically Dispersed Rh on Anatase TiO 2. **2020**, *2* (101), 1–21.

Chapter 5: NO reduction by CO: H_2O and NH_3 effects on the kinetics

5.1 Introduction

NO reduction by CO is one of the three key reactions occurring on the three-way catalyst. Rh catalysts have been recognized for being more active in reducing NO compared to Pt or Pd because of their ability to dissociate NO and selectively reduce it to N_2.[1–4] Under real-world conditions, where water is present in the feed composition, the products resulting from NO reduction by CO include: N_2, N_2O and NH_3. NH_3 and N_2O are undesired by-products and could cause damage to the environment and human health. NH_3 contributes to ecosystem eutrophication and enhances particulate matter formation,[5–7] while N_2O is a powerful greenhouse gas.[8] A decrease in N_2O and NH_3 formation, which increases N_2 selectivity, requires a detailed understanding of the reaction mechanism.

However, a well-understood NO reduction by CO reaction mechanism is still lacking, even under simplified conditions like in the absence of water. These challenges are attributed to the intrinsic structure sensitivity of the reaction. In fact, the NO + CO activity obtained on single crystals is not consistent with results obtained on supported catalysts. Single crystals exhibit lower activation energies, higher rates and lower selectivity.[9–13] Several factors have been identified as responsible for these differences, including facets and sites present, temperature, feed composition (specifically NO/CO ratio) adsorbate-adsorbate interactions, coverage, bonding configuration, reaction intermediates and the support contribution.[12–17] In addition, in the case of Rh catalysts, Rh speciation also plays a role in the reaction mechanism. In TWC formulations, where the Rh content in minimal, 0.1-0.5wt%, Rh is present in the form of single atoms, nanoclusters and large nanoparticles. Each of these forms has its own activity and selectivity. For example, it has been shown that NO dissociation and high N_2 selectivity is favored on large nanoparticles on supported Rh

catalysts.[18] In addition, when considering the selectivity of NO reduction by CO in the presence of H_2O, previous studies indicate that Rh single atoms, Rh_{SA}, selectively convert NO into NH_3, when the feed composition is CO-rich, while Rh nanoparticles, Rh_{NP}, preferentially form N_2 and N_2O.[19]

The common approach to investigate the NO reduction by CO reaction mechanism involves a combination of kinetic and spectroscopic studies. Here, we present our preliminary study exploring the effect of water on the NO reduction by CO kinetics under different conditions experienced by a TWC: stoichiometric, reducing and oxidizing. We further studied the effect of NH_3 on the reaction rates. We then integrated the kinetic investigations with the analysis of the adsorbates present on the catalyst surface and their mobility.

5.2 Material and Methods

5.2.1 Catalysts

0.05wt% and 0.1wt% Rh/Al_2O_3 catalysts were synthesized via wetness impregnation. $Rh_3(NO)_3$ precursor purchased from Sigma Aldrich was added dropwise on gamma alumina purchased from Sigma Aldrich. The catalysts were dried in a Lindberg muffle furnace at 120°C for 4 h. Afterwards, the temperature was increased to 550°C at 1°C/min and held at the temperature for 4 h. To increase the particle size of the 0.1% Rh/Al_2O_3 catalyst, it was treated in 5% H_2 for 72 h at 900°C. This catalyst is described below as 0.1% Rh/Al_2O_3-900°C.

5.2.2 Dispersion measurements

H_2 chemisorption was used to obtain Rh dispersion. The catalysts were reduced in H_2 for 1 h at 500°C. The system was evacuated at 500°C for 2 hours. The temperature was decreased to 35°C and another evacuation was performed. The H_2 chemisorption isotherms were collected at 35°C.

The dispersion was calculated by considering the intercept derived from the linear part the total adsorption isotherm. Rh particle size was obtained as 100/D[%], assuming an octahedral shape.

5.2.3 Kinetic experiments

NO + CO kinetic experiments were performed in a fixed bed flow reactor. The catalyst was placed in a 4 mm quartz tube and positioned in a Thermo Scientific Lindberg Blue M furnace. The temperature was monitored using K-type thermocouples, purchased from Omega, at the inlet and the outlet of the catalyst. The amount of catalyst used was between 5 and 13 mg and was diluted with SiO_2 to obtain at a mass of 250 mg. To avoid internal mass transfer limitations the catalyst was pelletized and sieved using 80-170 mesh size. The total flowrate was 500 sccm. Before the reaction, the catalyst was reduced in 5% H_2, diluted in N_2 at 500°C for 30 minutes. The reaction mixture included 1000 ppm CO and NO was varied to obtain a NO/CO ratio of 0.5, 1 and 2. The reaction mixture was diluted in N_2. The experiments performed to evaluate the effect of NH_3 on the reaction included the addition of 100 ppm NH_3 to the feed composition. Wet experiments were performed by including 6% water, introduced using a Bronkhorst controlled evaporator mixer (CEM). CO, NO, NH_3, N_2O, CO_2 and H_2O were detected using a MKS MG2030 FT-IR analyzer. N_2 concentrations were calculated through a N balance. CO and NO, as well as the product reaction rates, were measured under steady-state conditions. The activation energies were caulcated by considering the slope derived from the Arrhenius plot.

5.2.4 DRIFTS experiments

DRIFTS experiments were performed to characterize the catalysts and analyze the surface species under reaction conditions. The catalysts were placed in a custom-made Harrick scientific reaction chamber designed to perform in-situ gas phase subtraction and minimize the dead volume.

Prior to each experiment the catalysts were pretreated in 1% O_2 at 500°C for 30 min, followed by an Ar purge for 10 min and finally 5% H_2 at 500°C for 30 min.

CO adsorption at 35°C was performed to characterize the catalysts. After the pretreatment, the catalysts were exposed to 5000 ppm CO, diluted in Ar.

In-situ NO + CO adsorption was performed on 0.1% Rh/Al_2O_3 at 265°C to analyze the surface species during the reaction. 5000 ppm CO and varying NO concentrations to reach NO/CO ratios of 0.5, 1 and 2 were used. Experiments including NH_3 were performed by introducing 500 ppm NH_3 into the reaction mixture. After the adsorption phase, the system was purged until no changes in the spectra were detected and a temperature programmed desorption was performed at 10°C/min until 500°C.

5.3 Results and Discussion

5.3.1 NO reduction by CO: preliminary data on 0.05% Rh/Al_2O_3

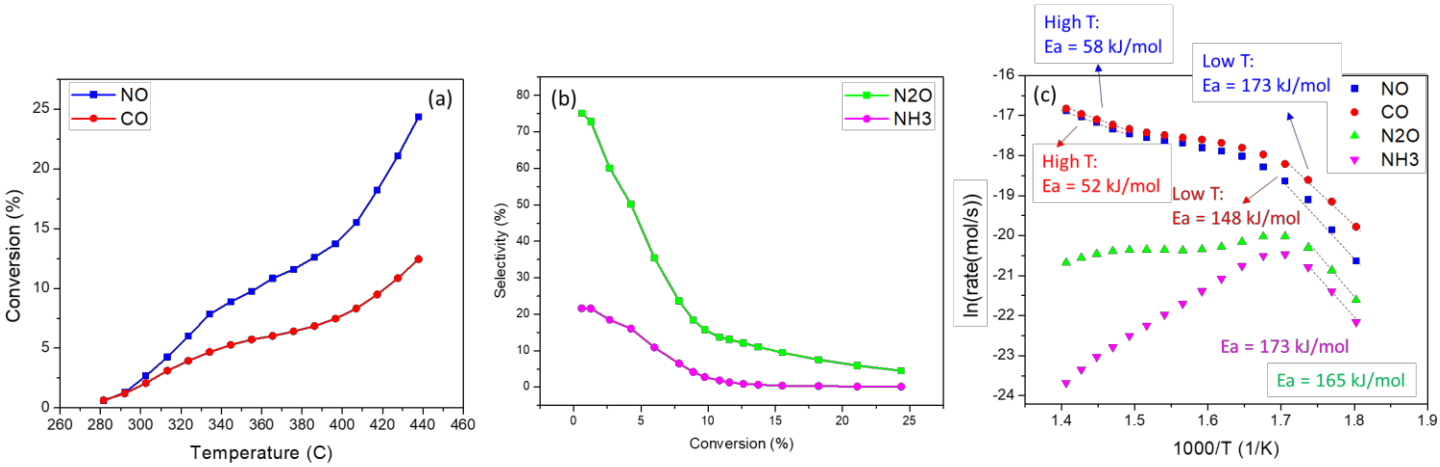

Figure 5.1: NO reduction by CO kinetics with a 0.05% Rh/Al_2O_3 catalyst. (a) NO (blue) and CO (red) conversion; (b) N_2O (green) and NH_3 (fuscia) selectivity; (c) Arrhenius plot of NO and CO consumption and N_2O and NH_3 formation rates. The catalyst was reduced in 5% H_2 for 30 min at 500°C. The reaction mixture included 1000 ppm CO, 500 ppm NO and 6% H_2O, diluted in N_2. The conversions shown were taken at steady-state.

Figure 5.1(a) and (b) show NO and CO conversions, N_2O and NH_3 selectivity, along with the corresponding Arrhenius plot obtained during NO reduction by CO, with NO/CO = 0.5, in the presence of 6% H_2O. The conversion profiles in Figure 5.1, obtained between 280 and 450°C, exhibit an unusual behavior, with an inflection point at around 330°C, which leads to a flattening of the conversion profile, followed by an increase in conversion at 400°C. The product distribution included N_2O, NH_3 and we assume N_2. NH_3 is an additional product present when water is included in the reaction mixture and the amount of NH_3 formed increases as the reaction mixture has an excess of reductant, CO.[20–22] The NH_3 formation rate has a positive order in CO concentration.[21] In our case, the NO/CO ratio is 0.5, therefore a higher NH_3 selectivity is expected. However, the majority of products formed are represented by N_2O, which exhibits a selectivity of around 75%. This is consistent with previous studies which reported that Rh catalysts mainly catalyze the formation of N_2O at low temperature and N_2 at higher temperature. As the temperature increases, as well as NO and CO conversion, the selectivity towards N_2O and NH_3 decreases to form the desired product, N_2. The Arrhenius plot in Figure 5.1 (c) follows the corresponding trend with the inflection point. Overall, three regimes are present: at low temperature, the NO activation energy is equal to 173 kJ/mol, in the mid temperature range the apparent activation energy decreases to a value close to zero and, finally, at high temperature it shows a higher activation energy with a value of 58 kJ/mol. The decrease in apparent activation energy in the mid temperature range is not correlated with the presence of internal and external mass transfer limitations. In fact, for these data points, the Weisz-Prater number is lower than one and the Mears criterion is satisfied. In addition, if mass transfer was limiting the reaction rate, the Arrhenius plot would not exhibit an increase in the values with a further increase in temperature. The reaction rates at higher temperature show an activation energy of 58 kJ/mol. Despite this value being higher than the one in mid temperature

range, these rates are limited by mass transfer, as the measure apparent activation energy is less than half of that one measured in the low temperature range. In addition, the Mears criterion is not satisfied and the Weisz-Prate number is higher than 1.

When evaluating the apparent activation energies calculated considering CO, N_2O and NH_3 reaction rates, we notice that in the low temperature regime, NH_3 and N_2O apparent activation energies are 173 and 165 kJ/mol respectively, similarly to what was measured for the NO rate. This suggests that NO, N_2O and NH_3 share the same rate limiting step. On the other hand, CO exhibits a lower apparent activation energy, indicating that the rate limiting step might differ and may involve either the reaction with water through the water gas shift reaction or the scavenging of adsorbed oxygen from the catalyst surface deriving from the dissociation of NO.

The focus of this work was to investigate the cause of the inflection point in the NO and CO conversion profiles and what leads to different apparent activation energies between CO and NO.

Several hypotheses have been proposed and they include:

- Structural changes occurring during the reaction involving the interconversion between single atoms and nanoparticles;
- Presence of multiple rate limiting steps in the reaction;
- Deactivation process occurring via formation of stable species on the active sites surface;
- Deactivating process via sintering of nanoparticles during the reaction.

These hypotheses have been studied with the 0.1% Rh/Al_2O_3 catalyst via the study of NO + CO kinetics, in the absence and presence of water, and in-situ DRIFTS.

5.3.2 NO reduction by CO in the absence of water

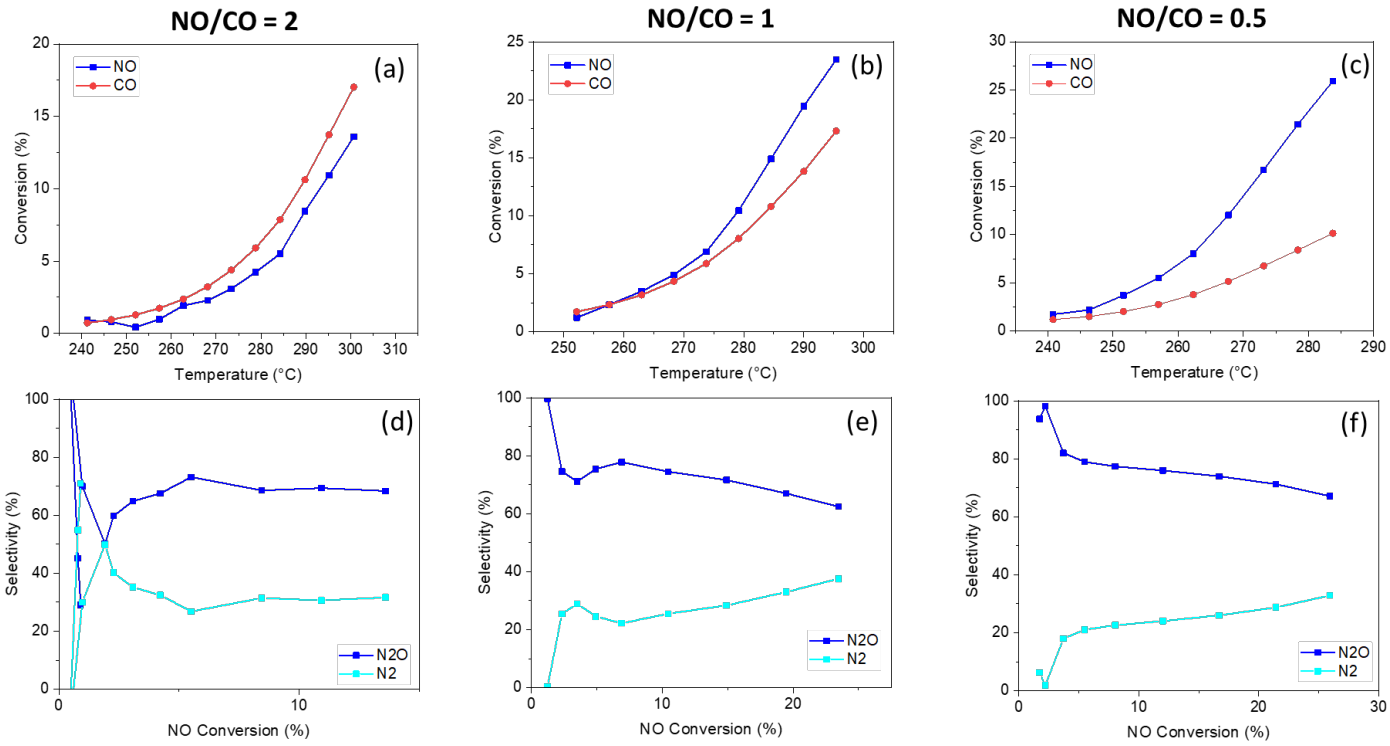

Figure 5.2: NO reduction by CO kinetics on 0.1% Rh/Al_2O_3. (a) NO (blue) and CO (red) conversions and (d) N_2O and N_2 selectivity for NO/CO = 2; (b) NO (blue) and CO (red) conversions and (e) N_2O and N_2 selectivity for NO/CO = 1; (c) NO (blue) and CO (red) conversions and (f) N_2O and N_2 selectivity for NO/CO = 0.5. The catalyst was reduced in 5% H_2 for 30 min at 500°C. The reaction mixture included 1000 ppm CO, NO varying to obtain NO/CO = 2, 1 and 0.5, diluted in N_2. The conversions were taken at steady-state.

NO reduction by CO kinetics in the absence of water was evaluated on a 0.1% Rh/Al_2O_3 catalyst and the conversions of reactants were obtained at steady-state. When the catalyst was exposed to the reaction mixture, deactivation was observed and it took several hours to reach a steady-state. A similar behavior was observed on Rh/Al_2O_3, Rh/SiO_2 and Pt/SiO_2.[23,24] On Pt/SiO_2 it was proposed that deactivation occurred due to an accumulation of NCO and CN species in the vicinity of Pt nanoparticles, leading to changes in the Pt electronic properties.[23]

This series of experiments serves as a control experiment to gain a better understanding of the impact of water on the reaction kinetics. Figure 5.2 shows the CO and NO conversion along with the selectivities towards N_2 and N_2O. The investigations involved varying the NO/CO ratio from 0.5 to 2 to simulate the different environments typically encountered in the three-way catalyst process, such as oxidizing, stoichiometric and reducing conditions. The product selectivity shown in Figure 5.2 for each NO/CO ratio investigated exhibited a constant selectivity towards N_2O at approximately 80%. Similar results were reported for NO reduction by CO on a Pd/Al_2O_3 catalyst.[25–29] It was shown that N_2O did not depend on the reactant concentration, the gas velocity or the catalyst temperature.[28,30] The remaining product formed is assumed to be N_2, derived from the material balance. These results are consistent with previous studies conducted on Rh/Al_2O_3 and Rh/SiO_2 catalysts showing that the major product of NO reduction at low temperature was N_2O. It was proposed that N_2O formation strongly depends on the NO coverage. Single crystal studies proposed that N_2O is formed via surface reaction between adsorbed N and molecularly adsorbed NO, which was not able to dissociate. It was indeed shown that on Rh(111), at low coverages (<0.25 ML) NO completely dissociated; at intermediate coverages (between 0.25 and 0.5 ML) only a portion of NO dissociated and at high coverages (> 0.5 ML) NO dissociation was hindered by the unavailability of free sites. As Rh sites become unavailable, NO dissociation is hindered, and N_2O formation is hindered. As temperature increases and more sites become available, N_2 selectivity increases.[31] Therefore, the rate and the selectivity primarily depend on the NO adsorption/desorption equilibrium.[32] In addition, the consistent selectivity across the different NO/CO ratio suggests that the catalyst surface remains relatively stable with varying feed composition and is populated by similar species to similar extents.

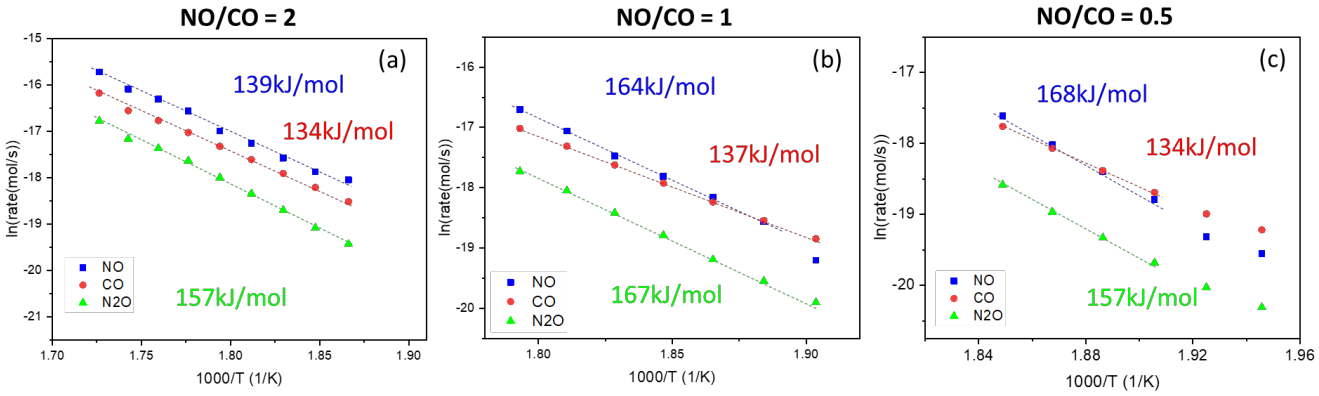

Figure 5.3: NO reduction by CO kinetics on 0.1% Rh/Al_2O_3. Arrhenius plots of NO, CO, N_2O rates. (a) NO/CO = 2; (b) NO/CO = 1; (c) NO/CO = 0.5. The catalyst was reduced in 5% H_2 for 30 min at 500°C. The reaction mixture included 1000 ppm CO, NO varying to obtain NO/CO = 2, 1 and 0.5, diluted in N_2.

Figure 5.3 shows the Arrhenius plots derived from the conversion profiles. The apparent activation energy derived from NO consumption had a value of 165 kJ/mol, similar to the value obtained from the N_2O formation. This similarity implies that NO consumption and N_2O formation share a common rate-limiting step, in the case of stoichiometric and reducing conditions. However, the apparent activation energy derived from CO consumption exhibits a lower value of 135 kJ/mol, across all NO/CO ratios, indicating a distinct reaction pathway for CO consumption. Under oxidizing conditions, NO/CO = 2, the apparent activation energy derived from NO consumption is similar to the one obtained from CO consumption. Differences among activation energies considering the same reaction were reported in literature in single crystal studies. Previous research on NO reduction by CO kinetics performed on Rh(111) and Rh(110) single crystals reported that the apparent activation energy measured from CO_2, N_2O and N_2 formation rates were different according to the crystal structure. CO_2 and N_2O apparent activation energy exhibited similar values on Rh(111), while CO_2 and N_2 $E_{a,app}$ showed similar values on Rh(110). This analysis was coupled with the product selectivity analysis, exhibiting a larger N_2O selectivity on Rh(111), compared to

Rh(110). These results highlight the structure sensitivity of NO reduction by CO. In fact, it was proposed that NO dissociation, which is a key factor influencing product selectivity, is more favorable on an open surface, such as Rh(110), compared to Rh(111). Therefore the selectivity towards N_2 is enhanced on Rh(110), whereas the reaction between NO and N is favored on Rh(111), due to challenges associated with NO dissociation.[33]

While the activation energy values we obtained are consistent with some of those reported in the literature,[13,18] we did not definitively identify a single rate-limiting step. Various rate limiting steps have been proposed: NO dissociation, N_2O formation, CO_2 formation and N recombination to form N_2. Given the complexity of the mechanism and of the structure, we refrain from assigning a specific rate limiting step. Furthermore, the difference observed in the apparent activation energy derived from NO and CO consumption, suggests that multiple reaction pathways may be at play. This is consistent with previous proposals indicating that N_2 and N_2O can form via different pathways[25] and that multiple active sites are likely present. [34,35]

5.3.3 NO reduction by CO in the presence of water

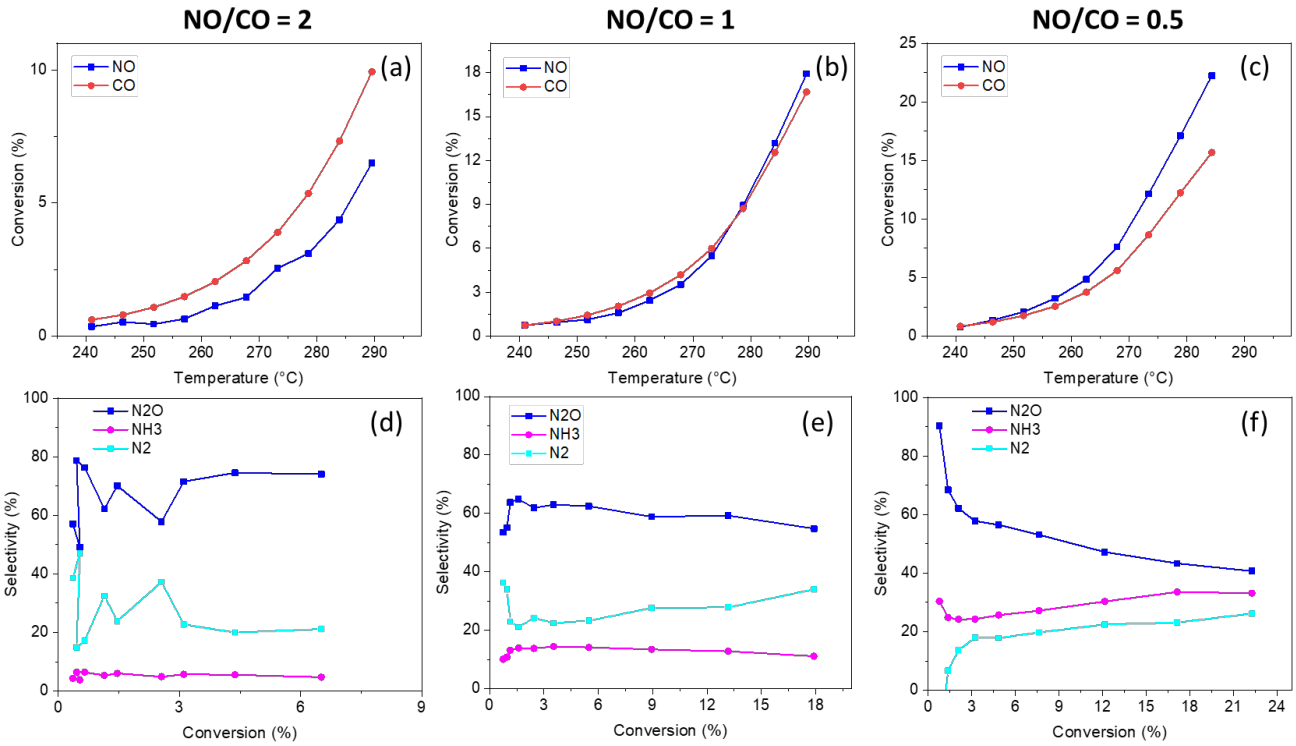

Figure 5.4: NO reduction by CO in the presence of 6% water over 0.1%Rh/Al_2O_3. NO and CO conversion and N_2, N_2O and NH_3 selectivity. The catalyst was reduced in 5% H_2 for 30 min at 500°C. The reaction mixture included CO = 1000 ppm, NO varying to obtain (a) and (d) NO/CO = 2*;* (b) and (e) 1 (b)*;* and (e) and (c) and (f) 0.5*;* and H_2O = 6%, diluted in N_2.

Figure 5.4 presents the conversion and the selectivity obtained on 0.1%Rh/Al_2O_3 during NO reduction by CO in the presence of 6% water and by exposing the catalysts to different NO/CO ratios. The conversions were obtained in the same temperature range as the reaction performed in the absence of water, indicating that the addition of water does not negatively impact the reaction rate. Analyzing the selectivity data, we observed the formation of N_2O, N_2 and NH_3. Notably, NH_3 is formed in the presence of water.

In contrast to the case without water where N_2O and N_2 selectivity remained the same regardless of the different NO/CO ratios, in the presence of water, we observe a trend. As the NO/CO ratio decreases, the selectivity towards NH_3 increases, while N_2O selectivity decreases. The trend of

increasing NH_3 formation with reducing conditions is consistent with previous reports [20–22] and, as previously mentioned, its formation follows a positive order dependency with respect to CO concentration, while N_2 and N_2O rates showed a negative correlation with CO concentration.[21] While it is not clear what the mechanism for NH_3 formation is, several mechanisms have been proposed. Some proposed the involvement of NCO on the support, which can be hydrolyzed by water to form NH_3.[21,36,37] In support of this hypothesis, IR spectra showed that NCO species on the support increased in intensity with decreasing NO/CO ratio and disappeared after exposing the catalyst to water, while forming NH_3.[21,36–38] A second hypothesis proposed the involvement of the water gas shit reaction (WGS).[39–41] It was shown that Rh single atoms catalyze the WGS reaction [42] and the H_2 produced can react with NO to form NH_3. During NO reduction by CO in the presence of water and under reducing conditions, it was observed that the selectivity towards NH_3 increased as the particle size decreased and the fraction of Rh single atoms relative to nanoparticle incresed.[19]

In our study, H_2 chemisorption revealed that the catalyst is highly dispersed, with 90% dispersion. However, our previous work and several literature studies demonstrated that Rh is mobile and can undergo structural changes under reaction conditions.[43–45] For example, at low temperature, CO adsorption leads to nanoparticle redispersion into single atoms, [46] but at higher temperature the agglomeration of single atoms into nanoparticles occurs.[47] In addition, the presence of NO can influence Rh speciation by favoring Rh nanoparticle disintegration.[48] These structural changes alter the number of active sites and might impact on the reactivity and selectivity. [42]

From the conversion profiles, we determined the apparent activation energies from the rates of NO and CO consumption, as well as N_2O and NH_3 formation.

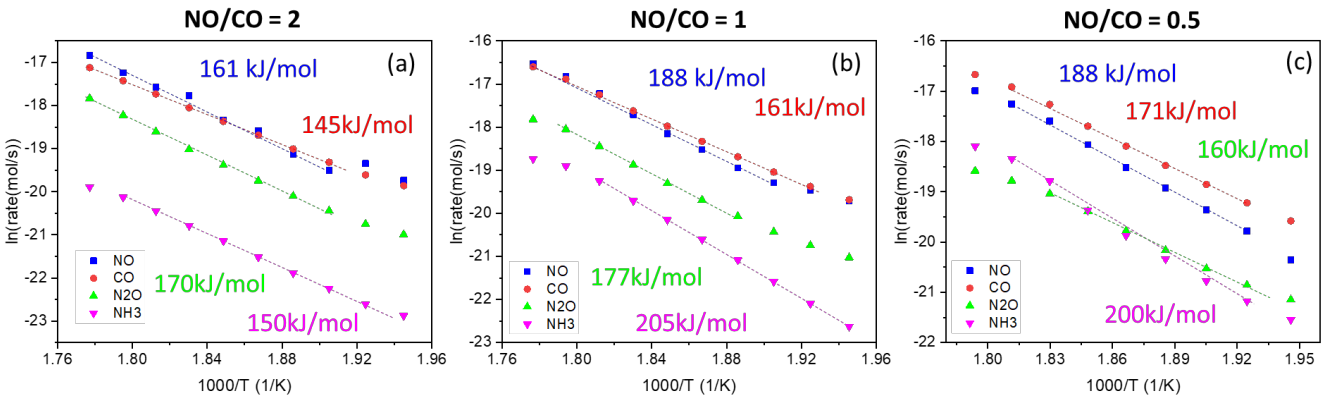

Figure 5.5: NO reduction by CO in the presence of water over 0.1%Rh/Al_2O_3. Arrhenius plots of NO, CO, N2O rates. (a) NO/CO = 2; (b) NO/CO = 1; (c) NO/CO = 0.5. The catalyst was reduced in 5% H_2 for 30 min at 500°C. The reaction mixture included 1000 ppm CO, NO varying to obtain NO/CO = 2, 1 and 0.5, H_2O = 6%, diluted in N_2

The activation energies obtained from the Arrhenius plots in Figure 5.5 exhibit different values according to the NO/CO ratio, unlike the case without water. The NO consumption activation energy increases with decreasing NO/CO ratio. While NO/CO = 2 shows similar apparent activation energy to the dry case, 160 kJ/mol, the apparent activation energy for NO/CO = 1 and 0.5 is higher, with values around 190 kJ/mol. Similarly, the apparent activation energies derived from CO consumption and NH_3 formation increase with decreasing NO/CO ratio. On the other hand, the activation energy derived from N_2O formation remains constant at 170 kJ/mol for all the ratios studied, similar to the activation energy obtained in the dry case. Based on these kinetic measurements, we concluded that H_2O affects the NO reduction by CO mechanism, except for the pathway that leads to the N_2O formation. To investigate the role of water in the NO + CO reaction mechanism, we proceeded with studying NO reduction by CO kinetics at varying concentrations.

5.3.4 The effect of water on NO reduction by CO kinetics

The effect of H_2O on the reaction kinetics was investigated by varying H_2O concentration from 1%, the minimum value that our instrument can flow, to 6%. It was expected to observe a change

in the activation energy value at a specific water concentration and a slight influence in the conversion profiles.

However, by analyzing the NO conversion profiles for different water concentrations in the feed (Figure 5.6), NO/CO = 2 and 1 do not show any changes, because all the conversion profiles overlap. Only a slight negative effect on the NO conversion profile was observed for the NO/CO ratio equal to 0.5. The analysis of the product selectivity revealed no significant changes, suggesting that H_2O concentration had no substantial effect on the product distribution. Even for the selectivity towards NH_3, where an increase in formation with an increase in water content was expected, no change was detected, and all the selectivity profiles were reproducible. This might be because 1% H_2O concentration is already exceeding the threshold at which any significant changes could be observed.

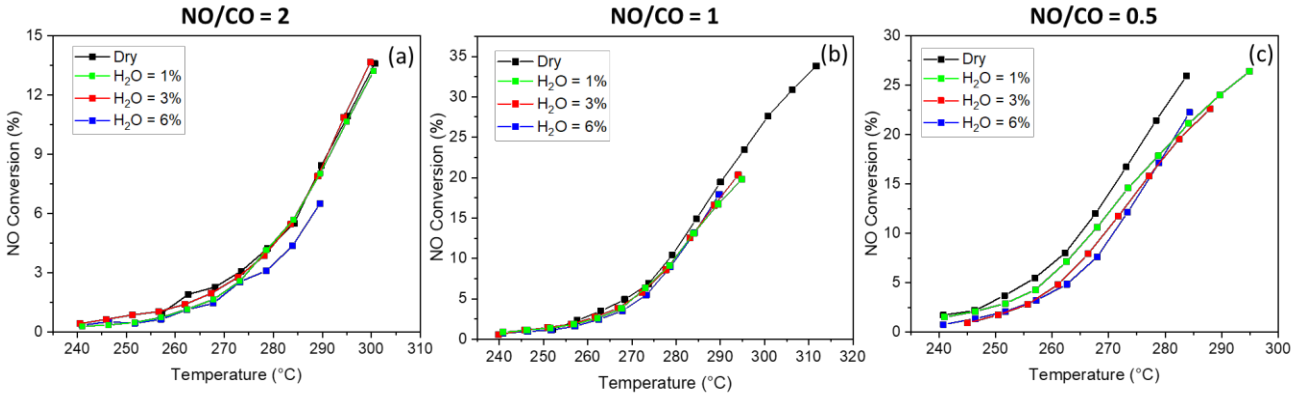

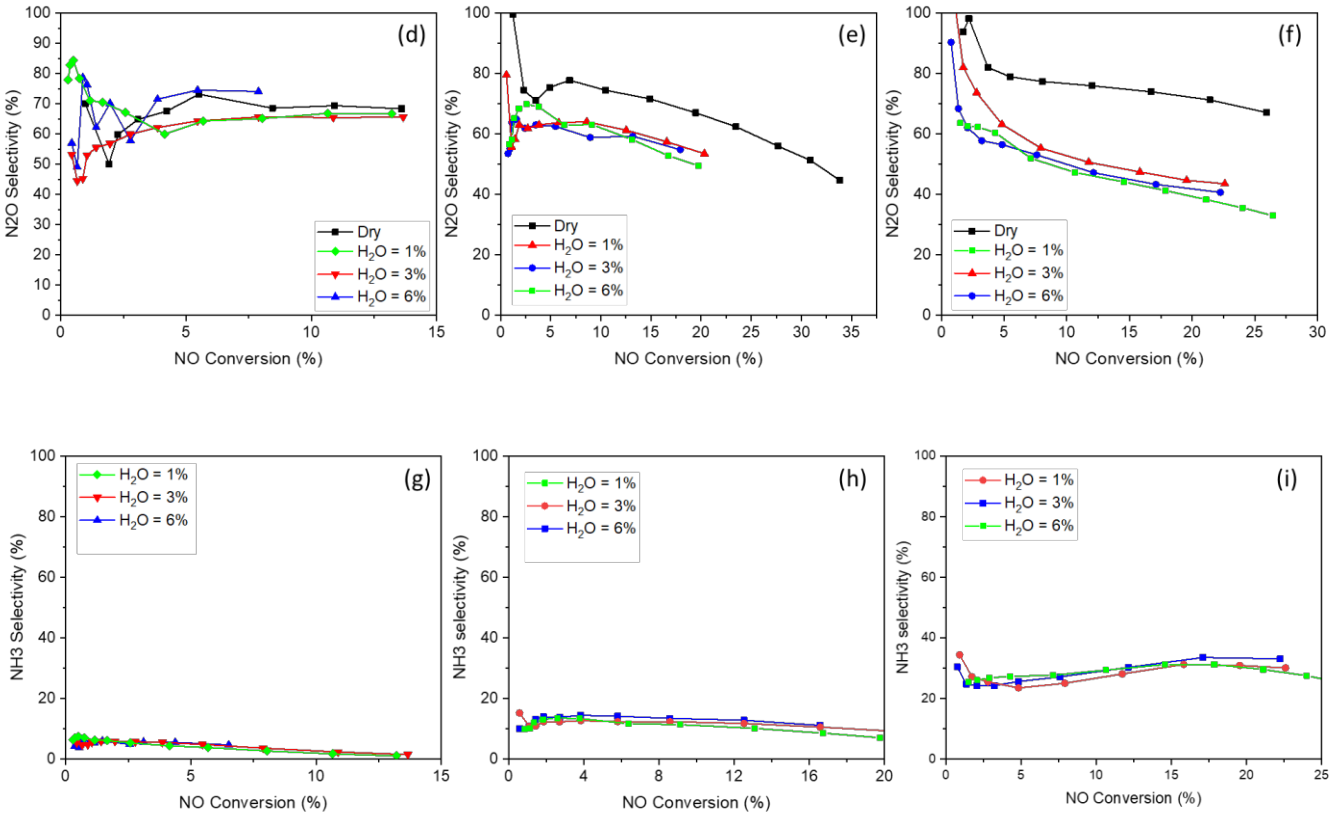

Figure 5.6: NO reduction by CO on 0.1% Rh/Al_2O_3 in the absence and in the presence of water. NO/CO = 0.5, 1 and 2. NO conversion, N_2O and NH_3 selectivity. The catalyst was reduced in 5% H_2 for 30 min at 500°C. The reaction mixture included CO = 1000 ppm, NO varying to obtain NO/CO = 2 (a), (d) and (g), 1 (b), (e) and (h) and 0.5 (c), (f) and (i) and H_2O = 1 (green), 3 (red) and 6% (blue), diluted in N_2.

Table 5.1: List of apparent activation energies measured from NO, CO, N_2O and NH_3 rates during NO reduction by CO in the absence and presence of 1, 3 and 6% over 0.1% Rh/Al_2O_3. NO/CO = 2, 1 and 0.5 The catalyst was reduced in 5% H_2 for 30 min at 500°C. The reaction mixture included CO = 1000 ppm, NO varying to obtain NO/CO = *2*, 1 and 0.5

Apparent activation energy [kJ/mol]					
		Dry	**Wet – 1%**	**Wet – 3%**	**Wet – 6%**
NO/CO = 0.5	**NO**	168	191	187	185
	N_2O	157	141	160	150
	CO	134	147	150	171
	NH_3		190	221	195
NO/CO = 1	**NO**	168	182	170	188
	N_2O	165	172	169	164
	CO	138	142	147	155
	NH_3		164	184	205
NO/CO = 2	**NO**	139	184-110	158	161
	N_2O	157	165	168	164
	CO	134	132	139	141
	NH_3		145	146	161

The analysis of the activation energy derived from NO and CO consumption, as well as N_2O and NH_3 formation, listed in Table 5.1, reveals consistent values with changing water concentrations. When water was co-fed for NO/CO = 2, there was no significant change in the apparent activation energy, which remained at 160 kJ/mol. However, for NO/CO = 1 and 0.5, co-feeding any concentration of water resulted in an increase in the apparent activation energy, compared to the dry case. Regardless of water concentration, the activation energy derived for NO/CO = 1 and 0.5 is higher than the one derived for NO/CO = 2. A common characteristic between the stoichiometric and reducing condition is the higher NH_3 selectivity compared to the oxidizing conditions. Therefore,

we further hypothesized that the increase in the apparent activation energy for NO and CO consumption could be influenced by the presence of NH_3.

5.3.5 The effect of NH_3 on the NO reduction by CO kinetics

The impact of NH_3 was investigated by introducing 100 ppm of NH_3 into the NO-CO feed with varying ratios and in the presence and absence of H_2O.

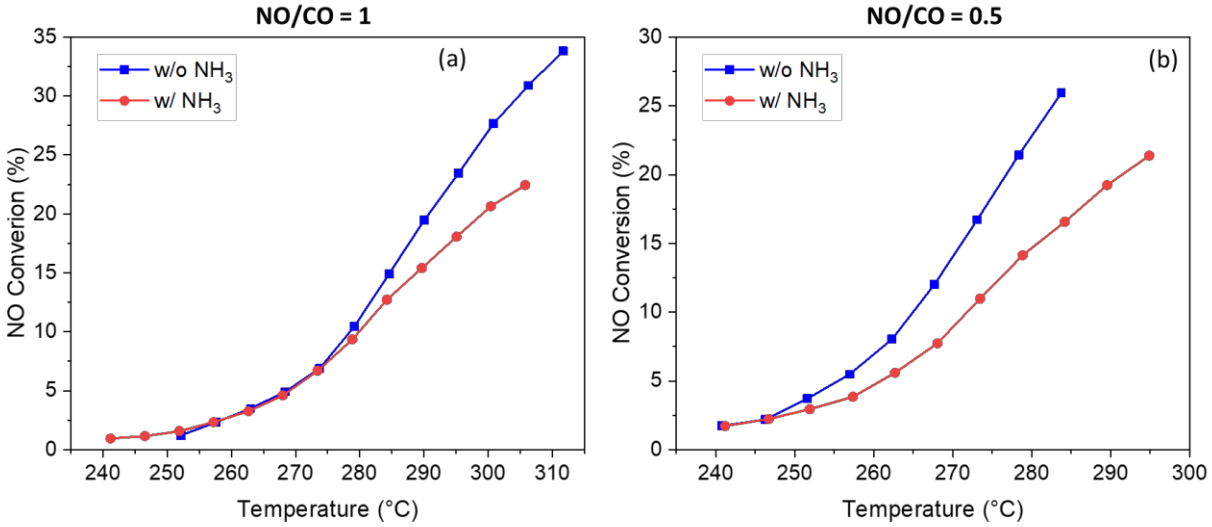

Figure 5.7: Comparison of NO conversion profile during dry NO reduction by CO in the presence and absence of 100 ppm NH_3 on 0.1% Rh/Al_2O_3. NO/CO = 1 and 0.5. The catalyst was reduced in 5% H_2 for 30 min at 500°C. The reaction mixture included CO = 1000 ppm, NO varying to obtain (a) NO/CO = 1 and (b) 0.5; NH_3 = 0 ppm (blue) or 100 ppm (red), diluted in N_2.

NO conversions in Figure 5.7 show a comparison between the NO conversion obtained in the presence and absence of NH_3. Under stoichiometric conditions, the conversions at low temperature are similar, but they deviate at high temperature, with the experiment performed with NH_3 showing lower conversion. Similarly, under reducing conditions, NO/CO = 0.5, the conversion obtained in the presence of NH_3 is also lower. This deviation may be attributed to the initiating of mass transfer limitations, a change in the mechanism or NH_3 inhibition.

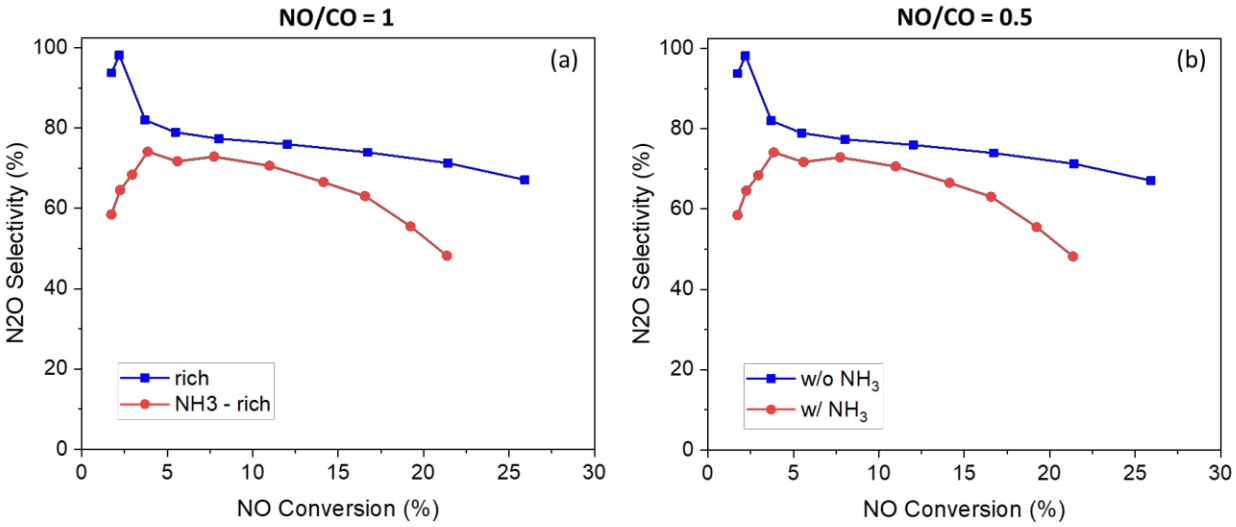

Figure 5.8: Comparison of N_2O selectivity during dry NO reduction by CO in the presence and absence of 100 ppm NH_3 on 0.1% Rh/Al_2O_3. NO/CO = 1 and 0.5. The catalyst was reduced in 5% H_2 for 30 min at 500°C. The reaction mixture included CO = 1000 ppm, NO varying to obtain (a) NO/CO = 1 and (b) 0.5; NH_3 = 0 ppm (blue) or 100 ppm (red), diluted in N_2.

From the product selectivities in Figure 5.8, we observe that, generally, the experiments performed in the presence of NH_3 exhibit lower selectivity towards N_2O, implying that NH_3 has a promoting effect on N_2 formation.

When water was introduced in the reducing feed, the inhibition on NO conversion induced by NH_3 was observed only at higher temperature. However, at low temperature the NO conversion profiles looked similar. Similar to the dry experiments, N_2O selectivity was lower in the presence of NH_3.

Also in this case, NH_3 hinders the formation of N_2O, and favors the formation of N_2 and NH_3, as shown in Figure 5.9b**.**

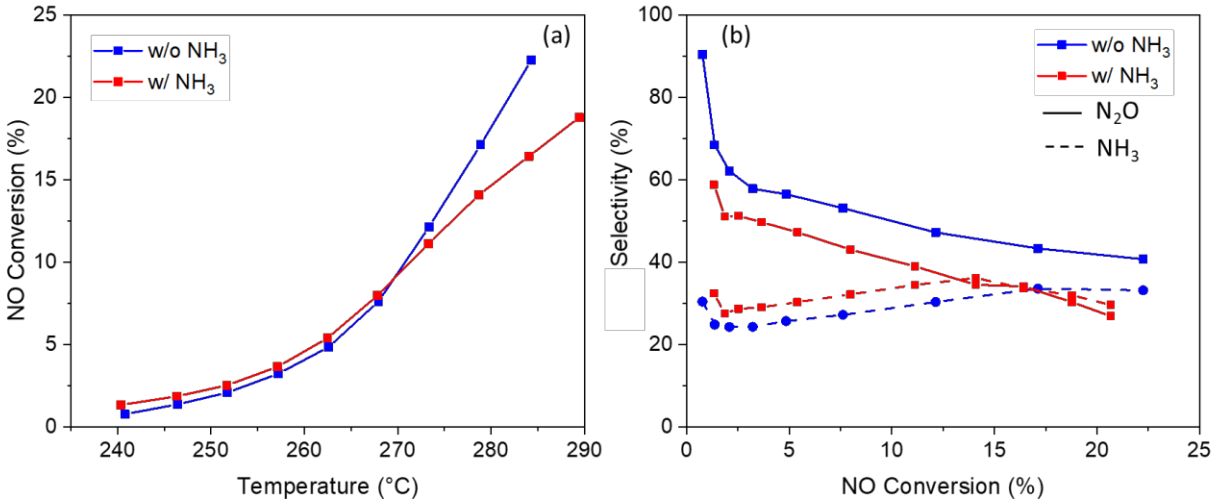

Figure 5.9: Comparison of NO conversion profile and product selectivity during wet NO reduction by CO in the presence and absence of 100 ppm NH_3 on 0.1% Rh/Al_2O_3. NO/CO = 0.5. The catalyst was reduced in 5% H_2 for 30 min at 500°C. The reaction mixture included CO = 1000 ppm, NO = 500 ppm; H_2O = 6%; NH_3 = 0 ppm (blue) or 100 ppm (red), diluted in N_2.(a) NO conversion; (b) N_2O and NH_3 selectivity

The effect of NH_3 on the NO reduction by CO kinetics was evaluated by comparing the activation energies measured in the presence and absence of NH_3 (Table 5.2). Under reducing conditions, the activation energies measured in the presence of NH_3 are lower compared to those measured in the absence of NH_3, in both dry and wet conditions. Under stoichiometric conditions, the apparent activation energies exhibit similar values, while under oxidizing conditions, the values obtained in the presence of NH_3 are larger than those obtained without NH_3, under wet and dry conditions.

Table 5.2: Apparent activation energy during dry and wet NO reduction by CO in the presence and absence of NH_3 The catalyst was reduced in 5% H_2 for 30 min at 500°C. The reaction mixture included CO = 1000 ppm, NO varying to obtain NO/CO = *2*, 1 and 0.5, NH_3 = 0/100 ppm; 0/6% H_2O.

Apparent activation energy [kJ/mol]					
		Dry	**Dry + NH_3**	**6% H_2O**	**6% H_2O + NH_3**
NO/CO = 0.5	**NO**	168	156	185	150
	N_2O	157	148	150	143
	CO	134	124	171	152
	NH_3	-	-	195	180
NO/CO = 1	**NO**	168	155	188	204
	N_2O	165	158	164	172
	CO	138	133	155	149
	NH_3	-	-	205	-
NO/CO = 2	**NO**	139	218	161	199
	N_2O	157	178	164	184
	CO	134	147	141	147
	NH_3	-	204	161	234

To further investigate the changes in reactivity in the presence and absence of NH_3, we studied the adsorbed species on the catalyst surface spectroscopically.

5.3.6 DRIFTS experiments

Before investigating the catalyst structure dynamics and the adsorbed species under reaction conditions, we first performed control experiments. During these preliminary investigations, we exposed the catalyst to simple feed which included: (i) CO/Ar; (ii) NO/Ar; and (iii) NH_3/Ar.

5.3.7 CO adsorption

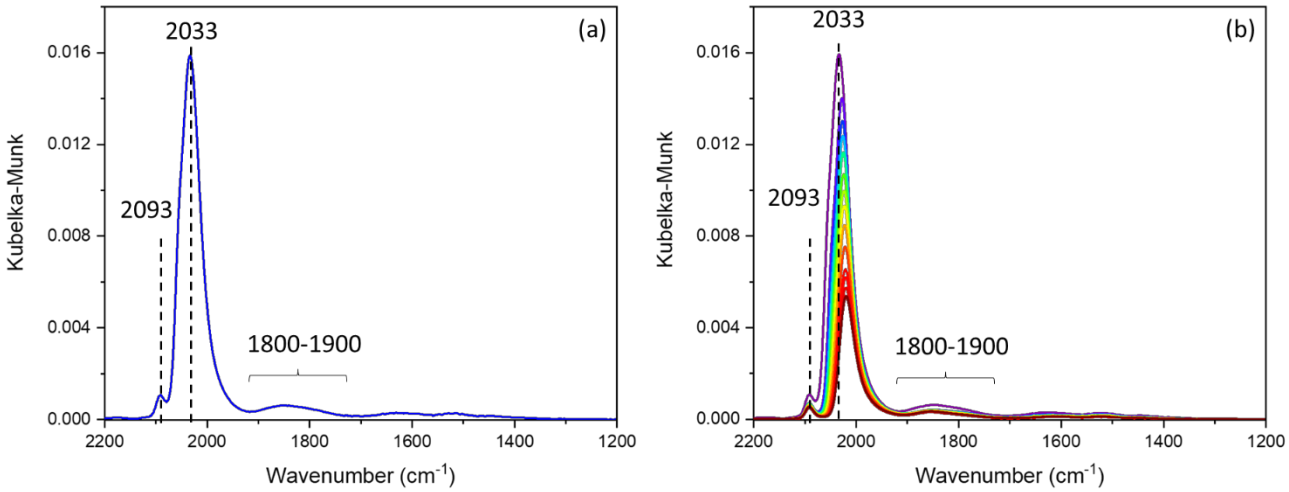

Figure 5.10: DRIFTS spectrum of CO adsorption on 0.1% Rh/Al_2O_3. The catalyst was treated in 1% O_2 at 500°C for 30 min, followed by Ar purge and reduced in 5% H_2 at 500°C for 30 min. The temperature was decreased to 265°C in Ar. The catalyst was then exposed to CO = 5000 ppm until no changes in the spectra were observed. (a) CO adsorption; (b) Ar purge.

CO adsorption on 0.1% Rh/Al_2O_3 is shown in Figure 5.10. In the spectral region spanning from 2100 to 1750 cm^{-1} three distinct features are observed. The peak centered at 2093 cm^{-1} and the shoulder within the feature at 2033 cm^{-1} are assigned to the symmetric and asymmetric gem-dicarbonyl species, respectively, where two CO molecules are bound to a Rh single atom, Rh_{SA}.[46,49–53] The shoulder at 2040 cm^{-1} corresponds to linear CO bound to a Rh nanoparticle, Rh_{NP},[46,49–52] while the broad feature between 1700 and 1900 cm^{-1} is assigned to Rh bridge bound to Rh_{NP}.[46,49–52] The low intensity features below 1700 cm^{-1} are attributed carbonates on the support.

The high intensity of the linear CO bound to Rh_{NP} suggests that at 265°C Rh mainly exists in nanoparticle form, while only a small portion underwent the oxidative CO-assisted disintegration. This is consistent with our previous data and with theoretical and experimental studies reported in the literature, suggesting that at higher temperature CO favors single atoms aggregation into nanoparticles.[47,54] After purging the IR cell with Ar, all the features decreased in intensity. The peak

containing both CO-Rh_{NP} and the asymmetric stretch of $Rh(CO)_2$ decrease their intensity much faster compared to the peak at 2090 cm^{-1}. This is consistent with previous studies that show that the bonding energy of CO to Rh_{NP} is lower than the two CO on Rh_{SA}. In addition, the peak at 2040 cm^{-1} shifts to lower wavenumbers, due to the dipole-dipole coupling of adjacent CO. On the other hand, as typical for isolated metal single atoms for which no such coupling exists, the other peak position remains fixed at 2090 cm^{-1}.

5.3.8 NO adsorption

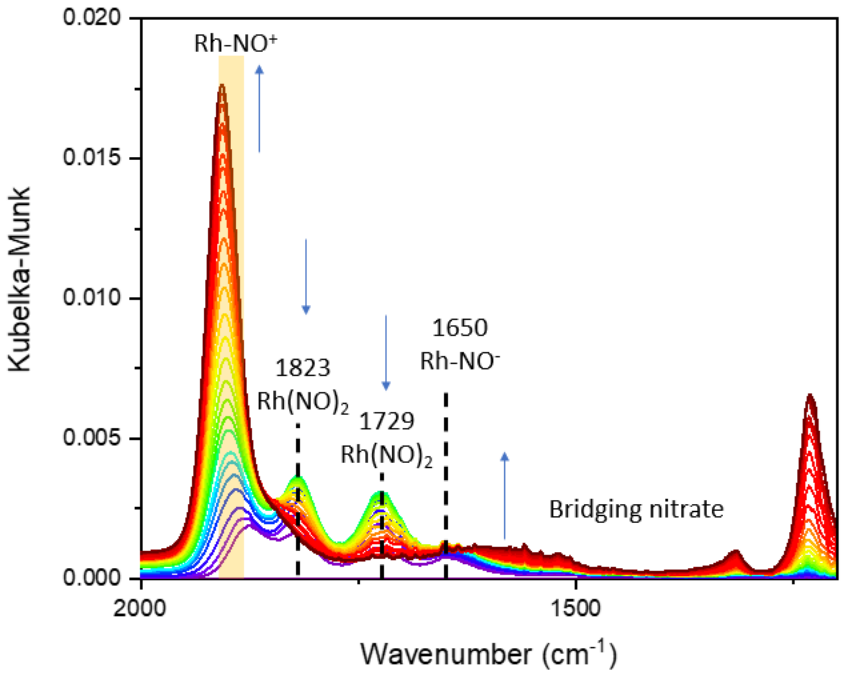

Figure 5.11: NO adsorption on 0.1% Rh/Al_2O_3 using DRIFTS. The catalyst was treated in 1% O_2 at 500°C for 30 min, followed by Ar purge and reduced in 5% H_2 at 500°C for 30 min. The temperature decreased to 265°C in Ar. The catalyst was then exposed to NO = 5000 ppm until saturation.

Figure 5.11 presents the temporal evolution of surface species formed during NO adsorption on 0.1% Rh/Al_2O_3. Initially NO is adsorbed as $Rh\text{-}NO^-$, evident from the feature centered at 1650 cm^{-1}.[55–63] This species, located in the low wavenumber region, has been reported to be characterized by a bent configuration, with strong bond between N and Rh, but a weaker bond between N and

O.[63,64] Previous research has suggested that Rh-NO^- may be responsible for NO dissociation.[31,65,66] The spectra in **Figure 5.11** reveal two features at 1823 and 1729 cm^{-1}, assigned to $Rh(NO)_2$. This assignment is consistent with their simultaneous increase and decrease in intensity.[67] The decrease in intensity during NO adsorption aligns with previous literature which reported that these species are highly unstable due to their weak bond to the metal, similar to the gem-nitrosyl species physisorbed on Ag(111).[68,69] The peak that shifts from 1870 to 1910 cm^{-1} is assigned to Rh-NO^+. [55–63] This species is characterized by a stronger bond between N to O and a weaker bond between N and Rh due to the lower electron back-donation from Rh to NO.[68] It has been proposed that the continuous formation of Rh-NO+ is caused by the accumulation on the metal surface of adsorbed oxygen, derived from NO dissociation, leading to insufficient sites available for further NO dissociation. Previous research also suggested that Rh-NO^+ plays a role in N_2O formation.[64] The features observed below 1640 cm^{-1} are assigned to nitrites and nitrates species.

5.3.9 NH_3 adsorption

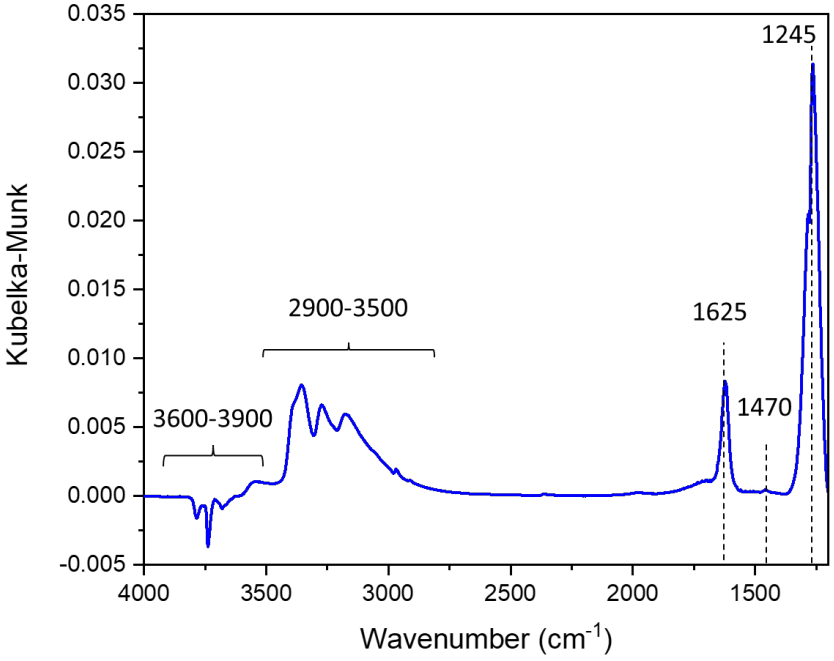

Figure 5.12: NH_3 adsorption on 0.1% Rh/Al_2O_3 using DRIFTS. The catalyst was treated in 1% O_2 at 500°C for 30 min, followed by Ar purge and reduced in 5% H_2 at 500°C for 30 min. The temperature decreased to 265°C in Ar. The catalyst was then exposed to NH_3 = 500 ppm until saturation.

A DRIFTS spectrum obtained during NH_3 adsorption on 0.1% Rh/Al_2O_3 is shown in Figure 5.12. In the spectral region between 3600 and 3900 cm^{-1}, we observe the consumption of OH groups on the alumina surface and the interactions of NH_3 with hydroxyls groups in the region between 2900 and 3500 cm^{-1}. Similar assignments were made for NH_3 adsorption on a Rh/SiO_2 catalyst.[70] The features at 1625 and 1245 cm^{-1} are assigned to NH_3 adsorbed in molecular form on Lewis acid sites, while the small feature at 1470 cm^{-1} is assigned to an ammonium ion resulting from the proton transfer from Bronsted acid sites on the alumina surface. [71]

NH_3 adsorption on Rh/Al_2O_3 does not indicate any NH_3 interaction with the metal, suggesting that the NH_3 exclusively interacts with the alumina support.

5.3.10 NO + CO adsorption

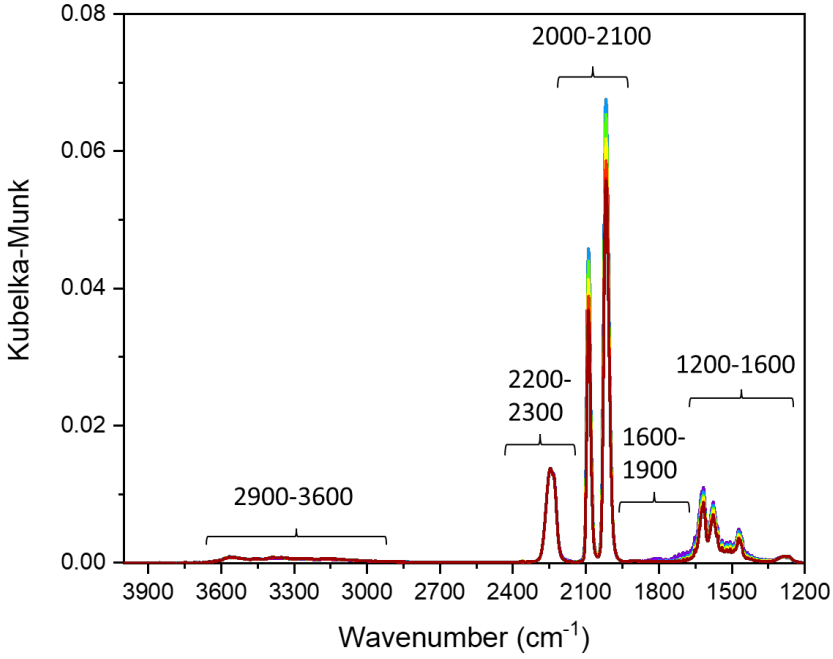

Figure 5.13: NO + CO adsorption on 0.1% Rh/Al_2O_3. The catalyst was treated in 1% O_2 at 500°C for 30 min, followed by Ar purge and reduced in 5% H_2 at 500°C for 30 min. The temperature decreased to 265°C in Ar. The catalyst was then exposed to a mixture of CO = 5000 and NO = 5000 ppm until saturation.

Figure 5.13 shows the spectra obtained during NO + CO adsorption at 265°C, with a NO/CO ratio equal to 1. The spectra consist of multiple features that will be analyzed individually. In the region spanning from 3600 to 2900 cm^{-1}, we observe the interactions between NO species and the hydroxyl groups of the alumina support. The features at 2300-2200 cm^{-1} are assigned to NCO on the support.[60,72–74] The peaks at 2090 and 2030 cm^{-1} correspond to the symmetric and antisymmetric rhodium gem-dicarbonyl species, respectively. In the region between 1900 and 1630 cm^{-1}, the observed species are attributed to NO adsorbed on Rh. Finally, below 1600 cm^{-1} the features are assigned to C- and N- containing species on alumina.

When analyzing the region of CO adsorbed on Rh, specifically from 2100 to 1900 cm^{-1}, the spectra exhibit very different features compared to the spectrum shown in Figure 5.10 where CO-only was adsorbed on the catalyst. In the presence of NO, CO adsorbs on isolated Rh single atoms. Unlike in Figure 5.10, no linear or bridge CO on Rh is observed. This is because the presence of NO enhances the CO-assisted Rh nanoparticle disintegration. As discussed in Chapter 3, CO-induced Rh nanoparticle redispersion is promoted in the presence of O_2, even at higher temperature, as this is an oxidative process. Similarly, both theoretical and experimental studies showed that NO can enhance the oxidative process of particle disruption.[45,75] However, despite the presence of small Rh nanoparticles, 1.1 nm, in 0.1% Rh/Al_2O_3, the particle disintegration process remains incomplete and some Rh nanoparticles are still present in the catalyst. While we do not observe CO on Rh_{NP}, we observe NO adsorbed on Rh, as evidenced from the spectral region between 1910 and 1630 cm^{-1}. This is because when a Rh catalyst is exposed to a mixture of NO and CO, NO preferentially adsorbs on Rh_{NP}, while CO preferentially adsorbs on Rh_{SA}.[76,77]

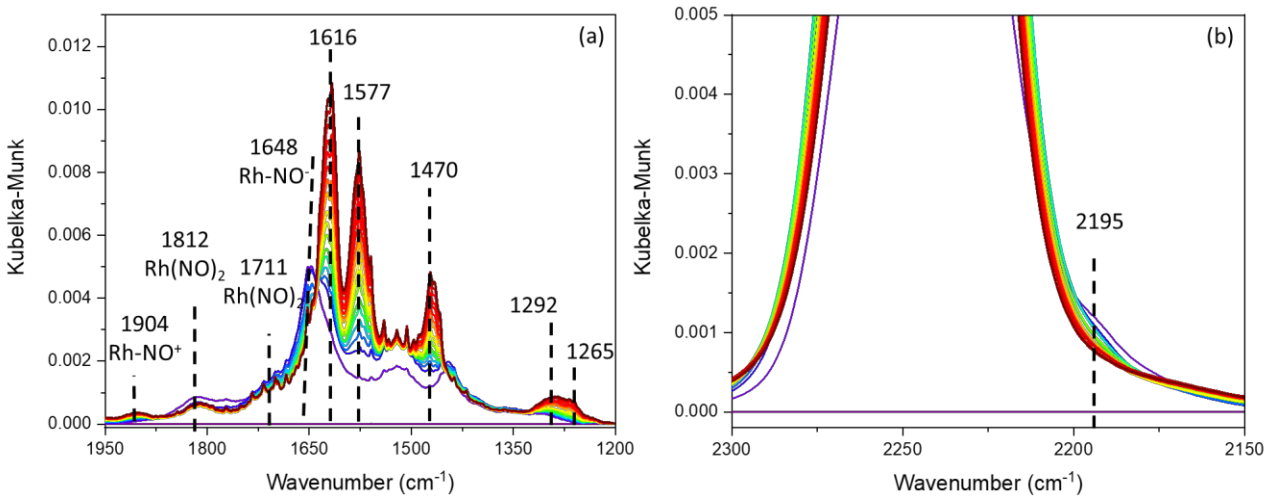

Figure 5.14: NO + CO adsorption on 0.1% Rh/Al_2O_3. The catalyst was treated in 1% O_2 at 500°C for 30 min, followed by Ar purge and reduced in 5% H_2 at 500°C for 30 min. The temperature decreased to 265°C in Ar. The catalyst was then exposed to a mixture of CO = 5000 and NO =

5000 ppm until saturation. (a) focus on the 1200-1900 cm^{-1} range; (b) focus on the 2150-2300 cm^{-1} range

In the region between 1950 and 1650 cm^{-1}, we observed the presence of Rh-NO^- at 1648 cm^{-1}, the symmetric and asymmetric $Rh(NO)_2$ at 1812 and 1711 cm^{-1} and Rh-NO^+ at 1904 cm^{-1}, as shown in Figure 5.14. Over time, Rh-NO^- dynamics are similar to that observed in Figure 5.11. In fact, its intensity initially increases before subsequently decreasing, consistent with the NO dissociation process. $Rh(NO)_2$ intensity remains stable, as well as Rh-NO^+, which, in contrast to the case of NO-only adsorption, does not increase over time. This suggests that there may not be sufficient available sites for NO adsorption, as a portion of them has re-dispersed into single atoms, making them accessible for CO adsorption.

The bands at 2310 cm^{-1} are assigned to NCO absorbed on the Al_2O_3. The proposed process for NCO formation involves its formation on the metal and the consequent spillover onto the support [24,78]. In the inset in Figure 5.14, we notice a shoulder at 2195 cm^{-1} that decreases over time. This feature is assigned to NCO on Rh and it was proposed to be the precursor to NCO on the support before it transfers to the support.[78–81]

The features centered at 1616, 1577, 1470 and 1292 cm^{-1} are assigned to C- and N- species. It was proposed that these species are connected to NCO species and involve the presence of H. Experiments performed on Pd/Al_2O_3 showed that these species increase in intensity simultaneously with the NCO species at 2300 cm^{-1}. In addition, to demonstrate the presence of H within these species, a NO + CO + D_2 mixture was adsorbed on the catalyst, which resulted in a red shift of the 1600-1200 species.[82]

The species observed during NO + CO adsorption under stoichiometric conditions were present also under reducing and oxidizing conditions, with NO/CO ratios of 0.5 and 2. A comparison of

all the spectra obtained at different rations is shown in Figure 5.15. While qualitatively, the spectra look similar, we observe that under reducing conditions the NCO on alumina feature results in a higher intensity compared to the other conditions, consistent with previous studies.[21] The similarities in the spectra among all the conditions under study are in line with our kinetic data showing similar activities, selectivity and apparent activation energies.

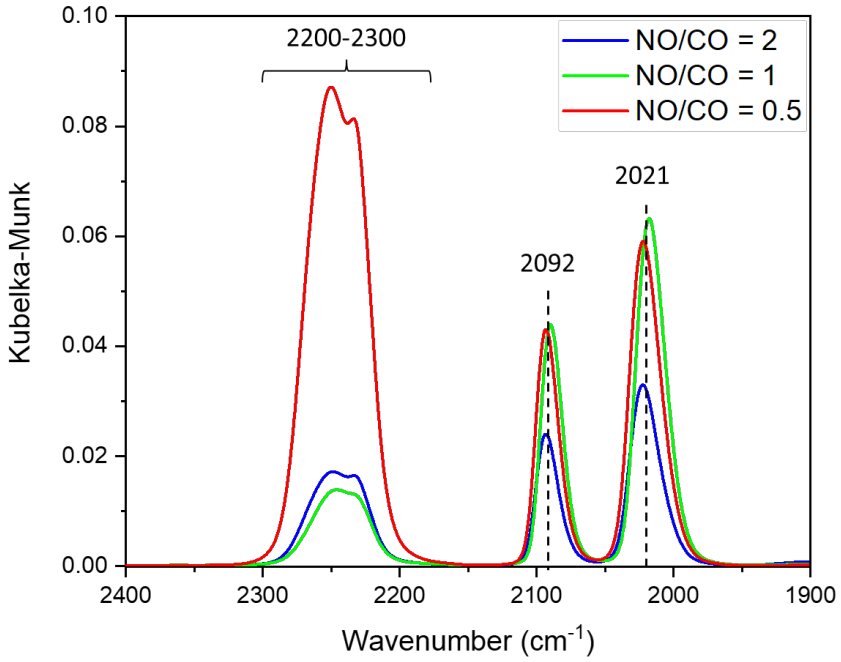

Figure 5.15: NO + CO adsorption – NO/CO = 2, 1 and 0.5 on 0.1% Rh/Al_2O_3. The catalyst was treated in 1% O_2 at 500°C for 30 min, followed by Ar purge and reduced in 5% H_2 at 500°C for 30 min. The temperature decreased to 265°C in Ar. The catalyst was then exposed to a mixture of CO = 5000 and NO = vary to obtain NO/CO = 0.5 (red), 1 (green) and 2 (blue) until saturation.

Following NO + CO adsorption and Ar purge, we performed a TPD to investigate the evolution of the adsorbed species with the temperature increased. Figure 5.16 shows the TPD spectra after NO + CO adsorption with NO/CO ratio = 1, focused on the Rh-CO region. Similar trends were observed for different NO/CO ratios.

The Rh gem-dicarbonyl species decrease in intensity and slightly shift to lower wavenumber during the temperature increase. The shift might be due to varying coordination environments at different temperatures. The presence of OH groups on the support can modify the CO desorption energy of each carbonyl, as was supported by experimental theoretical studies. [19,77,83–85] In addition, the ratio of the two carbonyl features changes, with the area of the asymmetric gem-dicarbonyl, centered at 2017 cm^{-1}, becoming larger. Previous research indicated that Rh mono-carbonyl forms as the temperature increases and it is positioned at 2012-1999 cm^{-1}.[19,83] It was indeed proposed that the presence of an OH group in the Rh coordination environment modifies the CO adsorption energy, allowing one of the CO molecules from the dicarbonyls to desorb. The other CO molecule remains on Rh even at higher temperature due to its high adsorption energy.[84] Here we observe a plausible Rh monocarbonyl species at 500°C, centered at 2000 cm^{-1}.

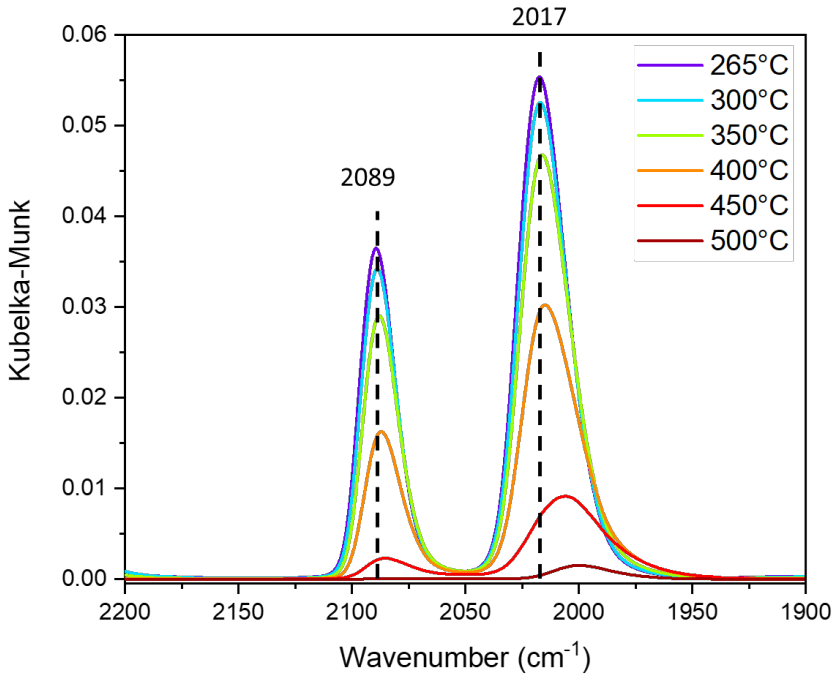

Figure 5.16: TPD after NO + CO adsorption on 0.1% Rh/Al_2O_3. The catalyst was treated in 1% O_2 at 500°C for 30 min, followed by Ar purge and reduced in 5% H_2 at 500°C for 30 min. The

temperature decreased to 265°C in Ar. After the catalyst then exposed to a mixture of CO = 5000 ppm and NO = 5000 ppm and purged with Ar at 265°C, the temperature was increased until 500°C at a ramp rate of 10°C /min.

5.3.11 NO + CO adsorption in the presence of NH_3

The impact of NH_3 on the speciation during NO + CO adsorption was investigated using DRIFTS. Figure 5.17 displays the time evolution of NO + CO + NH_3 with a NO/CO ratio of 0.5 adsorption. Overall, the species present on the catalyst surface are similar to the ones in the absence of NH_3: NCO species between 2300-2200 cm^{-1}, CO on Rh in the region between 2100-1900 cm^{-1}, NO on Rh between 1900-1600 and C- and N- containing species on alumina below 1600 cm^{-1}. However, the NCO intensity at 2300 cm^{-1} is much higher. This might be related to the greater consumption of the OH groups in the presence of NH_3, as we observe a correlation between the consumption of the OH groups and the increasing in intensity of the NCO species. Also, the features below 1600 cm^{-1} exhibit higher intensity, consistent with the hypothesis of these species being correlated to -NCO species centered at 2300-2200 cm^{-1}. However, the high intensity characterizing the features below 1600 cm^{-1} obscures the peaks associated with NO absorption on Rh, making them indiscernible. In the CO on Rh spectrum region, similar to spectra obtained in the absence of NH_3, $Rh(CO)_2$ features are observed, although with a lower intensity, which could be explained by NH_3 hindering the CO-assisted nanoparticle disintegration, as revealed by previous observations.[72]

However, when the catalyst is exposed to NH_3, we observe a red shift in the $Rh(CO)_2$ peak position. This suggests a change in the Rh coordination environment induced by NH_3.

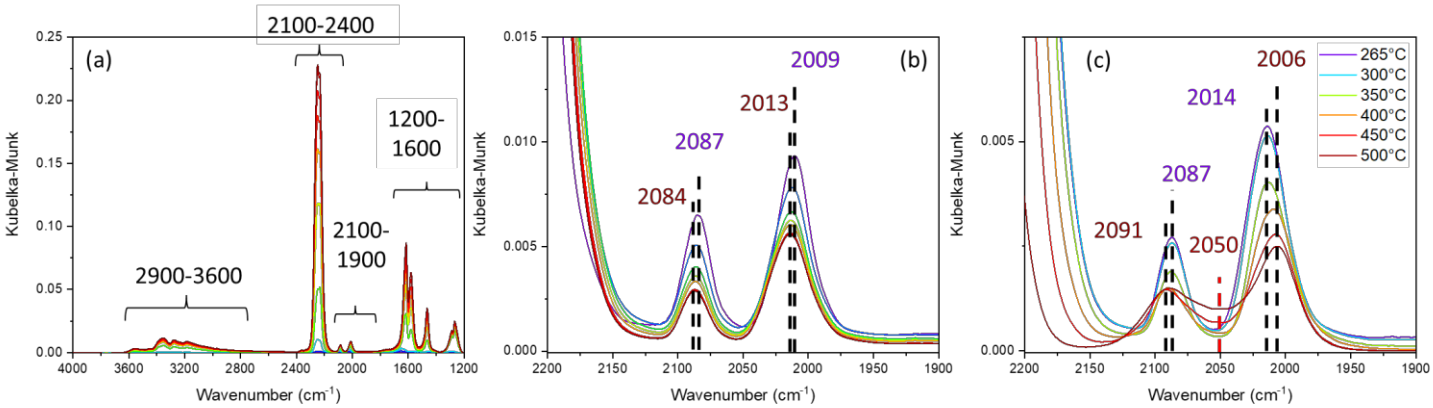

Figure 5.17: after NO + CO + NH_3 adsorption on 0.1% Rh/Al_2O_3. The catalyst was treated in 1% O_2 at 500°C for 30 min, followed by Ar purge and reduced in 5% H_2 at 500°C for 30 min. The temperature decreased to 265°C in Ar. After the catalyst then exposed to a mixture of CO = 5000 ppm; NO = 2500 ppm; NH_3 = 500 ppm. and purged with Ar at 265°C, the temperature was increased until 500°C at a ramp rate of 10°C /min. (a) NO + CO + NH_3 adsorption; (b) Ar purge focused on 1900-2200 cm^{-1} region; (c) TPD focused on 1900-2200 cm^{-1} region.

As the NO + CO + NH_3 gas phase is removed (Figure 5.17b), during the Ar purge, the gem-dicarbonyl species exhibit a decrease in intensity and a shift to higher wavenumber, however they do not return to the position observed in the absence of NH_3. This might be due to the partial removal of NH_3 and NH/NH_2 species from the catalyst. The features below 1600 cm^{-1} decrease in intensity, while the NCO species at 2300 cm^{-1} first increase in intensity before subsequently decreasing, reaching a value higher than the intensity at time = 0 min. This trend suggests that the peaks in the 1200-1600cm^{-1} region might lose the possible H atom and enrich the feature in the 2300 cm^{-1} region.

Interestingly, the TPD spectra resulting after NO + CO + NH_3 adsorption differ from the previous ones. After NO + CO adsorption, both the symmetric and asymmetric $Rh(CO)_2$ stretches shifted to lower wavenumber, while desorbing. In the case of co-adsorbed NH_3, as the temperature

increases, the two gem-dicarbonyl peaks shift in opposite directions. The symmetric gem-dicarbonyl shifts to higher wavenumber, while the symmetric gem-dicarbonyl shifts to lower wavenumber. This trend is consistent across all the NO/CO ratios studied and is more noticeable for the NO/CO ratio equal to 0.5, shown in Figure 5.17c. The opposite shifts could be attributed to a different coordination environment or to the presence of another species centered at higher wavenumbers. In addition to the different shifts of the gem-dicarbonyl, we observed the increase in intensity of a new feature at 2050 cm^{-1}, which increases with increasing temperature. The peak position suggests that this peak might be related to CO linearly bound on nanoparticles, as it is consistent with other CO adsorption spectra obtained at lower temperature, when NO is not co-fed (Figure 5.10). However, given the high temperature and the low coverage, the peak position relative to Rh_{NP}-CO should theoretically be located at lower frequencies, as shown in previous literature.[76] While the exact nature of this peak remains unknown, we can hypothesize that it could represent a stable species that might hinder catalyst activity by blocking the active sites, as hinted by its presence at high temperature.

In addition, unlike in the spectra obtained in the absence of NH_3, where the NCO species desorbed by 450°C, co-adsorption with NH_3 results in the NCO species at 2300 cm^{-1} still being present even at 500°C, suggesting that this species is highly stable and it might have electronic effects on the metal, hindering the dissociation of NO, as proposed for Pt/Al_2O_3 catalysts. [23]

Based on the spectra obtained in the presence of NH_3, we can conclude that NH_3 might alter the surface speciation and it might lead to a different reaction mechanism.

5.3.12 Mid chapter conclusions

From the kinetic experiments we observed that water causes an increase in the apparent activation energy and this increase might be caused by the presence of NH_3 formed during the reaction.

Experiments performed in the presence of NH_3 showed that NH_3 has an inhibiting effect on the conversion profile under reducing conditions and on the N_2O selectivity. Spectroscopic studies conducted in the presence of NH_3 showed changes in the features related to CO adsorbed on Rh single atoms during TPD experiments. The information obtained by spectroscopy combined with kinetics led us to formulate two hypotheses:

1- NH_3 inhibits Rh single atoms mobility leading to a different amount of nanoparticles
2- NH_3 inhibits the NO reduction by CO kinetics

5.3.13 Hypothesis N.1: NH_3 hinders Rh SA mobility

This hypothesis was based on the presence of gem-dicarbonyl species even at higher temperature during the TPD after NO+CO+NH_3 adsorption. We approached the hypothesis in two ways:

- By analyzing how the mobility of single atoms and nanoparticles change during CO oxidation in the presence and absence of NH_3 using DRIFTS, with the results in the absence of NH_3 presented in Chapter 3;
- By studying the effect of NH_3 on NO reduction by CO performed on a catalyst characterized by large Rh nanoparticles.

5.3.14 In-situ CO oxidation in the presence of NH_3 using DRIFTS

DRIFTS spectra were obtained on the 0.1% Rh/Al_2O_3-700°C, used in Chapter 3 to study single atoms-nanoparticle interconversion during CO oxidation. Figure 5.18 shows a comparison of the spectra taken during CO oxidation in the presence (a) and absence (b) of NH_3 in the temperature range spanning from 220 and 300°C.

In the spectra in Figure 5.18 (a), we observed the presence of only Rh gem-dicarbonyls located at 2083 and 2009 cm^{-1}. The peak position of $Rh(CO)_2$ is shifted to lower wavenumbers when

ammonia is co-fed, similar to previous experiments when NH_3 was co-fed during NO + CO adsorption, confirming that NH_3 causes a change in Rh local coordination environment.[72] As the temperature increased, the peak assigned to the linear CO bond on Rh starts increasing in intensity, although at a slower rate compared to the case of CO + O_2 adsorption. However, in Figure 5.18 (a), we also observe the presence of a feature at 2174 cm^{-1}, assigned to the NCO on a Rh nanoparticle. Since the Rh-NCO extinction coefficient is unknown, we cannot directly compare the aggregation occurring during CO oxidation in the presence and absence of NH_3. In addition, aggregation of Rh nanoparticles still occurs, even in the presence of NH_3, disproving the hypothesis that NH_3 hinders the aggregation of single atoms into nanoparticles.

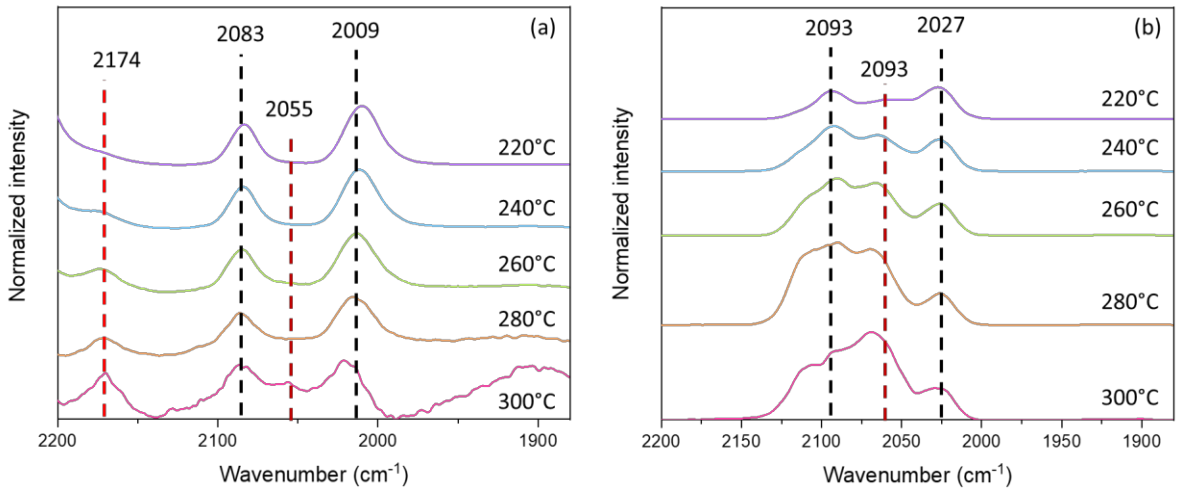

Figure 5.18: in-situ CO oxidation in the presence and absence of NH_3 on 0.1%Rh/Al2O3 – 700°C 220, 240, 260, 280 and 280°C using DRIFTS. CO = 8400 ppm ; O_2 = 9250 ppm. The catalyst was first exposed to 1% O_2 at 500 °C for 30 min, followed by He purge for 10 min and 5% H_2 at 500 °C for 30 min. The spectra were normalized by the intensity of the peak at 2026 cm^{-1}, after applying the gas phase subtraction.(a) NH_3 = 500 ppm; (b) NH_3 = 0 ppm.

While in-situ CO oxidation + NH_3 spectroscopic studies remained inconclusive, we proceeded with studying the effect of NH_3 during wet NO reduction by CO on large Rh nanoparticles, along with examining CO + NO adsorption using DRIFTS.

5.3.15 NO reduction by CO on large Rh nanoparticles

Figure 5.19 shows the NO conversion profiles obtained on 0.1 Rh/Al_2O_3 – 1.1 nm and on 0.1 Rh/Al_2O_3 – 9.2 nm during wet NO reduction by CO, with NO/CO = 0.5, 1 and 2, in the presence and absence of 100 ppm NH_3.

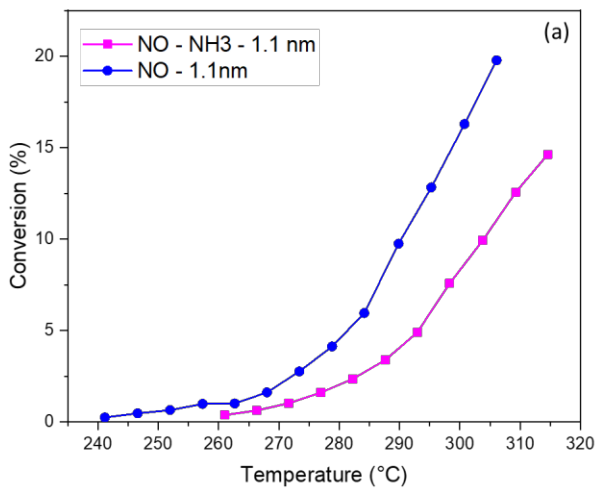
(a)
NO - NH3 - 1.1 nm
NO - 1.1nm
Conversion (%)
Temperature (°C)

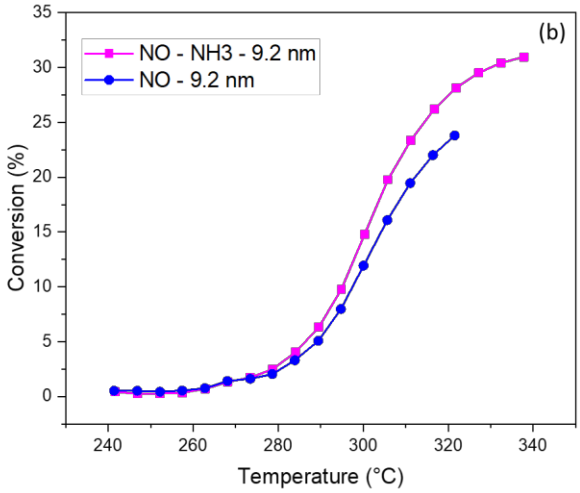
(b)
NO - NH3 - 9.2 nm
NO - 9.2 nm
Conversion (%)
Temperature (°C)

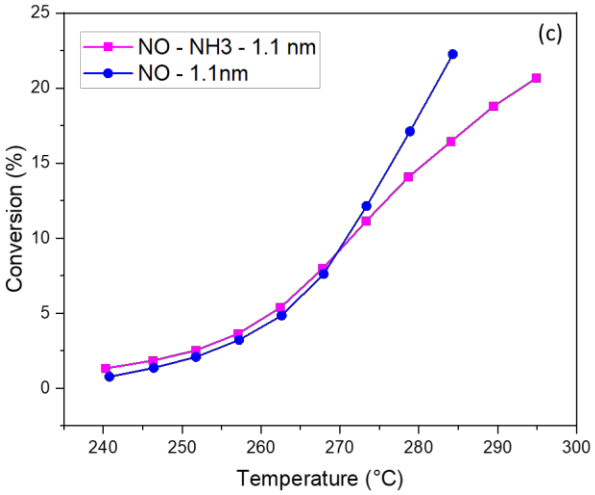
(c)
NO - NH3 - 1.1 nm
NO - 1.1nm
Conversion (%)
Temperature (°C)

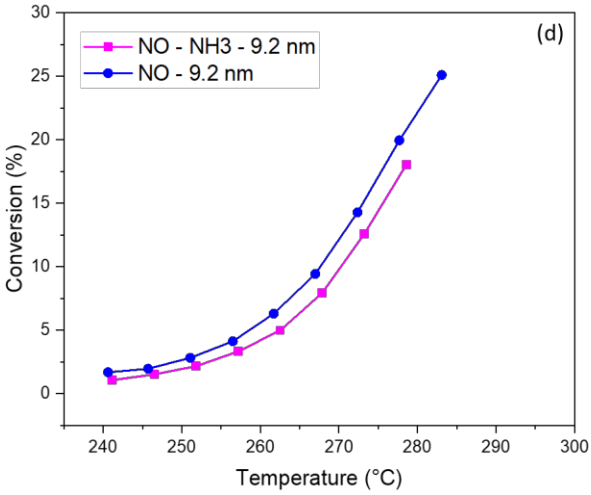
(d)
NO - NH3 - 9.2 nm
NO - 9.2 nm
Conversion (%)
Temperature (°C)

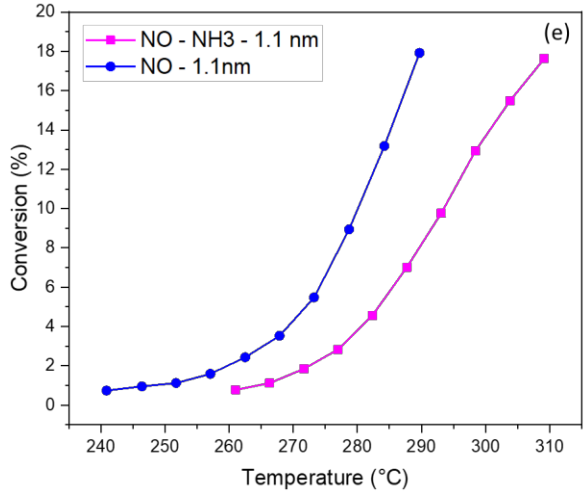
(e)
NO - NH3 - 1.1 nm
NO - 1.1nm
Conversion (%)
Temperature (°C)

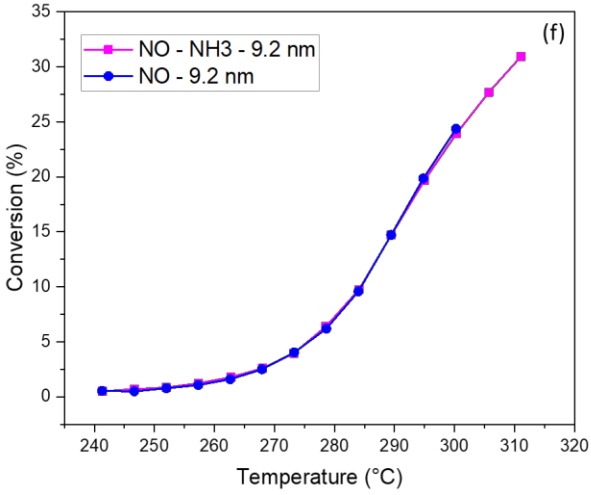
(f)
NO - NH3 - 9.2 nm
NO - 9.2 nm
Conversion (%)
Temperature (°C)

Figure 5.19: Comparison of wet NO reduction by CO in the presence and absence of NH_3 on 0.1% Rh/Al_2O_3-1.1 and 9.2 nm. The catalysts were reduced in 5% H_2 for 30 min at 500°C. The reaction mixture included CO = 1000 ppm; NO varying to obtain (a) and (b) NO/CO = 2*;* (c) and (d) 0.5 (b)*;* and (e) and (f) and (f) 1, NH_3 = 0 (blue) or 100 ppm (fuscia) and H_2O = 6%, diluted in N_2. (a), (c) and (e) 0.1% Rh/Al_2O_3 – 1.1 nm; (b), (d) and (f) 0.1% Rh/Al_2O_3 – 9,2 nm;

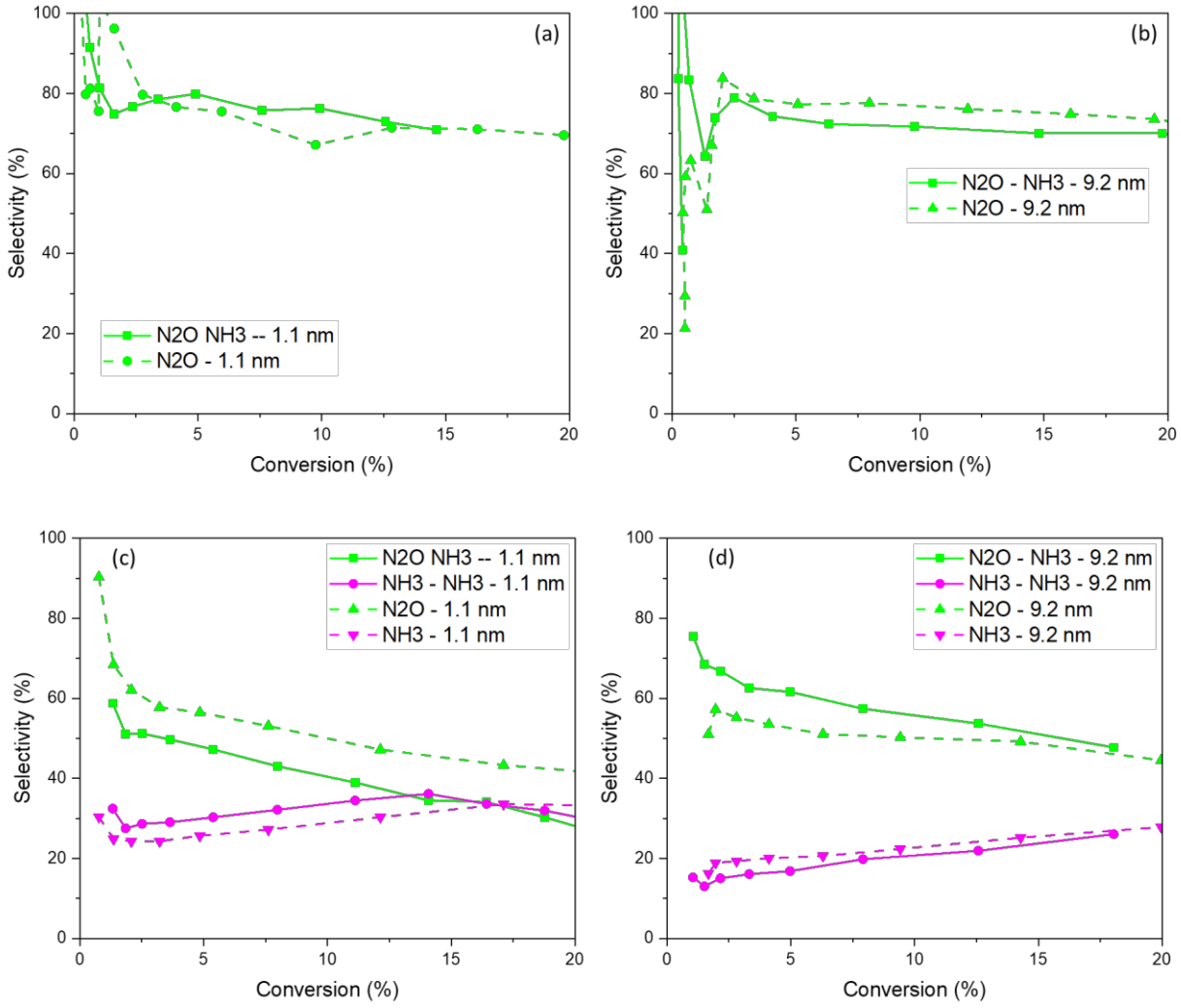

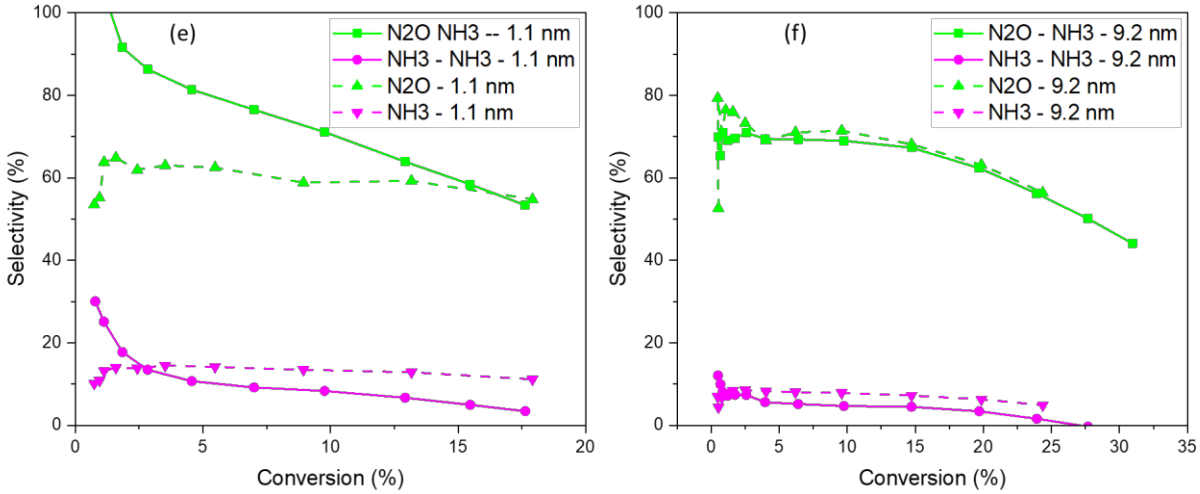

Figure 5.20: Selectivity towards N_2O and NH_3 on 0.1% Rh/Al_2O_3 – 1.1 nm and 9.2 nm. The catalysts were reduced in 5% H_2 for 30 min at 500°C. The reaction mixture included CO = 1000 ppm; NO varying to obtain (a) and (b) NO/CO = 2*;* (c) and (d) 0.5 (b)*;* and (e) and (f) 1, NH_3 = 0 (dashed line) or 100 ppm (solid line) and H_2O = 6%, diluted in N_2. (a), (c) and (e) 0.1% Rh/Al_2O_3 – 1.1 nm; (b), (d) and (f) 0.1% Rh/Al_2O_3 – 9,2 nm;

Table 5 3: Apparent activation energy measured on 0.1% Rh/Al_2O_3 – 1.1 nm and 9.2 nm during NO reduction by CO in the presence of water. The catalysts were reduced in 5% H_2 for 30 min at 500°C. The reaction mixture included CO = 1000 ppm; NO varying to obtain NO/CO = 0.5, 1 and 2, NH_3 = 0 or 100 ppm and H_2O = 6%, diluted in N_2.

Apparent activation energy [kJ/mol]								
	0.1% Rh/Al_2O_3 – 9.2 nm				0.1% Rh/Al_2O_3 – 1.1 nm			
	NO	CO	N_2O	NH_3	NO	CO	N_2O	NH_3
NO/CO = 0.5	180	160	170	213	185	161	150	195
NO/CO = 1	208	160	189	200	193	155	164	205
NO/CO = 2	215	157	205	215	161	141	164	161
NO/CO = 0.5 + NH_3	193	176	172	238	166	165	141	180

NO/CO = 1 + NH_3	201	165	198	160	204	149	173	124
NO/CO = 2 + NH_3	211	151	195	-	193	147	184	-

The 1.1 nm Rh catalyst exhibited an inhibition by NH_3 both at low T and high temperature, resulting in changes in the apparent activation energy. In contrast, the 9.2 nm Rh catalyst showed no changes in the conversion profiles. The selectivities towards N_2O and NH_3, shown in Figure 5.20, follow a similar trend as that of the highly dispersed Rh. The selectivity towards NH_3 increases with NO/CO ratio varying from oxidizing to reducing conditions at the expense of N_2O. However, consistent with previous literature, the selectivity towards NH_3 on the sample with an average particle size of 9.2 nm Rh is lower than on the highly dispersed Rh.[19]

The apparent activation energies obtained during wet NO + CO on 1.1 nm and 9.2 nm Rh yielded similar values, suggesting that the step limiting the reaction rate remains the same regardless of particle size. However, due to the structural changes occurring in the presence of NO and CO,[86] the number of active sites might change and alter the turnover frequency measurement, similar to the case of CO oxidation.

The comparison of the apparent activation energies obtained in the presence and absence of NH_3 on 9.2 nm Rh catalyst does not exhibit the same behavior as observed for highly dispersed Rh. All the values are similar to each other, suggesting that NH_3 does not affect the reaction mechanism for larger nanoparticles. Therefore, the increase in apparent activation energy might not be attributed to the presence of NH_3, since larger Rh nanoparticles show consistently the same high apparent activation energy values. However, it can be hypothesized that H_2O induced an increase in apparent activation energy values, by causing structural changes. Previous studies indeed

showed that water can increase the fraction of step sites on Pt-Pd catalysts.[87] We can then hypothesize that also in the case of Rh, water might cause similar changes in the particle. This might be explored in future work, using electron microscopy.

To better understand the similarities between the two catalysts characterized by different dispersions, we investigated the surface species present during NO + CO using DRIFTS.

In Figure 5.21, we show the spectra obtained during NO + CO adsorption. Overall, 4 features are observed: NCO on the support at 2300 cm^{-1} and the three bands related to C- and N- species below 1600 cm^{-1}. The intensity of the species assigned to NCO on alumina at 2300 cm^{-1} increases as the NO/CO ratios decreases, varying from oxidizing to reducing conditions. The species below 1600 cm^{-1} follow a similar trend, suggesting again a potential correlation between these species.

In addition, we do not find correlations between the high NCO intensity and NH_3 formation. It was proposed that NCO might be involved in NH_3 formation, via NCO hydrolysis. However, this catalyst, characterized by large Rh particle size does not exhibit higher NH_3 formation, compared to the smaller particle size. However, the NCO intensity is an order of magnitude larger. This suggests that NCO is not involved, or it is not the only species involved in NH_3 formation.

To investigate the species present on the Rh surface, we focused on the region between 2100 and 1600 cm^{-1}. No linear CO bound on Rh^0 is observed, consistent with previous observations according to which when the catalyst is exposed to NO and CO, NO preferentially adsorbs on the nanoparticle. $Rh(CO)_2$ species are positioned at 2020 and 2090 cm^{-1} and exhibits low intensity,. The peaks assigned to NO on Rh are barely noticeable, most likely because they are obscured by the high intensity features located below 1600 cm^{-1}. However, under oxidizing conditions, with a NO/CO ratio of 2, Rh-NO^+ is observed, consistent with previous data and consistent with a Rh

surface mainly covered by O adatoms and molecularly adsorbed NO, which cannot dissociate due to the lack of available sites.

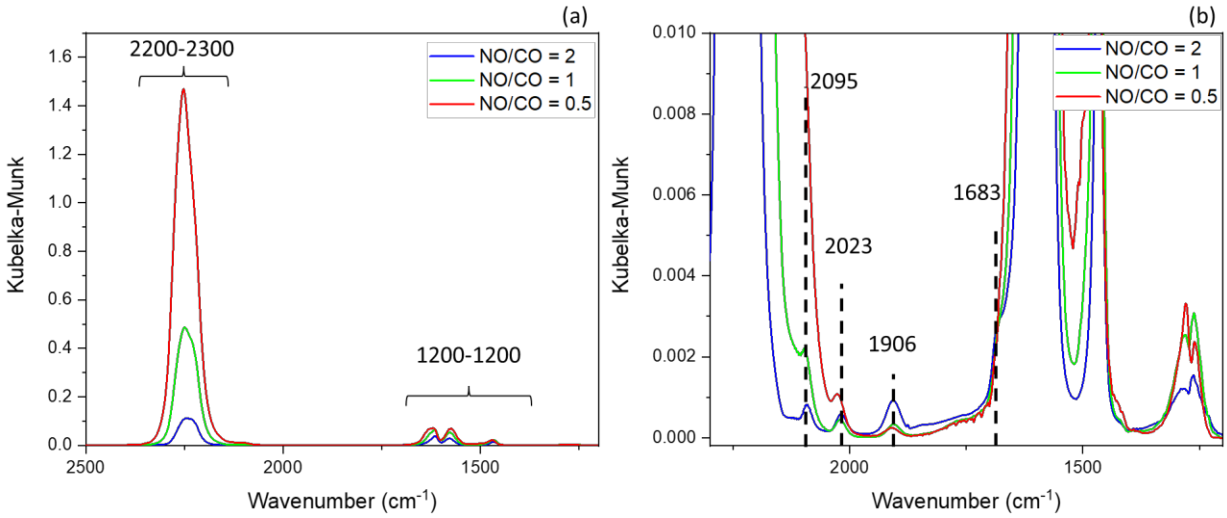

Figure 5.21: CO + NO adsorption on 0.1% Rh/Al_2O_3 – 9.1nm using DRIFTS. The catalyst was treated in 1% O_2 at 500°C for 30 min, followed by Ar purge and reduced in 5% H_2 at 500°C for 30 min. The temperature decreased to 265°C in Ar. The catalyst was then exposed to NO-CO mixture until no changes in spectra were detected. CO = 5000 ppm; NO varying to obtain NO/CO = 2 (blue), 1 (green) and 0.5 (red). (a) spectral region between 1200 and 2500 cm^{-1}; (b) focus on the region between 1200 and 2500 cm^{-1}

The kinetic and spectroscopic data on the Rh catalyst with larger particle size indicate that NH_3 has no effect on the conversion profile or the activation energy, indicating that only highly dispersed catalysts are affected. In addition, these results suggest that NCO, which forms in large amount on larger Rh nanoparticle catalysts, is not responsible for the change in kinetics or NH_3 formation.

5.3.16 Hypothesis N. 2: negative effect of NH_3 on the reaction rate

We hypothesized that the change in the apparent activation energy was due to the inhibiting effect of NH_3 on the NO + CO reaction rate. It was previously shown that product inhibition could induce

changes in kinetic parameters.[88–90] Therefore, we measured the NH_3 reaction order on the NO reduction rare in the presence of water and for NO/CO = 2, 1 and 0.5.

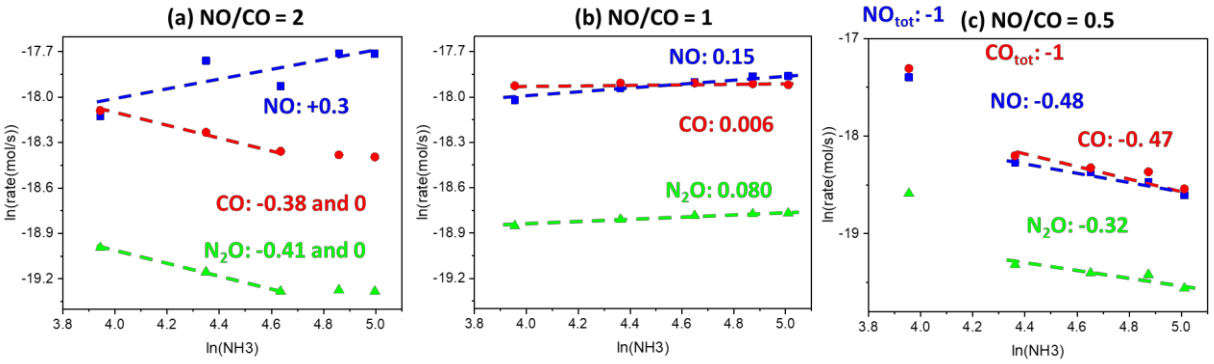

Figure 5.22: NH_3 reaction order on 0.1% Rh/Al_2O_3 1.1 nm.. The catalyst was reduced in 5% H_2 for 30 min at 500°C. The reaction mixture included CO = 1000 ppm; NO varying to obtain (a) NO/CO = 2; (b) NO/CO = 1; (c);NO/CO = 0.5, H_2O = 6%; NH_3 varied between 50 and 150 ppm

Figure 5.22 shows the NH_3 reaction order dependency of NO and CO consumption rates as well as the N_2O formation rate. Each point took 24h to reach a steady state. Under NO/CO = 0.5, under reducing conditions, we measured a slightly negative NH_3 reaction order. For NO/CO = 1 the NH_3 order was 0, while for NO/CO = 2, NH_3 has a slightly positive order on NO consumption rate, consistent with a reaction between NO and NH_3. However, it displayed a slightly negative reaction order on N_2O formation and CO consumption rates.

We also observed that under reducing conditions, the net NH_3 formation decreased with increasing NH_3 concentration. This could be attributed to two potential factors:

- Negative NH_3 reaction order in NH_3 formation
- Deactivation due to sintering or formation of stable species which block the active sites.

5.3.17 TPD performed after NH_3 order measurement

To test the hypothesis of possible formation of stable surface species on the active sites, we performed a TPD after the NH_3 reaction order measurements in the presence of water (Figure 5.22). This hypothesis was corroborated by the DRIFTS spectra obtained during TPD after NO+CO+NH_3 under reducing conditions, revealing the presence of stable surface species at 500°C. Figure 5.22 shows the desorption of NH_3 (a) and CO (b) during the TPD. NH_3 exhibited two features: one at 358°C and another one at 526°C, while CO showed a desorption peak at 517°C. A quantification analysis of the area under the CO profile, normalized by the Rh surface moles, yielded a value higher than 1. This suggests that CO does not only desorb from the metal site but that the support is also involved.

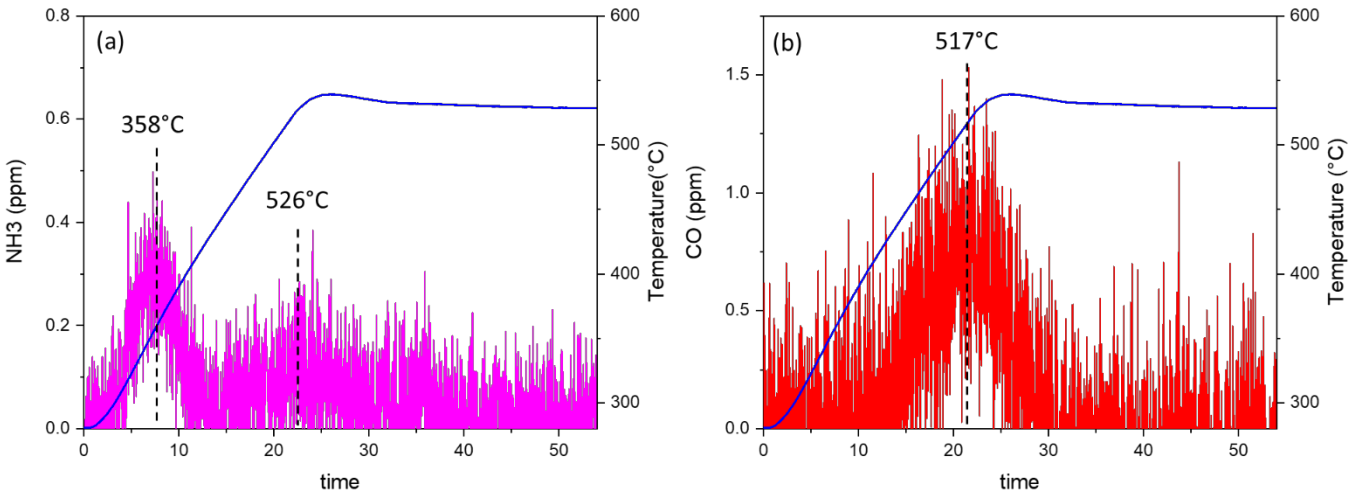

Figure 5.23: TPD after NO + CO wet – NH_3 reaction order with NO/CO = 0.5. The catalyst was reduced in 5% H_2 for 30 min at 500°C. After the catalyst was exposed to the reaction mixture including CO = 1000 ppm; NO = 500 ppm; H_2O = 6%; NH_3 varied between 50 and 150 ppm, diluted in N_2, the system was purged with N_2 and the temperature was increased to 500°C at 10°C/min.

In addition, to investigate the possibility of deactivation, we replicated the experiment of NO reduction by CO under reducing conditions and in the presence of water. The conversion profiles

exhibited a shift to higher temperature, confirming an irreversible deactivation after the NH_3 order of reaction experiment. In addition, a change in product selectivity was observed. The new N_2O selectivity is similar at low conversion but higher at high conversions. N_2 selectivity increased at the expense of NH_3 selectivity. The reduced NH_3 selectivity is consistent with both hypothesis of deactivation due to sintering and the aggregation of single atoms into nanoparticles.

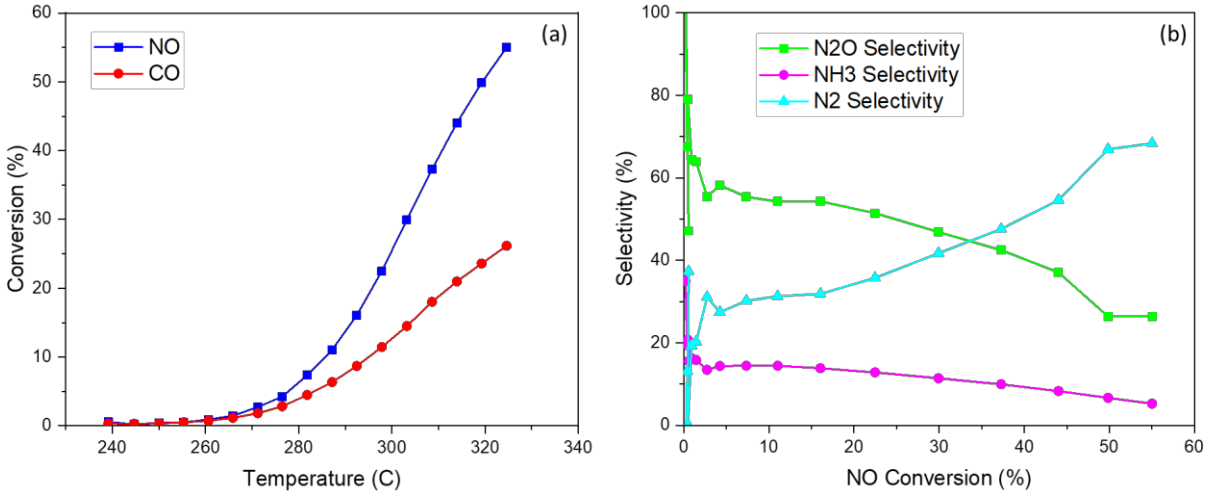

Figure 5. 24 repeated NO reduction by CO in the presence of water – NO and CO conversion and N_2O and NH_3 selectivity. The catalyst was reduced in 5% H_2 for 30 min at 500°C. The reaction mixture included CO = 1000 ppm; NO = 500 ppm; H_2O = 6%;

To investigate the hypothesis of deactivation due to sintering, we took several approaches:

- Particle size measurements via H_2 chemisorption of a 0.1% Rh/Al_2O_3 after treatments under several reaction mixtures including NO, CO, NH_3 and H_2O for 24 h at 300°C;
- Investigation of surface species during the adsorption of NO, CO (and NH_3) for 24 h

5.3.18 CO DRIFTS post NO + CO (and NH_3) exposure for 24h at 300°C

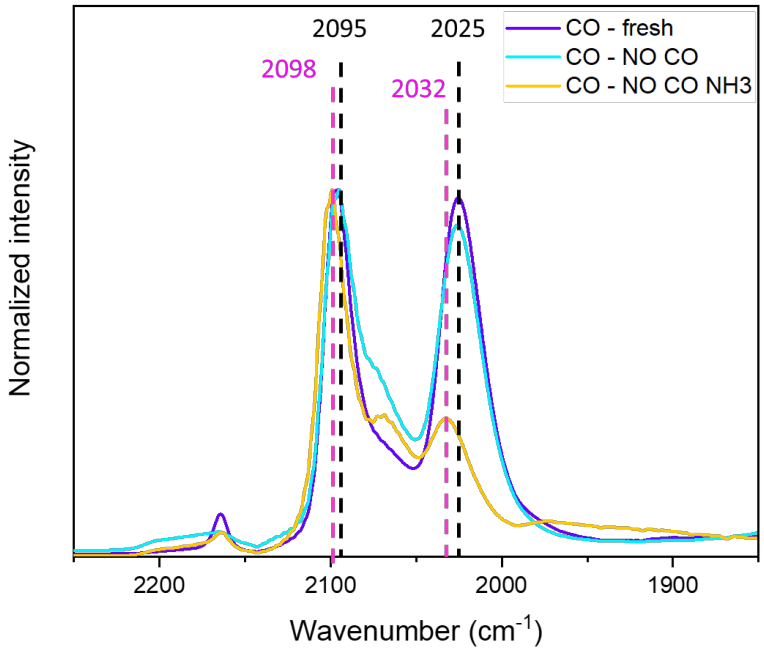

Figure 5.25: CO adsorption using DRIFTS on 0.05% Rh/Al_2O_3 fresh (purple), NO CO 24 h treated at 300°C (light-blue) and NO CO NH_3 for 24 h treated at 300°C (yellow). The catalyst was exposed to the reaction mixture including CO = 5000 ppm; NO = 2500 ppm for 24 h at 300°C and CO = 5000 ppm; NO = 2500 ppm; NH_3 = 500 ppm for 24 h at 300°C. Prior to CO adsorption, the catalyst was treated in 1% O_2 for 30 min at 500°C, followed by a purge in Ar and reduction in 5% H_2 for 30 min at 500°C. The temperature was then decreased to 35°C in At and the catalysts were exposed to CO = 5000 ppm until saturation.

CO DRIFTS was performed on a 0.05% Rh/Al_2O_3 catalyst, characterized by 100% dispersion, measured via H_2 chemisorption. The catalyst was treated in-situ with a mixture of NO + CO and NO + CO + NH_3 at 300°C for 24 h. Afterwards, the catalyst was reduced in 5%H_2/Ar at 400°C and exposed to CO at 35°C. In Figure 5.25, the fresh catalyst exhibits two peaks at 2098 and 2025 cm^{-1}, assigned to the gem-dicarbonyl species. These two peaks are consistent with the CO-assisted disintegration of Rh_{NP} into Rh_{SA}, especially for smaller particle size catalysts. The peak at 2095 cm^{-1} shows a small shoulder, assigned to linear CO on Rh_{NP}. No CO bridge bound to Rh_{NP} is

observed, consistent with the high dispersion measure via H_2 chemisorption. After the exposure to NO and CO, we still observe $Rh(CO)_2$ species, however, the peak assigned to Rh_{NP} at 2075 cm^{-1} shows an increased intensity, suggesting that aggregation occurred. After exposure to CO, NO and NH_3, we observe that the feature assigned to Rh_{NP} centered at 2070 cm^{-1} increased in intensity, suggesting significant aggregation has occurred. In addition, two peaks centered at 1974 and 1923 cm^{-1} are also observed. These are assigned to CO bridge bound to Rh_{NP}. The gem-dicarbonyl features are still present, however, they show a blue-shift compared to the other spectra. The slight blue shift might be related to the lack of OH groups in the Rh coordination environment.[77]

Interestingly, when comparing the spectra after purging CO from the gas phase, shown in Figure 5. ***26***, the catalyst exposed to NO, CO and NH_3 shows a peak at 2145 cm^{-1}. The peak position is similar to the feature observed during the CO + NO exposure in Figure 5.13. This peak might be related to NCO on Rh,[56,58,72] however, this hypothesis is unlikely as we do not observe the spillover of NCO onto the alumina, typically positioned in the spectral region above 2200 cm^{-1}. Alternatively, the peak at 2145 cm^{-1} could be attributed to oxidized Rh, given its position above 2100 cm^{-1}. The peak present at 2180 is assigned to CO on alumina.[91]

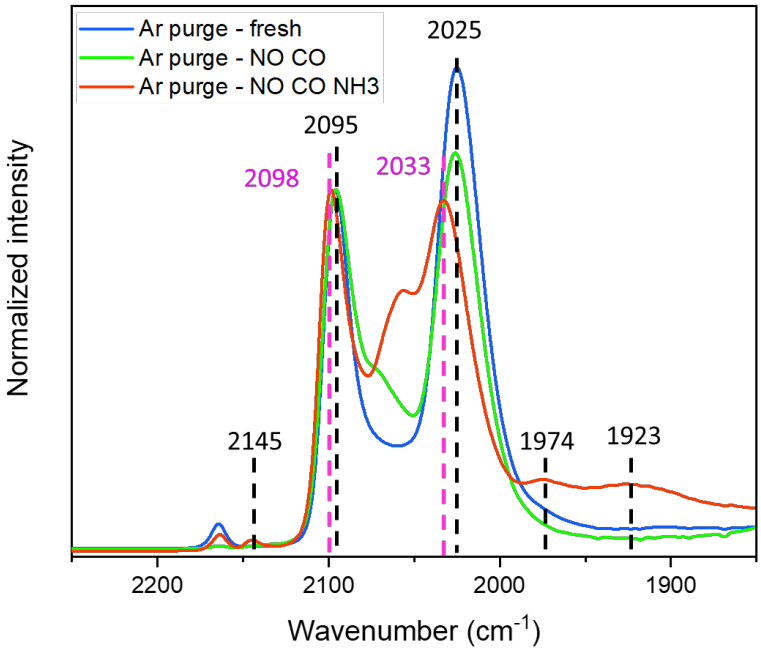

Figure 5. 26: Ar purge after CO adsorption. using DRIFTS on 0.05% Rh/Al_2O_3 fresh (purple), NO CO 24 h treated at 300°C (light-blue) and NO CO NH_3 for 24 h treated at 300°C (yellow). The catalyst was exposed to the reaction mixture including CO = 5000 ppm; NO = 2500 ppm for 24 h at 300°C and CO = 5000 ppm; NO = 2500 ppm; NH_3 = 500 ppm for 24 h at 300°C. Prior to CO adsorption, the catalyst was treated in 1% O_2 for 30 min at 500°C, followed by a purge in Ar and reduction in 5% H_2 for 30 min at 500°C. The temperature was then decreased to 35°C in Ar and the catalysts were exposed to CO = 5000 ppm until saturation. The system was finally purged with Ar until no changes in spectra were detected.

5.3.19 H_2 chemisorption after NO CO (H_2O and NH_3) treatments.

To have a quantitative analysis of how NH_3 and water contribute to sintering and to relate that to the changes in kinetics and product selectivity, we exposed a 0.1% Rh/Al_2O_3 at 300°C for 24 h to a mixture of gases containing:

- NO + CO/N_2
- NO + CO + NH_3/N_2
- NO + CO + H_2O/N_2

- $NO + CO + H_2O + NH_3/N_2$

This allowed us to study the effect of H_2O and NH_3.

The effect of $NO + CO + H_2O$ for 24 h was also investigated at 350C, because it is the temperature at which the inflection point in Figure 1 occurs.

Table 3 lists the dispersions derived from H_2 chemisorption. The fresh catalyst exhibited a dispersion of 143% dispersion. A H:Rh higher than 1 was previously reported for particle sizes smaller than 1 nm.[92] Therefore, even though 143% dispersion represents an unphysical realistic value, we will use it to compare with the other obtained dispersions, knowing that the real dispersion is near 100% and the catalyst is characterized by sub nanometer clusters. The dispersion obtained after treating the catalyst with $NO + CO$ and $NO + CO + NH_3$ show similar values around 130%. This suggests that exposure to $NO + CO$, and NH_3, does not vary the particle size. The dispersions obtained after exposing the catalyst to the wet feeds show around 90% dispersion. Also in this case, NH_3 does not affect the particle size, suggesting water is most likely the cause of the decrease in dispersion. We can conclude that significant sintering does not occur after exposing the catalyst to a dry $NO + CO$ feed for 24 h. However, water causes a decrease in Rh adsorption capacity, caused either by sintering or sites blocked by stable surface species. The decrease in Rh adsorption capacity was further decreased after the catalyst was exposed to a mixture of NO, CO and H_2O at 350°C for 24 h. Future work should focus on studying spectroscopically how the Rh changes its structure on the 0.1% Rh/Al_2O_3 during NO and CO exposure in the presence and absence of water.

Table 5. 4: H_2 chemisorption dispersion measurements, assuming the stoichiometry of H:Rh = 1:1

Catalyst	**Dispersion (%)**	**Particle size (nm)**
0.1% Rh/Al_2O_3 fresh	143	<1
0.1% Rh/Al_2O_3 – NO CO 300°C	128	<1

0.1% Rh/Al_2O_3 – NO CO NH_3 300°C	127	<1
0.1% Rh/Al_2O_3 – NO CO H_2O 300°C	92	1.1
0.1% Rh/Al_2O_3 – NO CO H_2O NH_3 300°C	94	1.1
0.1% Rh/Al_2O_3 – NO CO H_2O 350°C	72	1.4

5.3.20 DRIFTS during NO + CO exposure

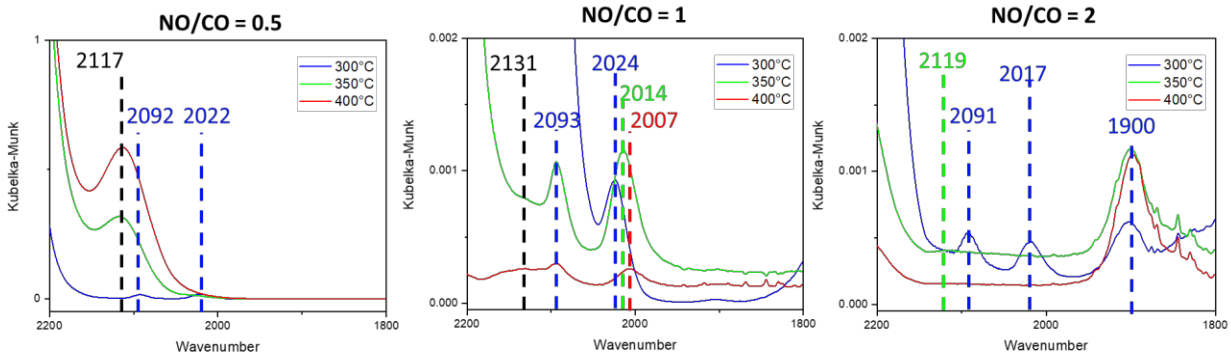

Figure 5.27: NO + CO exposure on 0.1% Rh-Al_2O_3 at 300, 350 and 400°C. The catalyst was treated in 1% O_2 for 30 min at 500°C, followed by a purge in Ar and reduction in 5% H_2 for 30 min at 500°C. The catalyst was the exposed to a reaction mixture including CO = 5000 ppm, NO varying to obtain NO/CO = 0.5 (b); NO/CO = 1 (c); NO/CO = 2. The effect of the reaction mixtures on the surface speciation was investigated at 300, 350 and 400°C. Spectra were taken until no changes were detected.

Figure 5.27 shows the preliminary spectra obtained after exposing the catalyst at 300, 350 and 400°C, under NO/CO ratio = 0.5, 1 and 2. We mainly focus the analysis in the region between 2200 and 1800 cm^{-1} since it is the region that showed the clearest differences. With NO/CO = 0.5, under reducing conditions, we initially observe the gem-dicarbonyl species. As the temperature increases, $Rh(CO)_2$ species decrease in intensity, while a feature at 2117 cm^{-1} increases in intensity. A similar feature is observed under stoichiometric conditions, NO/CO = 1, at a slightly higher frequency. However, under stoichiometric conditions, $Rh(CO)_2$ species remain present until 400°C, even though their intensity is decreased. Under oxidizing conditions, at 300°C we observe

the presence of $Rh(CO)_2$ species and Rh-NO^+, suggesting a lower extent of particle disintegration. At higher temperature, we do not observe the presence of gem-dicarbonyl species, but we still observe Rh-NO^+, suggesting that NO still preferentially adsorbs on Rh nanoparticles. Unlike the other ratios under investigation, we cannot distinguish the presence of the species at high wavenumber. It could be related to NCO on the metal surface or some Rh oxide species, given the location at frequencies higher than 2100 cm^{-1}.

5.4 Conclusions

The investigations into NO reduction by CO reactions remain inconclusive. However, we can summarize our findings as follows:

- The presence of water induces a change in the apparent activation energy, leading to an increase in its value;
- NH_3 effect was investigated to explore its role in altering the kinetics. NH_3 exhibited a slight negative order during NO reduction by CO reaction in the presence of water. However, the observed decrease in reaction rates with an increase in NH_3 concentration might be indicative of catalyst deactivation;
- Spectroscopic studies showed that NH_3 causes changes in the gem-dicarbonyl species behavior during temperature programmed desorption;
- Two potential causes of catalyst deactivation were explored: sintering and the presence of stable surface species. H_2 chemisorption confirmed a decrease in Rh adsorption capacity after the catalyst was exposed to NO, CO and H_2O, with NO/CO ratio = 0.5, at 350°C for 24 h, while spectroscopic studies confirmed the presence of a surface species located at higher wavenumber, which still remains unassigned.

More work is required to understand the identity and the role of this species during the reaction. In addition, the cause of the lower adsorption capacity showed by the chemisorption needs further investigation.

5.5 References

(1) Heck, R. M.; Farrauto, R. J. Automobile Exhaust Catalysts. *Appl Catal A Gen* **2001**, *221*, 443–457.

(2) Farrauto, R. J.; Heck, R. M. Catalytic Converters: State of the Art and Perspectives. **1999**, *51*, 351–360.

(3) Farrauto, R. J.; Deeba, M.; Alerasool, S. Gasoline Automobile Catalysis and Its Historical Journey to Cleaner Air. *Nature Catalysis*. Nature Publishing Group July 1, 2019, pp 603–613. https://doi.org/10.1038/s41929-019-0312-9.

(4) Ronald M. Heck, R. J. F. with S. T. G. *Catalytic Air Pollution Control Commercial Technology*, Third Edit.; John Wiley & Sons: Hoboken, New Jersey, 2008.

(5) Fangmeier, A.; Hadwiger-Fangmeier, A.; Van der Eerden, L.; Jäger, H.-J. Effects of Atmospheric Ammonia on Vegetation—A Review. *Environmental Pollution* **1994**, *86* (1), 43–82. https://doi.org/10.1016/0269-7491(94)90008-6.

(6) Gong, L.; Lewicki, R.; Griffin, R. J.; Tittel, F. K.; Lonsdale, C. R.; Stevens, R. G.; Pierce, J. R.; Malloy, Q. G. J.; Travis, S. A.; Bobmanuel, L. M.; Lefer, B. L.; Flynn, J. H. Role of Atmospheric Ammonia in Particulate Matter Formation in Houston during Summertime. *Atmos Environ* **2013**, *77*, 893–900. https://doi.org/10.1016/j.atmosenv.2013.04.079.

(7) Behera, S. N.; Sharma, M. Investigating the Potential Role of Ammonia in Ion Chemistry of Fine Particulate Matter Formation for an Urban Environment. *Science of The Total Environment* **2010**, *408* (17), 3569–3575. https://doi.org/10.1016/j.scitotenv.2010.04.017.

(8) Richardson, D.; Felgate, H.; Watmough, N.; Thomson, A.; Baggs, E. Mitigating Release of the Potent Greenhouse Gas N2O from the Nitrogen Cycle – Could Enzymic Regulation Hold the Key? *Trends Biotechnol* **2009**, *27* (7), 388–397. https://doi.org/10.1016/j.tibtech.2009.03.009.

(9) Hendershot~, R. E.; Hansen, R. S. *Reduction of Nitric Oxide with Carbon Monoxide on the Rh(LOO) Single-Crystal Surface*; 1986; Vol. 98.

(10) Wolf, R. M.; Siera, J.; Van Delft, F. C. M. J. M.; Nieuwenhuys, B. E. A Comparative Study of the Behaviour of Single-Crystal Surfaces and Supported Catalysts in NO Reduction and CO Oxidation over Pt-Rh Alloys. *Faraday Discuss Chem Soc* **1989**, *87* (1), 275–289. https://doi.org/10.1039/DC9898700275.

(11) Kahlweit, M.; Strey, R. Kinetics of CO Oxidation by O2 or NO on Rh(Ll1) and Rh(100) Single Crystals. *J. Phys. Chem* **1988**, *92* (13), 124–142.

(12) Peden, C. H. F.; Goodman, D. W.; Blair, D. S.; Berlowitz, P. J.; Fisher, G. B.; Oh, S. H. Kinetics of CO Oxidation by O2 or NO on Rh(111) and Rh(100) Single Crystal. *Journal of Physical Chemistry* **1988**, *92* (6), 1563–1567. https://doi.org/10.1021/j100317a038.

(13) Oh, S. H.; Fisher, G. B.; Carpenter, J. E.; Goodman, D. W. Comparative Kinetic Studies of CO□O2 and CO□NO Reactions over Single Crystal and Supported Rhodium Catalysts. *J Catal* **1986**, *100* (2), 360–376. https://doi.org/10.1016/0021-9517(86)90103-X.

(14) Pande, N. K.; Bell, A. T. Influence of Support Composition on the Reduction of Nitric Oxide over Rhodium Catalysts. **1986**, *16*, 7–16.

(15) Cortés, J.; Jimenez, R.; Araya, P. Infrared Study of the Influence of Surface Hydrophobicity of the Support of Rh/SiO2 Catalysts. *Catal Letters* **2002**, *82* (3–4), 255–259. https://doi.org/10.1023/A:1020587500070.

(16) Granger, P.; Dathy, C.; Lecomte, J. J.; Leclercq, L.; Prigent, M.; Mabilon, G.; Leclercq, G. *Kinetics of the NO and CO Reaction over Platinum Catalysts I. Influence of the Support*; 1998; Vol. 173.

(17) Holles, J. H.; Switzer, M. A.; Davis, R. J. Influence of Ceria and Lanthana Promoters on the Kinetics of NO and N2O Reduction by CO over Alumina-Supported Palladium and Rhodium. *J Catal* **2000**, *190* (2), 247–260. https://doi.org/10.1006/jcat.1999.2780.

(18) Oh, S. H.; Eickel, C. C. Influence of Metal Particle Size and Support on the Catalytic Properties of Supported Rhodium: COO2 and CONO Reactions. *J Catal* **1991**, *128* (2), 526–536. https://doi.org/10.1016/0021-9517(91)90310-Z.

(19) Asokan, C.; Yang, Y.; Dang, A.; Getsoian, A.; Christopher, P. Low-Temperature Ammonia Production during NO Reduction by CO Is Due to Atomically Dispersed Rhodium Active Sites. *ACS Catal* **2020**, *10* (9), 5217–5222. https://doi.org/10.1021/acscatal.0c01249.

(20) Wang, C.; Tan, J.; Harle, G.; Gong, H.; Xia, W.; Zheng, T.; Yang, D.; Ge, Y.; Zhao, Y. Ammonia Formation over Pd/Rh Three-Way Catalysts during Lean-to-Rich Fluctuations: The Effect of the Catalyst Aging, Exhaust Temperature, Lambda, and Duration in Rich Conditions. *Environ Sci Technol* **2019**, *53* (21), 12621–12628. https://doi.org/10.1021/acs.est.9b03893.

(21) Yoo, C. J.; Getsoian, A. (Bean); Bhan, A. NH3 Formation Pathways from NO Reduction by CO in the Presence of Water over Rh/Al2O3. *Appl Catal B* **2021**, *286*. https://doi.org/10.1016/j.apcatb.2021.119893.

(22) Prikhodko, V. Y.; Parks, J. E.; Pihl, J. A.; Toops, T. J. Ammonia Generation and Utilization in a Passive SCR (TWC+SCR) System on Lean Gasoline Engine. *International Journal of Engines* **2016**, *9* (2), 1289–1295. https://doi.org/10.2307/26284897.

(23) Lorimer, A.; Bell, A. T. *Reduction of NO by CO over a Silica-Supported Platinum Catalyst: Infrared and Kinetic Studies*; 1979; Vol. 59.

(24) Hecker' And, W. C.; Bell, A. T. *Reduction of NO by CO over Silica-Supported Rhodium: Infrared and Kinetic Studies*; 1983; Vol. 84.

(25) Muraki, H.; Shinjoh, H.; Fujitani, Y. *Reduction of NO by CO over Alumina-Supported Palladium Catalyst*; Kummer, 1986; Vol. 25. https://pubs.acs.org/sharingguidelines.

(26) Granger, P.; Parvulescu, V. I. Catalytic NOx Abatement Systems for Mobile Sources: From Three-Way to Lean Burn after-Treatment Technologies. *Chem Rev* **2011**, *111* (5), 3155–3207. https://doi.org/10.1021/cr100168g.

(27) Granger, P.; Delannoy, L.; Leclercq, L.; Leclercq, G. On the Effect of Deactivation on the Kinetics of CO Oxidation by NO over Pt-Rh Catalysts. *J Catal* **1998**, *177* (1), 147–151. https://doi.org/10.1006/jcat.1998.2086.

(28) Granger, P.; Dujardin, C.; Paul, J. F.; Leclercq, G. An Overview of Kinetic and Spectroscopic Investigations on Three-Way Catalysts: Mechanistic Aspects of the CO + NO and CO + N2O Reactions. In *Journal of Molecular Catalysis A: Chemical*; 2005; Vol. 228, pp 241–253. https://doi.org/10.1016/j.molcata.2004.09.081.

(29) Granger, P.; Lecomte, J. J.; Dathy, C.; Leclercq, L.; Leclercq, G. Kinetics of the CO + NO Reaction over Rhodium and Platinum-Rhodium on Alumina: II. Effect of Rh Incorporation to Pt. *J Catal* **1998**, *175* (2), 194–203. https://doi.org/10.1006/jcat.1998.2014.

(30) Granger, P.; Malfoy, P.; Leclercq, G. Kinetics of the CO + N2O Reaction over Noble Metals: II. Rh/Al2O3and Pt-Rh/Al2O3. *J Catal* **2004**, *223* (1), 142–151. https://doi.org/10.1016/j.jcat.2004.01.017.

(31) Borg, H. J.; Reijerse, J. F. C.-J. M.; van Santen, R. A.; Niemantsverdriet, J. W. The Dissociation Kinetics of NO on Rh(111) as Studied by Temperature Programmed Static Secondary Ion Mass Spectrometry and Desorption. *J Chem Phys* **1994**, *101* (11), 10052–10063. https://doi.org/10.1063/1.467994.

(32) Peden - Structure Sensitivity of the NO CO Reaction over Rh 110 and Rh 111.

(33) Peden, C. H. F.; Belton, D. N.; Schmieg, S. J. Structure Sensitive Selectivity of the NO-CO Reaction over Rh(110) and Rh(111). *Journal of Catalysis*. 1995, pp 204–218. https://doi.org/10.1006/jcat.1995.1204.

(34) Oh, S. H.; Fisher, G. B.; Carpenter, J. E.; Goodmant, D. W. *Comparative Kinetic Studies of CO-O2 and CO-NO Reactions over Single Crystal and Supported Rhodium Catalysts*; 1986.

(35) Oh, S. H.; Eickel, C. C. *Influence of Metal Particle Size and Support on the Catalytic Properties of Supported Rhodium" CO-O2 and CO-NO Reactions*; 1991; Vol. 128.

(36) Unland, M. L. Isocyanate Intermediates in Ammonia Formation over Noble Metal Catalysts for Automobile Exhaust Reactions. *Science (1979)* **1973**, *179* (4073), 567–569. https://doi.org/10.1126/science.179.4073.567.

(37) Unland, M. L. Isocyanate Intermediates in the Reaction of NO and CO over Noble Metal Catalysts. *J Catal* **1973**, *31* (3), 459–465. https://doi.org/10.1016/0021-9517(73)90318-7.

(38) Unland, M. L. Isocyanate Intermediates in the Reaction NO + CO over a Pt/Al2O3 Catalyst. *Journal of Physical Chemistry* **1973**, *77* (16), 1952–1956. https://doi.org/10.1021/j100635a006.

(39) Asokan, C.; Yang, Y.; Dang, A.; Getsoian, A.; Christopher, P. Low-Temperature Ammonia Production during NO Reduction by CO Is Due to Atomically Dispersed Rhodium Active Sites. *ACS Catal* **2020**, *10* (9), 5217–5222. https://doi.org/10.1021/acscatal.0c01249.

(40) Dasari, P. R.; Muncrief, R.; Harold, M. P. Elucidating NH 3 Formation during NO x Reduction by CO on Pt-BaO/Al 2O 3 in Excess Water. In *Catalysis Today*; 2012; Vol. 184, pp 43–53. https://doi.org/10.1016/j.cattod.2011.12.009.

(41) Adams, E. C.; Skoglundh, M.; Elmøe, T.; Carlsson, P.-A. Water–Gas-Shift Assisted Ammonia Formation over Pd/Ce/Alumina. *Catal Today* **2018**, *307*, 169–174. https://doi.org/10.1016/j.cattod.2017.05.035.

(42) Matsubu, J. C.; Yang, V. N.; Christopher, P. Isolated Metal Active Site Concentration and Stability Control Catalytic CO2 Reduction Selectivity. *J Am Chem Soc* **2015**, *137* (8), 3076–3084. https://doi.org/10.1021/ja5128133.

(43) Marino, S.; Wei, L.; Cortes-Reyes, M.; Cheng, Y.; Laing, P.; Cavataio, G.; Paolucci, C.; Epling, W. Rhodium Catalyst Structural Changes during, and Their Impacts on the Kinetics of, CO Oxidation. *JACS Au* **2023**, *3* (2), 459–467. https://doi.org/10.1021/jacsau.2c00595.

(44) Ouyang, R.; Liu, J. X.; Li, W. X. Atomistic Theory of Ostwald Ripening and Disintegration of Supported Metal Particles under Reaction Conditions. *J Am Chem Soc* **2013**, *135* (5), 1760–1771. https://doi.org/10.1021/ja3087054.

(45) Goldsmith, B. R.; Sanderson, E. D.; Ouyang, R.; Li, W. X. CO- and NO-Induced Disintegration and Redispersion of Three-Way Catalysts Rhodium, Palladium, and Platinum: An Ab Initio Thermodynamics Study. *Journal of Physical Chemistry C* **2014**, *118* (18), 9588–9597. https://doi.org/10.1021/jp502201f.

(46) Yates, J. T.; Kolasinski, K. Infrared Spectroscopic Investigation of the Rhodium Gem-Dicarbonyl Surface Species. *J Chem Phys* **1983**, *79* (2), 1026–1030. https://doi.org/10.1063/1.445844.

(47) Berkó, A.; Solymosi, F. Adsorption-Induced Structural Changes of Rh Supported by TiO2(110)-(1×2): An STM Study. *J Catal* **1999**, *183* (1), 91–101. https://doi.org/10.1006/JCAT.1998.2368.

(48) Novs, E.; Sprinceana, D.; Solymosi, F. CO-Induced Structural Changes of Supported Rh Promoted by NO. *Appl Catal A Gen* **1997**, *149*, 89–101.

(49) Rice, C. A.; Worley, S. D.; Curtis, C. W.; Guin, J. A.; Tarrer, A. R. The Oxidation State of Dispersed Rh on Al2O3. *J Chem Phys* **1981**, *74* (11), 6487–6497. https://doi.org/10.1063/1.440987.

(50) Cavanagh, R. R.; Yates, J. T. Site Distribution Studies of Rh Supported on Al2O3 - An Infrared Study of Chemisorbed CO. *J Chem Phys* **1981**, *74* (7), 4150–4155. https://doi.org/10.1063/1.441544.

(51) Wang, H. P.; Yates, J. T. Spectroscopic Study of the Interconversion of Chemisorbed Surface Species: The Reaction RhI(CO)2 + CO → Rh1(CO)3. *J Catal* **1984**, *89* (1), 79–92. https://doi.org/10.1016/0021-9517(84)90282-3.

(52) Yates, J. T.; Duncan, T. M.; Vaughan, R. W. Infrared Spectroscopic Study of Activated Surface Processes: CO Chemisorption on Supported Rh. *Journal of Chemical Physics* **1979**, *71* (10), 3908–3915. https://doi.org/10.1063/1.438159.

(53) Yates, J. T.; Duncan, T. M.; Worley, S. D.; Vaughan, R. W. Infrared Spectra of Chemisorbed CO on Rh. *J Chem Phys* **1979**, *70* (3), 1219–1224. https://doi.org/10.1063/1.437603.

(54) Yates, D. J. C.; Sinfelt, J. H. The Catalytic Activity of Rhodium in Relation to Its State of Dispersion. *J Catal* **1967**, *8* (4), 348–358. https://doi.org/10.1016/0021-9517(67)90331-4.

(55) Almusaiteer, K. A.; Chuang, S. S. C. Infrared Characterization of Rh Surface States and Their Adsorbates during the NO-CO Reaction. *Journal of Physical Chemistry B* **2000**, *104* (10), 2265–2272. https://doi.org/10.1021/JP9922155/ASSET/IMAGES/MEDIUM/JP9922155E00003.GIF.

(56) Araya, P.; Gracia, F.; Cortés, J.; Wolf, E. E. FTIR Study of the Reduction Reaction of NO by CO over Rh/SiO2 Catalysts with Different Crystallite Size. *Appl Catal B* **2002**, *38* (2), 77–90. https://doi.org/10.1016/S0926-3373(02)00019-X.

(57) Anderson, J. A.; Millar, G. J.; Rochester, C. H. Infrared Study of the Adsorption of NO, NO2 and CO on Rh/Al2O3 Catalysts. *Journal of the Chemical Society, Faraday Transactions* **1990**, *86* (3), 571–576. https://doi.org/10.1039/FT9908600571.

(58) Chuang, S. S. C.; Tan, C.-D. *Combined Infrared and Mass Spectrometric Study of Reactions of Adsorbed NO and CO on 0.5 Wt% Rh/SiO2 Catalyst*; 1997; Vol. 35.

(59) Dictor, R. O. N. An Infrared Study of the Behavior of CO , NO , and CO + NO over Rh / A1203 Catalysts. **2000**, *99* (1988), 89–99.

(60) Solymosi, F.; Sárkány, J. An Infrared Study of the Surface Interaction between NO and CO on Rh/Al2O3 Catalyst. *Applications of Surface Science* **1979**, *3* (1), 68–82. https://doi.org/10.1016/0378-5963(79)90061-8.

(61) Srinivas, G.; Chuang, S. S. C.; Debnath Santanu. An in Situ Infrared Study of the Reactivity of Adsorbed NO and CO on Rh Catalysts. *J Catal* **1994**, *148*, 748–758.

(62) Srinivas, G.; Chuang, S. S. C.; Debnath, S. Interaction of NO and CO on Rh—SiO 2 and Ce—Rh—SiO 2 Catalysts ; 1994; pp 157–167. https://doi.org/10.1021/bk-1994-0552.ch012.

(63) Arai, H.; Tominaga, H. An Infrared Study of Nitric Oxide Adsorbed on Rhodium-Alumina Catalyst. *J Catal* **1976**, *43* (1–3), 131–142. https://doi.org/10.1016/0021-9517(76)90300-6.

(64) Chafik, T.; Kondarides, D. I.; Verykios, X. E. Catalytic Reduction of NO by CO over Rhodium Catalysts: 1. Adsorption and Displacement Characteristics Investigated by In Situ FTIR and Transient-MS Techniques. *J Catal* **2000**, *190* (2), 446–459. https://doi.org/10.1006/jcat.1999.2763.

(65) Root, T. W.; Schmidt, L. D.; Fisher, G. B. *NITRIC OXIDE REDUCTION BY CO ON Rh(Ll1): TEMPERATURE PROGRAMMED REACTION **; 1985; Vol. 150.

(66) Baraldi, A.; Dhanak, V. R.; Comelli, G.; Kiskinova, M.; Rosei, R. *NO Dissociation and NO + CO Reaction on Rh(110): Influence of the Surface Structure and Composition on the Reaction Rates*; 1993; Vol. 68.

(67) Liang, J.; Wang, P.; Spicer, L. D. FT-IR Study of Nitric Oxide Chemisorbed on Rh / Al203. **1985**, 5840–5845. https://doi.org/10.1021/j100272a053.

(68) Brown, W. A.; King, D. A. NO Chemisorption and Reactions on Metal Surfaces: A New Perspective. *Journal of Physical Chemistry B* **2000**, *104* (12), 2578–2595. https://doi.org/10.1021/jp9930907.

(69) Brown, W. A.; Gardner, P.; Jigato, M. P.; King, D. A. Characterization and Orientation of Adsorbed NO Dimers on Ag{111} at Low Temperatures. *J Chem Phys* **1995**, *102* (18), 7277–7280. https://doi.org/10.1063/1.469039.

(70) Leewis, C. M.; Kessels, W. M. M.; Sanden, M. C. M. van de; Niemantsverdriet, J. W. Ammonia Adsorption and Decomposition on Silica Supported Rh Nanoparticles Observed by in Situ Attenuated Total Reflection Infrared Spectroscopy. *Appl Surf Sci* **2006**, *253* (2), 572–580. https://doi.org/10.1016/j.apsusc.2005.12.115.

(71) Paganelli, S.; Tassini, R.; Rathod, V. D.; Onida, B.; Fiorilli, S.; Piccolo, O. A Low Rhodium Content Smart Catalyst for Hydrogenation and Hydroformylation Reactions. *Catal Letters* **2021**, *151* (5), 1508–1521. https://doi.org/10.1007/s10562-020-03407-5.

(72) Paul, D. K.; Marten, C. D. Spectroscopic Observation of a Precursor Complex to Rh-NCO and Al3+-NCO Formation during CO/NH3 Reactions on Rh/Al2O3. *Langmuir* **1998**, *14* (14), 3820–3824. https://doi.org/10.1021/la980108g.

(73) Paul, D. K.; Marten, C. D. *Spectroscopic Observation of a Precursor Complex to Rh-NCO and Al 3+-NCO Formation during CO/NH 3 Reactions on Rh/Al 2 O 3*; 1998. https://pubs.acs.org/sharingguidelines.

(74) Macleod, N.; Lambert, R. M. An in Situ DRIFTS Study of Efficient Lean NOx Reduction with H2 + CO over Pd/Al2O3: The Key Role of Transient NCO Formation in the Subsequent Generation of Ammonia. *Appl Catal B* **2003**, *46* (3), 483–495. https://doi.org/10.1016/S0926-3373(03)00289-3.

(75) Solymosi, F.; Bansagi, T.; Novak, &a. *Effect of NO on the CO-Induced Disruption of Rhodium Crystallites*; 1988; Vol. 112.

(76) Hoffman, A. J.; Asokan, C.; Gadinas, N.; Kravchenko, P.; Getsoian, A. “Bean”; Christopher, P.; Hibbitts, D. Theoretical and Experimental Characterization of Adsorbed CO and NO on γ-Al2O3-Supported Rh Nanoparticles. *Journal of Physical Chemistry C* **2021**, *125* (36), 19733–19755. https://doi.org/10.1021/acs.jpcc.1c05160.

(77) Alexander J. Hoffman, Chithra Asokan, Nicholas Gadinas, Pavlo Kravchenko, Andrew “Bean” Getsoian, Phillip Christopher, and D. H. Experimental and Theoretical Characterization of Rh Single Atoms Supported on

Γ-Al2O3 with Varying Hydroxyl Contents during NO Reduction by CO. **2022**, *12*, 11697–11715. https://doi.org/10.1021/acscatal.2c02813.

(78) Hecker, W. C.; Bell, A. T. Infrared Observations of RhNCO and SiNCO Species Formed during the Reduction of NO by CO over Silica-Supported Rhodium. *J Catal* **1984**, *85* (2), 389–397. https://doi.org/10.1016/0021-9517(84)90228-8.

(79) Kondarides, D. I.; Chafik, T.; Verykios, X. E. Catalytic Reduction of NO by CO over Rhodium Catalysts: 3. The Role of Surface Isocyanate Species. *J Catal* **2000**, *193* (2), 303–307. https://doi.org/10.1006/jcat.2000.2892.

(80) Raskó, J.; Bánsági, T.; Solymosi, F. HCN Adsorption on Silica and Titania Supported Rh Catalysts Studied by FTIR. *Physical Chemistry Chemical Physics* **2002**, *4* (14), 3509–3513. https://doi.org/10.1039/b202672b.

(81) Chambers, D. C.; Angove, D. E.; Cant, N. W. The Formation and Hydrolysis of Isocyanic Acid during the Reaction of NO, CO, and H2 Mixtures on Supported Platinum, Palladium, and Rhodium. *J Catal* **2001**, *204* (1), 11–22. https://doi.org/10.1006/jcat.2001.3359.

(82) Neyertz, C.; Volpe, M.; Perez, D.; Costilla, I.; Sanchez, M.; Gigola, C. NO Reduction with CO in the Presence and Absence of H2O over Pd/γ-Al2O3 and Pd-VOx/γ-Al2O3 Catalysts: The Formation of HNCO, NH3 and Stable Surface Species. *Appl Catal A Gen* **2009**, *368* (1–2), 146–157. https://doi.org/10.1016/j.apcata.2009.08.023.

(83) Schroeder, E. K.; Finzel, J.; Christopher, P. Photolysis of Atomically Dispersed Rh / Al 2 O 3 Catalysts : Controlling CO Coverage in Situ and Promoting Reaction Rates.

(84) Asokan, C.; Thang, H. V.; Pacchioni, G.; Christopher, P. Reductant Composition Influences the Coordination of Atomically Dispersed Rh on Anatase TiO2. *Catal Sci Technol* **2020**, *10* (6), 1597–1601. https://doi.org/10.1039/d0cy00146e.

(85) Tang, Y.; Asokan, C.; Xu, M.; Graham, G. W.; Pan, X.; Christopher, P.; Li, J.; Sautet, P. Rh Single Atoms on TiO2 Dynamically Respond to Reaction Conditions by Adapting Their Site. *Nature Communications 2019 10:1* **2019**, *10* (1), 1–10. https://doi.org/10.1038/s41467-019-12461-6.

(86) Kašpar, J.; de Leitenburg, C.; Fornasiero, P.; Trovarelli, A.; Graziani, M. NO Reduction by CO over Rh Al2O3. Effects of Rhodium Dispersion on the Catalytic Properties. *J Catal* **1994**, *146* (1), 136–143. https://doi.org/10.1016/0021-9517(94)90016-7.

(87) Yang, A.-C.; Choksi, T.; Streibel, V.; Aljama, H.; Wrasman, C. J.; Roling, L. T.; Goodman, E. D.; Thomas, D.; Bare, S. R.; Sánchez-Carrera, R. S.; Schäfer, A.; Li, Y.; Abild-Pedersen, F.; Cargnello, M. Revealing the Structure of a Catalytic Combustion Active-Site Ensemble Combining Uniform Nanocrystal Catalysts and Theory Insights. *Proceedings of the National Academy of Sciences* **2020**, *117* (26), 14721–14729. https://doi.org/10.1073/pnas.2002342117.

(88) Harris, J. W.; Verma, A. A.; Arvay, J. W.; Shih, A. J.; Delgass, W. N.; Ribeiro, F. H. Consequences of Product Inhibition in the Quantification of Kinetic Parameters. *J Catal* **2020**, *389*, 468–475. https://doi.org/10.1016/j.jcat.2020.06.014.

(89) Hamzehlouyan, T.; Sampara, C.; Li, J.; Kumar, A.; Epling, W. Experimental and Kinetic Study of SO2 Oxidation on a Pt/γ-Al2O3 Catalyst. *Appl Catal B* **2014**, *152–153*, 108–116. https://doi.org/10.1016/j.apcatb.2014.01.005.

(90) MULLA, S.; CHEN, N.; CUMARANATUNGE, L.; BLAU, G.; ZEMLYANOV, D.; DELGASS, W.; EPLING, W.; RIBEIRO, F. Reaction of NO and O2 to NO2 on Pt: Kinetics and Catalyst Deactivation. *J Catal* **2006**, *241* (2), 389–399. https://doi.org/10.1016/j.jcat.2006.05.016.

(91) Busca, G.; Lorenzelli, V. INFRARED SPECTROSCOPIC IDENTIFICATION OF SPECIES ARISING FROM REACTIVE ADSORPTION OF CARBON OXIDES ON METAL OXIDE SURFACES G BUSCA, V LORENZELLI. *Materials Chemistry* **1982**, *7*, 89–126. https://doi.org/10.1016/0390-6035(82)90059-1.

(92) Kip, B. J.; Duivenvoorden, F. B. M.; Koningsberger, D. C.; Prins, R. Determination of Metal Particle Size of Highly Dispersed Rh, Ir, and Pt Catalysts by Hydrogen Chemisorption and EXAFS. *J Catal* **1987**, *105* (1), 26–38. https://doi.org/10.1016/0021-9517(87)90005-4.

Chapter 6 : Adapted CO chemisorption technique to measure metal particle dispersion on ceria-containing catalysts

This chapter has been adapted from the article: "Silvia Marino, Raneed Taha, Yuntao Gu and William Epling, Adapted CO chemisorption technique to measure metal particle dispersion on ceria-containing catalysts" (submitted)

6.1 Introduction

The turnover frequency (TOF) is an important parameter in describing a catalytic reaction, providing a measure of catalytic activity and mechanistic insight for improved catalyst design or process development, and allows for the evaluation and comparison of catalysts. [1] By definition, TOF is defined as the moles of product formed per active site per unit time. For metal supported catalysts, TOF is determined as the reaction rate normalized by the number of active sites, which are assumed to be the number of exposed metal atoms. [1–3] Therefore, determination of the active metal surface area is key to quantifying a reaction rate via TOF and studying fundamental catalytic properties of metal supported catalysts.

Several methods are often used to calculate the number of active sites and common techniques include chemisorption, X-ray diffraction (XRD) and transmission electron microscopy (TEM). However, for some catalysts, these traditional techniques present challenges. For example, in the case of Pd/CeO_2 catalysts, the use of TEM can be difficult because of the poor Z contrast between ceria and Pd. [4] Cerium is a heavier element than Pd; therefore, Pd particles are indistinguishable in images because they are obscured by the support. X-ray diffraction (XRD) can be used to estimate the metal crystallite size characterized by particles on average larger than 3 nm. [5,6] However, with smaller particle size, there is less crystallinity leading to weak, or no, diffraction patterns and peak broadening could be difficult to discern in the ceria scattering pattern. [5] Another commonly

employed method for determining metal catalyst active surface area is chemisorption of probe molecules such as CO or H_2. [7] However, again, the accuracy of such measurements performed on Pd/CeO_2 catalysts is compromised. H_2 is known to be soluble in Pd nanoparticles at room temperature, leading to the formation of beta-phase palladium hydride. [8,9] The ability of H_2 to diffuse into Pd bulk affects the H_2 uptake during H_2 chemisorption, leading to a higher than actual dispersion measurement. This phenomenon does depend on Pd particle size, with increasing H_2 solubility with increasing Pd nanoparticle size. [8,10] The formation of beta-phase PdH can be overcome by performing the analysis at 100°C, which is above PdH decomposition temperature. Yet, on ceria supported Pd catalysts, exposure to H_2 at higher temperature leads to a reaction between H_2 and the mobile lattice oxygen of ceria, again leading to a dispersion measurement higher than the actual value. [11–13] CO chemisorption also results in an overestimation of the active surface area, often exceeding unity. This is attributed to the interaction between CO and the support via the formation of carbonates. [14–16] This phenomenon primarily involves the catalyst support; therefore, it remains consistent even when metals other than Pd are deposited onto the ceria.

Challenges in measuring metal dispersion are not limited to Pd/CeO_2 catalysts. Similar difficulties are encountered with other metals and supports. For example, structural changes occurring during probe molecule adsorption on metals can lead to inaccurate dispersion measurements. This has been reported for Rh- and Ir-supported catalysts. Upon CO adsorption at room temperature, Rh and Ir nanoparticles are redispersed into single atoms via the formation of gem-dicarbonyl species, which is characterized by two CO molecules per isolated metal single atom. [17–22] These structural changes lead to a change in the stoichiometric factor used to quantify dispersion, and of course the measurement itself changes the dispersion of the metal in comparison to that under reaction

conditions. Since this process is size dependent, with smaller nanoparticles being more susceptible to particle disintegration into single atoms, the use of CO as a probe molecule for these metals introduces uncertainty in dispersion measurements. Also, phenomena such as H_2 spillover have been observed with other catalysts characterized by oxygen storage material supports and can alter dispersion measurements. [23–25] Considering these complexities, the use of conventional techniques to measure exposed metal sites can become challenging.

Identifying a technique able to measure ceria-supported catalyst dispersion is important given ceria's widespread use in catalysis.[26–29] Ceria is well-known for its ability to store and release oxygen, which can play a role in enhancing reaction rates.[15] When combined with a noble metal, ceria can provide oxygen vacancy and defect sites that facilitate the activation of reactants and promote catalytic reactions.[30] Furthermore, strong-metal support interactions between the active metal and a reducible support can lead to higher catalytic activity.[31] This interaction also can promote metal nanoparticle dispersion, improve stability and enhance resistance to sintering. [32] Due to these properties, ceria is an excellent support material for various catalytic applications, such as gasoline engine aftertreatment systems, [33–35] catalysts for H_2 production, [36–38] oxidation reactions, [37,38] and CO_2 hydrogenation.[39]

Several metal dispersion characterization methods have been proposed for ceria supported catalysts that circumvent the challenges noted above; nonetheless, these are often less accessible or may still lead to complexities in correlating to reaction conditions. For example, colloidal synthesis offers the possibility of gaining deeper understanding of the catalytic properties of a material by precisely controlling the shape and size of catalysts nanoparticles. However, this advantage is

counterbalanced by the use of surfactants that might negatively affect the catalytic activity unless carefully and fully removed.[40] And changes in particle size and morphology often occur during reaction, or during simulated or real aging protocols that lead to heterogeneous particle size distribution or morphology.[17,41] H_2 or CO chemisorption at -78/81°C has been proposed as a viable technique to count active sites. [42,43] At such low temperature, H (or CO) spillover, which normally occurs at ambient temperature and contributes to unrealistically high CO/H_2 uptake, is hindered. However, the longer time required to attain this low temperature allows impurities, such as oxygen, to contaminate the sample and alter the oxidation state of the catalyst that exists in a reduced state.[44] Additionally, the use of structural insensitive reactions kinetics, such as alkene hydrogenation, is an option, even though in some cases it could require a longer time for an accurate analysis, or catalyst deactivation through coke formation occurs influencing available site measurements.[45] Also, the turnover frequency of a structure insensitive reaction at a specific temperature is needed to obtain the total number of exposed metal atoms, This requires the availability of a catalyst with a well-defined dispersion which allows that measure of TOF.

Takeguchi at al.[46] previously proposed a CO pulse chemisorption method that allowed the determination of Pt dispersion on a Pt/CeO_2 catalyst after a sequential pretreatment involving exposure to H_2, O_2, CO_2 then H_2 again. Through IR spectroscopy, the authors showed that the CO_2 preadsorption step led to carbonate formation on ceria and during the subsequent CO pulse no further carbonate formation occurred. Without carbonate formation during the CO exposure, or bound CO formation on Pt during the prior CO_2 exposure, only the metal sites were available for CO adsorption, leading to a reliable CO uptake. However, in the case of Pd-supported catalysts, the last H_2 pretreatment step can be detrimental due to the formation of Pd hydrides, as previously mentioned.

Here, we present a modified method proposed by Takeguchi for quantifying surface Pd at room temperature through static chemisorption, a technique that is more readily available. The modified method involves the exposure of the catalyst to CO_2 before performing CO chemisorption, removing the intermediate H_2 reduction. As previously shown, CO_2 exposure causes the formation of carbonates on the support, leaving the metal site accessible for CO adsorption. This prevents the CO uptake from being influenced by carbonate formation. We evaluated the effectiveness of this technique across different ceria particle sizes as well as Pd/Al_2O_3 catalysts and confirmed its reliability through spectroscopic studies and CO oxidation kinetics.

6.2 Material and Methods

6.2.1 Catalysts synthesis

1 wt% Pd/CeO_2 catalysts with different CeO_2 support particle sizes were prepared via incipient wetness impregnation. $Pd(NO_3)_2$ (10 wt% in 10% HNO_3 solution) purchased from Sigma Aldrich was used as a precursor. Different ceria supports were used in the synthesis process. CeO_2 nanoparticles with advertised sizes of 10 and 100 nm were purchased from US Research Nanomaterials. A material with advertised 25 nm CeO_2 nanoparticles was purchased from Sigma Aldrich. After Pd deposition, the catalysts were dried using a Thermo Scientific Lindberg muffle furnace at 120°C for 4h in static air. The temperature was then increased to 550°C at a rate of 1°C/min and held for 4h. Separately, CeO_2 with a nominal particle size of 1 μm was impregnated with $Pd(NO_3)_2*2H_2O$, purchased from Sigma Aldrich to obtain 0.2, 0.8 and 1.2 wt% Pd loadings. The catalysts were dried at 120°C for 10h and calcined at 550°C for 4h. Ceria supported catalysts are denoted as ceria, followed by the advertised ceria particle size. For example, a catalyst labeled as $1\%Pd/CeO_2$-100

nm indicates that ceria is characterized by 100 nm particle size. A Pd/Al_2O_3 reference catalyst with nominal 1.2% Pd weight loading was synthesized via wetness impregnation. Al_2O_3 was provided by BASF and contained 10% La to stabilize the Al_2O_3 in the gamma phase. The catalysts were dried at 120°C for 10h and calcined at 550°C for 4 h. Following the calcination, the Pd/Al_2O_3 catalyst underwent an aging treatment to increase the Pd particle size. The aging treatment was performed by exposing the catalyst for 50h to a gas mixture that cycled through neutral, reducing and oxidizing conditions. In each cycle, there was a sequence of 40s of 10% CO_2 and 10% H_2O, followed by 10s of 3% CO, 1% H_2, 10% CO_2 and 10% H_2O, and another 10s of 3% O_2, 10% CO_2 and 10% H_2O, all diluted in N_2. The ageing treatment was carried out at 550, 650, 750 and 850°C. This diverse set of samples was used to validate the technique and when it needed to be used.

6.2.2 Physical characterization

Ceria particle sizes were verified via scanning transmission electron micrographs (STEM), collected on a Themis 60-300 kV transmission electron microscope in HAADF mode. Ceria was also characterized using X-ray diffraction (XRD), using an Empyrean Multipurpose X-ray diffractometer with a Cu anode ($\lambda = 0.1542$ nm). Ceria particle sizes from the XRD patterns were estimated using the Scherrer equation.

Catalysts and support surface areas were measured with N_2 physisorption isotherms obtained at -196°C. The analysis was performed on a Micromeritics ASAP2020 Plus using the BET method.

H_2 chemisorption was performed on a Micromeritics ASAP2020 Plus. The catalysts were reduced with H_2 at 300°C for 1h and then the system was evacuated for 2h. The temperature was then

decreased to 35°C, and the system was evacuated for another hour before H_2 exposure. H_2 adsorption isotherms were obtained at 35°C. The dispersion was measured from the total adsorption isotherm, by assuming a H:Pd ratio 1:1.

6.2.3 CO and CO_2-CO chemisorption

Dispersion measurements were performed using a Micromeritics ASAP2020 Plus, using CO as a probe molecule. Two experimental procedures were used to validate the effectiveness of the modified CO chemisorption method.

Method 1 – conventional CO chemisorption: Prior to CO adsorption, the catalysts were reduced in pure H_2 at 300°C for 1h then evacuated at 300°C for 2h. The temperature was then decreased to 35°C, where the system remained under evacuation for 1h.

Method 2 – CO_2-CO chemisorption: The catalysts underwent a reduction treatment in pure H_2 at 300° for 1h, followed by evacuation for 2h at 300°C. The temperature was then decreased to 35°C and the system remained under evacuation for 1h. Afterwards, the catalysts were exposed to pure CO_2 for 1h and evacuated for 1h to remove any residual CO_2 from the system.

CO adsorption isotherms were collected at 35°C. The dispersion, obtained from the total chemisorption, was calculated by assuming a CO:Pd ratio of 1:1. The particle sizes were calculated using the inverse of the dispersion, assuming hemispherical shaped nanoparticles.

6.2.4 Diffuse reflectance infra-red Fourier transform spectroscopy (DRIFTS)

DRIFTS experiments were performed using a Nicolet iS50 FT-IR spectrometer. The catalyst was loaded in a custom-made Harrick Scientific cell with low dead volume that minimizes gas phase interference. A more detailed description on the DRIFTS cell is described elsewhere. [47] CO was used as a probe molecule to assess the extent of carbonate formation on the support and the metal speciation. All the inlet gases first flowed through an isopropanol-dry ice cold trap to remove any residual moisture. The catalysts were pretreated in 1% O_2/Ar at 400°C for 30 minutes to clean the catalyst surface. The temperature was then decreased to 300°C, the cell purged with Ar and then a reduction was performed with 5% H_2/Ar at 300°C for 30 minutes. After cooling in Ar, the catalyst was exposed to 5000 ppm CO at 35°C until saturation.

To evaluate the efficacy of the CO_2-CO chemisorption, following the treatment described above, the catalysts were exposed to 1% CO_2/Ar. The system was then purged with inert gas until no changes in the spectra were detected. A new background spectrum was recorded before exposing the catalysts to 5000 ppm CO, diluted in Ar, until saturation.

6.2.5 CO oxidation kinetics

The catalyst was placed in a 4 mm quartz tube, which was placed in a Thermo Scientific Lindberg Blue M tube furnace. Inlet and outlet temperatures were measured using K-type thermocouples purchased from Omega. The amount of catalyst used was between 4 and 8 mg and was diluted with SiO_2 to achieve a catalyst:SiO_2 ratio of 1:20-40, to help prevent heat transfer limitations. To avoid internal mass transfer limitations, the catalyst was pelletized and sieved to an 80-170 mesh size. The total flowrate was 500 sccm. The catalysts were pretreated in 5% H_2 diluted in N_2 at

300°C for 30 minutes. The reaction mixture included 5000 ppm CO and 2500 ppm O_2, diluted in N_2. The gases were metered using MKS mass flow controllers. Wet experiments were performed with the Pd/Al_2O_3 catalysts and included 6% H_2O, which was introduced using a Bronkhorst controlled evaporator mixer (CEM). The CO, CO_2 and H_2O concentrations were measured using a MKS MG2030 FT-IR analyzer. CO oxidation rates were measured at steady-state and obtained from high to low temperature. The turnover frequency (TOF) was ultimately calculated by normalizing the reaction rates to the metal perimeter sites, as follows:

$$TOF = \frac{reaction\ rate\ [\frac{mol}{s}]}{mol\ Pd\ perimeter\ sites}$$

The number of perimeter sites was calculated as $0.25d^{-1.9}$ as previously reported[47,48], where d is the average diameter measured via CO_2-CO chemisorption. The TOF was also obtained by normalizing the reaction by the fraction of surface and corner sites (SI section 3), calculated according to the same geometric model reported in the literature. [48,49]

6.3 Results and Discussion

6.3.1 Physical characterization

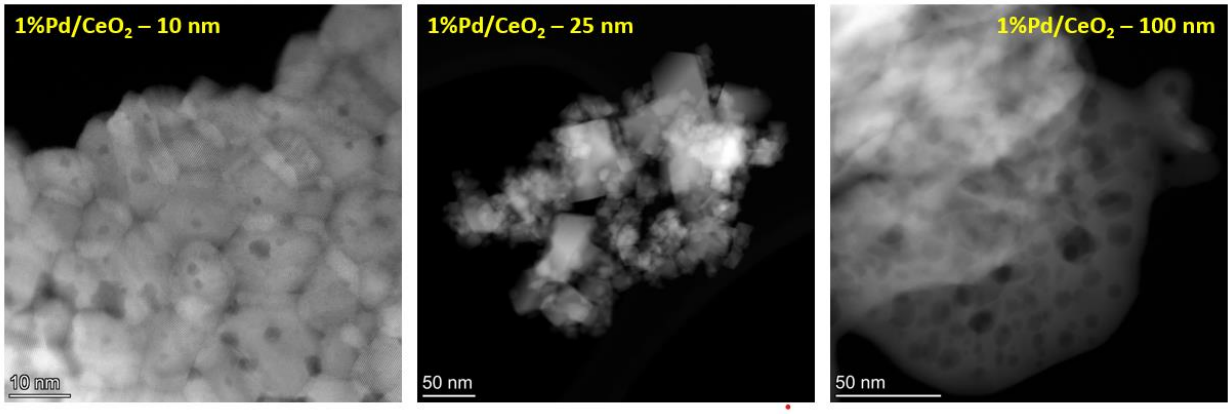

Figure 6.1: STEM images of the 1%Pd/CeO_2-10 nm, 1%Pd/CeO_2-25 nm and 1%Pd/CeO_2-100 nm samples

STEM images were used to verify the ceria particle size. Figure 6.1 shows STEM images captured from 1% Pd/CeO_2 with nominal 10, 25 and 100 nm ceria support particle sizes. The ceria particle size on 1% Pd/CeO_2-10 nm was found to range from 8 to 10 nm. A wider range of ceria particle sizes was observed with 1%Pd/CeO_2-25 nm, spanning from 5 to 30 nm. Similarly, 1% Pd/CeO_2-100 nm showed a broad particle distribution, ranging from 20 to 100 nm. Additional images captured at various sample locations are provided in the SI (Appendix B, Figures B1-B6). The dimensions acquired from the STEM images were compared with the average crystallite size derived from the XRD pattern, shown in Figure B7, using the Scherrer equation and they were consistent for the 10 and 25 nm samples, listed in Table 1. However, discrepancies between the two techniques were found for the 100 nm sample. This might be attributed to the fact that STEM images capture only a limited portion of the catalysts, while the XRD provides bulk analysis. We note that due to the low contrast between Pd and CeO_2, it was not possible to visualize any Pd particles. There was one exception, for the 1% Pd/CeO_2-25 nm sample, as shown in Figure S3, where *one* 1-1.5nm particle was detected and confirmed by EDS analysis. The dark spots observed on the 1% Pd/CeO_2-10 nm and 1% Pd/CeO_2-100 nm supports do not correspond to Pd nanoparticles, as confirmed by EDS in Figure B5. These dark spots might be pores inherent of the ceria structure or evidence of oxygen vacancies around the metal sites, similar to what was observed on a Pt/Fe_3O_4 catalyst. [50]

Table 6.1: Ceria particle sizes obtained using the Scherrer equation. The particle sizes were obtained by averaging the results from the features at 28, 32, 47 and 56°

Catalyst	**Ceria size [nm]**
1% Pd/CeO_2-10 nm	7.9
1% Pd/CeO_2-25 nm	17
1% Pd/CeO_2-100 nm	28

Surface areas measured via BET analysis on the 1%Pd/CeO_2 samples and the corresponding bare supports are listed in Table A1. Overall, the surface area increases as the ceria particle size decreases, for both bare ceria and Pd/CeO_2 catalysts.

6.3.2 CO DRIFTS

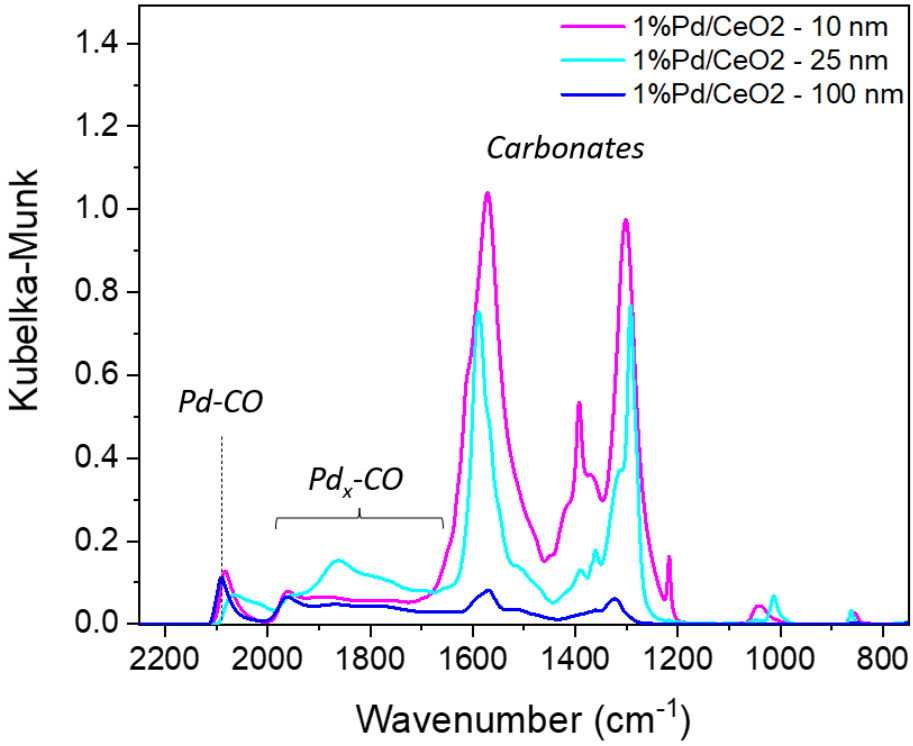

Figure 6.2: CO-DRIFTS obtained using the 1% Pd/CeO_2 catalysts characterized by 10 nm (purple), 25 nm (light blue) and 100 nm (blue) ceria nanoparticles. The catalysts were treated in 1% O_2 at 400°C for 30 min, followed by an Ar purge at 300°C and 5% H_2 for 30 minutes at 300°C. The catalysts were exposed to 5000 ppm CO/Ar at 35°C.

CO chemisorption has been found unreliable in measuring the number of active metal surface sites on ceria-supported catalysts, due to the interactions between CO and the ceria support. CO adsorbs on the metal site as intended, but carbonates form on the support through reaction between CO and ceria lattice oxygen and increase the CO uptake [51].

To characterize and confirm the interaction between CO and ceria-supported catalysts, we spectroscopically evaluated CO adsorption on 1% Pd/CeO_2 catalysts using DRIFTS. The results shown in Figure 6.2 were obtained from the 3 catalysts with ceria particle sizes ranging from 10 to 100 nm. The peaks at 2080 cm^{-1} correspond to CO linearly adsorbed on Pd, while the broad features spanning from 2000 to 1800 cm^{-1} are assigned to bridge bound CO on Pd. [52,53] The features below 1700 cm^{-1} correspond to carbonates on the support.[54] By comparing Figure 6.2 and Figure B8, where bare ceria was exposed to CO, carbonate formation on ceria is promoted by the presence of Pd.[46,55]

In comparing the carbonate bands in Figure 6.2, and noting the similarities in the intensities of the linear Pd-CO bands between the 3 samples, the relative intensity of the carbonate bands increases with a decrease in ceria nanoparticle size. Among all the catalysts studied, the Pd/CeO_2 10 nm sample results in the most carbonate formed, and Pd/CeO_2 100 nm led to the smallest. This trend could be related to the increase in oxygen mobility and the facile formation of oxygen vacancies with decreasing ceria size. Theoretical studies have demonstrated that the energy to form an oxygen-vacancy decreases as the ceria size decreases.[56–58] As a consequence, the so-called reverse spillover, which describes oxygen transfer from the support to the metal site, is enhanced for smaller ceria nanoparticles, while it was found to be energetically unfavorable on single crystal ceria.[56] Furthermore, it has been shown that with interaction between the metal and ceria nanoparticles, electron transfer from ceria to the metal takes place leading to partial oxidation of the metal and a reduction of Ce^{4+} to Ce^{3+}, which usually has a high energy cost on extended surfaces. However, theoretical studies showed that this cost decreases on undercoordinated sites, such as edges

and corners, and the fractions of these sites increase with decreasing particle size.[59–66] During CO adsorption, a reduction of Ce^{4+} to Ce^{3+} occurs with simultaneous reaction between the spilt-over oxygen and CO. This results in carbonate formation on the support.[67–69] A similar process was proposed to occur during H_2 reduction on a Pt/CeO_2 catalyst, where lattice oxygen migrates onto the metal and it continuously reacts with H_2, reducing the metal and forming water which desorbs.[70] The enhanced oxygen mobility with decreasing ceria particle size has also been confirmed experimentally via CO-TPR and Raman spectroscopy.[53]

In addition, the higher surface area that characterizes the 10 nm and 25 nm particles might contribute to the more intense carbonate bands observed. This is consistent with CO_2 adsorption DRIFTS spectra shown in Figure B9, performed on CeO_2 of 10 and 100 nm nominal particle sizes. Even in the absence of the metal site, more carbonate formation on the 10 nm ceria was observed. Therefore, this might be attributed not only to the higher lattice oxygen mobility, as mentioned above, but also to its higher surface area compared to the 100 nm sample, as shown in Table B1.

As previously suggested, carbonate formation on ceria-supported catalysts can undermine the reliability of both static and dynamic CO chemisorption, leading to an overestimation of the CO uptake. [71] During a typical chemisorption analysis, the catalyst is exposed to a probe molecule, in this case CO, until an adsorbed monolayer on the metal is achieved. At this point, the metal is saturated and is not able to adsorb additional gas. In the case of ceria-supported catalysts, when CO interacts with ceria's lattice oxygen, carbonate can form directly on the support and also at the metal-support interface. The latter can then move to the support, and as this CO migrates to the support, the metal site is available for more CO adsorption. This is consistent with the CO DRIFTS

spectra in Figure 6.2 and S8. Overall, this results in a higher CO uptake, which often leads to an erroneous CO:Pd ratio higher than 1. However, as shown in the DRIFTS spectra in Figure 6.2, we can hypothesize that the CO uptake is affected to different extents depending on ceria particle size. The CO uptake on Pd supported on small ceria nanoparticles is larger than the Pd supported on larger ceria nanoparticles, as a result of a higher oxygen mobility and therefore more carbonate formation.

This hypothesis is further supported when comparing the varying carbonate band intensities on ceria catalysts with different ceria sizes and the features observed during CO adsorption on the reference Pd/Al_2O_3 fresh catalyst. Figure B10 shows the CO adsorption spectra on Pd/Al_2O_3 catalysts. The spectrum has a feature at 2088 cm^{-1}, assigned to linear Pd-CO, and a broader feature between 2000 and 1800 cm^{-1}, corresponding to bridge Pd_x-CO. The features below 1700 cm^{-1} correspond to carbonates formed on the support, and for the fresh catalyst their intensity is comparable to the CO-Pd features intensity. It is known that the carbonate formation on irreducible supported catalysts, such as Al_2O_3, is usually minimal. In this case, the presence of 10% La could lead to some enhancement in carbonate formation, as reported for Al_2O_3 supports doped with alkali earth metals.[72–74] However, these carbonates formed on the alumina support are not expected to influence the measured dispersion from CO uptake during CO chemisorption, in the case of the fresh catalyst. This is attributed to the fact that Al_2O_3, unlike ceria, does not easily lose oxygen atoms that can react with CO.[57] Therefore, since carbonate formation observed on the alumina-supported catalyst exhibits comparable intensities to the ones relative to Pd-CO bands, we can then further hypothesize that if the carbonate intensity on some other sample is similar to that of the Pd-CO

features, the CO chemisorption measurement likely will not be overestimated. This is confirmed below.

6.3.3 CO_2-CO DRIFTS

CO_2 pre-adsorption was previously proposed as a step prior to CO adsorption, to saturate the ceria surface via carbonate formation and leave the metal sites available for CO adsorption.[46] The previous method included a H_2 treatment at room temperature between the CO_2 and CO exposure to reduce the metal site. Since exposing Pd/CeO_2 catalysts to H_2 at room temperature could cause beta Pd hydride formation, here, we propose a modified method without the intermediate reduction and verify it via DRIFTS CO_2-CO exposure. Figure 6. *3* shows the spectra taken after CO_2 adsorption, an Ar purge and subsequent CO adsorption on 1% Pd/CeO_2 25 nm. We reiterate that at the end of the purge after CO_2 adsorption and before CO adsorption, a new background spectrum was taken. This was done to better observe any changes in the portion of the spectrum between 1700 and 750 cm^{-1}. The first spectrum was obtained after saturating the catalyst with CO_2. CO_2 exposure caused carbonate and bicarbonate species formation, represented by the features below 1700 cm^{-1}.[54] The lack of features between 2100 and 1700 cm^{-1}, associated with CO adsorbed on Pd, confirms that there was no CO_2 dissociation and subsequent CO adsorption on the Pd sites. After purging the catalyst with Ar, carbonate species bands decreased in intensity, suggesting a partial decomposition/desorption of weakly adsorbed species on/from the ceria surface. The time evolution of the carbonate species is shown in detail in Figure B11. Despite the partial loss, the remaining carbonate species are stable on the ceria surface, suggesting that the ceria surface is at least partially covered by C-containing species. CO adsorption performed after CO_2 pre-adsorption shows that exclusively Pd metal sites are available for CO adsorption. Only features between 2100 and 1800 cm^{-1} are observed. The feature at 2078 cm^{-1} is assigned to CO linearly adsorbed to Pd,

while the broad peak in the 2000-1700 cm^{-1} range is assigned to bridge bound CO on Pd, characterized by different coordination environments.[52,53] No peaks above 2100 cm^{-1} were observed, confirming that the catalyst retained its metallic state and the CO_2 did not dissociate and partially oxidize the metal. No peaks below 1800 cm^{-1} were detected, showing that no further carbonates are formed upon CO exposure. The spectra shown in Figure 6. 3 indicate that CO_2 pre-adsorption is able to passivate the ceria surface, leaving Pd sites available for CO adsorption. As previously suggested, CO_2 reacts with lattice oxygen at the metal-support interface to form carbonates,[75] inhibiting any further reaction upon CO adsorption.

This experiment was also performed on 1% Pd/CeO_2 with 10 and 100 nm ceria as the support (Figure B12), along with Pd/CeO_2 with 1 μm ceria characterized by different Pd loadings (Figure B13). Additionally, CO_2-CO adsorption was validated using a 1.2% Pd/Al_2O_3 catalyst (Figure B14 (a)), which was selected as a reference catalyst due to the lack of oxygen storage capacity associated with the support and therefore its inability to form a large amount of carbonates. As shown in the DRIFTS spectra in Figure B12, during CO exposure after CO_2 saturation none of the catalysts showed new carbonate formation, except for 1% Pd/CeO_2 10 nm. In the case of the 1% Pd/CeO_2 with 10 nm ceria particles, we hypothesize that the small amount formed will not significantly affect the CO-uptake following CO_2 pre-adsorption. This is based on the intensity relative to the carbonates formed on the support being comparable to the intensity of Pd-CO features, similar to the carbonates observed on the fresh Pd/Al_2O_3 catalyst in Figure B10 as discussed above. Despite not knowing the extinction coefficient to quantify the amount of carbonates on the support, we assume that carbonates on Al_2O_3 and ceria supports with similar intensities to Pd-CO features do not significantly affect the CO uptake during CO chemisorption. These results suggest that CO_2

pre-adsorption successfully hinders carbonate formation upon CO adsorption, while also not modifying the metal sites. This step should allow CO-uptake measurements without carbonate interference. The DRIFTS spectra collected on the catalysts under investigation consistently show that the modified CO_2-CO adsorption method is effective across the sizes of ceria spanning from 10 nm to 1 μm.

Similar to the observations from the CO-DRIFTS spectra, the intensity of carbonates formed on the ceria surface during CO_2 adsorption depends on the ceria particle size, with the intensity increasing with decreasing ceria size. Ceria size influences the mobility and accessibility of lattice oxygen at the metal-support interface. However, CO_2 saturation effectively hinders any further reaction between CO and ceria lattice oxygen for all the ceria sizes under study (Figure B12). The effect of metal loading was also investigated. Using the same ceria support, as the Pd loading increases, carbonate formation on ceria decreases, as shown in Figure B13. Also in this case, varying the Pd loading does not negatively impact the efficacy of the CO_2-CO adsorption method.

In conclusion, the modified CO_2 pre-adsorption followed by CO adsorption method represents a viable method to reduce carbonate formation during CO adsorption and reduce interference on CO uptake. This method can be used on catalysts characterized by different CeO_2 particle sizes and different Pd loadings. Additionally, as shown by the DRIFTS spectra in Figure 6.2, carbonate formation more significantly affects the CO uptake on smaller ceria particles, because of the higher oxygen mobility and reactivity with CO. As a consequence, CO_2 pre-adsorption should have a more pronounced effect on smaller ceria particles compared to larger ones.

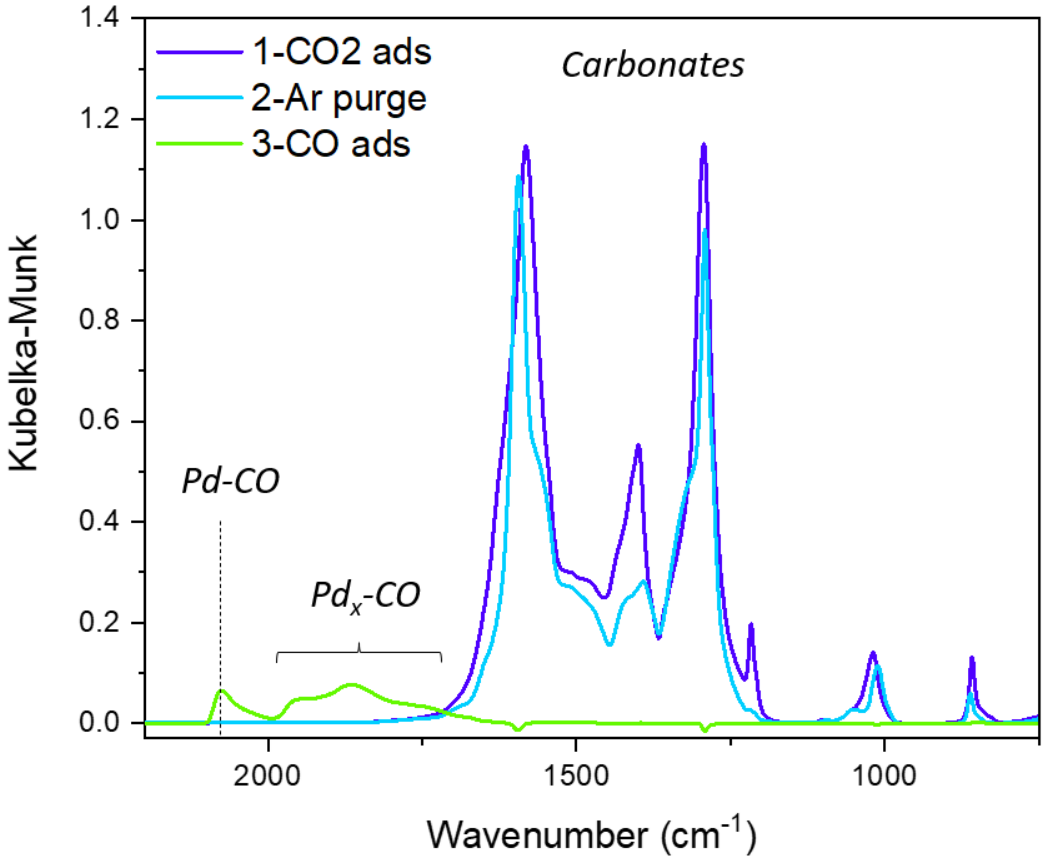

Figure 6. 3: DRIFTS spectra obtained during the CO_2-CO adsorption experiment using the 1% Pd/CeO_2 - 25 nm sample. The catalyst was treated in 1% O_2 for 30 min at 400°C, purged in Ar and reduced in 5% H_2 for 30 min at 300°C. The catalyst was exposed to 1% CO_2 at 35°C until saturation. This was followed by purging in Ar until carbonate decomposition/desorption stopped, then a new background was taken, and finally the sample was exposed to 5000 ppm CO.

6.3.4 CO and CO_2-CO chemisorption

Table 6.2: CO_2-CO and CO chemisorption results: dispersion and particle size. The dispersion was obtained using the total chemisorption isotherm, and the particle size was calculated as 100/D[%]. The ceria-containing catalysts were reduced in H_2 at 300°C, while the Pd/Al_2O_3 catalyst was reduced in H_2 at 400°C.

	CO_2-CO chemisorption	**CO chemisorption**

Catalyst	Dispersion [%]	Particle size [nm]	Dispersion [%]	Particle size [nm]
1.2%Pd/Al_2O_3	39	2.6	34	3
1%Pd/CeO_2 - 100 nm	41	2.5	37	2.7
1%Pd/CeO_2 - 25 nm	64	1.55	81	1.2
1%Pd/CeO_2 - 10 nm	67	1.55	148	<1
1.2%Pd/CeO_2 - 1µm	10	9.8	8.2	12
0.8%Pd/CeO_2 - 1µm	10	9.9	10	9.9
0.2%Pd/CeO_2 - 1µm	29	3.5	23	4.3

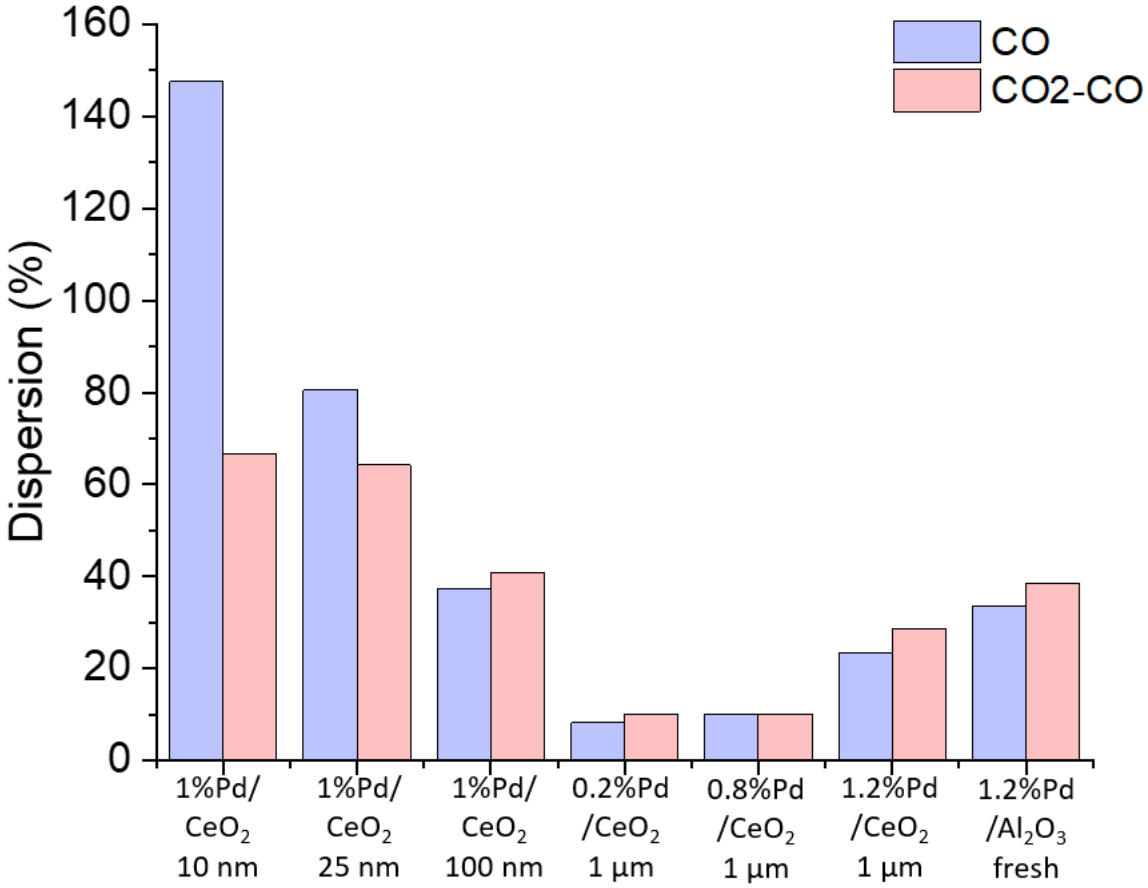

Figure 6.4: Comparison between the dispersion measurements obtained via CO and CO_2-CO chemisorption on 1% Pd/CeO_2-10, 25 and 100 nm, 0.2% Pd/CeO_2-1µm, 0.8% Pd/CeO_2-1µm, 1.2% Pd/CeO_2-1µm and fresh 1.2% Pd/Al_2O_3.

Dispersion measurements were performed on Pd/CeO_2 catalysts with different ceria particle sizes, along with a Pd/Al_2O_3 sample, used as a reference catalyst. Table 6.2 lists the results obtained by performing both CO_2-CO and CO chemisorption.

The modified CO_2-CO chemisorption method was initially validated on the Pd/Al_2O_3 reference catalyst. As expected, the dispersions measured on the fresh 1.2% Pd/Al_2O_3 catalyst using both CO_2-CO and CO chemisorption exhibit similar values, with differences falling within what we consider an acceptable 5% experimental error. These results confirm our previous assumption,

based on the analysis of DRIFTS spectra in Figure B10(a) and previous literature reports, that carbonate formation on Pd/Al_2O_3 does not have an effect on dispersion measurements. In addition, the similar dispersions obtained from both methods confirm that CO_2 is not affecting the metal site and causing any structural changes. As further support to this statement, DRIFTS spectra in Figure S14 also show that CO-Pd features obtained with and without CO_2 pre-adsorption are similar.

For ceria-containing catalysts, the dispersion obtained via CO chemisorption increases with decreasing ceria particle size, with the 10 nm resulting in a physically unrealistic 147% value. Typically, the CO uptake obtained from CO chemisorption on metals dispersed on non-reducible supports, such as Al_2O_3 or SiO_2, is indicative of metal dispersion, however, as previously discussed, CO chemisorption on reducible support catalysts is susceptible to errors due to carbonate formation, which leads to an overestimation of the CO uptake and consequently to an overestimation of dispersion measurements. Therefore, the observed increase in dispersion with decreasing ceria nanoparticle size measured by CO chemisorption is attributed to two factors: (i) a higher dispersion of Pd metal nanoparticles and (ii) carbonate formation on ceria enhanced by the high mobility of lattice oxygen. These reasons lead to unphysical values such as those measured on 1% Pd/CeO_2-10 nm, where the dispersion exceeded 100%.

CO_2 adsorption prior to CO chemisorption should limit the influence of carbonate formation on CO uptake. This is achieved by hindering the reaction between CO and lattice oxygen, as shown by the CO_2-CO adsorption DRIFTS spectra in Figure 6. 3**,** B12 and B13. The dispersions measured using CO_2-CO adsorption are lower than those determined via CO chemisorption, with the exception of Pd/CeO_2 catalysts with ceria nanoparticles larger than 100 nm.

While with CO_2-CO chemisorption, the 1% Pd/CeO_2 on 10 and 25 nm ceria particles show similar dispersion, the CO chemisorption shows higher dispersion for the smallest ceria NP under study, consistent with the CO DRIFTS results that showed the highest carbonate formation. This suggests that carbonate formation is not only related to the metal-support interface,[76] which, in this case is similar between the two catalysts, but also to the oxygen mobility of ceria.

However, in the case of Pd/CeO_2 with ceria nanoparticles larger than 100 nm, the dispersions measured with the two methods are similar. This implies that the amount of carbonates formed on larger ceria nanoparticles is insufficient to significantly impact the CO uptake during CO chemisorption, similar to what was observed in the fresh Pd/Al_2O_3 catalyst.

Overall, the dispersions obtained via CO_2-CO chemisorption show higher Pd dispersion as the ceria particle size decreases. This trend aligns with previous literature reporting that smaller ceria nanoparticles exhibit stronger metal support interactions, resulting in higher metal dispersion. Smaller nanoparticles are indeed characterized by a higher fraction of defect sites where the metal clusters bind more strongly.[77]

In addition, the dispersion measurements are consistent with CO-DRIFTS spectra in Figure 6.2. From the comparison of the linear CO-Pd peak position of the Pd/CeO_2 10 and 100 nm samples, with ceria purchased from the same supplier, it is located at a higher wavenumber for the Pd/CeO_2 100 nm compared to the Pd/CeO_2 10 nm sample, characterized by smaller Pd particle size. This is consistent with the Blyholder model which states that the stretching frequency depends on the π-

back donation, which is also related to the particle size.[78] As the particle size decreases, the back-bonding donation from the metal to CO increases, resulting in a red shift in the metal-CO stretching frequency. The catalyst with ceria purchased from a different supplier (Pd/CeO_2 25 nm) exhibits broader linear and bridged Pd-CO features, potentially caused by a different coordination environment,[79] a broader distribution of particle sizes and facets, having a very distinct cubic shape, and/or the lack of darker spots, as hinted from the observed particle heterogeneity in STEM images (Figure 6.1 and Figure B3).

CO_2-CO chemisorption results show that the CO_2 pre-adsorption step results in a lower count of exposed metal sites supported on ceria supports characterized by smaller ceria particle size. Figure 6.4 shows that CO chemisorption values obtained with the 25 nm ceria particle catalyst has a dispersion around 30% higher than that from the CO_2-CO chemisorption, while for the 10 nm ceria particle sample, the traditional CO chemisorption results in a value two-times higher than that of the modified method. However, the measurement difference decreased with the larger ceria nanoparticles as the amount of carbonate formed is not large enough to significantly affect CO uptake.

H_2 chemisorption at 35°C was also performed to compare to the results obtained from the CO_2-CO chemisorption analysis. Due to the small Pd particle size measured via CO_2-CO chemisorption, the formation of palladium hydrides would be impeded because of the low H_2 solubility in small particles.[8] In addition, previous literature reported that a H_2 pretreatment at temperatures lower than 400°C could suppress hydrogen spillover on a ceria-zirconia supported catalyst.[80] Given our reducing temperature of 300°C, it might therefore be possible that H spillover could be eliminated.

However, as shown in Table B2, the measured dispersion measurements exceeded the H:Pd of 1, giving unphysical results.

The 136% dispersion obtained via H_2 chemisorption on the 1.2% Pd/CeO_2-1 um catalyst can at least be partially explained by Pd hydride formation, as evidenced by the adsorption isotherm shown in Figure B15. This catalyst, characterized by an average Pd particle size of 10 nm, measured via CO_2-CO and CO chemisorption (Table 6.2), would have H_2 solubility, as suggested by literature.[81] However, we attribute the high dispersion measured on the Pd/CeO_2-10 and 25 nm samples to hydrogen spillover from the metal particles to the support. This is supported by the absence of the typical isotherm shape indicative of Pd hydride formation, instead displaying the typical Langmuirian isotherm, as shown in Figure B16. Typically, for particles smaller than 2.8 nm, hydrogen will "simply" adsorb on the catalyst surface and not participate in the formation of the hydride. This is because with decreasing particle size, there is a decrease in the number of interstitial sites relative to the surface sites and therefore a lower number of sites where hydrogen can diffuse.[10] Finally, in the case of Pd/CeO_2-100 nm, which exhibited the highest dispersion value, we speculate that the high H uptake could be a result of both Pd hydride formation and hydrogen spillover processes occurring at the same time.

CO_2-CO chemisorption was also performed on the Pd/Al_2O_3 catalysts exposed to high temperature. The comparison between the results obtained via CO_2-CO and CO chemisorption is listed in Table B3. From the CO DRIFTS spectra (Figure S10), we observed that carbonate band intensities increase relative to the Pd-CO intensity as the ageing temperature increases. This is consistent with a decrease in Pd surface area due to the sintering induced by the ageing treatment. However, as the

particle size exceeds 10 nm, and there is only a small amount of CO uptake on the large metal particle, the dispersions obtained via CO chemisorption may become unreliable due to increasing relative interference caused by the CO associated with formation of carbonates on the support, similar to what was observed on ceria-supported catalysts. To overcome this issue, we employed the CO_2-CO chemisorption method. From the comparison of the two methods, the dispersions obtained via CO chemisorption show a higher CO uptake, which correlates again with more carbonates observed, relative to CO bound to the metal site. For the 1.2% Pd/Al_2O_3 catalyst aged at 650°C, we compared the result from the CO_2-CO chemisorption and the result of the average Pd crystallite size calculated with the Scherrer equation (Figure B17). The results show similar values, implying that the CO_2-CO chemisorption could be used on catalysts with non-reducible supports which are characterized by larger metal particle sizes, such as those that underwent an ageing treatment. The 1.2% Pd/Al_2O_3 catalysts aged at 750 and 850°C resulted in a lower dispersion when using the CO_2-CO chemisorption in comparison to the measurement obtained via CO chemisorption, however, the values approach the 5% error measurement.

The modified CO_2-CO chemisorption technique is able to measure the metal site surface area, avoiding carbonate interference which particularly affects ceria containing catalysts. However, this method can also be expanded and employed with catalysts with irreducible supports but characterized by large particle size, since CO chemisorption might become affected by a relatively increasing carbonate interference.

6.3.5 CO oxidation kinetics

To validate the accuracy of the particle size measurements obtained via CO_2-CO chemisorption we used CO oxidation kinetics. CO oxidation on ceria-supported catalysts has been extensively studied and a consensus on the mechanism and the active site has been established.

On Pd/CeO_2 catalysts, CO oxidation reaction rates exhibit a particle size dependence, with the reaction rates increasing with decreasing metal nanoparticle size. Previous studies indeed demonstrate that the reaction occurs at the interface between the metal nanoparticle and the support, where CO adsorbed on the nanoparticle reacts with oxygen from the support.[82–84] A decrease in particle size correlates with an increase in the fraction of perimeter sites, as shown in Figure S19, and an increase in activity. The fraction of perimeter sites, along with the surface and corner sites, was obtained using reported correlations based on a geometric model which was developed from HRTEM images assuming an octahedral shape for metal nanoparticles.[49,85] Based on these findings, we expect that the CO oxidation turnover frequencies (TOF), obtained by normalizing the reaction rates by the perimeter sites, are the same for all the Pd/CeO_2 catalysts studied.

Figure 6.5 shows the CO oxidation Arrhenius plot obtained from the 1% Pd/CeO_2 catalysts. The measured apparent activation energy for all the catalysts was ~50 kJ/mol, consistent with previously reported activation energies ranging between 40 and 70 kJ/mol. CO oxidation on reducible oxide-supported catalysts often follows a Mars-van Krevelen mechanism.[57] In this case, the support is directly involved in the reaction by providing reactive oxygen atoms. Here, CO reacts with a lattice oxygen from the ceria, forming CO_2.[86–89] The process leads to formation of an oxygen vacancy, resulting in a change in the ceria stoichiometry from CeO_2 to CeO_{2-x} and a change in the

formal oxidation state from Ce^{4+} to Ce^{3+}. The catalytic cycle concludes with ceria reoxidation from 3+ to 4+ using molecular oxygen, which is able to refill the oxygen vacancy and restore the initial state of the support.[90,91] According to the proposed mechanism, the reaction rate was found to follow a 0^{th} order dependency on CO partial pressure, and 1^{st} order dependence on O_2.[49] This indicates that CO is not able to suppress the reaction by hindering O_2 adsorption and dissociation, which is the prevalent mechanism occurring on irreducible oxide-supported catalysts.[92] Due to the presence of the metal, the reducibility of the support is enhanced through the contact between the metal and the oxide. Therefore, it is easier to extract an oxygen. This is why, as mentioned above, CO oxidation occurs at the metal-support interface, where it is easier to remove the oxygen.[48]

Although there is evidence that very small ceria particle sizes can lead to changes in the reaction mechanism,[53] for the range of particle sizes we evaluated, there appears to be no change in the CO oxidation mechanism, with evidence stemming from the same activation energy measured on all the catalysts with varying ceria nanoparticles.

The TOFs derived by the normalization of the reaction rate by *the total number of Pd surface sites*, estimated from chemisorption, is shown in Figure S20 and exhibits decreasing TOF with increasing Pd particle size. Note that CO oxidation rates obtained on Pd/CeO_2-10, and 25 nm are overlapping, due to their similar dispersion, confirming the validity of CO_2-CO chemisorption method. However, if we normalize the reaction rates by the fraction of perimeter sites, and derive the Arrhenius plot, shown in Figure 6.5, the turnover frequencies for all the catalysts under study overlap. In addition, we normalized the reaction rates by the fraction of corner sites, as shown in Figure B21. The TOFs overlap suggesting that corner sites could also be assigned as the active sites. This

is consistent with a previous study, where it appears that rate measurements for metal nanoparticles smaller than 3 nm show that corner sites could be the most active.[49] This suggests that both corner and perimeter sites play a role, and their relative fractions change with particle size as shown in Figure B19. Corner sites activity appear to be predominant on smaller nanoparticles, while perimeter sites become predominant as the metal size increases.[85]

The CO_2-CO chemisorption validity on aged Pd/Al_2O_3 catalysts was also verified using CO oxidation. In the case of metals dispersed on irreducible oxides, CO oxidation follows a different mechanism from the one previously described for ceria-supported catalysts. CO oxidation on Pd/Al_2O_3 follows the Langmuir-Hinshelwood kinetics, and the mechanism includes CO initially adsorbs on the metal site, hindering adsorption and dissociation of O_2. CO has to desorb to allow O_2 dissociation and the surface reaction between CO and O.[92,93] For this reason, it is widely reported that the CO oxidation apparent activation energy corresponds to the CO desorption energy. Figure 6.6 shows the CO oxidation Arrhenius plot on Pd/Al_2O_3 aged catalysts. The TOF was obtained by normalizing the reaction rate by the number of surface active sites, measured via CO_2-CO chemisorption. The apparent activation energy derived was similar to the CO desorption energy from Pd metal. In addition, the TOFs are similar across all the catalysts, suggesting that the CO_2-CO chemisorption provided a good particle size estimate, including for metal supported catalysts with metal nanoparticles larger than 10 nm.

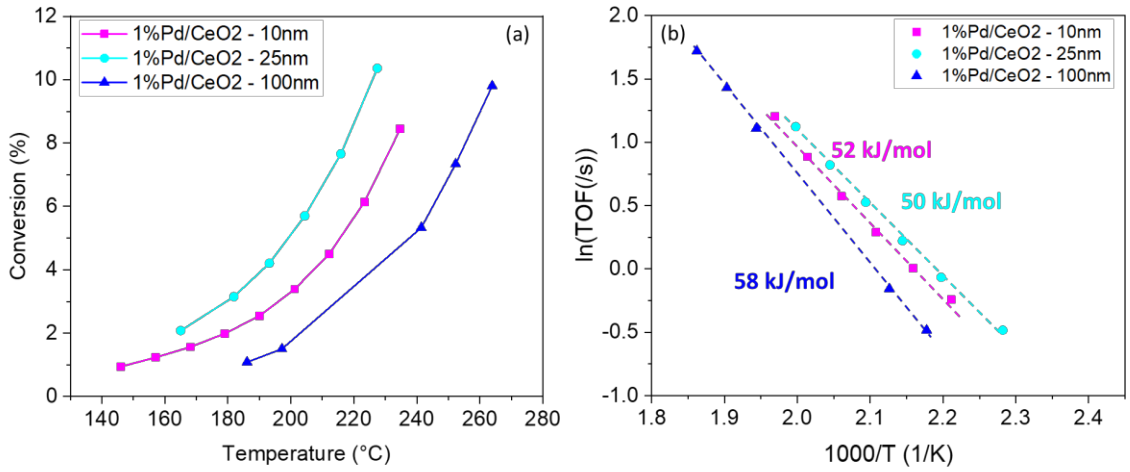

Figure 6.5: CO oxidation (a) conversion profiles and (b) Arrhenius plot on 1%Pd/CeO_2 - 10, 25 and 100 nm. The catalysts were reduced at 300°C in 5% H_2 for 30 min. The catalysts were exposed to 5000 ppm CO and 2500 ppm O_2, balanced in N_2. The rates were taken at steady-state. The rates were normalized by Pd perimeter sites.

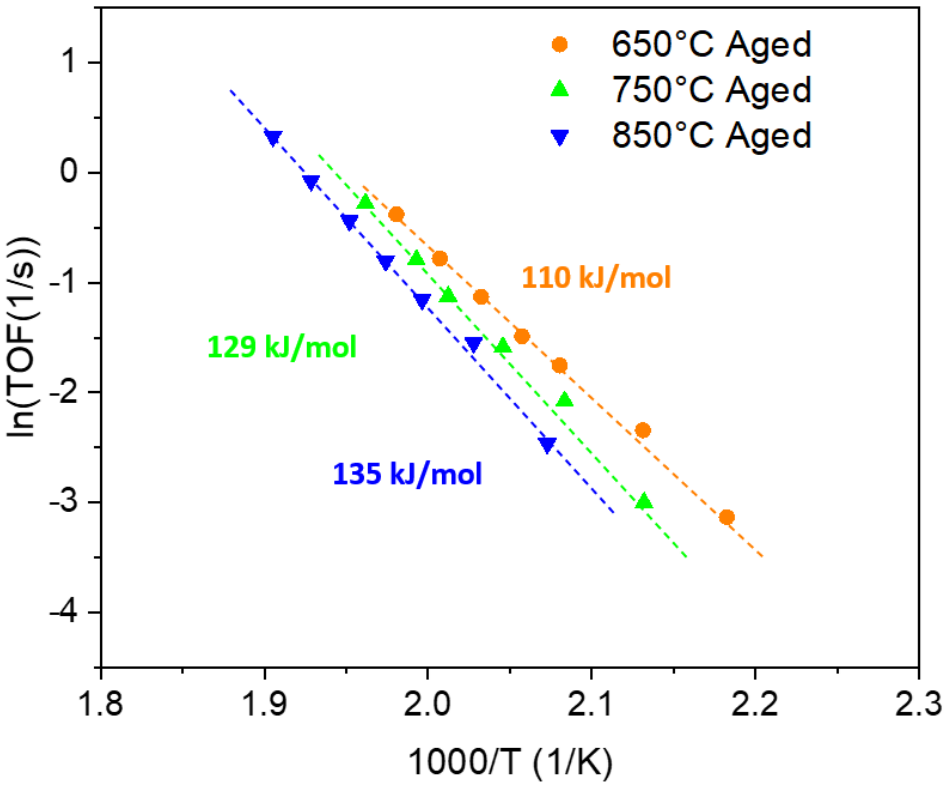

Figure 6.6: CO oxidation Arrhenius plot on 1.2%Pd/Al_2O_3 aged at 650, 750 and 850°C. The catalysts were reduced in 5% H_2 for 30 min at 400°C. The catalysts were exposed to CO = 5000 ppm, O_2 = 2500 ppm, H_2O = 6% balanced in N_2. The rates were taken at steady-state. The rates were normalized by Pd surface sites measured via CO_2-CO chemisorption.

6.4 Conclusions

Characterizing ceria-supported catalysts via CO chemisorption is challenging due to the interactions between CO and the support. In fact, CO reacts with ceria lattice oxygen leading to carbonate formation, which contributes to an overestimation of the CO uptake and, consequently, metal dispersion. The extent of carbonate formation depends on the ceria particle size with smaller ceria nanoparticles showing the most carbonate formation, while larger particle sizes less. This trend is consistent with the higher oxygen mobility as the ceria size decreases.[57,58,66]

We show that ceria nanoparticles larger than 100 nm exhibit minimal carbonate formation, similar to the case of irreducible oxide-supported catalysts. This leads to a negligible effect on the CO uptake and a reliable dispersion measurement. However, as the ceria particle size decreases, the dispersion measurement becomes impacted by the growing carbonate formation, often providing unphysical results with CO:Pd ratios exceeding 1.

To reduce carbonate formation during CO adsorption, CO_2 pre-adsorption was added as an additional step in the static CO chemisorption procedure. DRIFTS experiments confirmed that CO_2 interacts with lattice oxygen forming carbonates and prevents any further reaction between CO and ceria lattice oxygen during CO exposure. We validated the dispersion measurements obtained through CO_2-CO chemisorption by performing CO oxidation kinetics. The turnover frequencies obtained by the normalization of the reaction rate by the number of perimeter sites – the active site for CO oxidation – were similar, confirming that CO_2-CO chemisorption can provide a good particle size estimate.

Despite this work being mainly focused on Pd/CeO_2 catalysts, this CO_2-CO chemisorption also proved useful when measuring CO uptake on Pd/Al_2O_3 samples characterized by larger Pd particles, as the relative amount of CO on the metal vs the amounts of carbonates formed shifted to the latter, ultimately being enough to alter the dispersion measurement.

6.5 References

(1) Boudart, M. Turnover Rates in Heterogeneous Catalysis. *Chem Rev* **1995**, *95* (3), 661–666. https://doi.org/10.1021/cr00035a009.

(2) Ribeiro, F. H.; Von Wittenau, A. E. S.; Bartholomew, C. H.; Somorjai, G. A. Reproducibility of Turnover Rates in Heterogeneous Metal Catalysis: Compilation of Data and Guidelines for Data Analysis. *Catal Rev Sci Eng* **1997**, *39* (1–2), 49–76. https://doi.org/10.1080/01614949708006468.

(3) Kozuch, S.; Martin, J. M. L. "Turning over" Definitions in Catalytic Cycles. *ACS Catal* **2012**, *2* (12), 2787–2794. https://doi.org/10.1021/CS3005264.

(4) Hill, A. J.; Seo, C. Y.; Chen, X.; Bhat, A.; Fisher, G. B.; Lenert, A.; Schwank, J. W. Thermally Induced Restructuring of Pd@ceo2 and Pd@sio2 Nanoparticles as a Strategy for Enhancing Low-Temperature Catalytic Activity. *ACS Catal* **2020**, *10* (3), 1731–1741. https://doi.org/10.1021/acscatal.9b05224.

(5) Hargreaves, J. S. J. Some Considerations Related to the Use of the Scherrer Equation in Powder X-Ray Diffraction as Applied to Heterogeneous Catalysts. *Catalysis, Structure and Reactivity* **2016**, *2* (1–4), 33–37. https://doi.org/10.1080/2055074X.2016.1252548.

(6) Langford, J. I.; Wilson, A. J. C. Scherrer after Sixty Years: A Survey and Some New Results in the Determination of Crystallite Size. *J Appl Crystallogr* **1978**, *11* (2), 102–113. https://doi.org/10.1107/s0021889878012844.

(7) Scholten, J. J. F. Metal Surface Area and Metal Dispersion in Catalysts. *Stud Surf Sci Catal* **1979**, *3* (C), 685–714. https://doi.org/10.1016/S0167-2991(09)60244-5.

(8) Boudart And, M.; Hwang, H. S. *Solubility of Hydrogen in Small Particles of Palladium*; 1975; Vol. 39.

(9) Sá, J.; Arteaga, G. D.; Daley, R. A.; Bernardi, J.; Anderson, J. A. Factors Influencing Hydride Formation in a Pd/TiO2 Catalyst. *Journal of Physical Chemistry B* **2006**, *110* (34), 17090–17095. https://doi.org/10.1021/jp062205l.

(10) Tew, M. W.; Miller, J. T.; Van Bokhoven, J. A. Particle Size Effect of Hydride Formation and Surface Hydrogen Adsorption of Nanosized Palladium Catalysts: L3 Edge vs K Edge X-Ray Absorption Spectroscopy. *Journal of Physical Chemistry C* **2009**, *113* (34), 15140–15147. https://doi.org/10.1021/jp902542f.

(11) Lee, J.; Tieu, P.; Finzel, J.; Zang, W.; Yan, X.; Graham, G.; Pan, X.; Christopher, P. How Pt Influences H 2 Reactions on High Surface-Area Pt /CeO2 Powder Catalyst Surfaces. **2023**, 1–27. https://doi.org/10.1021/jacsau.3c00330.

(12) Bernal, S.; Calvino, J. J.; Cifredo, G. A.; Rodrfguez-Izquierdo, J. M.; Perrichon, V.; Laachir, A. Reversibility of Hydrogen Chemisorption on a Ceria-Supported Rhodium Catalyst. *J Catal* **1199**, *137*, 1–11. https://doi.org/https://doi.org/10.1016/0021-9517(92)90134-4.

(13) Beck, A.; Kazazis, D.; Ekinci, Y.; Li, X.; Müller Gubler, E. A.; Kleibert, A.; Willinger, M. G.; Artiglia, L.; Van Bokhoven, J. A. The Extent of Platinum-Induced Hydrogen Spillover on Cerium Dioxide. *ACS Nano* **2022**. https://doi.org/10.1021/acsnano.2c08152.

(14) Takeguchi, T.; Manabe, S.; Kikuchi, R.; Eguchi, K.; Kanazawa, T.; Matsumoto, S.; Ueda, W. Determination of Dispersion of Precious Metals on CeO2- Containing Supports. *Appl Catal A Gen* **2005**, *293* (1–2), 91–96. https://doi.org/10.1016/j.apcata.2005.07.013.

(15) Holmgren, A.; Andersson, B. Oxygen Storage Dynamics in Pt/CeO2/Al2O3 Catalysts. *J Catal* **1998**, *25* (1448), 14–25. https://doi.org/https://doi.org/10.1006/jcat.1998.2114.

(16) Holmgren, A.; Andersson, B.; Duprez, D. Interactions of CO with Pt/Ceria Catalysts. *Appl Catal B* **1999**, *22*, 215–230. https://doi.org/https://doi.org/10.1016/S0926-3373(99)00047-8.

(17) Marino, S.; Wei, L.; Cortes-reyes, M.; Cheng, Y.; Laing, P.; Cavataio, G. Rhodium Catalyst Structural Changes during , and Their Impacts on the Kinetics of , CO Oxidation. 1–17.

(18) Yates, J. T.; Kolasinski, K. Infrared Spectroscopic Investigation of the Rhodium Gem-Dicarbonyl Surface Species. *J Chem Phys* **1983**, *79* (2), 1026–1030. https://doi.org/10.1063/1.445844.

(19) Cavanagh, R. R.; Yates, J. T. Site Distribution Studies of Rh Supported on Al2O3 - An Infrared Study of Chemisorbed CO. *J Chem Phys* **1981**, *74* (7), 4150–4155. https://doi.org/10.1063/1.441544.

(20) Yates, J. T.; Duncan, T. M.; Worley, S. D.; Vaughan, R. W. Infrared Spectra of Chemisorbed CO on Rh. *J Chem Phys* **1979**, *70* (3), 1219–1224. https://doi.org/10.1063/1.437603.

(21) Berkó, A.; Solymosi, F. Adsorption-Induced Structural Changes of Rh Supported by TiO2(110)-(1×2): An STM Study. *J Catal* **1999**, *183* (1), 91–101. https://doi.org/10.1006/JCAT.1998.2368.

(22) Berkó, A.; Solymosi, F. CO-Induced Changes of Ir Nanoparticles Supported on TiO2 (110)-(1×2) Surface. *Surf Sci* **1998**, *411* (3), L900–L903. https://doi.org/10.1016/S0039-6028(98)00420-8.

(23) Karim, W.; Spreafico, C.; Kleibert, A.; Gobrecht, J.; Vandevondele, J.; Ekinci, Y.; Van Bokhoven, J. A. Catalyst Support Effects on Hydrogen Spillover. *Nature* **2017**, *541* (7635), 68–71. https://doi.org/10.1038/nature20782.

(24) Beck, A.; Rzepka, P.; Marshall, K. P.; Stoian, D.; Willinger, M. G.; Van Bokhoven, J. A. Hydrogen Interaction with Oxide Supports in the Presence and Absence of Platinum. *Journal of Physical Chemistry C* **2022**, *126* (41), 17589–17597. https://doi.org/10.1021/acs.jpcc.2c05478.

(25) Mahdavi-Shakib, A.; Whittaker, T. N.; Yun, T. Y.; Sravan Kumar, K. B.; Rich, L. C.; Wang, S.; Rioux, R. M.; Grabow, L. C.; Chandler, B. D. The Role of Surface Hydroxyls in the Entropy-Driven Adsorption and Spillover of H2 on Au/TiO2 Catalysts. *Nat Catal* **2023**. https://doi.org/10.1038/s41929-023-00996-3.

(26) Trovarelli, A. Catalytic Properties of Ceria and CeO2-Containing Materials. *Catal Rev Sci Eng* **1996**, *38* (4), 439–520. https://doi.org/10.1080/01614949608006464.

(27) Trovarelli, A.; Llorca, J. Ceria Catalysts at Nanoscale: How Do Crystal Shapes Shape Catalysis? *ACS Catal* **2017**, *7* (7), 4716–4735. https://doi.org/10.1021/acscatal.7b01246.

(28) Kašpar, J.; Fornasiero, P.; Graziani, M. Use of CeO2-Based Oxides in the Three-Way Catalysis. *Catal Today* **1999**, *50* (2), 285–298. https://doi.org/10.1016/S0920-5861(98)00510-0.

(29) Trovarelli, A.; De Leitenburg, C.; Boaro, M.; Dolcetti, G. The Utilization of Ceria in Industrial Catalysis. *Catal Today* **1999**, *50*, 353–367. https://doi.org/https://doi.org/10.1016/S0920-5861(98)00515-X.

(30) Acerbi, N.; Golunski, S.; Tsang, S. C.; Daly, H.; Hardacre, C.; Smith, R.; Collier, P. Promotion of Ceria Catalysts by Precious Metals: Changes in Nature of the Interaction under Reducing and Oxidizing Conditions. *Journal of Physical Chemistry C* **2012**, *116* (25), 13569–13583. https://doi.org/10.1021/jp212233u.

(31) Farmer, J. A.; Campbell, C. T. Ceria Maintains Smaller Metal Catalyst Particles by Strong Metal-Support Bonding. *Science (1979)* **2010**, *329* (August), 933–936. https://doi.org/DOI: 10.1126/science.1191778.

(32) An, Y.; Chen, S.-Y.; Zhou, L.; Wang, B.; Hao, G.; Chen, J.; Wang, Y.; Zhang, H.; Peng, Z.; Yang, T.-C.; Yang, C.-M.; Chen, J.-L.; Tsung, C.-K.; Liu, Z.; Chou, L.-Y. Sintering Resistance of Pd Single Atoms on Steam-Modified Ceria: Deciphering the Role of Hydroxyl Groups. *J Mater Chem A Mater* **2023**. https://doi.org/10.1039/D3TA04200F.

(33) Zheng, T.; He, J.; Zhao, Y.; Xia, W.; He, J. Precious Metal-Support Interaction in Automotive Exhaust Catalysts. *Journal of Rare Earths* **2014**, *32* (2), 97–107. https://doi.org/10.1016/S1002-0721(14)60038-7.

(34) Kašpar, J.; Fornasiero, P.; Graziani, M. Use of CeO2-Based Oxides in the Three-Way Catalysis. *Catal Today* **1999**, *50* (2), 285–298. https://doi.org/10.1016/S0920-5861(98)00510-0.

(35) Tan, W.; Xie, S.; Wang, X.; Wang, C.; Li, Y.; Shaw, T. E.; Ma, L.; Ehrlich, S. N.; Liu, A.; Ji, J.; Gao, F.; Dong, L.; Liu, F. Highly Efficient Pt Catalyst on Newly Designed CeO2-ZrO2-Al2O3 Support for Catalytic Removal of Pollutants from Vehicle Exhaust. *Chemical Engineering Journal* **2021**, *426*. https://doi.org/10.1016/j.cej.2021.131855.

(36) Ahmed, W.; Awadallah, A. E.; Aboul-Enein, A. A. Ni/CeO2–Al2O3 Catalysts for Methane Thermo-Catalytic Decomposition to COx-Free H2 Production. *Int J Hydrogen Energy* **2016**, *41* (41), 18484–18493. https://doi.org/10.1016/j.ijhydene.2016.08.177.

(37) Rodriguez, J. A.; Grinter, D. C.; Liu, Z.; Palomino, R. M.; Senanayake, S. D. Ceria-Based Model Catalysts: Fundamental Studies on the Importance of the Metal-Ceria Interface in CO Oxidation, the Water-Gas Shift, CO2 Hydrogenation, and Methane and Alcohol Reforming. *Chem Soc Rev* **2017**, *46* (7), 1824–1841. https://doi.org/10.1039/c6cs00863a.

(38) Bruix, A.; Rodriguez, J. A.; Ramírez, P. J.; Senanayake, S. D.; Evans, J.; Park, J. B.; Stacchiola, D.; Liu, P.; Hrbek, J.; Illas, F. A New Type of Strong Metal-Support Interaction and the Production of H 2 through the Transformation of Water on Pt/CeO 2(111) and Pt/CeO x/TiO 2(110) Catalysts. *J Am Chem Soc* **2012**, *134* (21), 8968–8974. https://doi.org/10.1021/ja302070k.

(39) Parastaev, A.; Muravev, V.; Huertas Osta, E.; van Hoof, A. J. F.; Kimpel, T. F.; Kosinov, N.; Hensen, E. J. M. Boosting CO2 Hydrogenation via Size-Dependent Metal–Support Interactions in Cobalt/Ceria-Based Catalysts. *Nat Catal* **2020**, *3* (6), 526–533. https://doi.org/10.1038/s41929-020-0459-4.

(40) Quinson, J.; Kunz, S.; Arenz, M. Surfactant-Free Colloidal Syntheses of Precious Metal Nanoparticles for Improved Catalysts. *ACS Catal* **2023**, *13* (7), 4903–4937. https://doi.org/10.1021/acscatal.2c05998.

(41) Newton, M. A.; Belver-Coldeira, C.; Martinez-Arias, A.; Fernandez-Garcia, M. Dynamic in Situ Observation of Rapid Size and Shape Change of Supported Pd Nanoparticles during CO/NO Cycling. *Nature Materials 2007 6:7* **2007**, *6* (7), 528–532. https://doi.org/10.1038/nmat1924.

(42) Perrichon, V.; Retailleau, L.; Bazin, P.; Daturi, M.; Lavalley, J. C. Metal Dispersion of CeO2-ZrO2supported Platinum Catalysts Measured by H2or CO Chemisorption. *Appl Catal A Gen* **2004**, *260* (1), 1–8. https://doi.org/10.1016/j.apcata.2003.09.031.

(43) Bernal, S.; Botana, F. J.; Calvino, J. J.; Cauqui, M. A.; Cifredo, G. A.; Jobacho, A.; Pintado, J. M.; Rodriguez-Izquierdo, J. M. Microstructural and Chemical Properties of Ceria-Supported Rhodium Catalysts Reduced at 773 K. *J. Phys. Chem* **1993**, *97*, 4118–4123. https://doi.org/http://dx.doi.org/10.1021/j100118a031.

(44) Tanabe, T.; Nagai, Y.; Hirabayashi, T.; Takagi, N.; Dohmae, K.; Takahashi, N.; Matsumoto, S.; Shinjoh, H.; Kondo, J. N.; Schouten, J. C.; Brongersma, H. H. Low Temperature CO Pulse Adsorption for the Determination of Pt Particle Size in a Pt/Cerium-Based Oxide Catalyst. *Appl Catal A Gen* **2009**, *370* (1–2), 108–113. https://doi.org/10.1016/j.apcata.2009.09.030.

(45) Blanchard, G.; Fajardie, F. Benzene Hydrogenation as a Tool for the Determination of the Percentage of Metal Exposed on Low Loaded Ceria Supported Rhodium Catalysts. *J Catal* **1996**, *163* (1), 77–86. https://doi.org/https://doi.org/10.1006/jcat.1996.0306.

(46) Takeguchi, T.; Manabe, S.; Kikuchi, R.; Eguchi, K.; Kanazawa, T.; Matsumoto, S.; Ueda, W. Determination of Dispersion of Precious Metals on CeO2- Containing Supports. *Appl Catal A Gen* **2005**, *293* (1–2), 91–96. https://doi.org/10.1016/j.apcata.2005.07.013.

(47) Marino, S.; Wei, L.; Cortes-Reyes, M.; Cheng, Y.; Laing, P.; Cavataio, G.; Paolucci, C.; Epling, W. Rhodium Catalyst Structural Changes during, and Their Impacts on the Kinetics of, CO Oxidation. *JACS Au* **2023**, *3* (2), 459–467. https://doi.org/10.1021/jacsau.2c00595.

(48) Cargnello, M.; Doan-Nguyen, V. V. T.; Gordon, T. R.; Diaz, R. E.; Stach, E. A.; Gorte, R. J.; Fornasiero, P.; Murray, C. B. Control of Metal Nanocrystal Size Reveals Metal-Support Interface Role for Ceria Catalysts. *Science (1979)* **2013**, *341* (6147), 771–773. https://doi.org/10.1126/science.1240148.

(49) Cargnello, M.; Doan-Nguyen, V. V. T.; Gordon, T. R.; Diaz, R. E.; Stach, E. A.; Gorte, R. J.; Fornasiero, P.; Murray, C. B. Control of Metal Nanocrystal Size Reveals Metal-Support Interface Role for Ceria Catalysts. *Science (1979)* **2013**, *341* (6147), 771–773. https://doi.org/DOI: 10.1126/science.1240148.

(50) Roland Bliem, Jessi van der Hoeven, Adam Zavodny, Oscar Gamba, Jiri Pavelec, Petra E. de Jongh, Michael Schmid, Ulrike Diebold, and G. S. P. An Atomic-Scale View of CO and H2 Oxidation on a Pt-Fe3O4 Model Catalyst. 2015.

(51) Holmgren, A.; Andersson, B. Oxygen Storage Dynamics in Pt/CeO2/Al2O3 Catalysts. *J Catal* **1998**, *25* (1448), 14–25.

(52) Jiang, D.; Wan, G.; García-Vargas, C. E.; Li, L.; Pereira-Hernández, X. I.; Wang, C.; Wang, Y. Elucidation of the Active Sites in Single-Atom Pd1/CeO2Catalysts for Low-Temperature CO Oxidation. *ACS Catal* **2020**, *10* (19), 11356–11364. https://doi.org/10.1021/acscatal.0c02480.

(53) Muravev, V.; Parastaev, A.; Bosch, Y. Van Den; Ligt, B.; Claes, N.; Bals, S.; Kosinov, N.; Hensen, E. J. M. Size of Cerium Dioxide Support Nanocrystals Dictates Reactivity of Highly Dispersed Palladium Catalysts. **2023**, *1178* (June), 1174–1178. https://doi.org/10.1126/science.adf9082.

(54) Binet, C.; Badri, A.; Boutonnet-Kizlingt, M.; Lavalley, J.-C. FTIR Study of Carbon Monoxide Adsorption on Ceria: CO2 Carbonite Dianion Adsorbed Species. *J. Chem. Soc. Faraday Trans.* **1994**, No. 7, 1023–1028. https://doi.org/DOI: 10.1039/FT9949001023.

(55) Bruix, A.; Migani, A.; Vayssilov, G. N.; Neyman, K. M.; Libuda, J.; Illas, F. Effects of Deposited Pt Particles on the Reducibility of CeO 2(111). *Physical Chemistry Chemical Physics* **2011**, *13* (23), 11384–11392. https://doi.org/10.1039/c1cp20950g.

(56) Vayssilov, G. N.; Lykhach, Y.; Migani, A.; Staudt, T.; Petrova, G. P.; Tsud, N.; Skála, T.; Bruix, A.; Illas, F.; Prince, K. C.; Matolín, V.; Neyman, K. M.; Libuda, J. Support Nanostructure Boosts Oxygen Transfer to Catalytically Active Platinum Nanoparticles. *Nat Mater* **2011**, *10* (4), 310–315. https://doi.org/10.1038/nmat2976.

(57) Puigdollers, A. R.; Schlexer, P.; Tosoni, S.; Pacchioni, G. Increasing Oxide Reducibility: The Role of Metal/Oxide Interfaces in the Formation of Oxygen Vacancies. *ACS Catal* **2017**, *7* (10), 6493–6513. https://doi.org/10.1021/acscatal.7b01913.

(58) Pacchioni, G.; Pescarmona, P. Structure and Stability of Oxygen Vacancies on Sub-Surface, Terraces, and Low-Coordinated Surface Sites of MgO: An Ab Initio Study. *Surf Sci* **1998**, *412–413*, 657–671. https://doi.org/10.1016/S0039-6028(98)00501-9.

(59) Pacchioni, G.; Pescarmona, P. Structure and Stability of Oxygen Vacancies on Sub-Surface, Terraces, and Low-Coordinated Surface Sites of MgO: An Ab Initio Study. *Surf Sci* **1998**, *412–413*, 657–671. https://doi.org/10.1016/S0039-6028(98)00501-9.

(60) Ruiz Puigdollers, A.; Illas, F.; Pacchioni, G. Reduction of Hydrogenated ZrO2 Nanoparticles by Water Desorption. *ACS Omega* **2017**, *2* (7), 3878–3885. https://doi.org/10.1021/acsomega.7b00799.

(61) Puigdollers, A. R.; Illas, F.; Pacchioni, G. Structure and Properties of Zirconia Nanoparticles from Density Functional Theory Calculations. *Journal of Physical Chemistry C* **2016**, *120* (8), 4392–4402. https://doi.org/10.1021/acs.jpcc.5b12185.

(62) Migani, A.; Vayssilov, G. N.; Bromley, S. T.; Illas, F.; Neyman, K. M. Greatly Facilitated Oxygen Vacancy Formation in Ceria Nanocrystallites. *Chemical Communications* **2010**, *46* (32), 5936–5938. https://doi.org/10.1039/c0cc01091j.

(63) Kozlov, S. M.; Neyman, K. M. Effects of Electron Transfer in Model Catalysts Composed of Pt Nanoparticles on CeO2(1 1 1) Surface. *J Catal* **2016**, *344*, 507–514. https://doi.org/10.1016/j.jcat.2016.10.014.

(64) Suchorski, Y.; Kozlov, S. M.; Bespalov, I.; Datler, M.; Vogel, D.; Budinska, Z.; Neyman, K. M.; Rupprechter, G. The Role of Metal/Oxide Interfaces for Long-Range Metal Particle Activation

during CO Oxidation. *Nat Mater* **2018**, *17* (6), 519–522. https://doi.org/10.1038/s41563-018-0080-y.

(65) Pacchioni, G. Electronic Interactions and Charge Transfers of Metal Atoms and Clusters on Oxide Surfaces. *Physical Chemistry Chemical Physics* **2013**, *15* (6), 1737–1757. https://doi.org/10.1039/c2cp43731g.

(66) Vayssilov, G. N.; Migani, A.; Neyman, K. Density Functional Modeling of the Interactions of Platinum Clusters with CeO2 Nanoparticles of Different Size. *Journal of Physical Chemistry C* **2011**, *115* (32), 16081–16086. https://doi.org/10.1021/jp204222k.

(67) Migani, A.; Vayssilov, G. N.; Bromley, S. T.; Illas, F.; Neyman, K. M. Greatly Facilitated Oxygen Vacancy Formation in Ceria Nanocrystallites. *Chemical Communications* **2010**, *46* (32), 5936–5938. https://doi.org/10.1039/c0cc01091j.

(68) Sharma, S.; Hilaire, S.; Vohs, J. M.; Gorte, R. J.; Jen, H. W. Evidence for Oxidation of Ceria by CO2. *J Catal* **2000**, *190* (1), 199–204. https://doi.org/10.1006/jcat.1999.2746.

(69) Puigdollers, A. R.; Schlexer, P.; Tosoni, S.; Pacchioni, G. Increasing Oxide Reducibility: The Role of Metal/Oxide Interfaces in the Formation of Oxygen Vacancies. *ACS Catal* **2017**, *7* (10), 6493–6513. https://doi.org/10.1021/acscatal.7b01913.

(70) Lykhach, Y.; Figueroba, A.; Camellone, M. F.; Neitzel, A.; Skála, T.; Negreiros, F. R.; Vorokhta, M.; Tsud, N.; Prince, K. C.; Fabris, S.; Neyman, K. M.; Matolín, V.; Libuda, J. Reactivity of Atomically Dispersed Pt2+ Species towards H2: Model Pt-CeO2 Fuel Cell Catalyst. *Physical Chemistry Chemical Physics* **2016**, *18* (11), 7672–7679. https://doi.org/10.1039/c6cp00627b.

(71) Holmgren, A.; Andersson, B. Oxygen Storage Dynamics in Pt/CeO2/Al2O3 Catalysts. *J Catal* **1998**, *25* (1448), 14–25.

(72) Panagiotopoulou, P.; Kondarides, D. I. Effects of Promotion of TiO2 with Alkaline Earth Metals on the Chemisorptive Properties and Water-Gas Shift Activity of Supported Platinum Catalysts. *Appl Catal B* **2011**, *101* (3–4), 738–746. https://doi.org/10.1016/j.apcatb.2010.11.016.

(73) Panagiotopoulou, P.; Kondarides, D. I. Effects of Alkali Promotion of TiO2 on the Chemisorptive Properties and Water-Gas Shift Activity of Supported Noble Metal Catalysts. *J Catal* **2009**, *267* (1), 57–66. https://doi.org/10.1016/j.jcat.2009.07.014.

(74) He, Z.; Hu, M.; Wang, X. Highly Effective Hydrodeoxygenation of Guaiacol on Pt/TiO2: Promoter Effects. *Catal Today* **2018**, *302*, 136–145. https://doi.org/10.1016/j.cattod.2017.02.034.

(75) Del Río, E.; Collins, S. E.; Aguirre, A.; Chen, X.; Delgado, J. J.; Calvino, J. J.; Bernal, S. Reversible Deactivation of a Au/Ce0.62Zr0.38O 2 Catalyst in CO Oxidation: A Systematic Study of CO 2-Triggered Carbonate Inhibition. *J Catal* **2014**, *316*, 210–218. https://doi.org/10.1016/j.jcat.2014.05.016.

(76) Kotobuki, M.; Leppelt, R.; Hansgen, D. A.; Widmann, D.; Behm, R. J. Reactive Oxygen on a Au/TiO2 Supported Catalyst. *J Catal* **2009**, *264* (1), 67–76. https://doi.org/10.1016/j.jcat.2009.03.013.

(77) Farmer, J. A.; Campbell, C. T. Catalyst Particles by Strong Metal Catalyst Particles by Strong Metal-Support Bonding. *Science (1979)* **2010**, *329* (August), 933–936.

(78) Blyholder, G. Molecular Orbital View of Chemisorbed Carbon Monoxide. *Journal of Physical Chemistry* **1964**, *68* (10), 2772–2778. https://doi.org/10.1021/j100792a006.

(79) Hoffman, A. S.; Fang, C. Y.; Gates, B. C. Homogeneity of Surface Sites in Supported Single-Site Metal Catalysts: Assessment with Band Widths of Metal Carbonyl Infrared Spectra. *Journal of Physical Chemistry Letters* **2016**, *7* (19), 3854–3860. https://doi.org/10.1021/acs.jpclett.6b01825.

(80) Collins, S. E.; Cíes, J. M.; Del Río, E.; López-Haro, M.; Trasobares, S.; Calvino, J. J.; Pintado, J. M.; Bernal, S. Hydrogen Interaction with a Ceria-Zirconia Supported Gold Catalyst Influence of CO Co-Adsorption and Pretreatment Conditions. *Journal of Physical Chemistry C* **2007**, *111* (39), 14371–14379. https://doi.org/10.1021/jp0719681.

(81) Boudart, M.; Hwang, H. S. Solubility of Hydrogen in Small Particles of Palladium. *J Catal* **1975**, *39*, 44–52. https://doi.org/https://doi.org/10.1016/0021-9517(75)90280-8.

(82) Goodman, E. D.; Carlson, E. Z.; Dietze, E. M.; Tahsini, N.; Johnson, A.; Aitbekova, A.; Nguyen Taylor, T.; Plessow, P. N.; Cargnello, M. Size-Controlled Nanocrystals Reveal Spatial Dependence and Severity of Nanoparticle Coalescence and Ostwald Ripening in Sintering Phenomena. *Nanoscale* **2021**, *13* (2), 930–938. https://doi.org/10.1039/d0nr07960j.

(83) Dong, C.; Zong, X.; Jiang, W.; Niu, L.; Liu, Z.; Qu, D.; Wang, X.; Sun, Z. Recent Advances of Ceria-Based Materials in the Oxidation of Carbon Monoxide. *Small Struct* **2021**, *2* (2). https://doi.org/10.1002/sstr.202000081.

(84) Kim, H. J.; , Myeong Gon Jang,Dongjae Shin, and J. W. H. Design of Ceria Catalysts for Low-Temperature CO Oxidation. *ChemCatChem* **2020**, *12*, 11–26. https://doi.org/https://doi.org/10.1002/cctc.201901787.

(85) Shekhar, M.; Wang, J.; Lee, W. S.; Williams, W. D.; Kim, S. M.; Stach, E. A.; Miller, J. T.; Delgass, W. N.; Ribeiro, F. H. Size and Support Effects for the Water-Gas Shift Catalysis over Gold Nanoparticles Supported on Model Al2O3 and TiO2. *J Am Chem Soc* **2012**, *134* (10), 4700–4708. https://doi.org/10.1021/ja210083d.

(86) Bunluesin, T.; Cordatos, H.; Gorte, R. J. Study of CO Oxidation Kinetics on Rh/Ceria. *Journal of Catalysis*. 1995, pp 222–226. https://doi.org/10.1006/jcat.1995.1282.

(87) Liu, B.; Liu, J.; Li, T.; Zhao, Z.; Gong, X. Q.; Chen, Y.; Duan, A.; Jiang, G.; Wei, Y. Interfacial Effects of CeO2-Supported Pd Nanorod in Catalytic CO Oxidation: A Theoretical Study. *Journal of Physical Chemistry C* **2015**, *119* (23), 12923–12934. https://doi.org/10.1021/acs.jpcc.5b00267.

(88) Lohrenscheit, M.; Hess, C. Direct Evidence for the Participation of Oxygen Vacancies in the Oxidation of Carbon Monoxide over Ceria-Supported Gold Catalysts by Using Operando Raman Spectroscopy. *ChemCatChem* **2016**, *8* (3), 523–526. https://doi.org/10.1002/cctc.201501129.

(89) G.S. Zafiris G.S.; Gorte, R. J. Evidence for a Second CO Oxidation Mechanism on Rh/Ceria. *Journal of Catalysis*. 1993, pp 86–91. https://doi.org/https://doi.org/10.1006/jcat.1993.1255.

(90) Martínez-Arias, A.; Coronado, J. M.; Cataluñ, R.; Conesa, J. C.; Soria, J. *Influence of Mutual Platinum-Dispersed Ceria Interactions on the Promoting Effect of Ceria for the CO Oxidation Reaction in a Pt/CeO2/Al2O3 Catalyst*; 1998. https://doi.org/https://doi.org/10.1021/jp9805306.

(91) Martínez-Arias, A.; Hungría, A. B.; Fernández-García, M.; Conesa, J. C.; Munuera, G. Interfacial Redox Processes under CO/O2 in a Nanoceria-Supported Copper Oxide Catalyst. *Journal of Physical Chemistry B* **2004**, *108* (46), 17983–17991. https://doi.org/10.1021/jp0465837.

(92) Rainer, D. R.; Koranne, M.; Vesecky, S. M.; Goodman, D. W. CO + O2 and CO + NO Reactions over Pd/Al2O3 Catalysts. *Journal of Physical Chemistry B* **1997**, *101* (50), 10769–10774. https://doi.org/10.1021/jp971262z.

(93) Gaudet, J. R.; De La Riva, A.; Peterson, E. J.; Bolin, T.; Datye, A. K. Improved Low-Temperature CO Oxidation Performance of Pd Supported on La-Stabilized Alumina. *ACS Catal* **2013**, *3* (5), 846–855. https://doi.org/10.1021/CS400024U/SUPPL_FILE/CS400024U_SI_001.PDF.

Chapter 7: Conclusions and future work

7.1 Conclusions

The three-way catalyst is the key component of gasoline vehicle aftertreatment systems. Despite its high efficiency for todays' regulatory cycles, the TWC must adapt to new technologies and improve in low-temperature performance and durability to comply with increasingly stringent emission regulations. Along with the challenges posed by these new emission regulations, automotive manufacturers and catalyst suppliers must consider the catalyst cost. The high volatility of PGM price has prompted extensive research aimed at optimizing catalyst formulations. Effort has been directed towards reducing the precious metal content and developing new catalyst formulations. To accomplish these goals, a detailed understanding of the reaction mechanism is needed. In this work we focused on Rh/Al_2O_3 and Pd/CeO_2, considered as model catalysts representative of TWC. Both catalysts face similar challenges, particularly in accurately measuring active site amounts.

On Rh/Al_2O_3 we investigated CO oxidation and NO reduction by CO kinetics. Our main goal was to gain insights into the mobility of the active sites. Rh catalysts exhibit high mobility and can change their structure when exposed to varying feed compositions and temperature. Rh structural changes during the reaction introduce uncertainty in active site quantities, measured via ex-situ characterization techniques, such as H_2 chemisorption. We showed that the Rh nanoparticles undergo redispersion into single atoms when the catalysts are exposed to oxidizing mixtures of CO and O_2, with $CO/O_2 < 2$. The structural changes during CO oxidation lead to a lower activity in the low temperature region, where particle disintegration is favored. However, at higher temperature, CO-assisted single atoms aggregation occurs, resulting in a larger amount of nanoparticles - the active sites for CO oxidation - and therefore a higher activity. CO oxidation kinetics showed

that the temperature at which these structural changes occurring during the reaction depend on the Rh particle size, with smaller nanoparticles being more prone to disintegration and maintaining the single atoms form to higher temperature. In addition, the presence of water did not show any effect on the nanoparticle-single atoms interconversion. Spectroscopy studies played a crucial role in reconciling the differences in turnover frequencies measured at low and high temperatures, indicating that the differences lie in the amount of active sites, with less nanoparticles in the low temperature regime compared to the high temperature one.

Spectroscopy studies also showed that the mobility of nanoparticles and single atoms in the presence of CO, O_2 and water influences the conversion profile observed before reaching a steady state. Under dry conditions, oxygen leads to an enhancement in Rh nanoparticles redispersion into single atoms, promoting the oxidative process which changes the metal oxidation state from 0 to 1. In the presence of water, which modifies the Rh coordination environment, O_2 also stabilizes Rh single atoms formed during the nanoparticle redispersion process. These spectroscopic analyses provided more insights into how variation in the feed composition and the presence of hydroxyl groups in the vicinity of the metal cation modify Rh mobility.

After a detailed investigation on the effect of CO, O_2 and H_2O on the Rh structure, we proceeded to explore the NO reduction by CO kinetics in the presence and absence of water. NO reduction by CO is indeed one of the main reactions in the TWC and a consensus on the reaction mechanism has not been reached. Our findings indicate that H_2O influences the kinetics by increasing the apparent activation energies under reducing, stoichiometric and oxidizing conditions. Our study stood on the hypothesis that NH_3 was the cause of the change in activation energy, leading to a form of catalyst deactivation. Our study remained inconclusive, and more work is needed to elucidate the cause of the change in kinetics and deactivation.

The concluding part of our work is dedicated to Pd/CeO_2. Ceria-supported catalysts presents difficulties in the active site surface area measurements when using traditional techniques, complicating the determination of turnover frequencies. In our work, we proposed a modified CO chemisorption method to measure metal dispersion, using static chemisorption. Conventional CO chemisorption results in an overestimation of the CO uptake, because of the reaction between CO and mobile lattice oxygen leading to carbonate formation. Pre-adsorbing CO_2 and forming carbonates before CO chemisorption can hinder further carbonate formation, ensuring good dispersion measurement estimations. This method validated via spectroscopic studies and CO oxidation kinetics using Pd/CeO_2 catalysts characterized by different ceria sizes. We showed that the degree of overestimation in CO uptake depends on ceria size. Small ceria nanoparticles exhibit high oxygen mobility, facilitating carbonate formation. In contrast, ceria nanoparticles larger than 100 nm form carbonates to an extent that does not impact dispersion measurements. A comparison between CO and CO_2-CO chemisorption highlights this distinction. Larger nanoparticles showed similar dispersion measurement values obtained with both methods, while smaller nanoparticles showed a larger difference in the dispersion measurements obtained with the two methods. This approach can allow dispersion measurements on new catalyst formulations which include ceria and other promoters which increase the oxygen storage capacity and can alter the dispersion measurements obtained with traditional CO chemisorption.

7.2 Future work

Based the work presented in this thesis, the following recommendations for future research are listed below:

- Future work should focus on understanding the Rh single atoms aggregation mechanism occurring at high temperature. While a mechanism of nanoparticle dispersion in the

presence of CO at low temperature has been suggested and involved a WGS-like mechanism, a mechanism for Rh single atoms aggregation at high temperature is still lacking. The single atoms aggregation can be investigated using catalysts with the more homogeneous supports. This approach could allow the determination of the coordination environment surrounding the metal ions and provides insights into how the support and the environment can influence the single atoms mobility towards nanoparticle formation.

- The NO reduction by CO kinetics and the effect of water and NH_3 have not provided conclusive results. The cause of the deactivation observed in the conversion profile obtained on the 0.05% Rh/Al_2O_3 catalyst under reducing conditions and in the presence of water remains unknown. The cause could be attributed to deactivation, such as sintering or the presence of stable surface species acting as site blockers. Electron microscopy could be employed to assess the presence of larger nanoparticles or an adsorbate overlayer/oxide layer on the nanoparticles.
- The factors contributing to the increase in activation energy in the presence of water need further elucidation. The identification of the rate-limiting step and the development of a kinetic model can be helpful to gain understanding of the mechanism involved.
- Rh single atom activity is still unclear. Modulation excitation spectroscopy could be used as a tool to evaluate Rh single atoms activity in the NO reduction by CO in the presence and absence of water.
- Regarding the Pd/CeO_2 catalysts, the proposed method can be used to measure the active surface area of newly formulated catalysts which include additives and promoters intended to increase TWC activity. Future work will include the comparison of the turnover

frequency measured on these catalysts to determine if they can replace the current formulation in use.

- The kinetic data presented in the appendix will be incorporated in a more extensive study, including further characterization of these catalysts, using XRD, STEM/EDS and XAS. This will help understand the role of SrO in the catalyst formulation in slowing the catalyst deactivation and whether it has an impact on hindering the formation of Rh aluminates or preventing sintering.

Appendix A - Supporting Information of Chapter 3: Rhodium catalyst structural changes during CO oxidation

Section A1. Dispersion measurements

Table A.1: Dispersion and particle size measurements on Rh/Al_2O_3 catalysts

Catalyst	Dispersion	Particle size
0.05%Rh/Al_2O_3	150	<1
0.1% Rh/Al_2O_3	96	1.1
0.1% Rh/Al_2O_3 H_2 -700	64	1.6
0.1% Rh/Al_2O_3 H_2 -800	30	3.3
0.1%Rh/Al_2O_3 - Cycling Aged	18	5.5
0.1% Rh/Al_2O_3 H_2 -900	10.5	9.2

All the dispersions listed in Table A.1 were calculated considering a H:Rh ratio 1:1. The 0.05% Rh/Al_2O_3 catalyst resulted in a dispersion higher the 100%. This is due to the hydrogen-to-metal ratio exceeding 1 for highly dispersed Rh catalysts[1]. Therefore, we infer that the particle size of this specific catalyst is lower than 1 nm.

Section A2. Cordierite activity

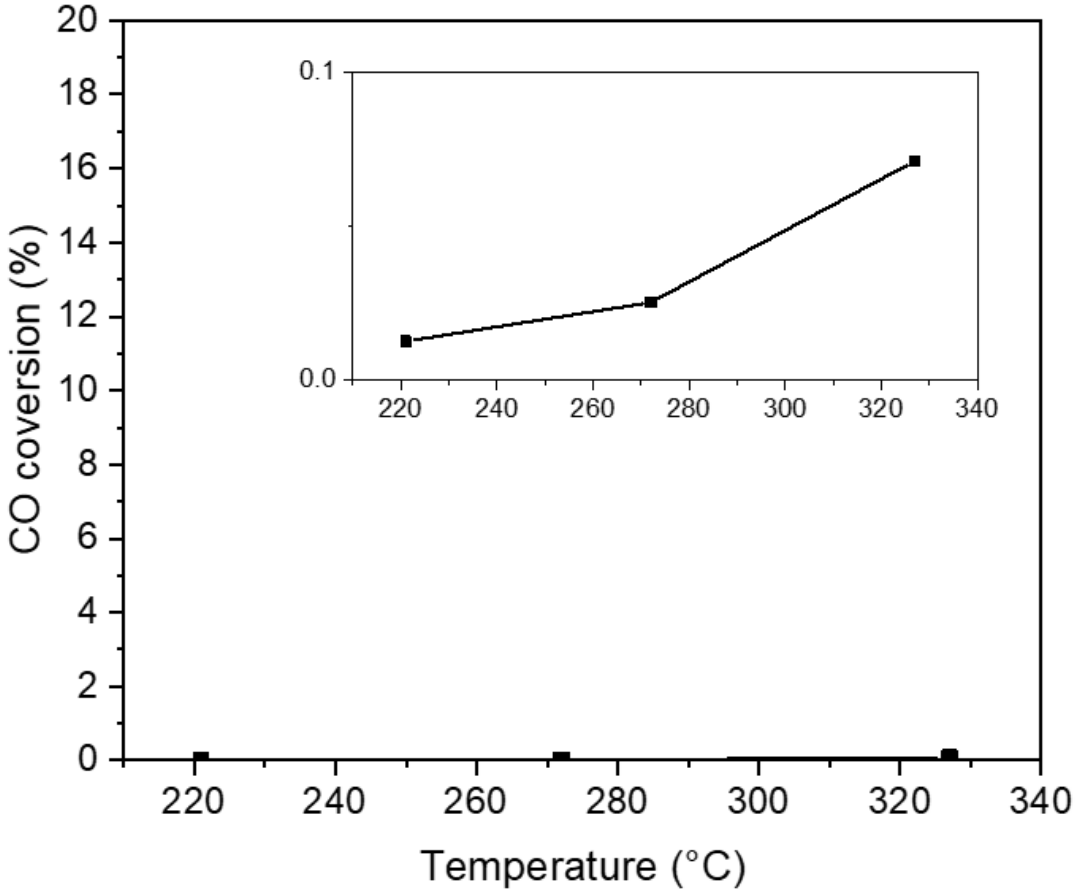

Figure A.1: CO oxidation conversion from cordierite. CO = 8400 ppm, CO/O_2 = 0.9, total flowrate = 500. Cordierite = 250 mg. The cordierite was pretreated in 5% H_2 at 500°C for 30 min. All the data were obtained after reaching steady-state.

Section A3. CO oxidation Arrhenius plots

A 3.1 CO oxidation

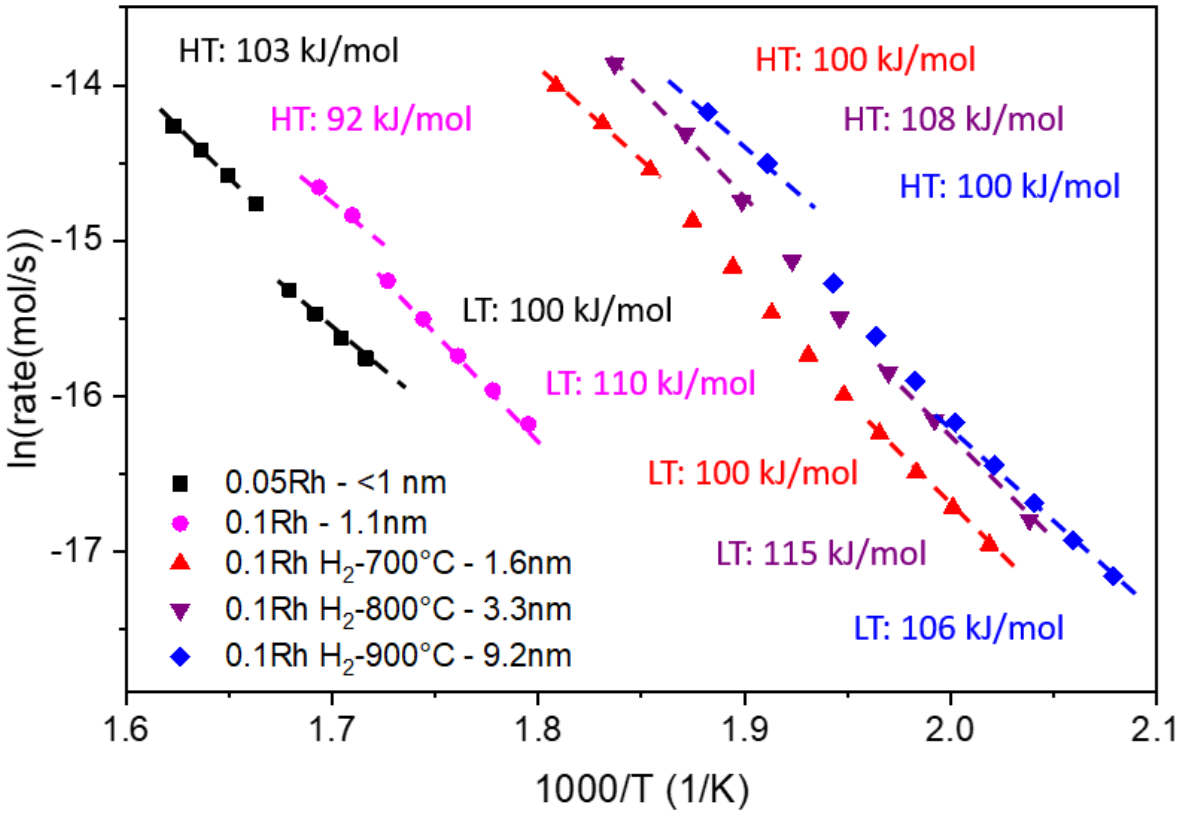

Figure A.2: CO oxidation Arrhenius plots obtained from the 0.05%Rh/Al_2O_3, 0.1%Rh/Al_2O_3, 0.1%Rh/Al_2O_3 H_2-700°C, 0.1%Rh/Al_2O_3 H_2-800°C and 0.1%Rh/Al_2O_3 H_2-900°C samples. CO = 8400-13000 ppm; CO/O_2 = 0.9, total flowrate = 500-750. Catalyst weight = 5-13 mg. The catalysts were pretreated in 5% H_2 at 500°C for 30 min. The temperature was changed from high to low temperature. All the rate measurements were obtained at steady-state.

A 3.2 CO oxidation in the presence of water

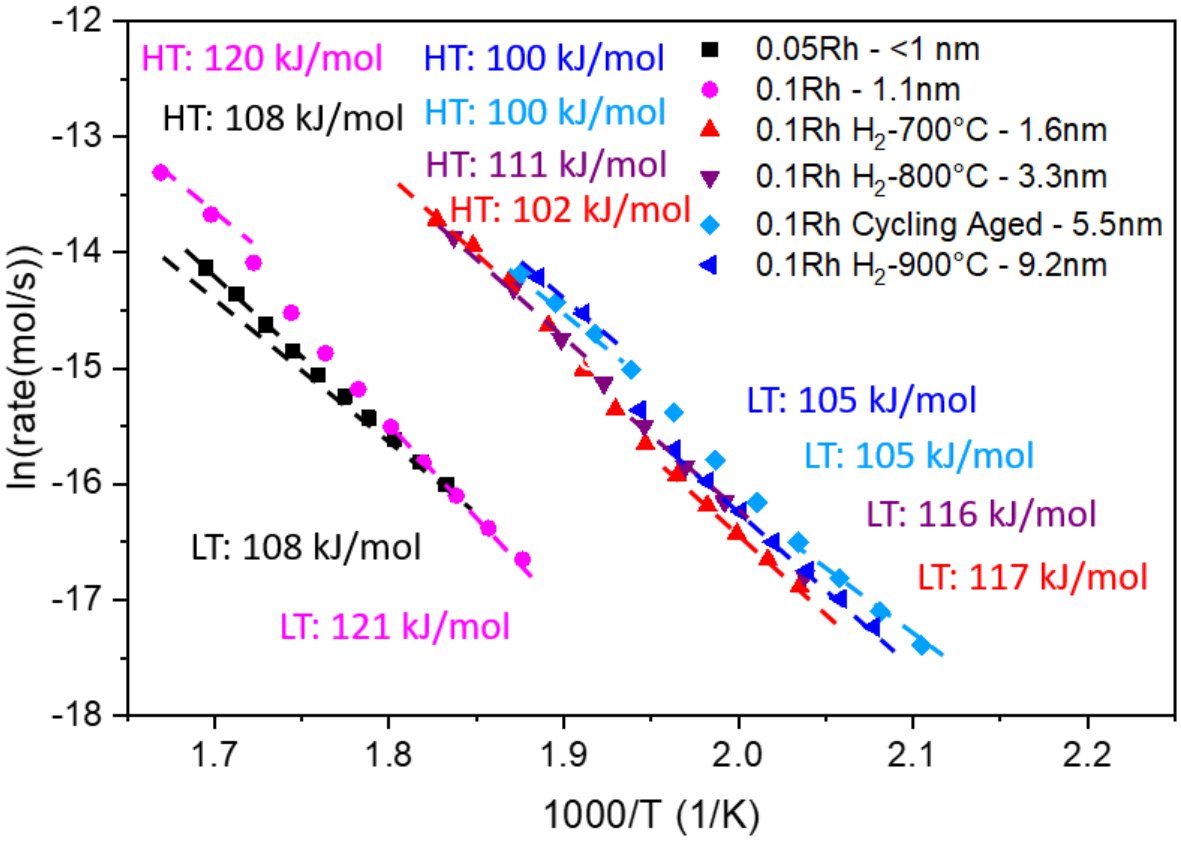

Figure A.3: CO oxidation Arrhenius plots obtained from the 0.05%Rh/Al_2O_3, 0.1%Rh/Al_2O_3, 0.1%Rh/Al_2O_3 H_2-700°C, 0.1%Rh/Al_2O_3 H_2-800°C, 0.1%Rh/Al_2O_3 Ford aged and 0.1%Rh/Al_2O_3 H_2-900°C. CO = 8400-13000 ppm; CO/O_2 = 0.9, H_2O = 6%, total flowrate = 500-750. Catalyst weight = 5-13 mg. The catalysts were pretreated in 5% H_2 at 500°C for 30 min. The temperature was changed from high to low temperature for all the samples with the exception of the 0.1%Rh/Al_2O_3, for which the temperature was changed from low to high temperature. All the rate measurements were obtained at steady-state.

A 3.3 Internal mass transfer check

$$Nwp = \frac{r_{obs}\rho_{cat}d_P^2}{4D_eC_b} < 1$$

- r_{obs} = measure reaction rate [mol g^{-1} s^{-1}]
- ρ_{cat} = catalyst pellet density [g cm^{-3}]
- d_P = pellet diameter [cm]

- D_e = gas diffusivity [cm^2 s^{-1}]
- C_b = gas concentration [mol cm^{-3}]

A 3.4 External mass transfer check

$$\frac{r_{obs}\rho_{cat}d_P}{k_g C_b} < 0.15$$

Where:

- r_{obs} = measure reaction rate [mol g^{-1} s^{-1}]
- ρ_{cat} = catalyst pellet density [g cm^{-3}]
- d_P = pellet diameter [cm]
- k_g = external mass transfer coefficient [cm s^{-1}]
- C_b = gas concentration [mol cm^{-3}]

A 3.5 Internal heat transfer check

$$\frac{(-\Delta H)r_{obs}\rho_{cat}d_P^2}{60\lambda_c T_s} < 0.05$$

Where:

- ΔH reaction enthalpy [J mol^{-1}]
- r_{obs} = measure reaction rate [mol g^{-1} s^{-1}]
- ρ_{cat} = catalyst pellet density [g cm^{-3}]
- d_P = pellet diameter [cm]
- λ_c = heat conductivity [W cm^{-1} s^{-1}]
- C_b = gas concentration [mol cm^{-3}]

A 3.6 External heat transfer check

$$\frac{(-\Delta H)r_{obs}\rho_{cat}d_P}{6h_g T_b} < 0.05$$

- ΔH reaction enthalpy [J mol^{-1}]
- r_{obs} = measure reaction rate [mol g^{-1} s^{-1}]
- ρ_{cat} = catalyst pellet density [g cm^{-3}]
- d_P = pellet diameter [cm]
- h_g = heat transfer coefficient between gas and pellet [W cm^{-1} s^{-1}]
- C_b = gas concentration [mol cm^{-3}]

All the experiments met the criteria listed above. The Weisz-Prater number was lower than 1, the external mal transfer ratio lower than 0.15 and the internal and external heat transfer ratios were lower than 0.05.

When the criteria were not met and the reaction was not under kinetic regime, the flowrate and/or the CO and O_2 concentrations were adjusted in order to meet the criteria.

Section A.4. Water effect on CO oxidation

Figure A4 shows the Arrhenius plots obtained during CO oxidation in the presence and absence of water. The rates were normalized by the amount of catalyst used. The rates of the experiment in the presence of water are higher compared to the dry CO oxidation, suggesting water affects the single atoms agglomeration and therefore the amount of active sites. However, the *T change* is not affected and it occurs at 300°C

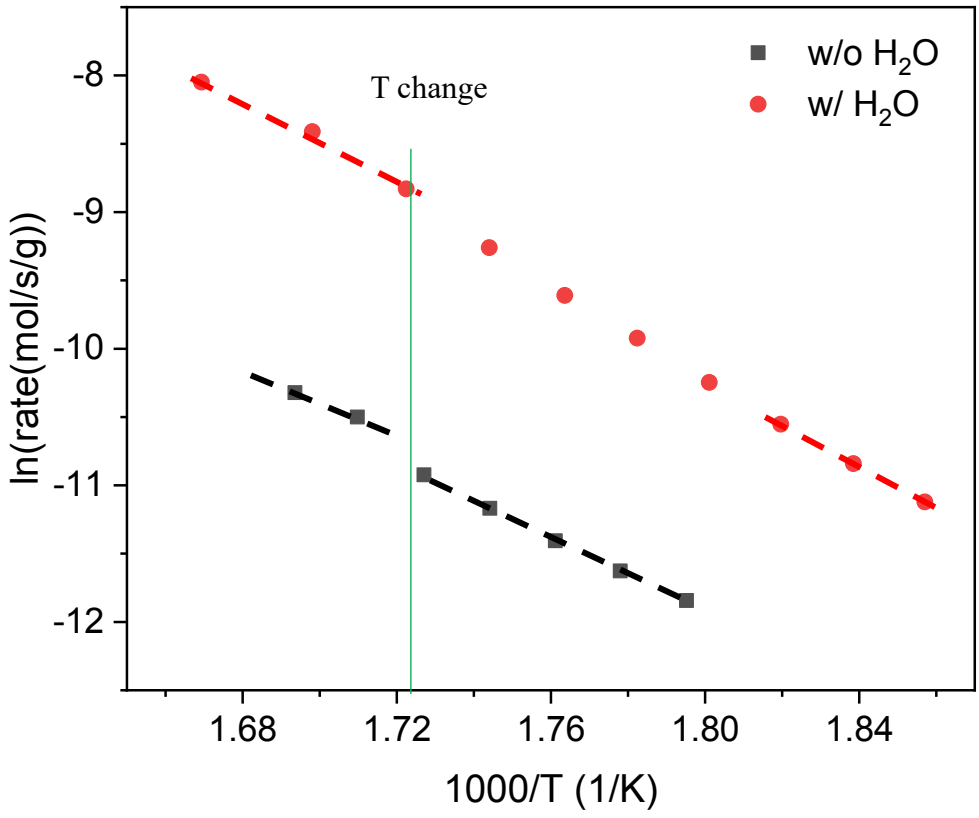

Figure A.4: CO oxidation Arrhenius plot obtained from the 0.1%Rh/Al_2O_3. CO = 10000 ppm, H_2O = 6%, total flowrate = 500. Catalyst weight = 5 (w/ H_2O) and 13 (w/ H_2O) mg. The catalysts were pretreated in 5% H_2 at 500°C for 30 min. All the rate measurements were obtained at steady-state.

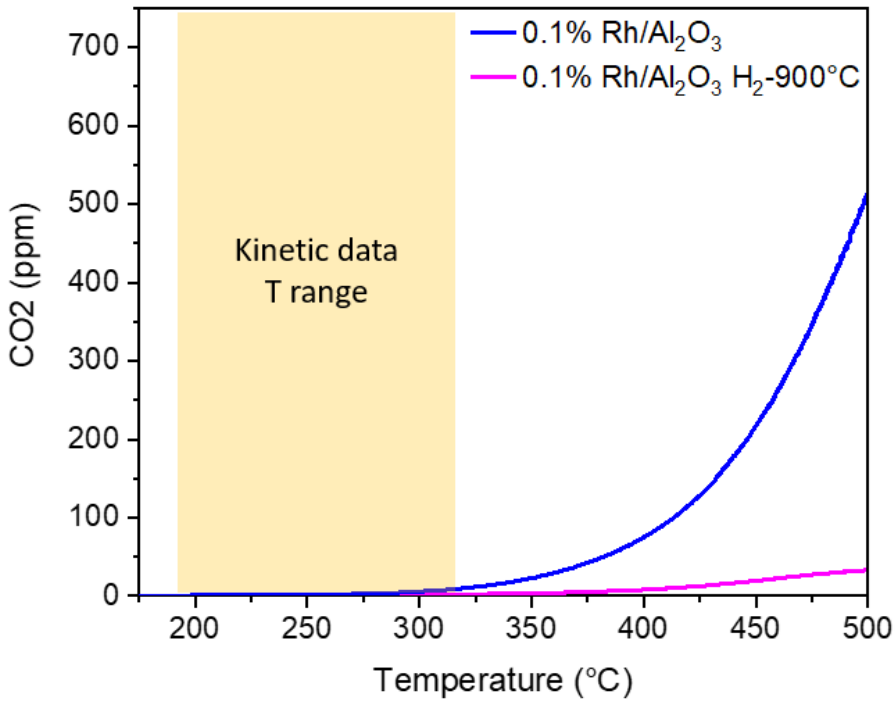

Figure A.5: CO_2 formation during Temperature Programmed Reaction on 0.1%Rh/Al_2O_3 and 0.1%Rh/Al_2O_3 H_2-900°C. CO = 8400 ppm, H_2O = 6%, total flowrate = 500. Catalyst weight = 13 mg. The catalysts were pretreated in 5% H_2 at 500°C for 30 min. The temperature was increased by 10°C/min.

Figure A6 shows CO and H_2O consumptions during temperature programmed reaction of CO oxidation in the presence of 0.8%H_2O in the temperature range of interest (200-350°C). As CO concentration decreases, H_2O concentration remains stable at 0.8%. This result suggests that the CO is oxidized by O_2 and water gas shift has little or no effect.

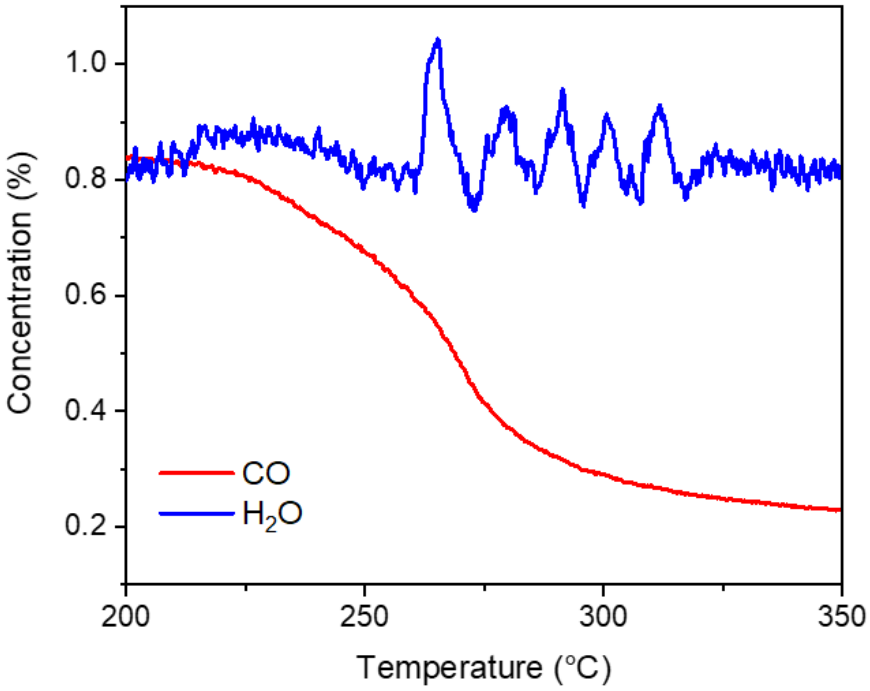

Figure A.6: CO and H_2O consumption during Temperature Programmed Reaction on 0.1%Rh/Al_2O_3 . CO = 8400 ppm, O_2 = 9250 ppm, H_2O = 0.8%, total flowrate = 500. Catalyst weight = 13 mg. The catalyst was pretreated in 5% H_2 at 500°C for 30 min.

Section A5. DRIFTS Spectra

A 5.1 CO + O_2 at 260°C on 0.1% Rh/Al_2O_3 – H_2 700°C

The deconvolution of the overlapping features of each spectrum corrected at different temperature during in-situ CO oxidation was carried out using Gaussian functions. Figure A.7 represents an example of a deconvolution performed on 0.1% Rh/Al_2O_3 – H_2 700°C.

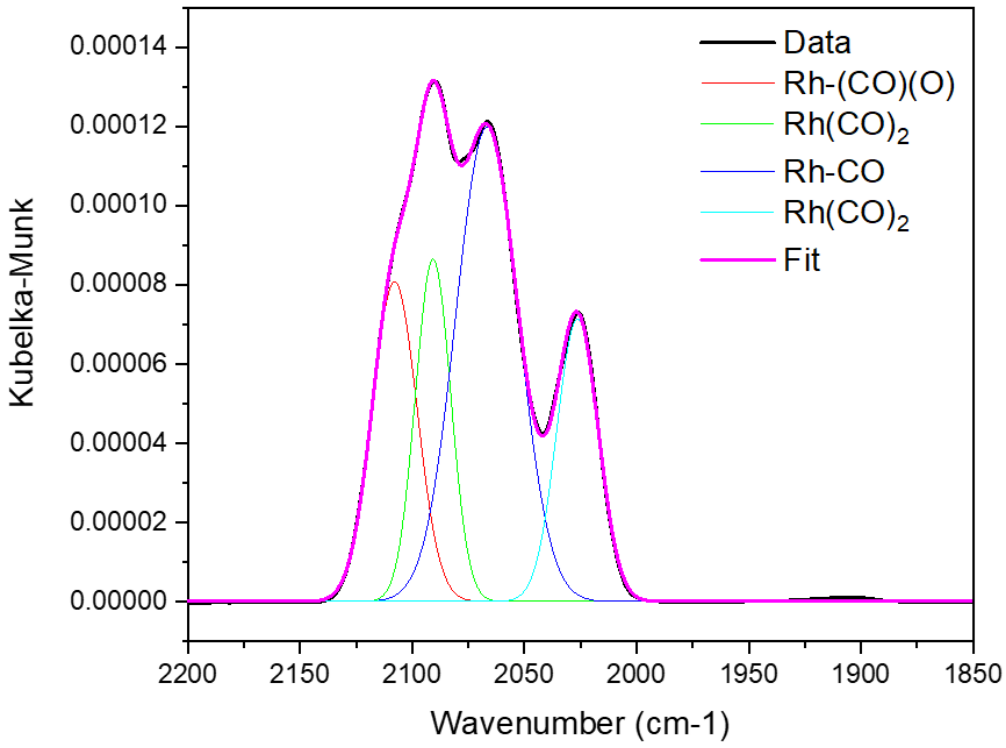

Figure A.7: DRIFTS spectrum of 0.1%Rh/Al_2O_3 H_2-700°C during CO oxidation at 260°C. CO = 8400 ppm; O_2 = 9250 ppm. The catalyst was exposed to 1% O_2 at 500°C for 30 min, followed by He purge for 10 min and 5% H_2 at 500°C for 30 min.

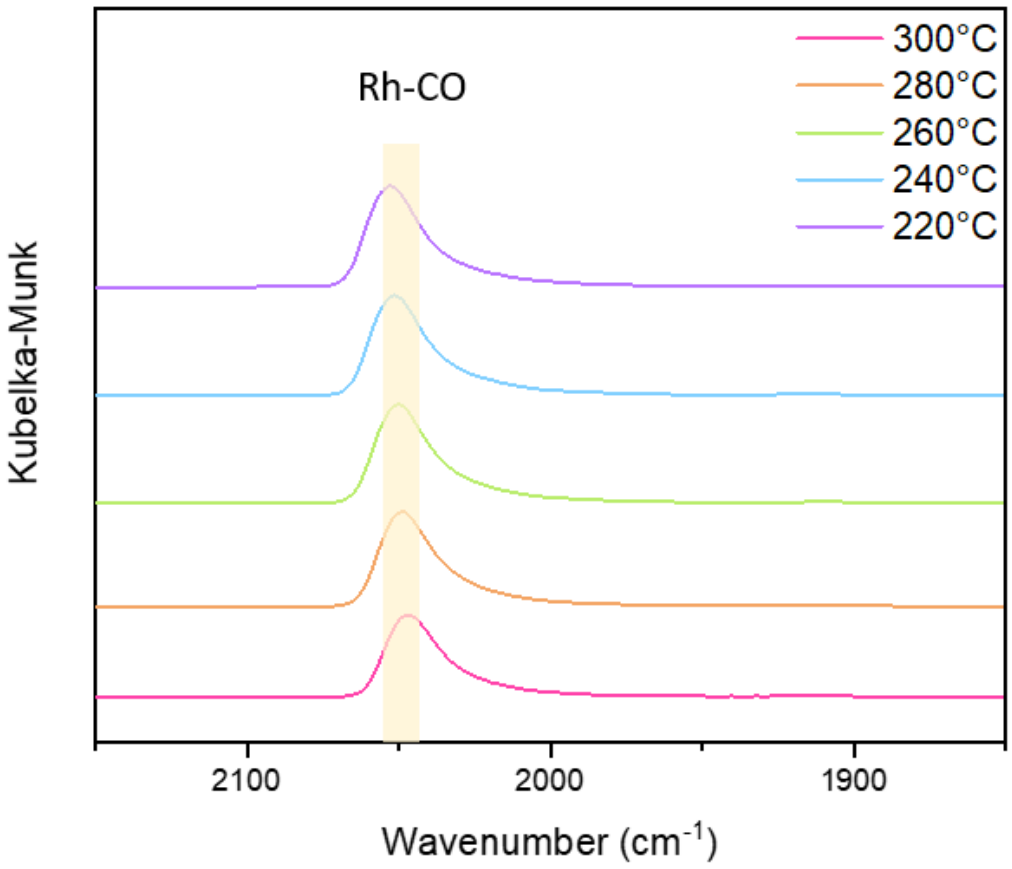

Figure A.8: DRIFTS spectra of 0.1%Rh/Al_2O_3 H_2-700°C during CO adsorption at 220, 240, 260, 280, 300°C. CO = 8400 ppm. The catalyst was exposed to 1% O_2 at 500°C for 30 min, followed by He purge for 10 min and 5% H_2 at 500°C for 30 min

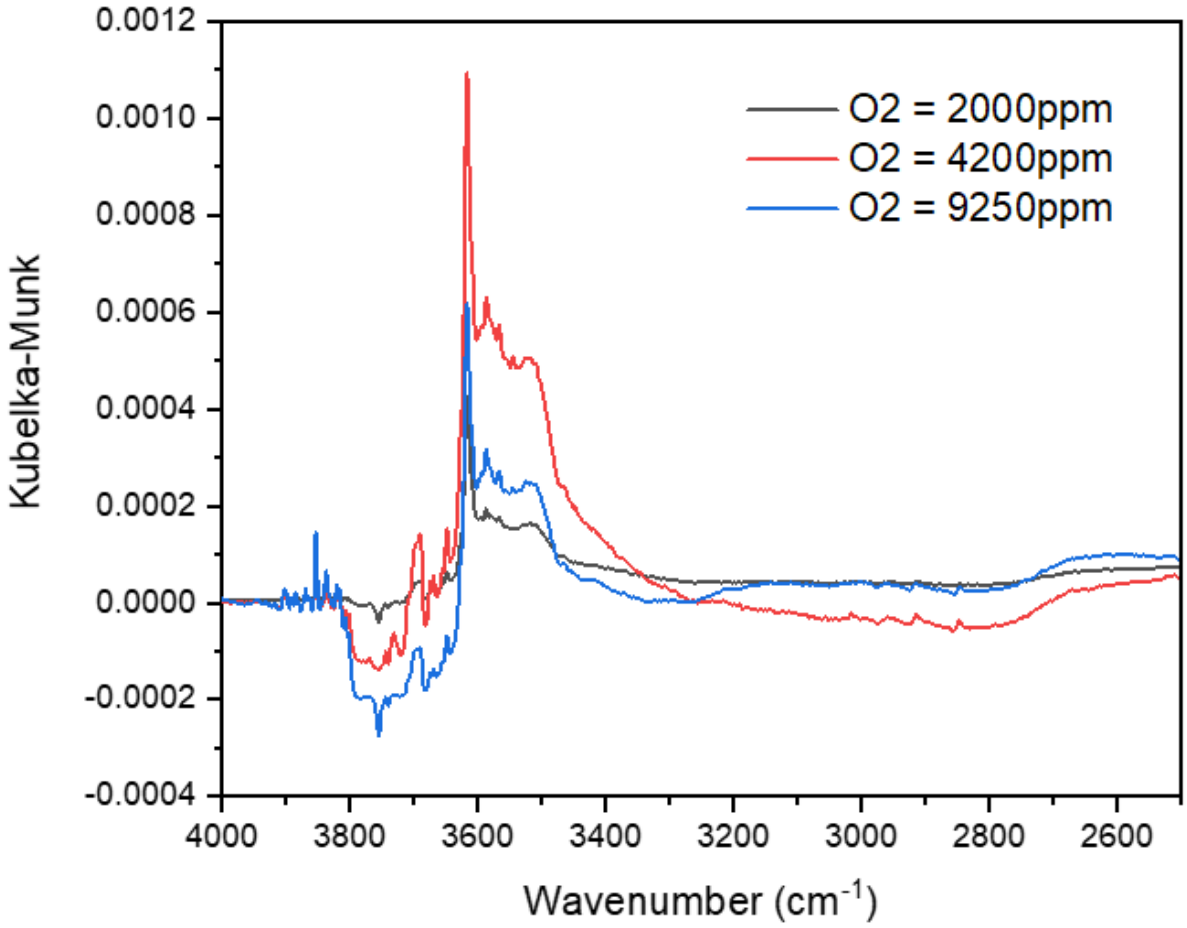

Figure A.9: DRIFTS spectrum of 0.1%Rh/Al_2O_3 H_2-700°C during CO oxidation at 260°C. CO = 8400 ppm; O_2 = 2000, 4200, 9250 ppm. The catalyst was exposed to 1% O_2 at 500°C for 30 min, followed by He purge for 10 min and 5% H_2 at 500°C for 30 min

Appendix B - Supporting information of Chapter 6: Adapted CO chemisorption technique to measure metal particle dispersion on ceria-containing catalysts

Section B1: Physical characterization

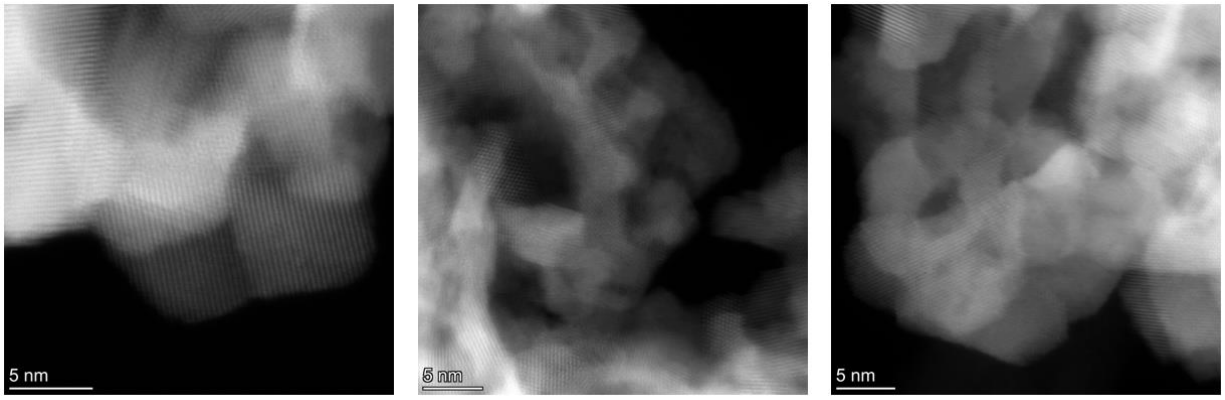

Figure B.1: STEM images of 1% Pd/CeO_2 10 nm

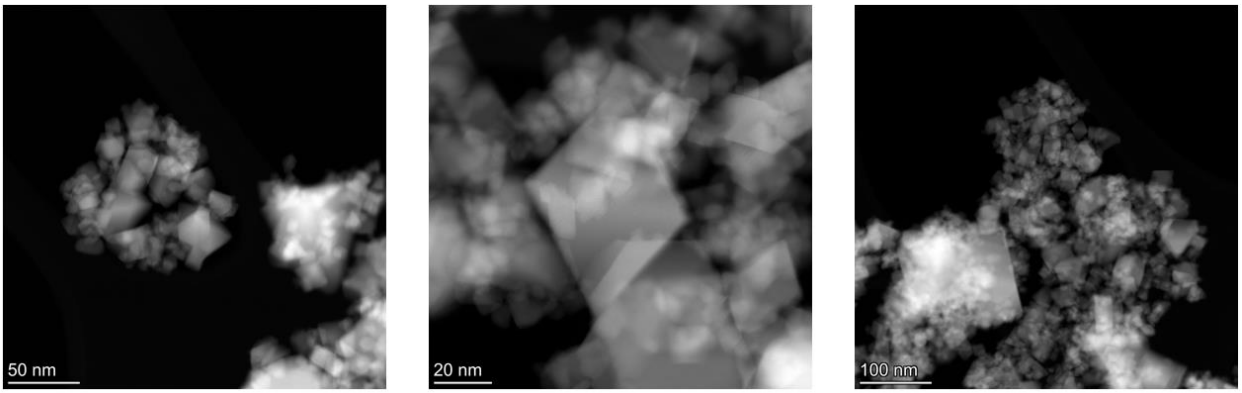

Figure B.2: STEM images of 1% Pd/CeO_2 25 nm

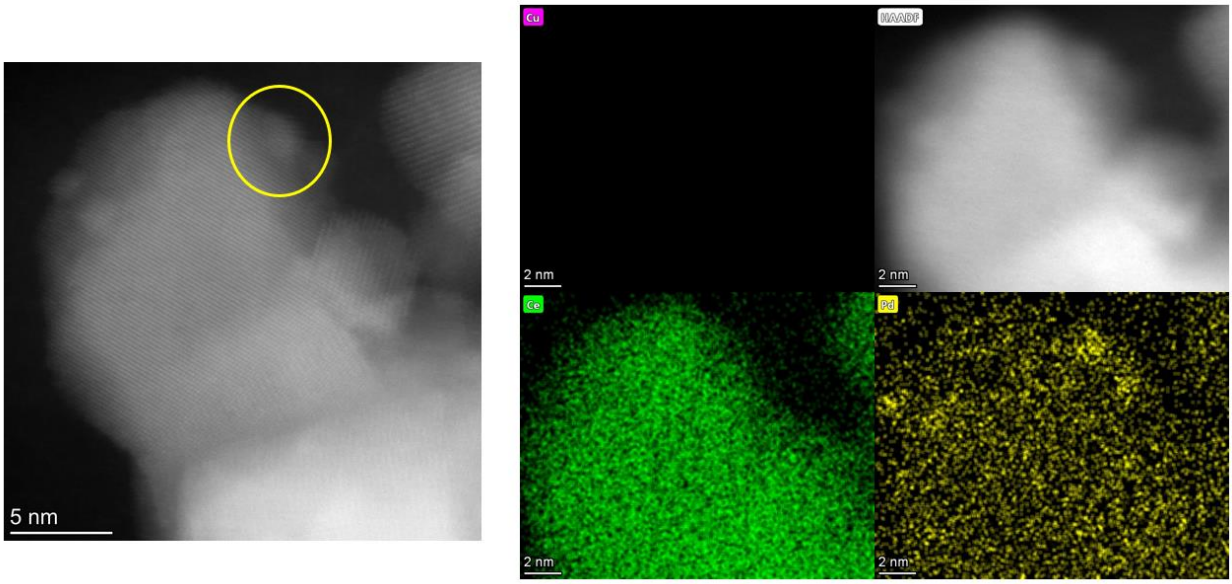

Figure B.3: STEM images and EDS of 1% Pd/CeO_2 25 nm

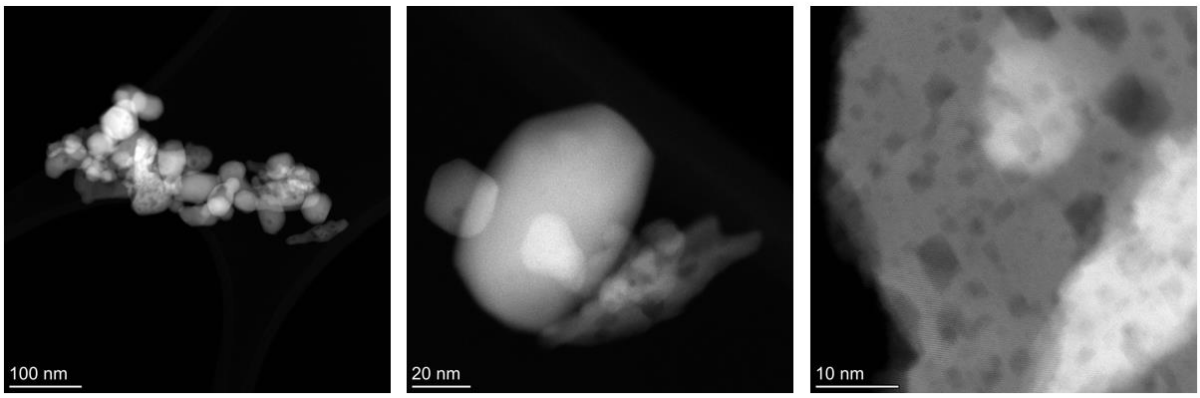

Figure B.4: STEM images of 1% Pd/CeO_2 100 nm

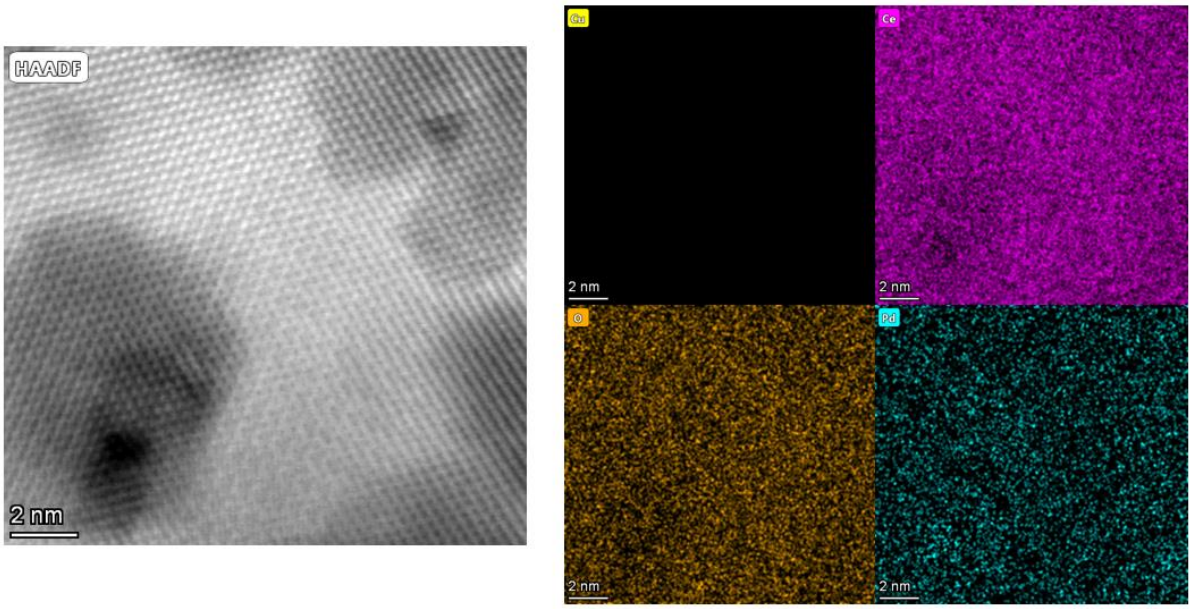

Figure B.5: EDS of 1% Pd/CeO_2 100 nm

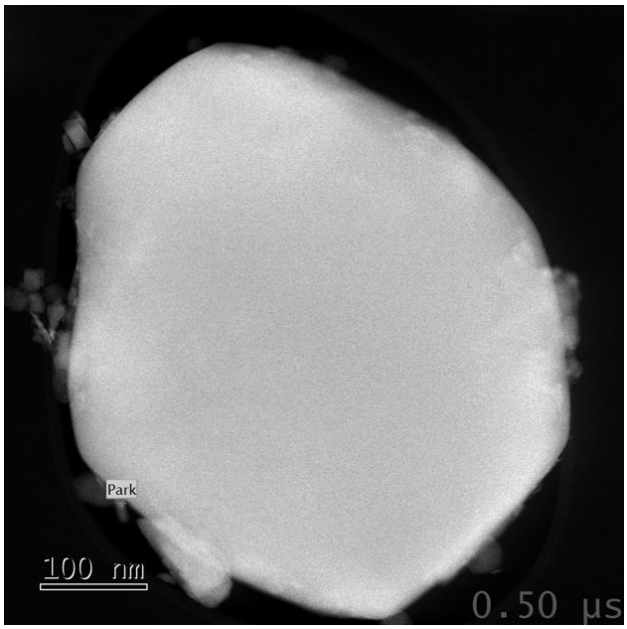

Figure B.6: STEM image of 1.2% Pd/CeO_2 1 µm

From XRD analysis, particle size estimates were determined using the Scherrer equation:

$$d = \frac{K\,\lambda}{\beta\,cos\theta}$$

where: d is the average crystallite size, λ is the wavelength of the x-ray source, K is the shape constant, β is the reflection width and θ the Bragg angle.

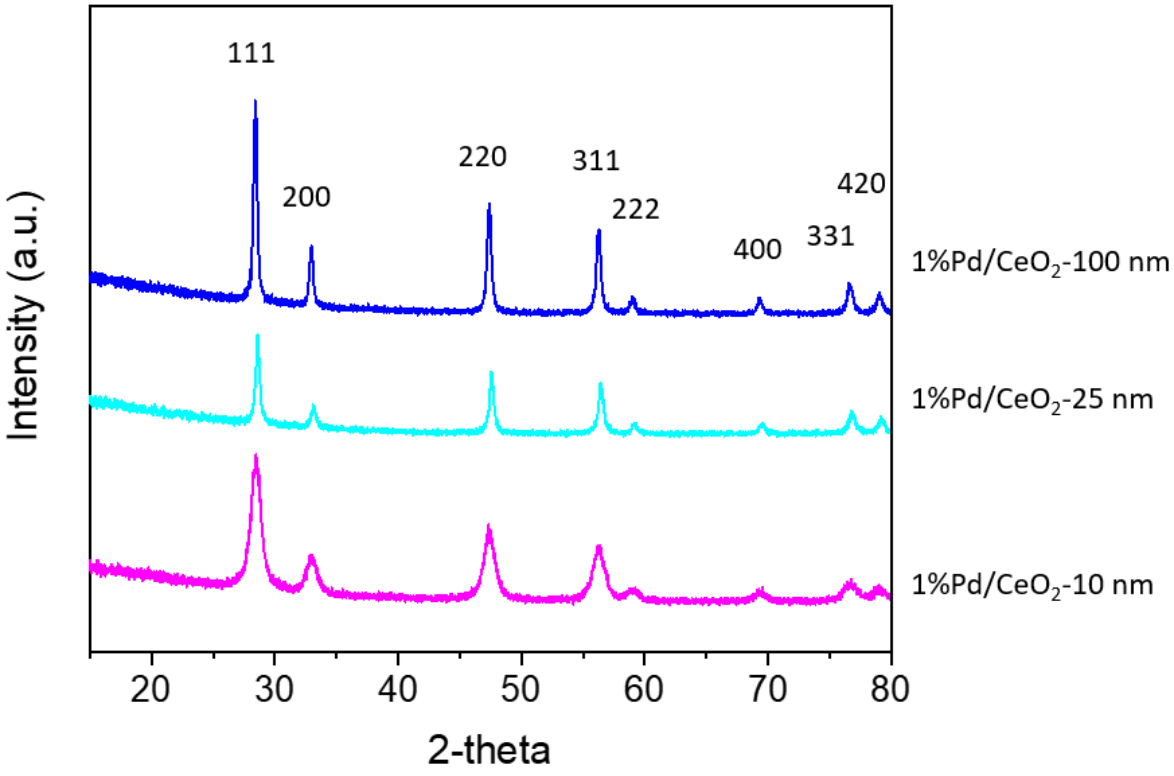

Figure B.7: XRD pattern of the 1% Pd/CeO_2-10, 25 and 100 nm samples

Table B.1: BET surface areas measured on bare 10, 15 and 100 nm ceria and 1% Pd/CeO_2 10, 25 and 100 nm

Catalyst	**Surface area [m^2/g]**
CeO_2 10 nm	78

CeO_2 25 nm	51
CeO_2 100 nm	34
1% Pd/CeO_2 10 nm	60
1% Pd/CeO_2 25 nm	60
1% Pd/CeO_2 100 nm	31

Section B2: CO and CO_2 adsorption on bare CeO_2

Figure S8 shows the CO adsorption spectra spectra obtained on ceria 10 and 100 nm. The features centered at 2173 and 2188 cm^{-1} arising during CO adsorption on CeO_2 10 and 100 nm, respectively, are assigned to CO adsorbed on Ce^{4+} [1–3]. After purging the catalysts with Ar, CO desorbs from the two ceria surfaces, indicating weak CO adsorption on Ce^{4+}. The features below 1800cm^{-1} are assigned to carbonates on the ceria. The carbonates formed on ceria 10 nm exhibit an intensity one order of magnitude higher compared to the ones on ceria 100 nm. However, for both ceria 10 and 100 nm the carbonate formation is limited because of the absence of the metal sites which promote the carbonate formation.

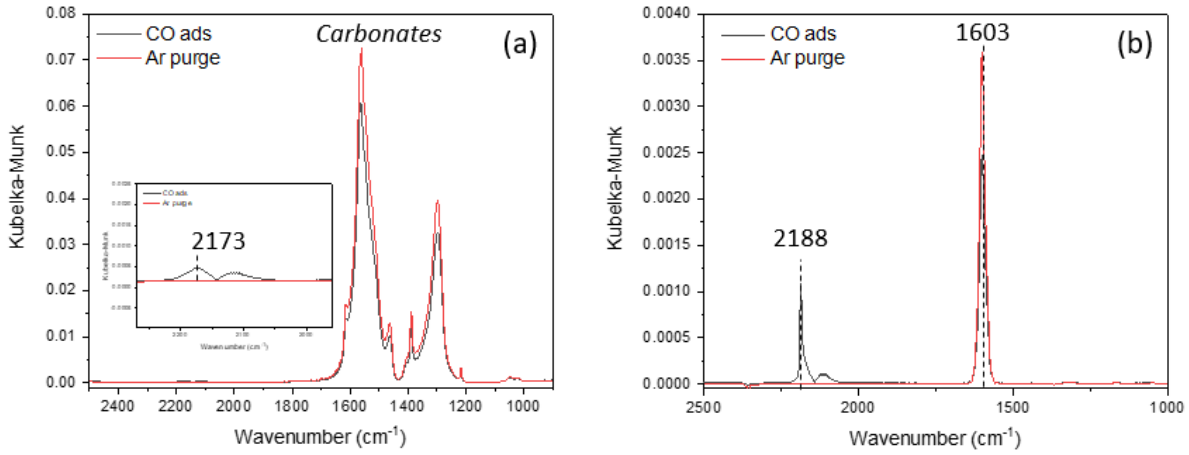

Figure B.8: CO adsorption on (a) CeO_2 10 nm; (b) CeO_2 100 nm; the materials were treated in 1% O_2/Ar for 30 min at 400°C, purged in Ar and reduced in 5% H_2/Ar for 30 min at 300°C. Finally, the two materials were exposed to 5000 ppm CO at 35°C until saturation.

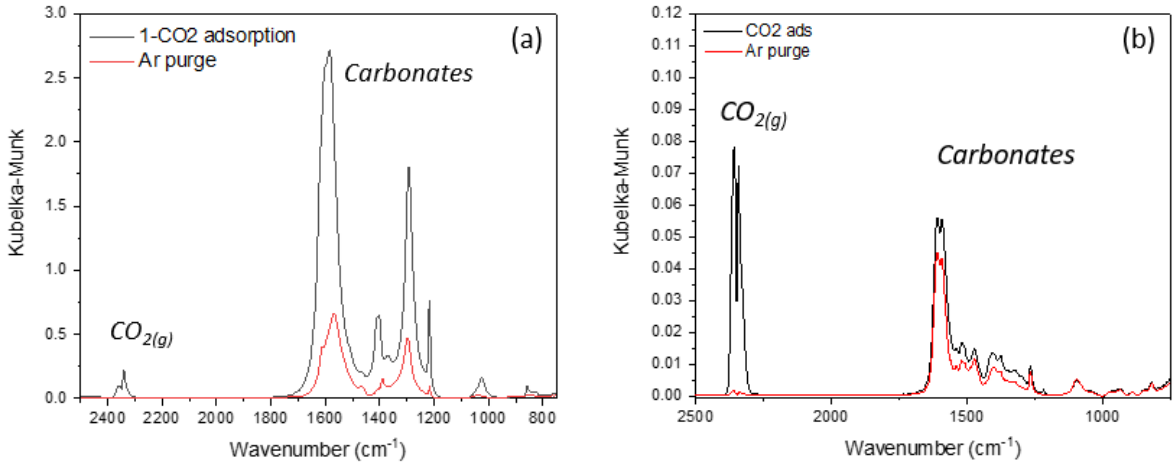

Figure B.9: CO_2 adsorption on (a) CeO_2 - 10 nm and (b) CeO_2 - 100 nm; the materials were treated in 1% O_2/Ar for 30 min at 400°C, purged in Ar and reduced in 5% H_2/Ar for 30 min at 300°C. The two materials were then exposed to 1% CO_2 at 35°C until saturation.

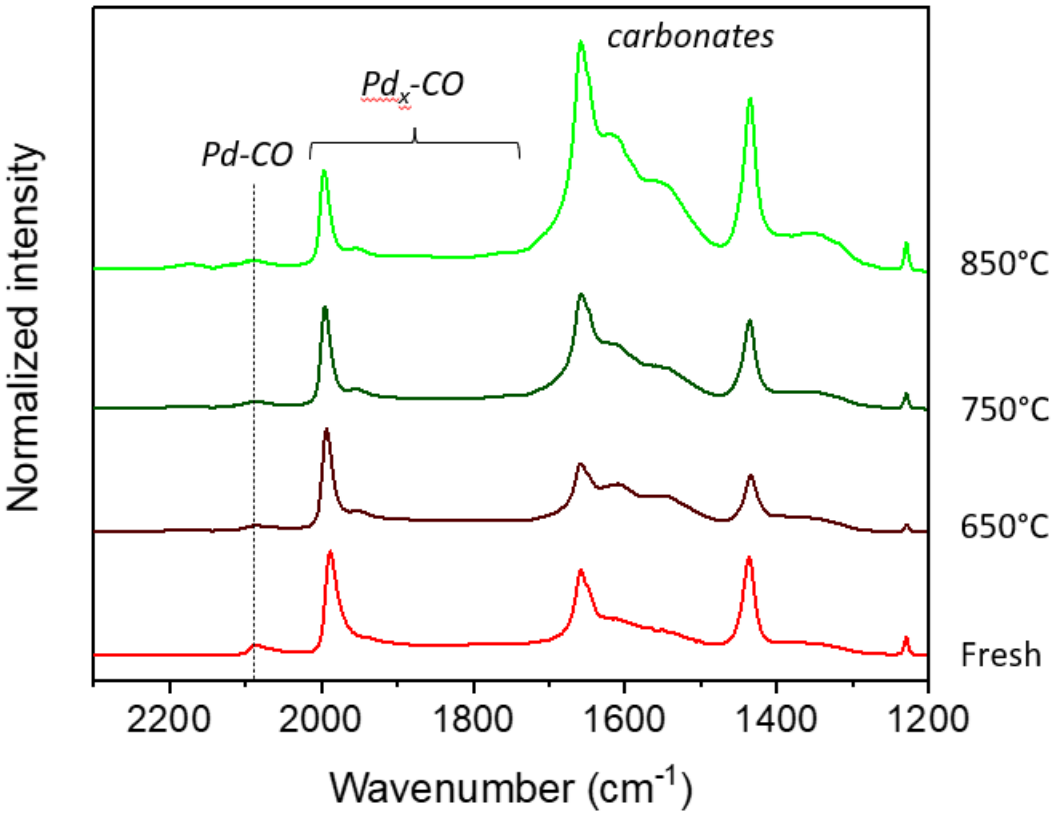

Figure B.10: CO adsorption using DRIFTS over 1.2% Pd/Al_2O_3- fresh, and 650, 750 and 850°C aged samples. The catalyst was treated in 1% O_2/Ar for 30 min at 400°C, purged in Ar and reduced in 5% H_2/Ar for 30 min at 400°C. The catalysts were exposed to 5000 ppm CO until saturation at 35°C.

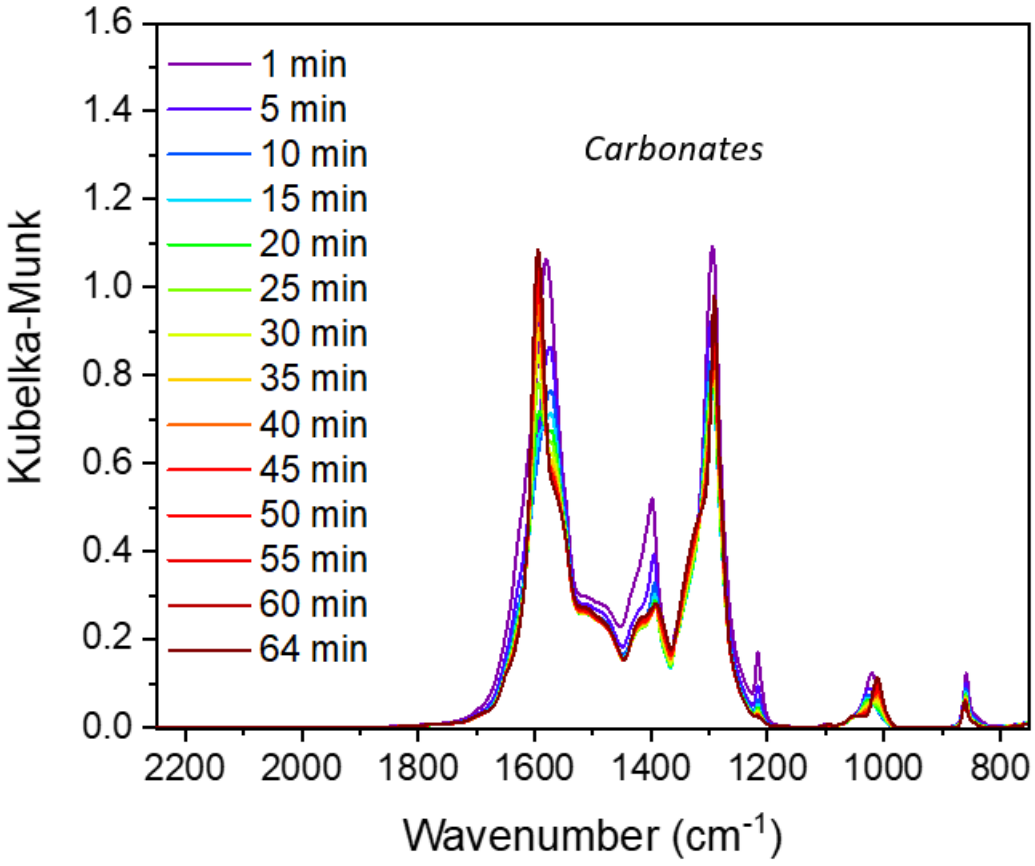

Figure B.11: Time evolution of carbonate species decomposing/desorbing from 1% Pd/CeO_2-25 nm during the Ar purge after CO_2 exposure.

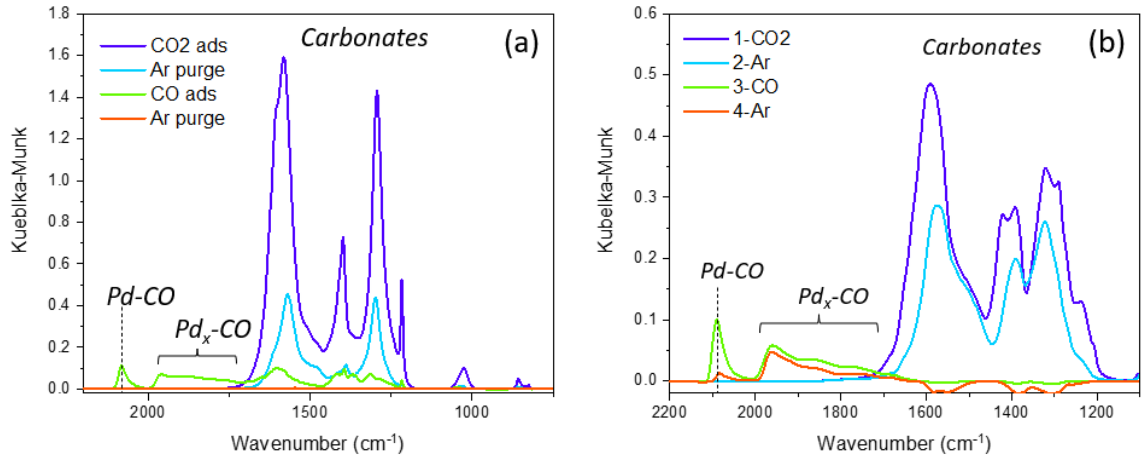

Figure B.12: DRIFTS spectra obtained during the CO_2-CO adsorption experiment over (a) 1% Pd/CeO_2-10 nm and (b) 1% Pd/CeO_2-100 nm. The catalysts were treated in 1% O_2/Ar for 30 min at 400°C, purged in Ar and reduced in 5% H_2/Ar for 30 min at 300°C. The catalysts were exposed to 1% CO_2 at 35°C until saturation and purged until no changes in the spectra were detected. A new background was collected before the sample was exposed to 5000 ppm CO until saturation.

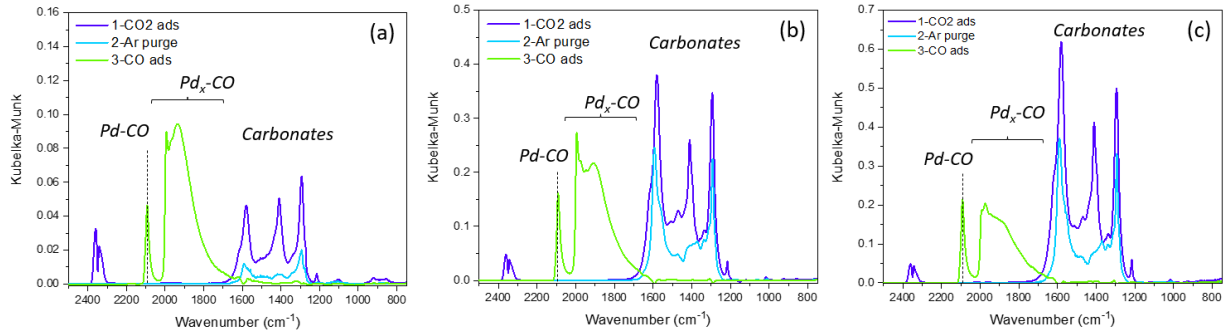

Figure B.13: DRIFTS spectra obtained during the CO_2-CO adsorption experiment over (a) 1.2% Pd/CeO_2 1um, (b) 0.8% Pd/CeO_2 1um, (c) 0.2% Pd/CeO_2 1um. The catalysts were treated in 1% O_2/Ar for 30 min at 400°C, purged in Ar and reduced in 5% H_2/Ar for 30 min at 400°C. The catalysts were exposed to 1% CO_2 at 35°C until saturation and purged until no changes in the spectra were detected. A new background was collected before exposure to 5000 ppm CO until saturation.

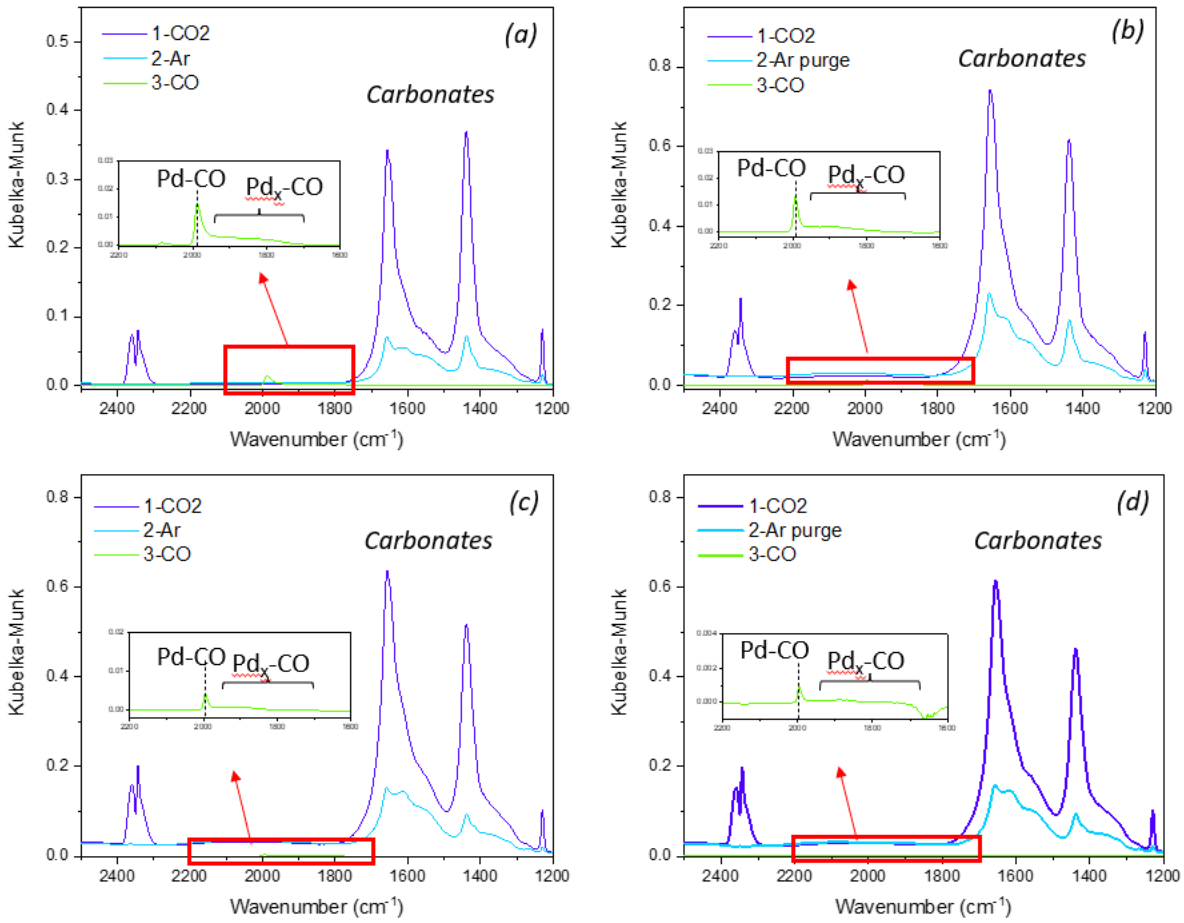

Figure B.14: DRIFTS spectra obtained during the CO_2-CO adsorption experiment over 1.2% Pd/Al_2O_3 (a) Fresh, (b) 650°C aged, (c) 750°C aged and (d) 850°C aged. The catalysts were treated in 1% O_2/Ar for 30 min at 400°C, purged in Ar and reduced in 5% H_2/Ar for 30 min at 400°C. The catalysts were exposed to 1% CO_2 at 35°C until saturation and purged until no changes in the spectra were detected. A new background was collected before exposure to 5000 ppm CO until saturation.

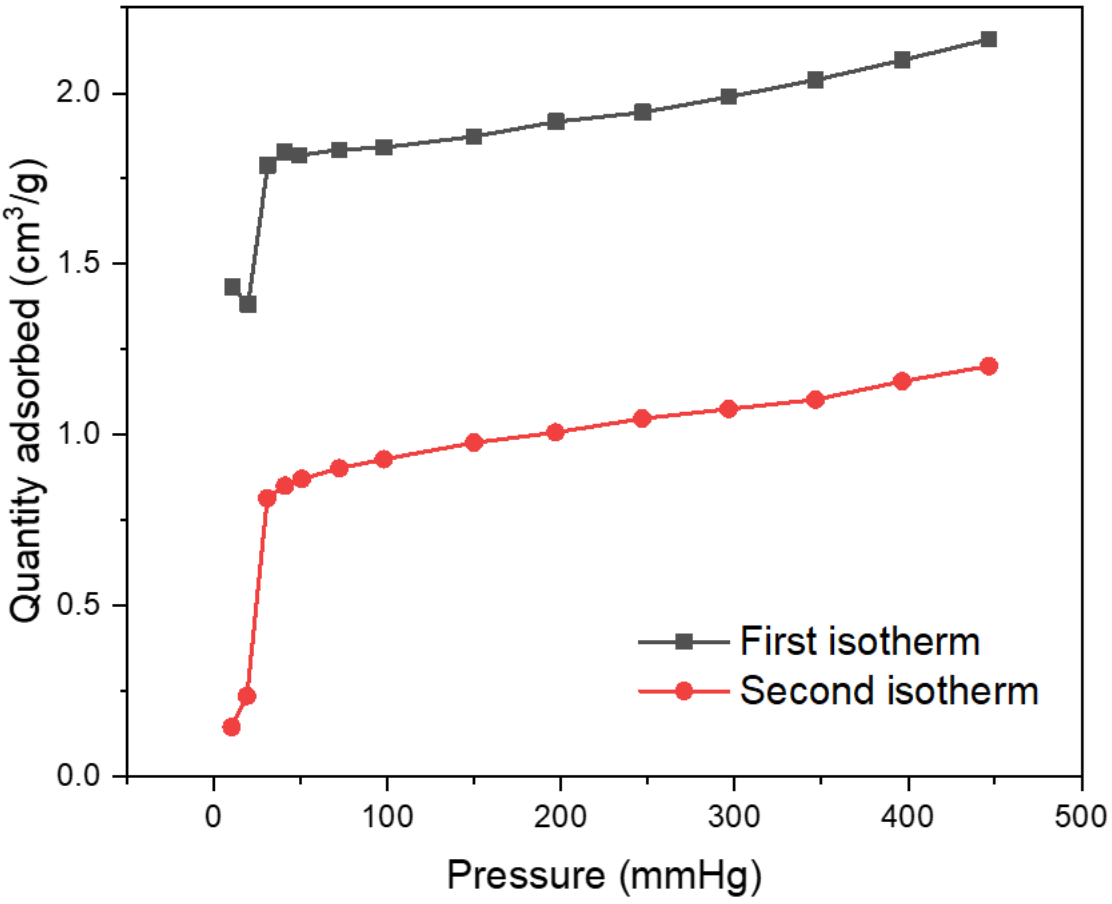

Figure B.15: H_2 chemisorption isotherms on 1.2% Pd/CeO_2 1um. The catalyst was pretreated at 400°C in H_2 for 1h. The analysis was performed at 35°C

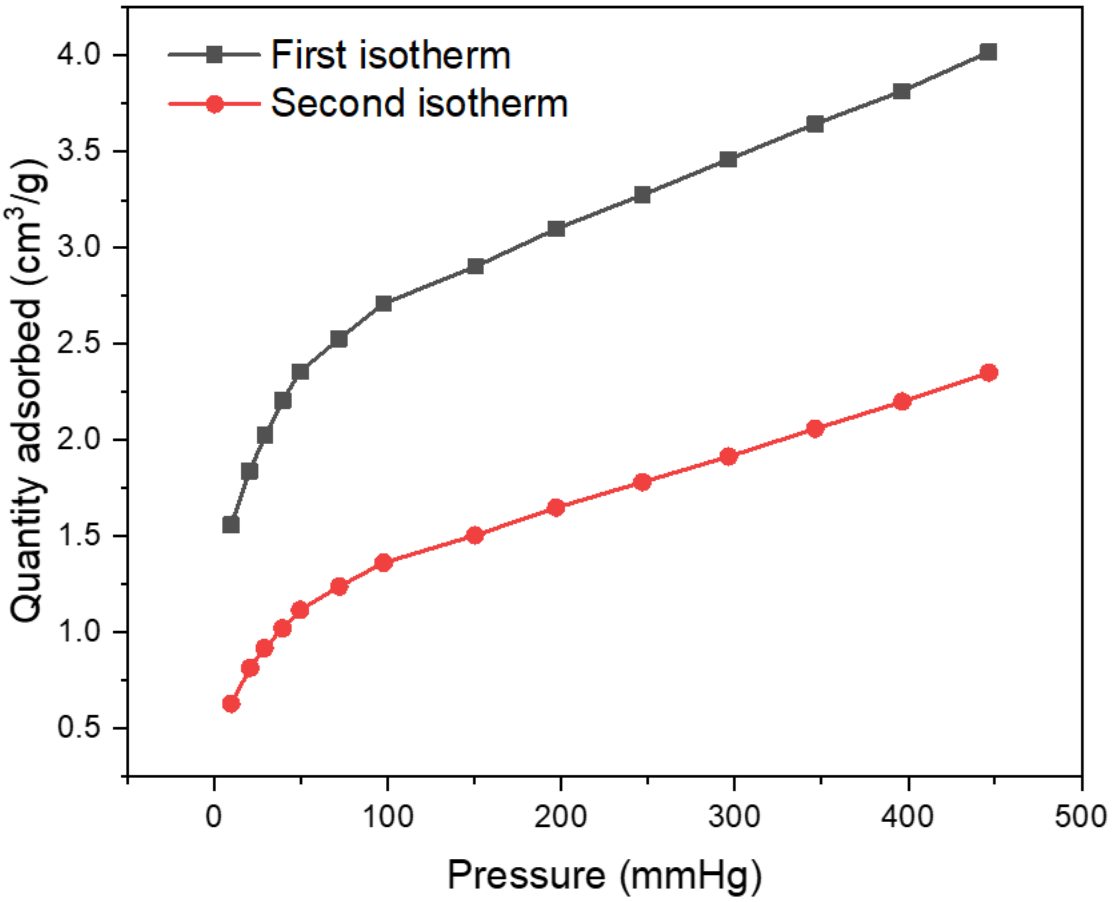

Figure B.16: H_2 chemisorption isotherms of 1% Pd/CeO_2 10 nm. The catalyst was pretreated at 400°C in H_2 for 1h. The analysis was performed at 35°C.

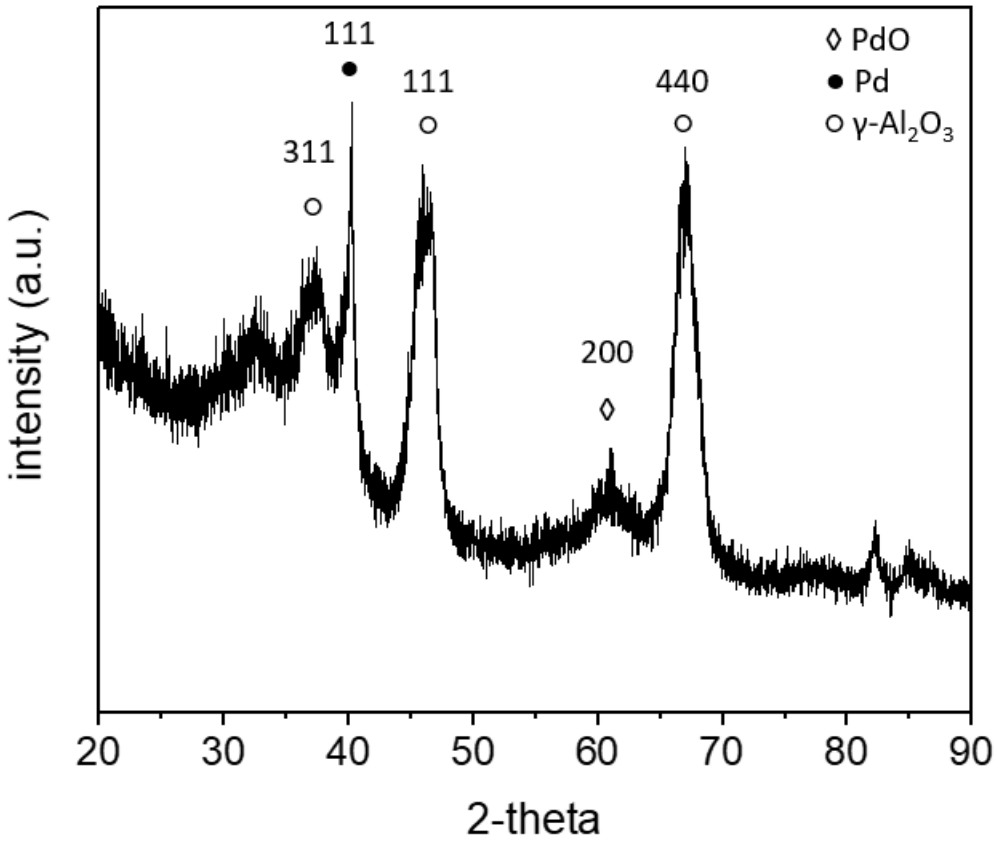

Figure B.17: XRD pattern of 1.2% Pd/Al_2O_3 that underwent the cyclic ageing treatment at 650°C for 50h

Pd crystallite size was determined using the Scherrer equation. The crystallite of the Pd(111) peak at ca. 40° resulted in 10.6 nm, consistent with the particle size obtained from the CO_2-CO chemi-sorption.

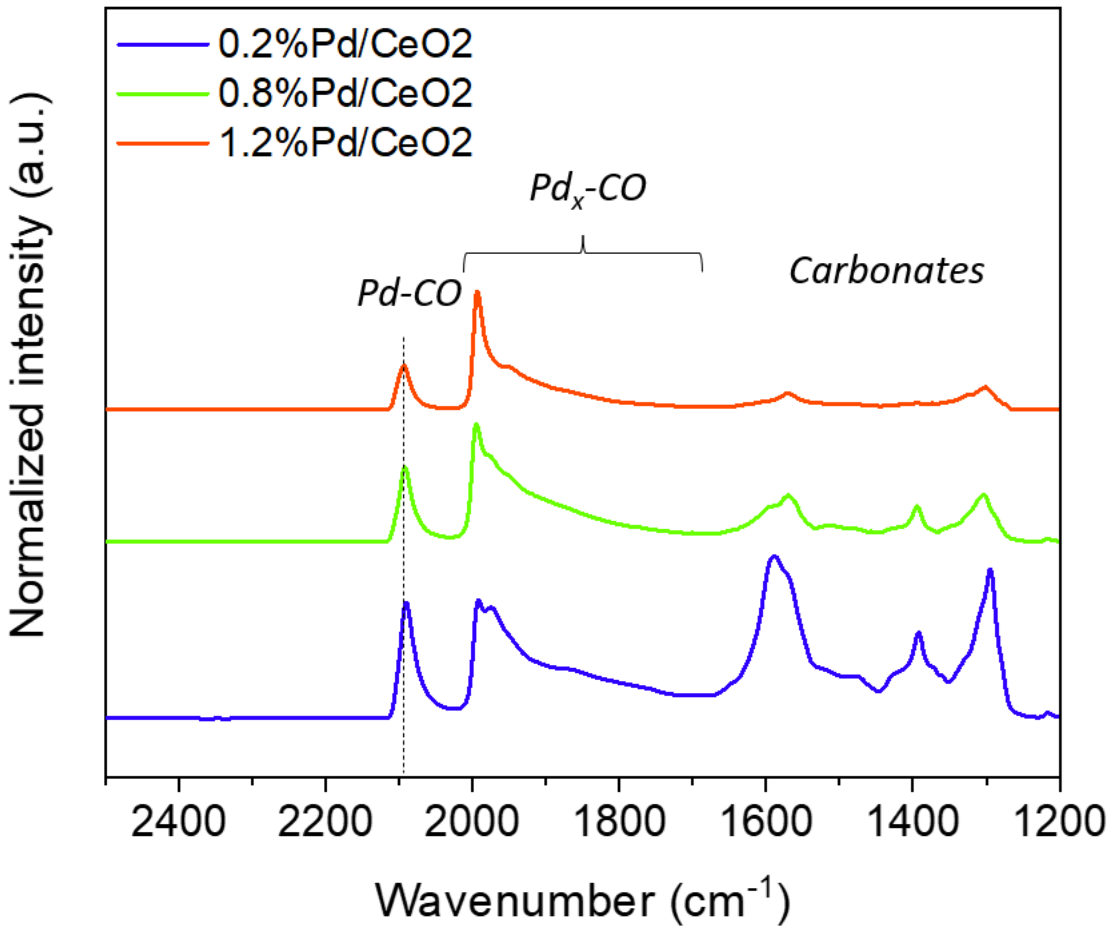

Figure B.18: DRIFTS spectra obtained during CO adsorption on 1.2, 0.8 and 0.2% Pd/CeO_2 1µm.

Section B3: CO and H_2 chemisorption

Table B.2: Dispersion measurements via H_2 chemisorption at 35°C on 1% Pd/CeO_2-10 25, 100 nm and 1.2% CeO_2-1µm

Catalyst	**Dispersion [%]**
1% Pd/CeO_2 10 nm	224
1% Pd/CeO_2 25 nm	206
1% Pd/CeO_2 100 nm	361
1.2% Pd/CeO_2 1 μm	136

Table B.3: Dispersions obtained via CO_2-CO and CO chemisorption. The catalysts were reduced in H_2 at 400°C for 1h. The analysis was performed at 35°C.

Catalyst	**CO_2-CO chemisorption**	**CO chemisorption**
1.2% Pd/Al_2O_3	38.6	33.5
1.2% Pd/Al_2O_3 – 650°C aged	9.1	19.5
1.2% Pd/Al_2O_3 – 750°C aged	7.4	8.8
1.2% Pd/Al_2O_3 – 850°C aged	4	6.9

Section B4: CO oxidation kinetics

The fractions of surface, perimeter and surface sites were calculated as follows[4]:

$x_{surface} = 0.82\ d^{-0.9\pm0.1}$

$x_{perimeter} = 0.25\ d^{-1.9\pm0.2}$

$x_{corner} = 0.08\ d^{-2.6\pm0.2}$

where d is the diameter measured via CO_2-CO chemisorption.

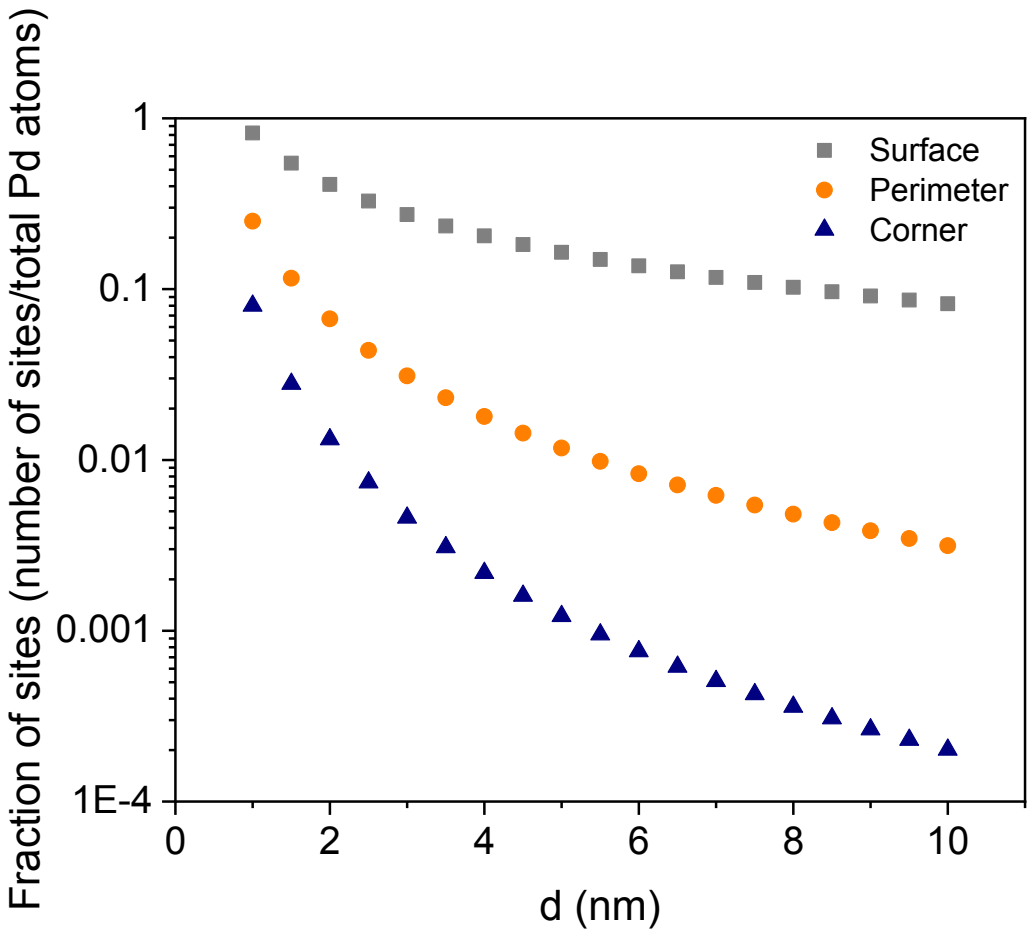

Figure B.19: Fraction of surface, perimeter and corner sites based on a geometric model

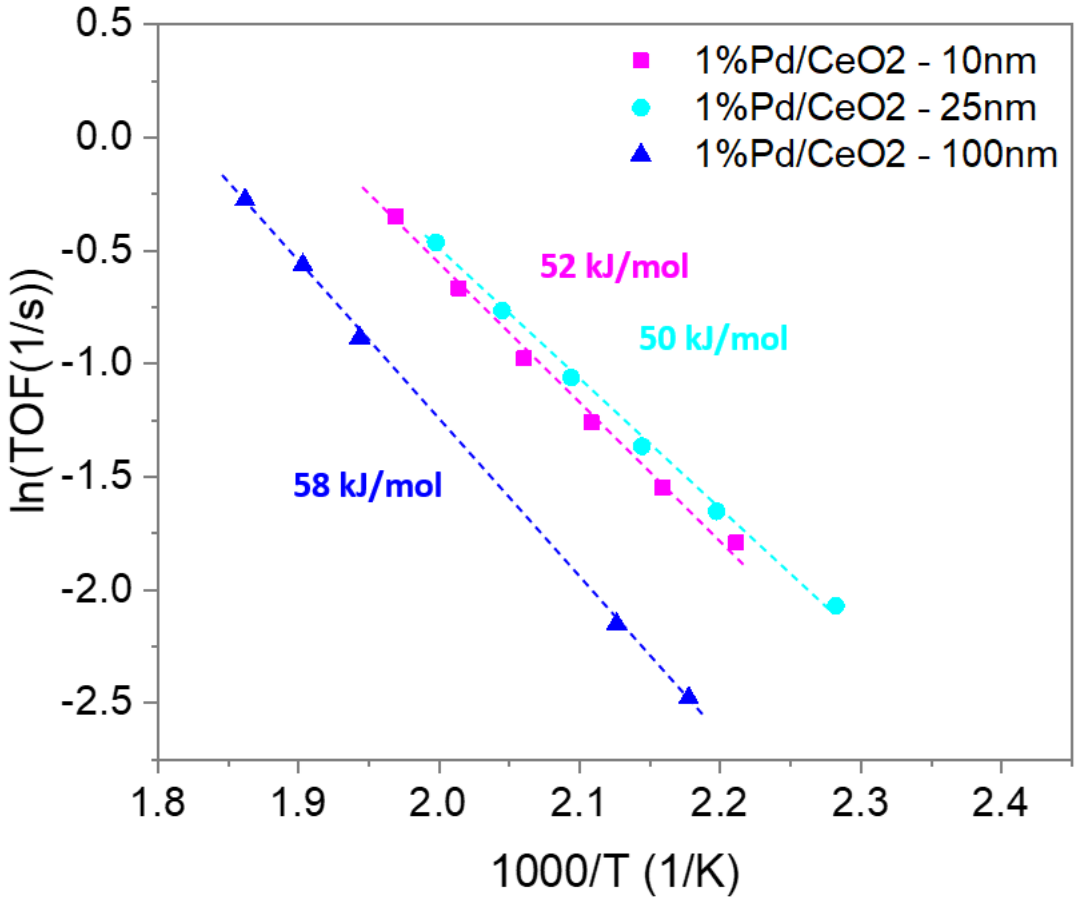

Figure B.20: CO oxidation Arrhenius plot over 1% Pd/CeO_2 10, 25 and 100 nm. The turnover frequency was obtained by normalizing the reaction rates by the number of total Pd surface sites.

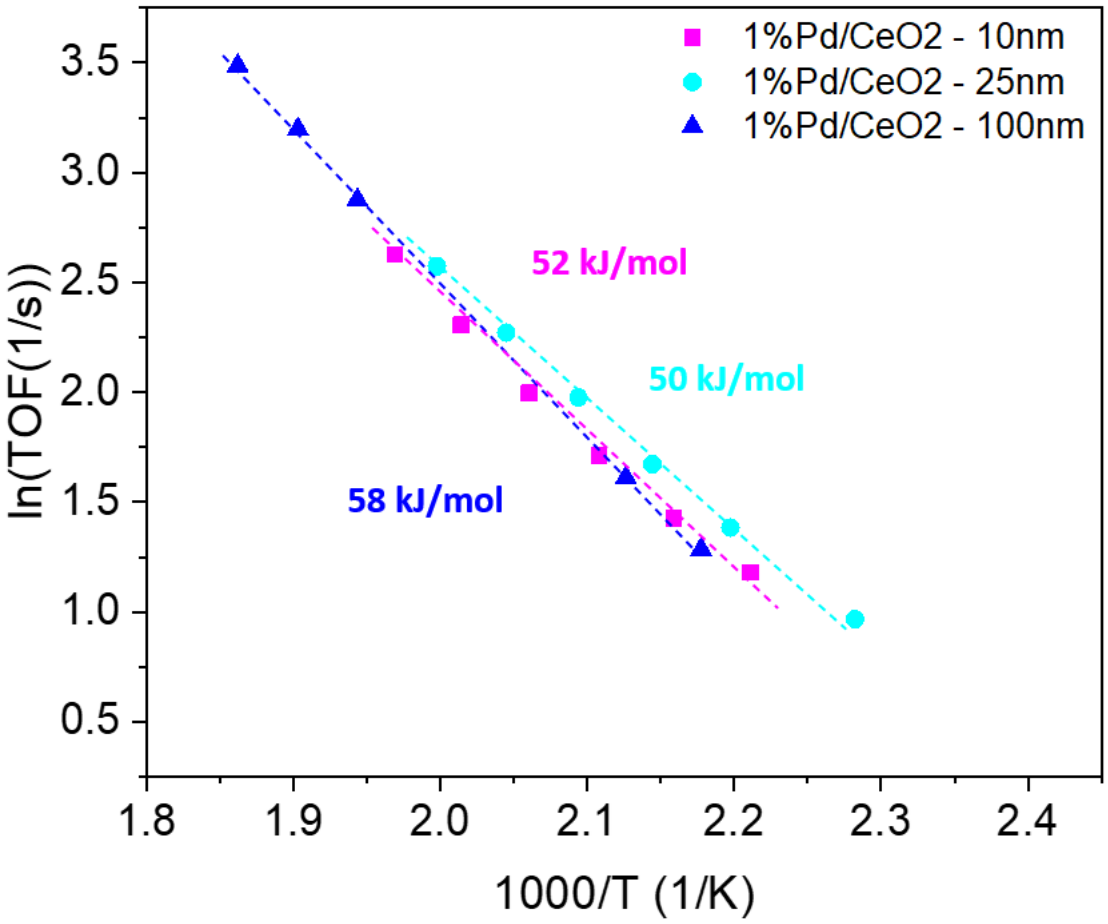

Figure B.21: CO oxidation Arrhenius plot over 1% Pd/CeO_2 10, 25 and 100 nm. The turnover frequency was obtained by normalizing the reaction rates by the number of Pd corner sites.

Section B5: Reference

[1] A. Bensalem, F. Bozon-Verduraz, M. Delamar, G. Bugli, Preparation and characterization of highly dispersed silica-supported ceria, Appl Catal A Gen. 121 (1995) 81–93. https://doi.org/10.1016/0926-860X(95)85012-0.

[2] A. Bensalem, J.C. Muller, D. Tessier, F. Bozon-Verduraz, Spectroscopic study of CO adsorption on palladium-ceria catalysts, Journal of the Chemical Society - Faraday Transactions. 92 (1996) 3233–3237. https://doi.org/10.1039/FT9969203233.

[3] P.G. Lustemberg, C. Yang, Y. Wang, C. Wöll, M.V. Ganduglia-Pirovano, Vibrational frequencies of CO bound to all three low-index cerium oxide surfaces: A consistent theoretical description of vacancy-induced changes using density functional theory, Journal of Chemical Physics. 159 (2023). https://doi.org/10.1063/5.0153745.

[4] M. Cargnello, V.V.T. Doan-Nguyen, T.R. Gordon, R.E. Diaz, E.A. Stach, R.J. Gorte, P. Fornasiero, C.B. Murray, Control of metal nanocrystal size reveals metal-support interface role for ceria catalysts, Science (1979). 341 (2013) 771–773. https://doi.org/10.1126/science.1240148/suppl_file/papv2.pdf.

Appendix C – Kinetic studies of C_3H_6 oxidation in the presence and absence of NO on newly formulated TWC catalysts

Section C1 0.2% Pt – 7.5% SrO/Al_2O_3

C 1.1 C_3H_6 oxidation + H_2O kinetics

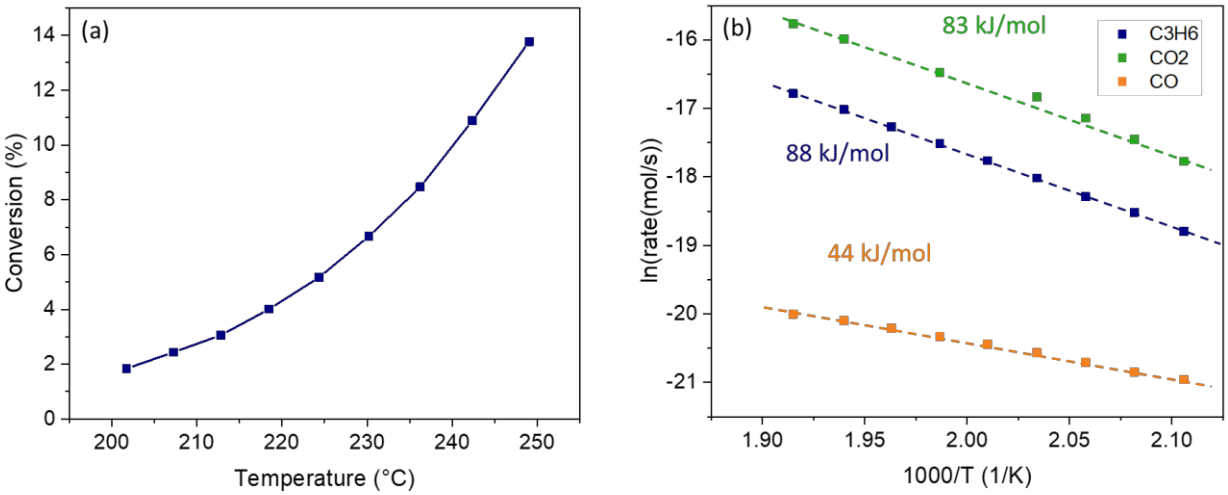

Figure C.1: C_3H_6 oxidation + H_2O on 0.2% Pt-7.5% SrO/Al_2O_3. 50 mg of catalyst was diluted with 150 mg silica. Pellet size was 250-420µm. The catalyst was reduced in 5% H_2/N_2 for 45 minutes at 600°C. The catalyst was then exposed to the reaction mixture including C_3H_6 = 1000 ppm; O_2 = 4500 ppm; H_2O = 6%, diluted in N_2. Total flowrate = 500 sccm. The conversions were obtained at steady-state. (a) C_3H_6 conversion; (b) Arrhenius plot obtained from C_3H_6 consumption rate and CO_2 and CO formation rates.

C 1.2 C_3H_6 oxidation + NO + H_2O kinetics

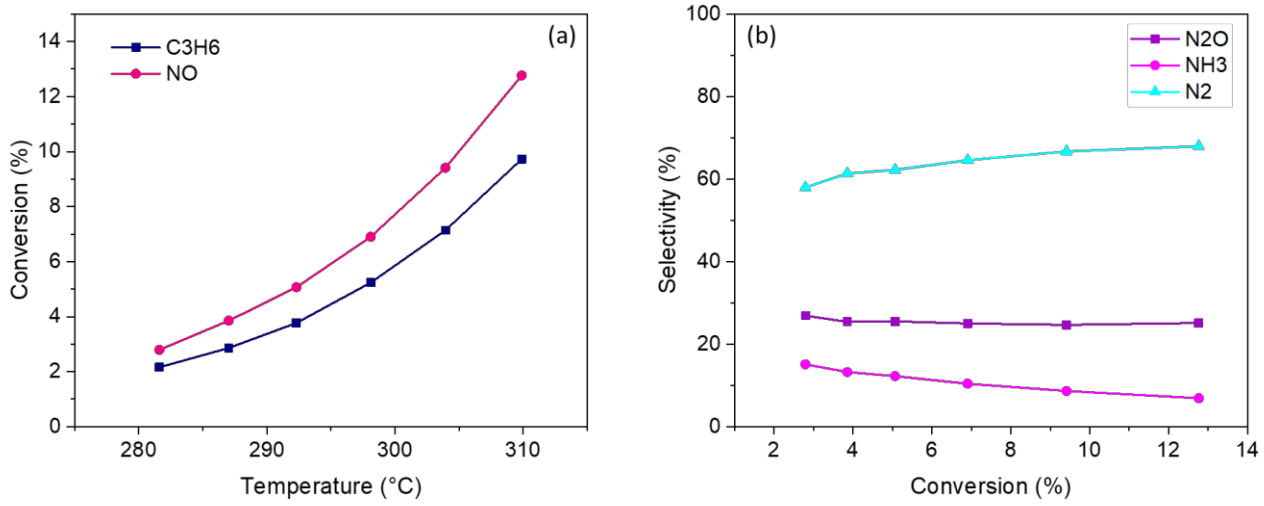

Figure C.2: C_3H_6 oxidation + NO + H_2O on 0.2% Pt-7.5% SrO/Al_2O_3. 50 mg of catalyst was diluted with 150 mg silica. The catalyst was reduced in 5% H_2/N_2 for 45 minutes at 600°C. The catalyst was then exposed to the reaction mixture including C_3H_6 = 1000 ppm; O_2 = 4000 ppm; NO = 1000 ppm; H_2O = 6%, diluted in N_2. Total flowrate = 500 sccm. The conversions were obtained at steady-state. (a) C_3H_6 and NO conversions; (b) N_2O, NH_3 and N_2O Selectivity.

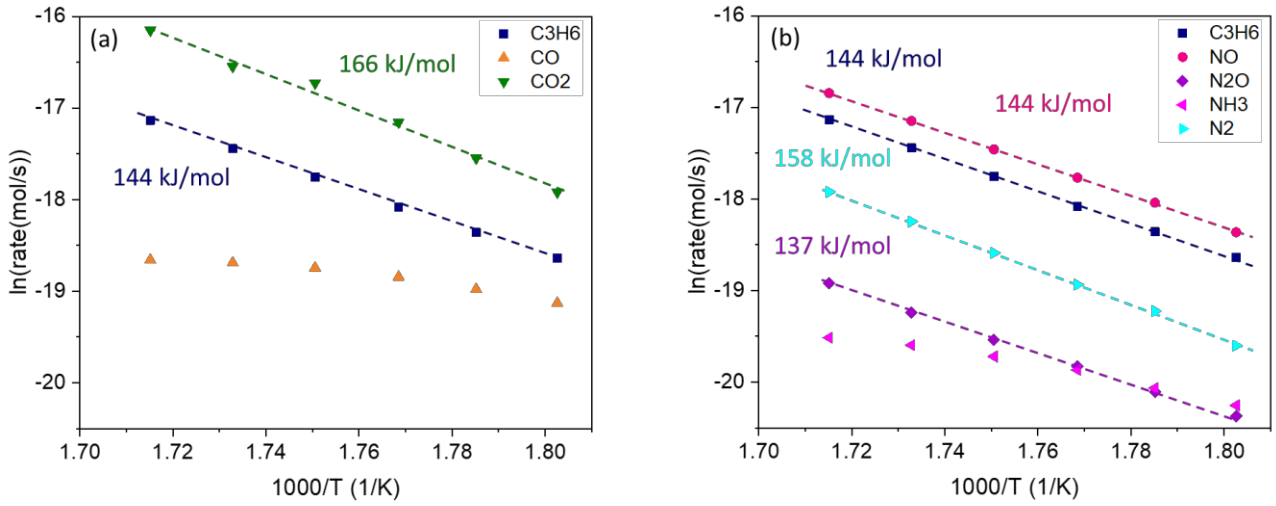

Figure C.3: C_3H_6 oxidation + NO + H_2O on 0.2% Pt-7.5% SrO/Al_2O_3. 50 mg of catalyst was diluted with 150 mg silica.The catalyst was reduced in 5% H_2/N_2 for 45 minutes at 600°C. The catalyst was then exposed to the reaction mixture including C_3H_6 = 1000 ppm; O_2 = 4000 ppm; NO = 1000 ppm; H_2O = 6%, diluted in N_2. Total flowrate = 500 sccm. The conversions were obtained at steady-state. (a) Arrhenius plot obtained from C_3H_6 consumption rate and CO_2 and CO

formation rates; (b) Arrhenius plot obtained from NO consumption rate and N_2O, NH_3 and N_2 formation rates. N_2 rates were obtained from N-material balance.

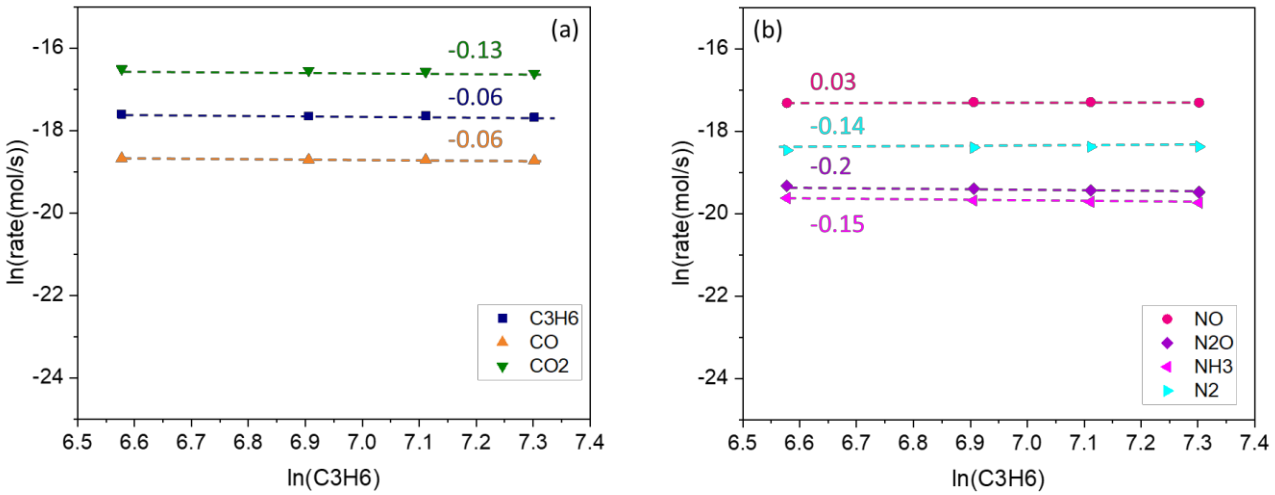

Figure C.5: C_3H_6 reaction order at 300C – C_3H_6 oxidation + NO + H_2O on 0.2% Pt-7.5% SrO/Al_2O_3. 50 mg of catalyst was diluted with 150 mg silica. The catalyst was reduced in 5% H_2/N_2 for 45 minutes at 600°C. The catalyst was then exposed to the reaction mixture including C_3H_6 = 720-1500 ppm; O_2 = 4000 ppm; NO = 1000 ppm; H_2O = 6%, diluted in N_2. Total flowrate = 500sccm. The conversions were obtained at steady-state. (a) C_3H_6 order with respect of C_3H_6 consumption rate and CO_2 and CO formation rates; (b) Arrhenius plot obtained from NO consumption rate and N_2O, NH_3 and N_2 formation rates. N_2 rates were obtained from N-material balance.

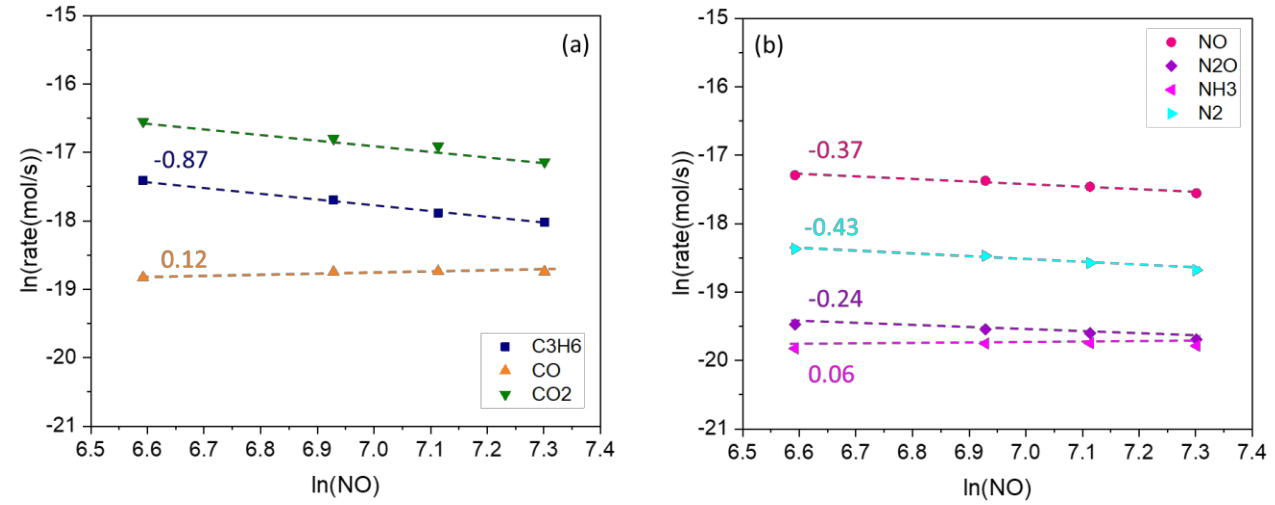

Figure C.4: NO reaction order at 300C – C_3H_6 oxidation + NO + H_2O on 0.2% Pt-7.5% SrO/Al_2O_3. 50 mg of catalyst was diluted with 150 mg silica. The catalyst was reduced in 5% H_2/N_2 for 45 minutes at 600°C. The catalyst was then exposed to the reaction mixture including C_3H_6 = 1000 ppm; O_2 = 4000 ppm; NO = 720-1500 ppm; H_2O = 6%, diluted in N_2. Total flowrate = 500sccm. The conversions were obtained at steady-state. (a) C_3H_6 order with respect of C_3H_6 consumption rate and CO_2 and CO formation rates; (b) Arrhenius plot obtained from NO consumption rate and N_2O, NH_3 and N_2 formation rates. N_2 rates were obtained from N-material balance.

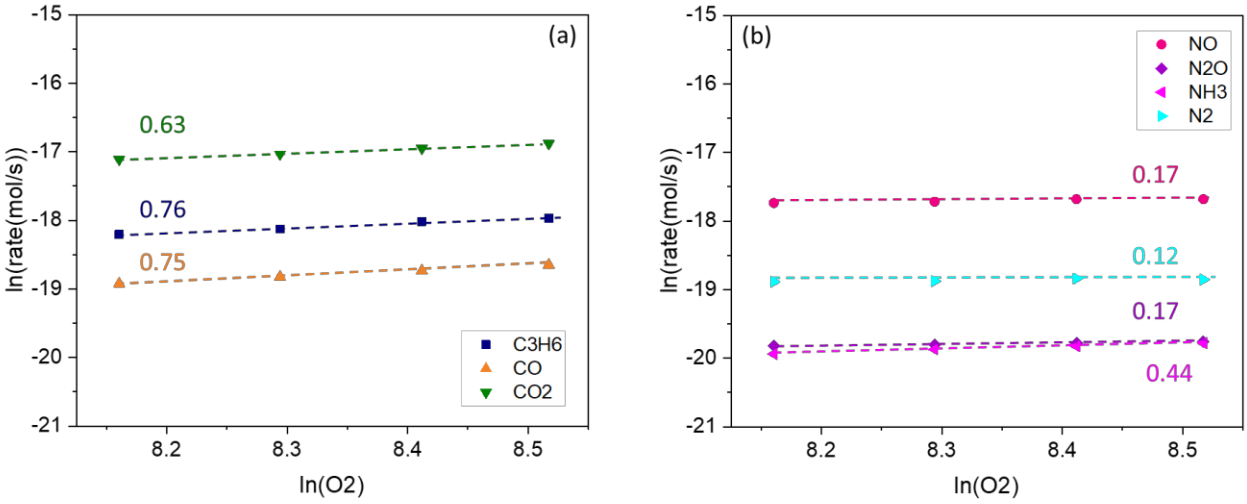

Figure C.6: O_2 reaction order at 300C – C_3H_6 oxidation + NO + H_2O on 0.2% Pt-7.5% SrO/Al_2O_3. 50 mg of catalyst was diluted with 150 mg silica. The catalyst was reduced in 5% H_2/N_2 for 45 minutes at 600°C. The catalyst was then exposed to the reaction mixture including C_3H_6 = 1000 ppm; O_2 = 3500-5000 ppm; NO = 1000 ppm; H_2O = 6%, diluted in N_2. Total flowrate = 500sccm. The conversions were obtained at steady-state. (a) C_3H_6 order with respect of C_3H_6 consumption rate and CO_2 and CO formation rates; (b) Arrhenius plot obtained from NO consumption rate and N_2O, NH_3 and N_2 formation rates. N_2 rates were obtained from N-material balance.

Section C2 0.2% Rh – 7.5% SrO/Al_2O_3

C 2.1 C_3H_6 oxidation + H_2O

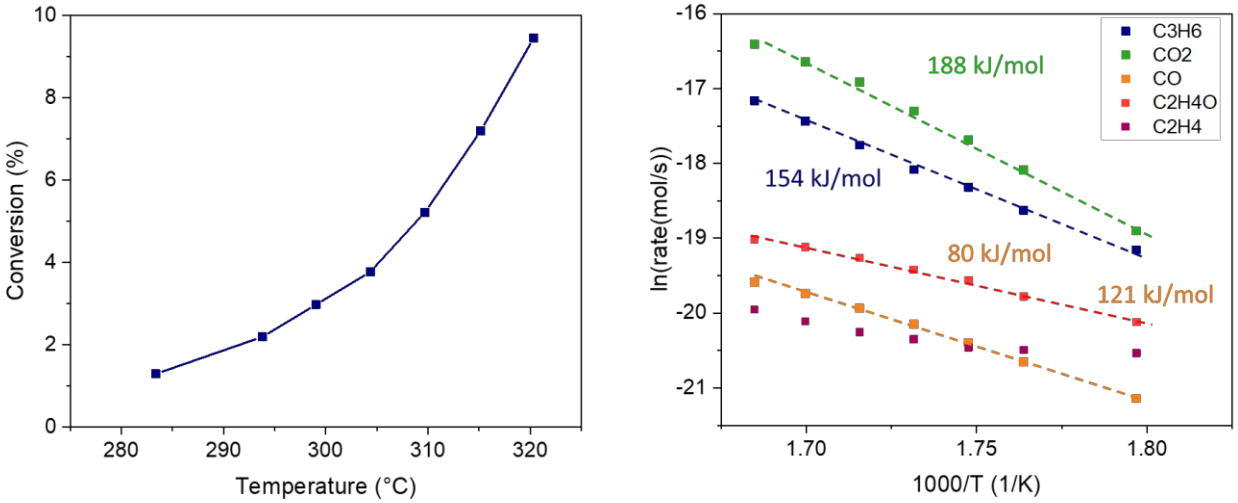

Figure C.7: C_3H_6 oxidation + H_2O on 0.2% Rh-7.5% SrO/Al_2O_3. 50 mg of catalyst was diluted with 150 mg silica. Pellet size was 250-420µm. The catalyst was reduced in 5% H_2/N_2 for 45 minutes at 600°C. The catalyst was then exposed to the reaction mixture including C_3H_6 = 1000 ppm; O2 = 4500 ppm; H_2O = 6%, diluted in N_2. Total flowrate = 500 sccm. The conversions were obtained at steady-state. (a) C_3H_6 conversion; (b) Arrhenius plot obtained from C_3H_6 consumption rate and CO_2 and CO formation rates.

C 2.2 C_3H_6 oxidation + NO + H_2O

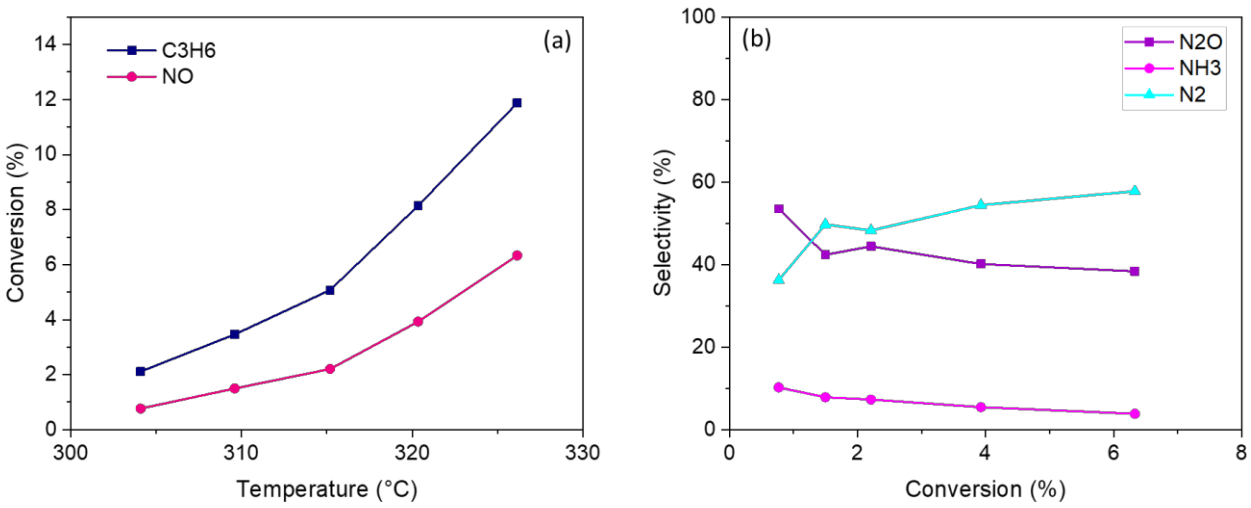

Figure C.8: C_3H_6 oxidation + NO + H_2O on 0.2% Rh-7.5% SrO/Al_2O_3. 50 mg of catalyst was diluted with 150 mg silica. The catalyst was reduced in 5% H_2/N_2 for 45 minutes at 600°C. The catalyst was then exposed to the reaction mixture including C_3H_6 = 1000 ppm; O_2 = 4000 ppm; NO = 1000 ppm; H_2O = 6%, diluted in N_2. Total flowrate = 500 sccm. The conversions were obtained at steady-state. (a) C_3H_6 and NO conversions; (b) N_2O, NH_3 and N_2O Selectivity.

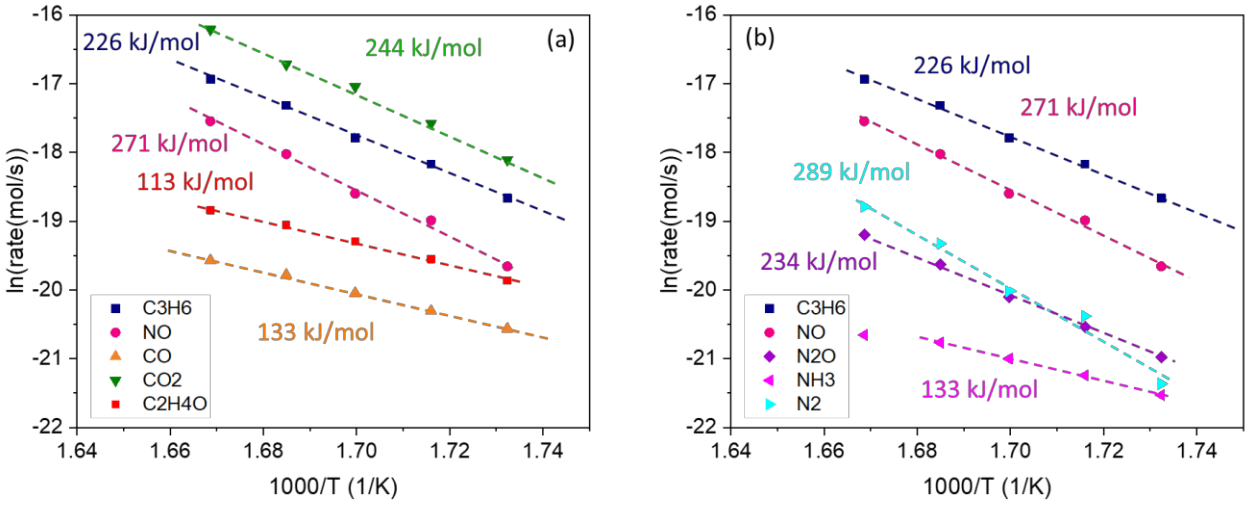

Figure C.9: C_3H_6 oxidation + NO + H_2O on 0.2% Rh-7.5% SrO/Al_2O_3. 50 mg of catalyst was diluted with 150 mg silica. The catalyst was reduced in 5% H_2/N_2 for 45 minutes at 600°C. The catalyst was then exposed to the reaction mixture including C_3H_6 = 1000 ppm; O_2 = 4000 ppm; NO = 1000 ppm; H_2O = 6%, diluted in N_2. Total flowrate = 500 sccm. The conversions were obtained at steady-state. (a) Arrhenius plot obtained from C_3H_6 consumption rate and CO_2 and CO

formation rates; (b) Arrhenius plot obtained from NO consumption rate and N_2O, NH_3 and N_2 formation rates. N_2 rates were obtained from N-material balance.

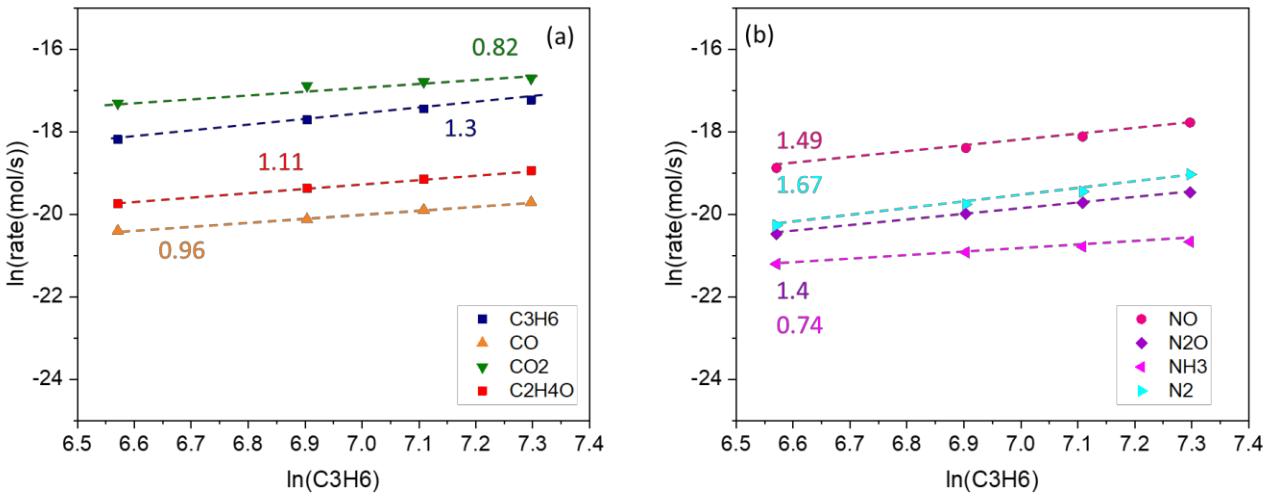

Figure C.10: C_3H_6 reaction order at 320°C – C_3H_6 oxidation + NO + H_2O on 0.2% Rh-7.5% SrO/Al_2O_3. 50 mg of catalyst was diluted with 150 mg silica. The catalyst was reduced in 5% H_2/N_2 for 45 minutes at 600°C. The catalyst was then exposed to the reaction mixture including C_3H_6 = 720-1500 ppm; O_2 = 4000 ppm; NO = 1000 ppm; H_2O = 6%, diluted in N_2. Total flowrate = 500sccm. The conversions were obtained at steady-state. (a) C_3H_6 order with respect of C_3H_6 consumption rate and CO_2 and CO formation rates; (b) Arrhenius plot obtained from NO consumption rate and N_2O, NH_3 and N_2 formation rates. N_2 rates were obtained from N-material balance.

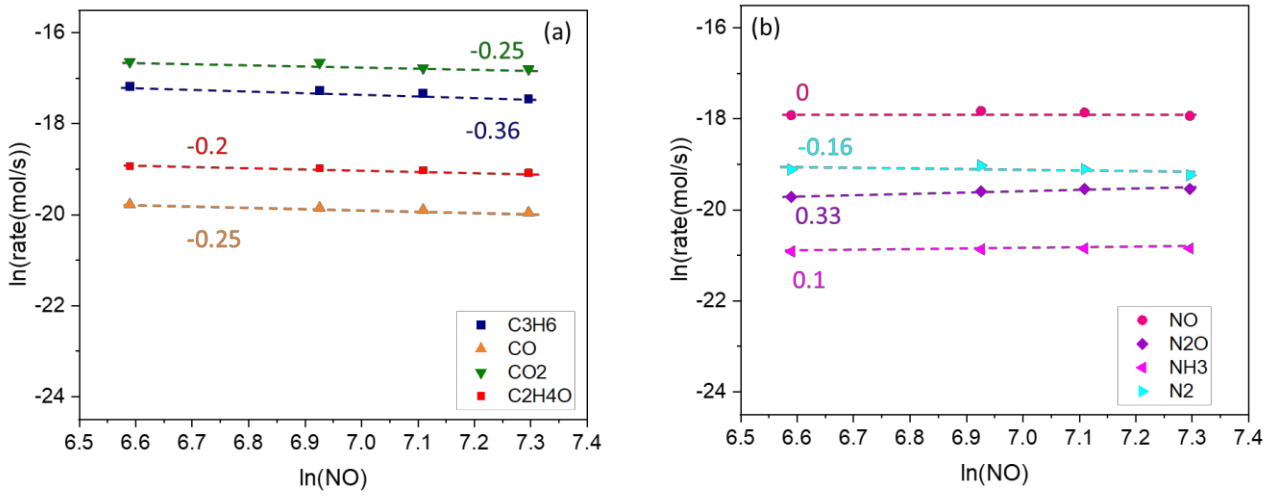

Figure C.11: NO reaction order at 320°C – C_3H_6 oxidation + NO + H_2O on 0.2% Rh-7.5% SrO/Al_2O_3. 50 mg of catalyst was diluted with 150 mg silica. The catalyst was reduced in 5% H_2/N_2 for 45 minutes at 600°C. The catalyst was then exposed to the reaction mixture including C_3H_6 = 1000 ppm; O_2 = 4000 ppm; NO = 720-1500 ppm; H_2O = 6%, diluted in N_2. Total flowrate = 500sccm. The conversions were obtained at steady-state. (a) C_3H_6 order with respect of C_3H_6 consumption rate and CO_2 and CO formation rates; (b) Arrhenius plot obtained from NO consumption rate and N_2O, NH_3 and N_2 formation rates. N_2 rates were obtained from N-material balance.

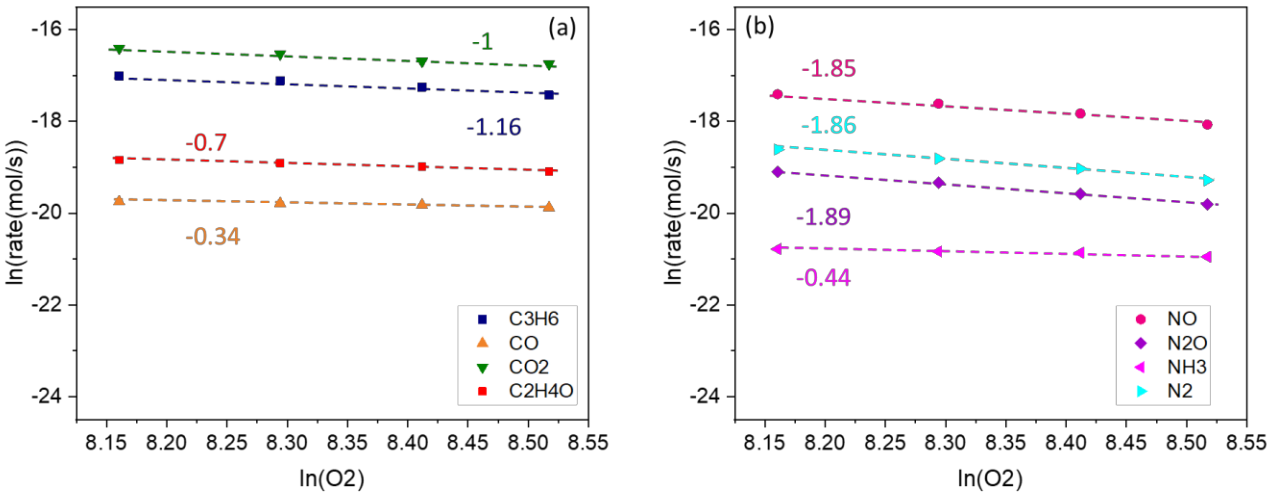

Figure C.12: O_2 reaction order at 320°C – C_3H_6 oxidation + NO + H_2O on 0.2% Pt-0.2% Rh-7.5% SrO/Al_2O_3. 50 mg of catalyst was diluted with 150 mg silica. The catalyst was reduced in 5% H_2/N_2 for 45 minutes at 600°C. The catalyst was then exposed to the reaction mixture including C_3H_6 = 1000 ppm; O_2 = 3500-5000 ppm; NO = 1000 ppm; H_2O = 6%, diluted in N_2. Total flowrate = 500sccm. The conversions were obtained at steady-state. (a) C_3H_6 order with respect of C_3H_6 consumption rate and CO_2 and CO formation rates; (b) Arrhenius plot obtained from NO consumption rate and N_2O, NH_3 and N_2 formation rates. N_2 rates were obtained from N-material balance.

Section C3: 0.2% Pt-0.2% Rh-7.5% SrO/Al_2O_3

C 3.1 CO oxidation + H_2O

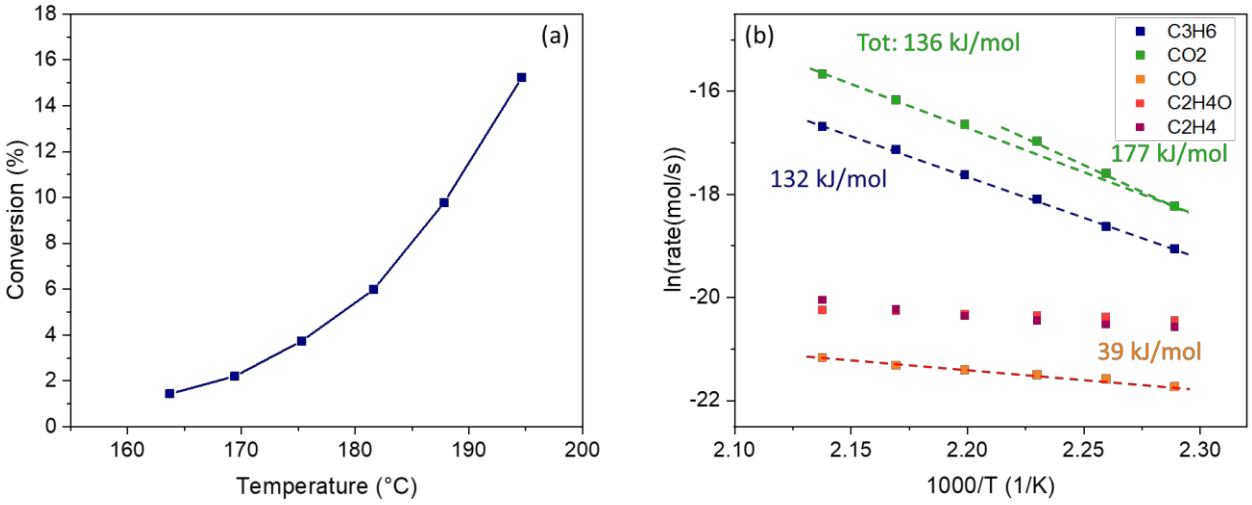

Figure C.13: C_3H_6 oxidation + H_2O on 0.2% Pt-0.2% Rh-7.5% SrO/Al_2O_3. 50 mg of catalyst was diluted with 150 mg silica. Pellet size was 250-420µm. The catalyst was reduced in 5% H_2/N_2 for 45 minutes at 600°C. The catalyst was then exposed to the reaction mixture including C_3H_6 = 1000 ppm; O2 = 4500 ppm; H_2O = 6%, diluted in N_2. Total flowrate = 500 sccm. The conversions were obtained at steady-state. (a) C_3H_6 conversion; (b) Arrhenius plot obtained from C_3H_6 consumption rate and CO_2 and CO formation rates.

C 3.2 CO oxidation + NO + H_2O

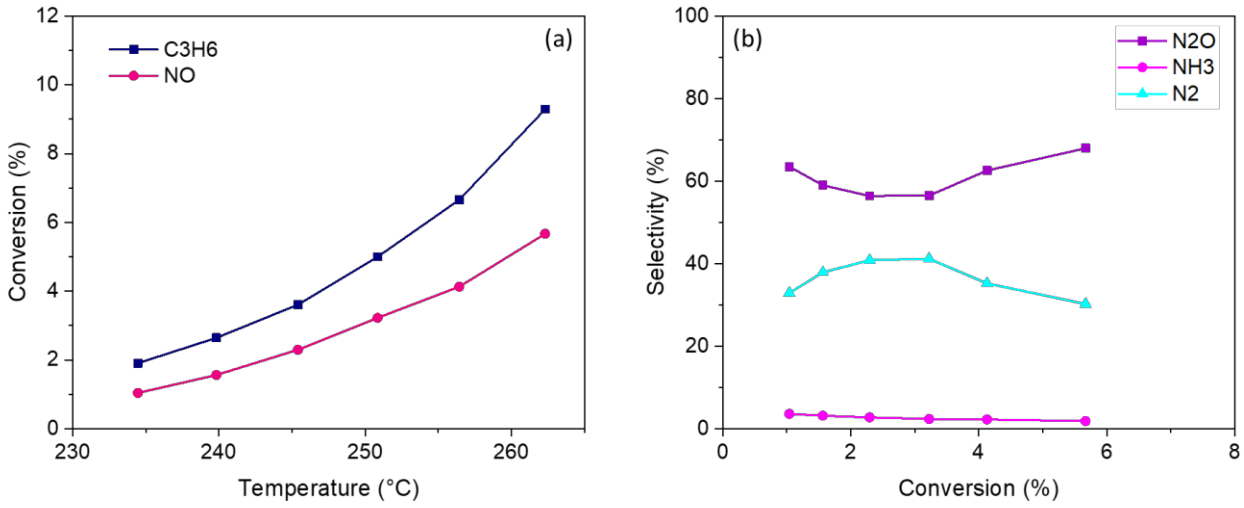

Figure C.14: C_3H_6 oxidation + NO + H_2O on 0.2% Pt-0.2% Rh-7.5% SrO/Al_2O_3. 50 mg of catalyst was diluted with 150 mg silica. The catalyst was reduced in 5% H_2/N_2 for 45 minutes at 600°C. The catalyst was then exposed to the reaction mixture including C_3H_6 = 1000 ppm; O_2 = 4000 ppm; NO = 1000 ppm; H_2O = 6%, diluted in N2. Total flowrate = 500 sccm. The conversions were obtained at steady-state. (a) C_3H_6 and NO conversions; (b) N_2O, NH_3 and N_2O Selectivity.

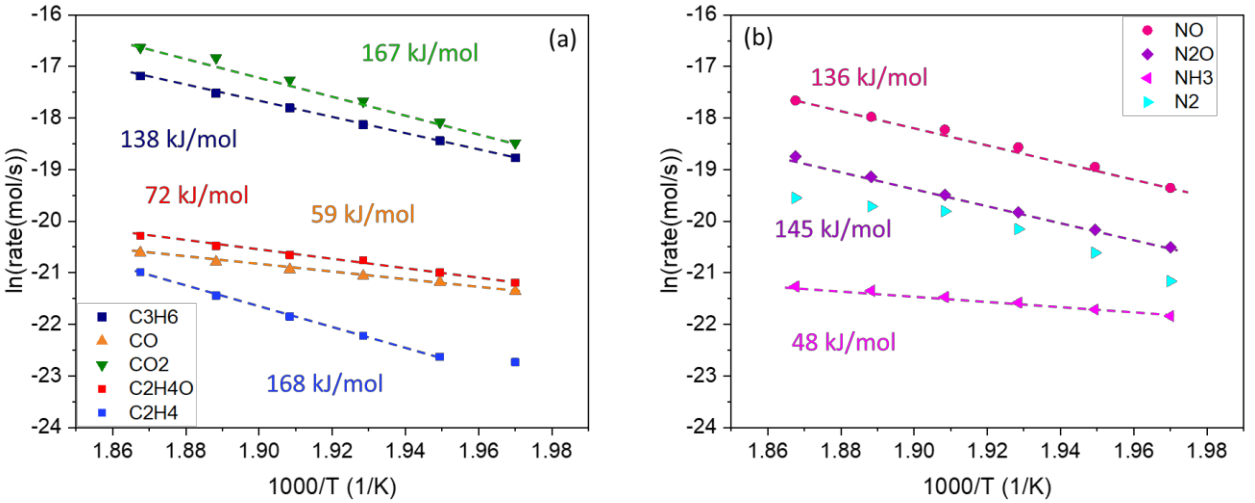

Figure C.15: C_3H_6 oxidation + NO + H_2O on 0.2% Pt-0.2% Rh-7.5% SrO/Al_2O_3. 50 mg of catalyst was diluted with 150 mg silica. The catalyst was reduced in 5% H_2/N_2 for 45 minutes at 600°C. The catalyst was then exposed to the reaction mixture including C_3H_6 = 1000 ppm; O_2 = 4000 ppm; NO = 1000 ppm; H_2O = 6%, diluted in N_2. Total flowrate = 500 sccm. The conversions were obtained at steady-state. (a) Arrhenius plot obtained from C_3H_6 consumption rate and CO_2 and CO

formation rates; (b) Arrhenius plot obtained from NO consumption rate and N_2O, NH_3 and N_2 formation rates. N_2 rates were obtained from N-material balance.

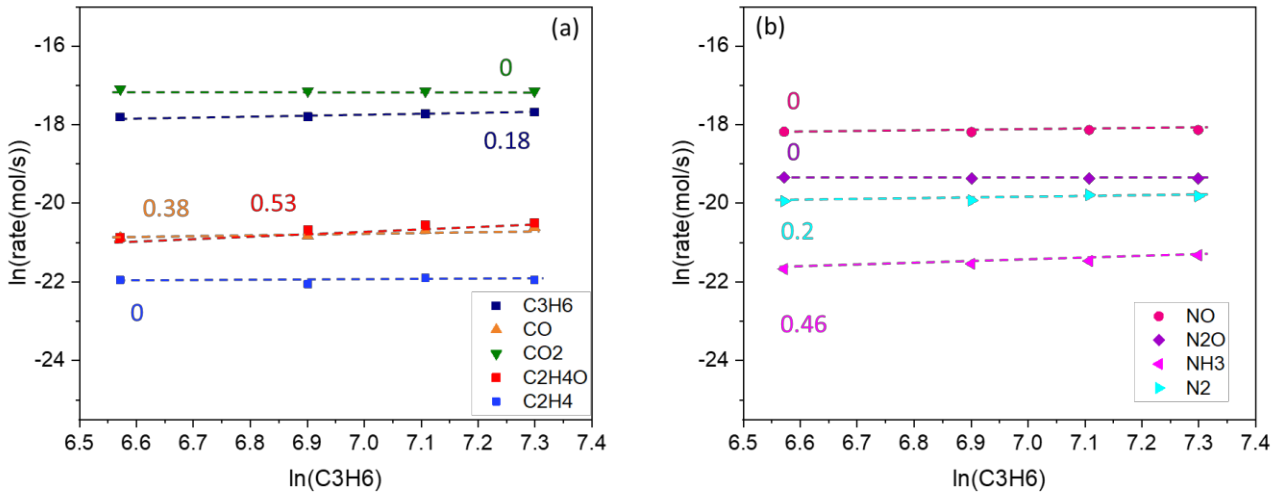

Figure C.16: C_3H_6 reaction order at 250°C – C_3H_6 oxidation + NO + H_2O on 0.2% Pt-0.2% Rh-7.5% SrO/Al_2O_3. 50 mg of catalyst was diluted with 150 mg silica. The catalyst was reduced in 5% H_2/N_2 for 45 minutes at 600°C. The catalyst was then exposed to the reaction mixture including C_3H_6 = 720-1500 ppm; O_2 = 4000 ppm; NO = 1000 ppm; H_2O = 6%, diluted in N_2. Total flowrate = 500sccm. The conversions were obtained at steady-state. (a) C_3H_6 order with respect of C_3H_6 consumption rate and CO_2 and CO formation rates; (b) Arrhenius plot obtained from NO consumption rate and N_2O, NH_3 and N_2 formation rates. N_2 rates were obtained from N-material balance.

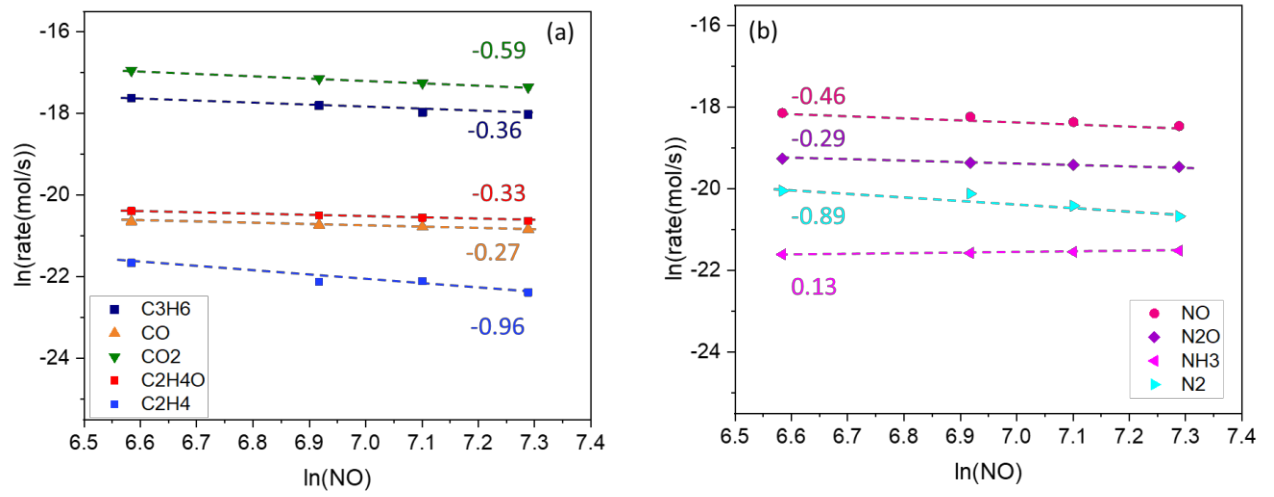

Figure C.17: NO reaction order at 250°C – C_3H_6 oxidation + NO + H_2O on 0.2% Pt-0.2% Rh-7.5% SrO/Al_2O_3. 50 mg of catalyst was diluted with 150 mg silica. The catalyst was reduced in 5% H_2/N_2 for 45 minutes at 600°C. The catalyst was then exposed to the reaction mixture including C_3H_6 = 1000 ppm; O_2 = 4000 ppm; NO = 720-1500 ppm; H_2O = 6%, diluted in N_2. Total flowrate = 500sccm. The conversions were obtained at steady-state. (a) C_3H_6 order with respect of C_3H_6 consumption rate and CO_2 and CO formation rates; (b) Arrhenius plot obtained from NO consumption rate and N_2O, NH_3 and N_2 formation rates. N_2 rates were obtained from N-material balance.

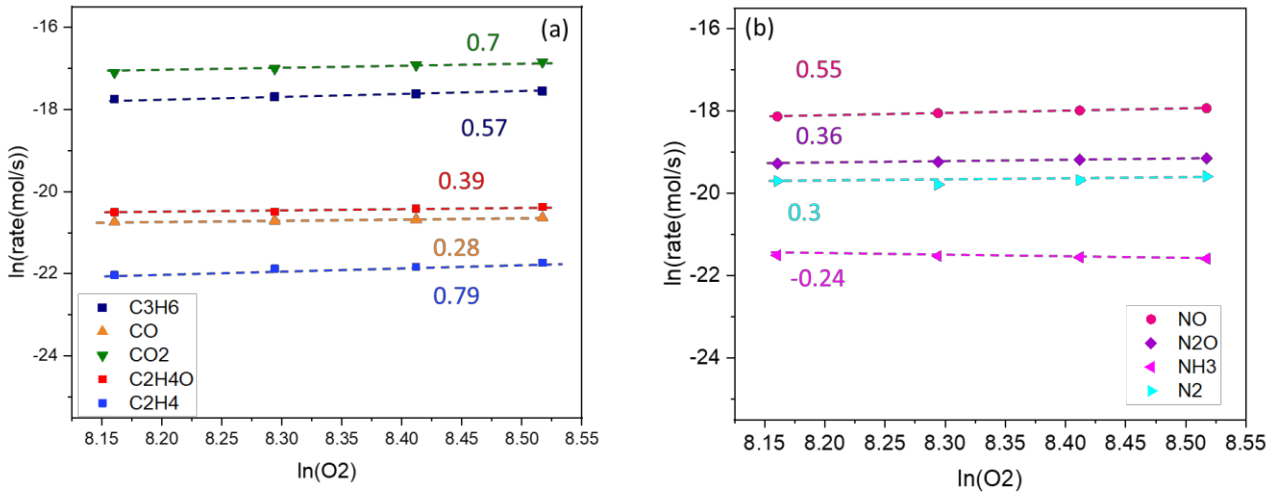

Figure C.18: O_2 reaction order at 250°C – C_3H_6 oxidation + NO + H_2O on 0.2% Pt-0.2% Rh-7.5% SrO/Al_2O_3. 50 mg of catalyst was diluted with 150 mg silica. The catalyst was reduced in 5% H_2/N_2 for 45 minutes at 600°C. The catalyst was then exposed to the reaction mixture including C_3H_6 = 1000 ppm; O_2 = 3500-5000 ppm; NO = 1000 ppm; H_2O = 6%, diluted in N_2. Total flowrate = 500sccm. The conversions were obtained at steady-state. (a) C_3H_6 order with respect of C_3H_6 consumption rate and CO_2 and CO formation rates; (b) Arrhenius plot obtained from NO consumption rate and N_2O, NH_3 and N_2 formation rates. N_2 rates were obtained from N-material balance.

Section 4: 0.2% Pt-0.2% Rh/Al_2O_3

C 4.1 C_3H_6 oxidation + H_2O

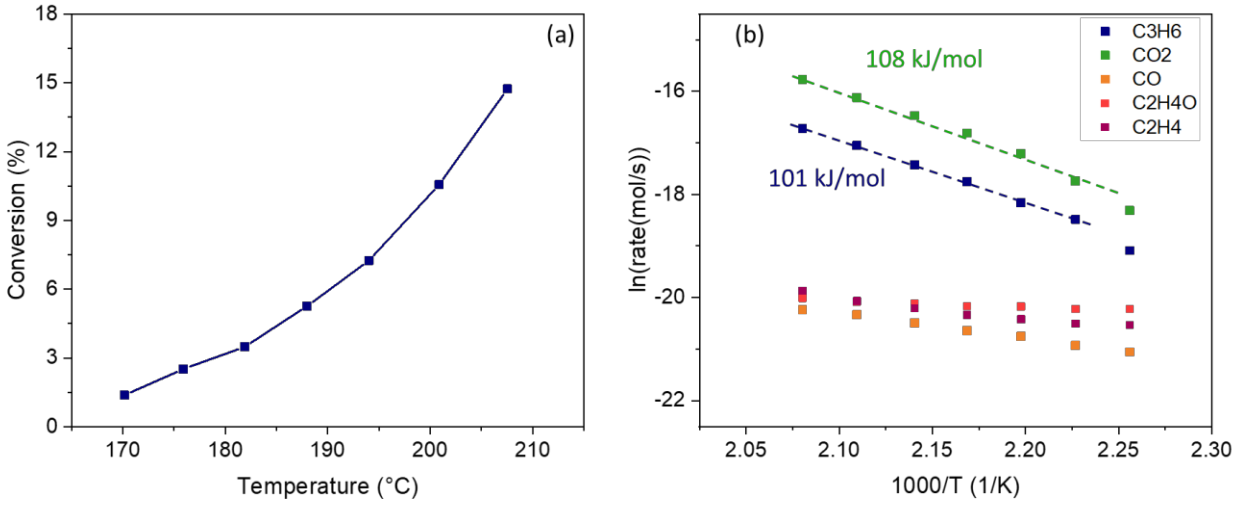

Figure C.19: C_3H_6 oxidation + H_2O on 0.2% Pt-0.2% Rh/Al_2O_3. 50 mg of catalyst was diluted with 150 mg silica. Pellet size was 250-420µm. The catalyst was reduced in 5% H_2/N_2 for 45 minutes at 600°C. The catalyst was then exposed to the reaction mixture including C_3H_6 = 1000 ppm; O_2 = 4500 ppm; H_2O = 6%, diluted in N_2. Total flowrate = 500 sccm. The conversions were obtained at steady-state. (a) C_3H_6 conversion; (b) Arrhenius plot obtained from C_3H_6 consumption rate and CO_2 and CO formation rates.

C 4.2 C_3H_6 oxidation + NO + H_2O

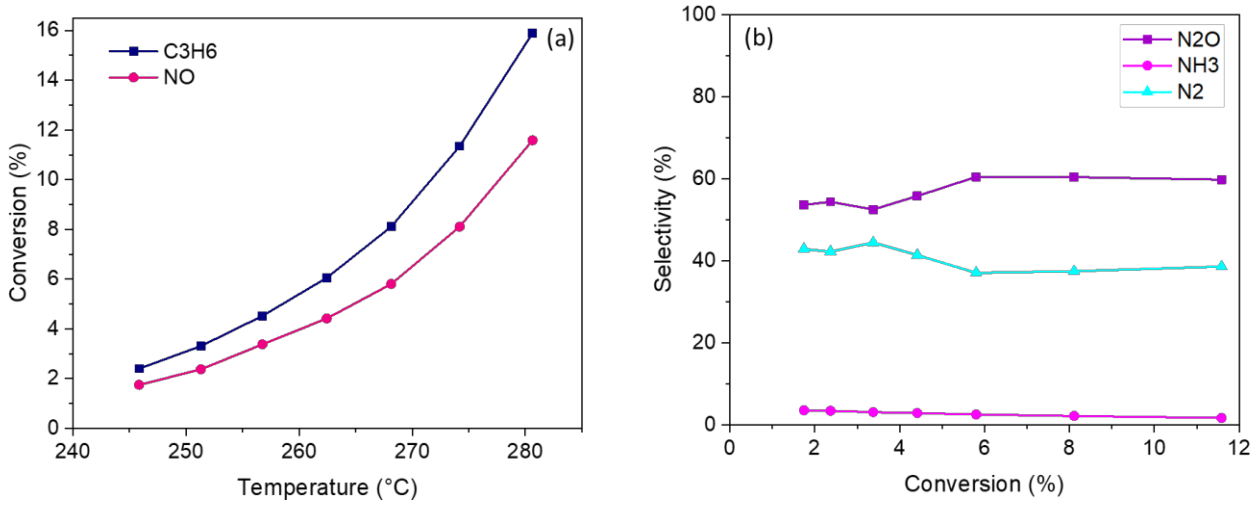

Figure C.20: C_3H_6 oxidation + NO + H_2O on 0.2% Pt-0.2% Rh/Al_2O_3. 50 mg of catalyst was diluted with 150 mg silica. The catalyst was reduced in 5% H_2/N_2 for 45 minutes at 600°C. The catalyst was then exposed to the reaction mixture including C_3H_6 = 1000 ppm; O_2 = 4000 ppm; NO = 1000 ppm; H_2O = 6%, diluted in N_2. Total flowrate = 500 sccm. The conversions were obtained at steady-state. (a) C_3H_6 and NO conversions; (b) N_2O, NH_3 and N_2O Selectivity.

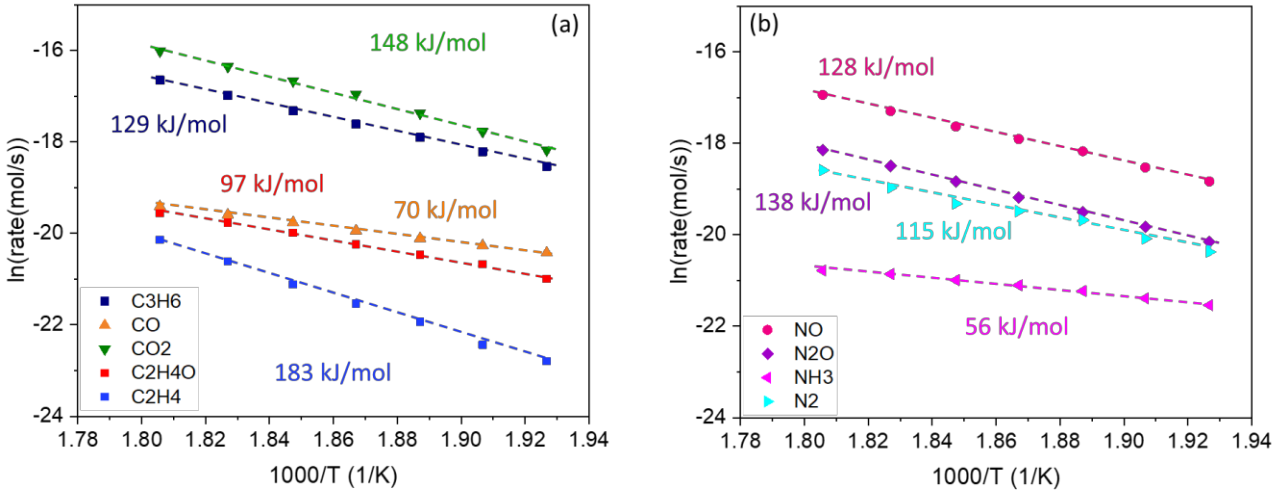

Figure C.21: C_3H_6 oxidation + NO + H_2O on 0.2% Pt-0.2% Rh/Al_2O_3. 50 mg of catalyst was diluted with 150 mg silica.The catalyst was reduced in 5% H_2/N_2 for 45 minutes at 600°C. The catalyst was then exposed to the reaction mixture including C_3H_6 = 1000 ppm; O_2 = 4000 ppm; NO = 1000 ppm; H_2O = 6%, diluted in N_2. Total flowrate = 500 sccm. The conversions were obtained at steady-state. (a) Arrhenius plot obtained from C_3H_6 consumption rate and CO_2 and CO

formation rates; (b) Arrhenius plot obtained from NO consumption rate and N_2O, NH_3 and N_2 formation rates. N_2 rates were obtained from N-material balance.

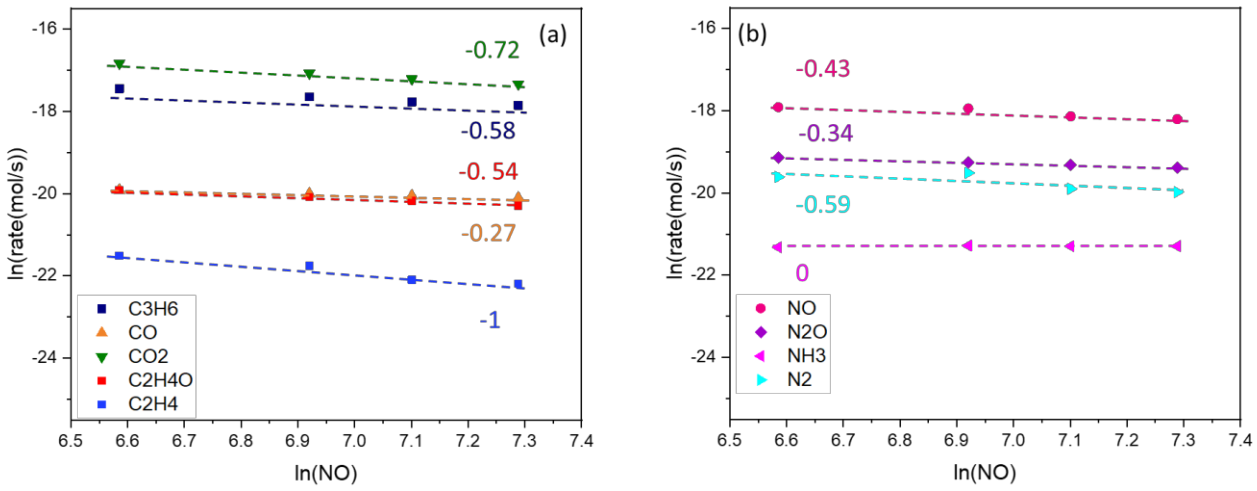

Figure C.22: C_3H_6 reaction order at 260°C – C_3H_6 oxidation + NO + H_2O on 0.2% Pt-0.2% Rh/Al_2O_3. 50 mg of catalyst was diluted with 150 mg silica. The catalyst was reduced in 5% H_2/N_2 for 45 minutes at 600°C. The catalyst was then exposed to the reaction mixture including C_3H_6 = 720-1500 ppm; O_2 = 4000 ppm; NO = 1000 ppm; H_2O = 6%, diluted in N_2. Total flowrate = 500sccm. The conversions were obtained at steady-state. (a) C_3H_6 order with respect of C_3H_6 consumption rate and CO_2 and CO formation rates; (b) Arrhenius plot obtained from NO consumption rate and N_2O, NH_3 and N_2 formation rates. N_2 rates were obtained from N-material balance.

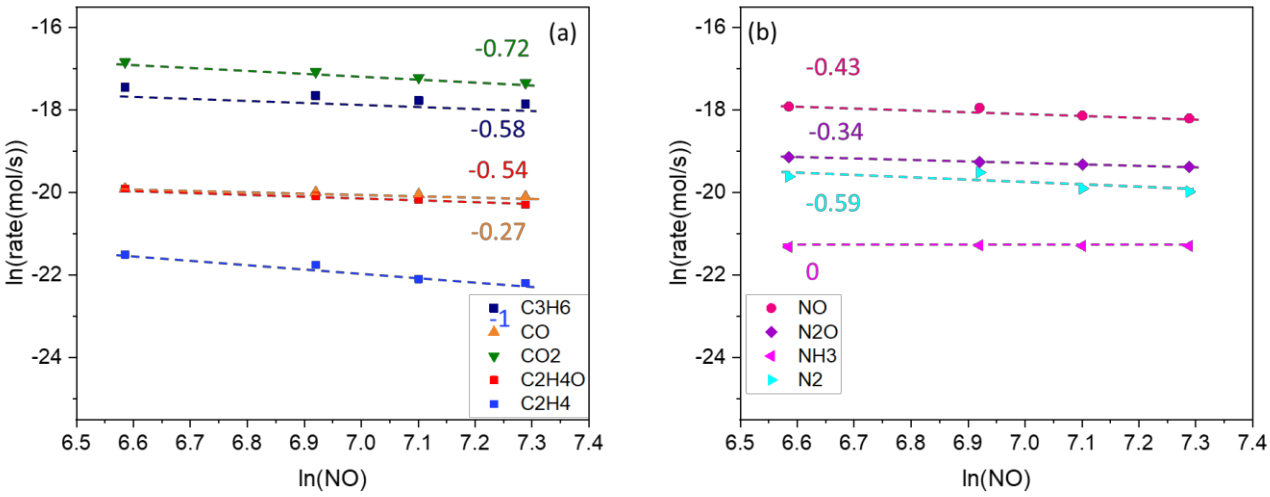

Figure C.23: NO reaction order at 260°C – C_3H_6 oxidation + NO + H_2O on 0.2% Pt-0.2% Rh/Al_2O_3. 50 mg of catalyst was diluted with 150 mg silica. The catalyst was reduced in 5% H_2/N_2 for 45 minutes at 600°C. The catalyst was then exposed to the reaction mixture including C_3H_6 = 1000 ppm; O_2 = 4000 ppm; NO = 720-1500 ppm; H_2O = 6%, diluted in N_2. Total flowrate = 500sccm. The conversions were obtained at steady-state. (a) C_3H_6 order with respect of C_3H_6 consumption rate and CO_2 and CO formation rates; (b) Arrhenius plot obtained from NO consumption rate and N_2O, NH_3 and N_2 formation rates. N_2 rates were obtained from N-material balance.

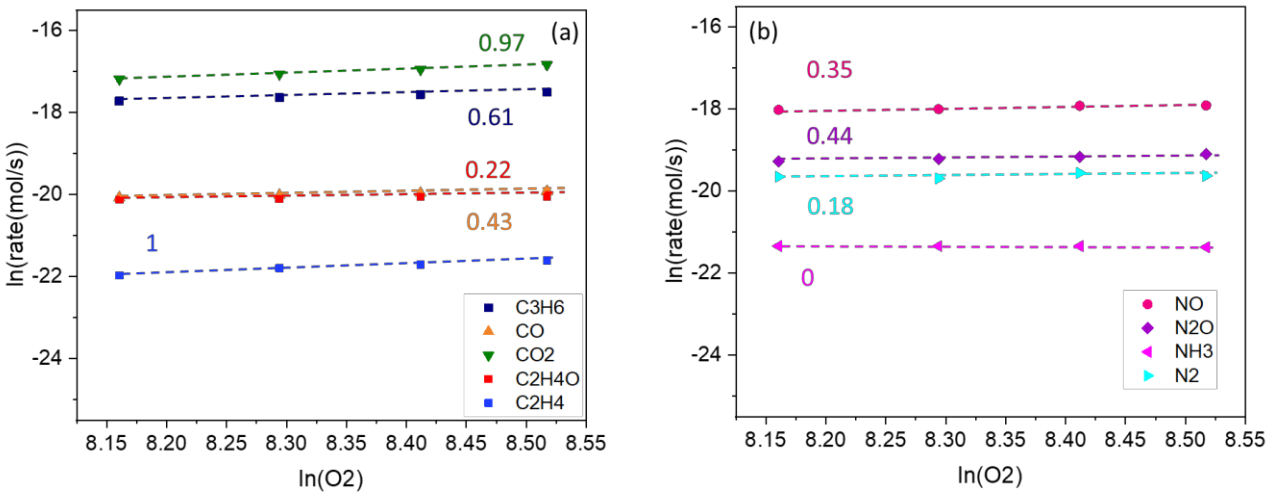

Figure C.24: O_2 reaction order at 260°C – C_3H_6 oxidation + NO + H_2O on 0.2% Pt-0.2% Rh/Al_2O_3. 50 mg of catalyst was diluted with 150 mg silica. The catalyst was reduced in 5% H_2/N_2 for 45 minutes at 600°C. The catalyst was then exposed to the reaction mixture including C_3H_6 = 1000 ppm; O_2 = 3500-5000 ppm; NO = 1000 ppm; H_2O = 6%, diluted in N_2. Total flowrate = 500sccm. The conversions were obtained at steady-state. (a) C_3H_6 order with respect of C_3H_6 consumption rate and CO_2 and CO formation rates; (b) Arrhenius plot obtained from NO consumption rate and N_2O, NH_3 and N_2 formation rates. N_2 rates were obtained from N-material balance.